UNIVERSITY OF CALGARY

Nonlinear dynamics of mathematical models and proposed implementations in ultracold atoms

by

Hon Wai Lau

A THESIS

SUBMITTED TO THE FACULTY OF GRADUATE STUDIES

IN PARTIAL FULFILLMENT OF THE REQUIREMENTS FOR THE

DEGREE OF DOCTOR OF PHILOSOPHY

GRADUATE PROGRAM IN PHYSICS AND ASTRONOMY

CALGARY, ALBERTA

JULY, 2017

Abstract

Nonlinear effects are ubiquitous in nature. Many interesting phenomena are described by differential equations that are nonlinear. Even richer dynamics can be observed with additional long-range spatial coupling. For example, an interesting type of pattern discovered recently can form in systems with nonlocal coupling. The pattern, called chimera states, is composed of both phase coherent and incoherent regions coexisting in the same system. Through numerical studies of oscillatory media with nonlocal diffusive coupling, I show here for the first time that stable chimera knot structures can exist in 3D. Knots were not previously known to be stable in oscillatory media, nor were such non-trivial chimera patterns known to exist in 3D.

To realize different nonlinear phenomena in a controlled way in experiments, a flexible physical system is required. Ultracold atomic systems, specifically, Bose-Einstein condensates (BECs), are good candidates because of the high controllability of almost all parameters, including the nonlinearity, in real time. Hence, experimental studies can be carried out for a variety physical systems, including many classical and quantum field equations. In particular, in this thesis I study a setup of BECs with a third-order Kerr nonlinearity to generate Schrödinger cat states, which have applications in quantum metrology. I showed that cat states involving hundreds of atoms should be realizable in BECs. This requires careful optimization of the experimental parameters and analysis of the atom loss.

Inspired by the previous two projects, it is an interesting question if chimera states can exist in BECs. By analyzing the underlying mechanism of the effective nonlocal diffusive coupling, I establish here a new analogous mechanism to achieve mediated nonlocal spatial hopping for particles in BECs with two interconvertible states. By adiabatically eliminating the fast mediating channel, I obtain the mean-field of Bose-Hubbard model with fully tunable hopping strength, hopping range, and nonlinearity. This is the first known conservative system exhibiting chimera patterns. More importantly, I show that the model should be implementable in BECs with current technology.

List of all published papers during PhD

1. Hon Wai Lau, Jörn Davidsen, Christoph Simon, "Matter-wave mediated hopping in ultracold atoms: Chimera patterns in conservative systems", To be submitted.

2. Hon Wai Lau, Jörn Davidsen, "Linked and knotted chimera filaments in oscillatory systems", Phys. Rev. E 94, 010204(R) (2016). [arXiv:1509.02774]

3. Mohammadsadegh Khazali, Hon Wai Lau, Adam Humeniuk, Christoph Simon, "Large Energy Superpositions via Rydberg Dressing", Phys. Rev. A 94, 023408 (2016). [arXiv:1509.01303]

4. Tian Wang, Hon Wai Lau, Hamidreza Kaviani, Roohollah Ghobadi, Christoph Simon, "Strong micro-macro entanglement from a weak cross-Kerr nonlinearity", Phys. Rev. A 92, 012316 (2015). [arXiv:1412.3090]

5. Hon Wai Lau, Zachary Dutton, Tian Wang, Christoph Simon, "Proposal for the Creation and Optical Detection of Spin Cat States in Bose-Einstein Condensates", Phys. Rev. Lett. 113, 090401 (2014). [arXiv:1404.1394]

6. Hon Wai Lau, Peter Grassberger, "Information theoretic aspects of the two-dimensional Ising model", Phys. Rev. E 87, 022128 (2013). [arXiv:1210.5707]

7. Hon Wai Lau, Maya Paczuski, Peter Grassberger, "Agglomerative percolation on bipartite networks: Nonuniversal behavior due to spontaneous symmetry breaking at the percolation threshold", Phys. Rev. E 86, 011118 (2012). [arXiv:1204.1329]

Acknowledgements

First of all, I would like to express my deep gratitude to Christoph Simon, my PhD supervisor, for his patience, encouragement, and advises, during my PhD study. He is able to give excellent guidance even if the projects I worked on is outside of his expertise. Research in our group is enjoyable, since he is actively improving the environment and reducing the stress of students. I am always impressed by his ability to find out the key points in new papers only in couple of seconds and to simplify complicated problems.

I especially thanks for the complexity science group at University of Calgary during my early PhD. The group was great and I enjoyed the occasional brainstorming with Peter Grassberger. I hoped that I could have worked with him for longer time. I also thanks for the guidance from Jörn Davidsen, in which the works with him formed part of this thesis. Thanks Golnoosh Bizhani, Aicko Yves Schumann, Chad Gu, and Arsalan Sattari for the advises during my hard time.

It was a great pleasure to work with my group members. I have had lots of long and insightful discussions, not only limited to academics, with Stephen Wein, Tian Wang, Sourabh Kumar, Sandeep Goyal, Mohammadsadegh Khazali, James Moncreiff, Sumit Goswami, Farid Ghobadi, and Khabat Heshami. Thanks for my friends Wei-wei Zhang, Akihiko Fujii, Jiawei Ji, Yadong Wu, Adarsh Prasad, Ish Dhand, and many others and people I met during my study here. All of them make the life here more fun.

I would also like to thank for the collaborators and the academic help from Farokh Mivehvar, Zachary Dutton, Lindsay J. LeBlanc, and the people that I get help through email exchanges including someone who I never met before. Thanks David Hobill, Michael K. Y. Wong, Alex Lavovsky, Barry Sanders, David Feder, and Maya Paczuski for sharing their knowledge, as well as offering academic and career advises.

A special thank goes to Kwok Yip Szeto, my undergraduate and MPhil research supervisor, for leading me into the academic world.

I would like to express my thanks to all my old friends in Hong Kong and scattered over the world. Specifically, the friends going through the academic life and exchanging experiences with me: Yun kuen Cheung, Cheung Chan, Alan Fung, Alan Tam, Lokman Tsui, Tin Yau Pang. They are like my companions in this long academic journey.

Last but not least, I would like to thank my parents, sister, and brother for their supports, which allows me to pursue my goal freely.

Table of Contents

List of Symbols, Abbreviations and Nomenclature

Symbol	Definition
BEC	Bose-Einstein Condensate
GPE	Gross-Pitaevskii equation
CLGE	Complex Ginzburg-Landau equation
IC	Initial condition
BC	Boundary condition
1D	One dimension
2D	Two dimension
3D	Three dimension
SDS	Synchronization defect sheets
TFA	Thomas-Fermi approximation
CSS	Coherent spin state
BHM	Bose-Hubbard model
NLHM	nonlocal hopping model

Chapter 1

Introduction

Many interesting dynamics and physical phenomena observed in nature can only be modeled by nonlinear differential equations. These phenomena include chaos, solitons, and many patterns that are unique to nonlinear systems. One of the most famous nonlinear differential equations yielding a variety of different patterns is the complex Ginzburg-Landau equation (CGLE) [1, 2], which describes many physical systems phenomenologically, such as superconductivity and nonlinear waves. The CGLE is famous because it is the normal form of any system close to a Hopf bifurcation - a critical point where a stationary system begins to oscillate [2, 3].

Chimera states are a particular type of pattern that have been recently discovered [4, 5], which are states that contain oscillators synchronized in some region, but unsynchronized in another region (see Fig. 1.3). This happens for oscillators that are completely identical. It is understood that the nonlocal diffusive coupling plays a key role in the formation of most chimera patterns. In particular, many chimera patterns can be observed in the nonlocal CGLE in 1D and 2D [6, 7]. In this thesis, I will present a new chimera pattern called chimera knots in 3D that have never been seen before [8]. It is a pattern with synchronized regions everywhere except around a knot structure in 3D. This is an important discovery because no stable knots were known to exist with local coupling in CGLE, or more generally, oscillatory media.

Another famous and related nonlinear differential equation is the Gross-Pitaevskii equation (GPE) [9], which was derived as a mean-field description of Bose-Einstein condensates (BECs). A BEC is a state with all bosons occupying the same single particle state [10]. Hence, in the limit of large numbers of particles, a simple description is possible by taking the mean of the corresponding quantum field equation . The GPE is the Schrödinger equation but with an extra nonlinearity originating from two-particle collisions, and it is identical to the CGLE in certain

parameter regimes.

In quantum systems, the nonlinearity from two-particle collisions can be used to generate Schrödinger cat states, which are superpositions of two macroscopically distinct states. The cat states in BECs can involve many atoms and are very sensitive to particle loss. Even the loss of a single particle can cause significant decoherence and destroy the cat states. Therefore, analyzing the effects of particle loss is important when making practical scheme proposals. Large cat states have applications from precise quantum metrology that can surpass the standard quantum limit, to detect the hypothetical energy collapse model [11]. In this thesis, I will propose and analyze a scheme using two-component BECs to generate cat states [12].

The differential equations CGLE and GPE are very similar to each other. For example, both of them have a third-order nonlinearity, are equivalent in some regime, and show similar patterns. This close relationship between CGLE and GPE suggests that chimera states may also exist in BECs. As mentioned, the nonlocal diffusive coupling in the CGLE is important for chimera states, so it is reasonable to speculate that there may be an analogue for the GPE too. After studying the underlying mediating mechanism of the nonlocal diffusive coupling, I have found such an analogue to be the mediated nonlocal hopping. The idea is similar to the typical mediating mechanisms for particle-particle interactions such as Coulomb's law: The complete description typically involves the consideration of the particle-field-particle interaction. However, if the field is orders of magnitude faster than the interesting dynamics of the particles, then the field can be eliminated adiabatically, resulting in an effective, simple, and instantaneous nonlocal description. By using two-component BECs with one of the components treated as a mediating channel with matter-wave as a mediating field, I show that an effective mediated nonlocal hopping can appear. This nonlocal hopping model (NLHM) allows experimentally tunable hopping range, hopping strength and, nonlinearity. Since ultracold atomic BECs are highly controllable, I have also found an experimentally realistic parameter regime in which my proposed mechanism should work, and where chimera states should be observable. This discovery will allow the study of chimera states in BECs

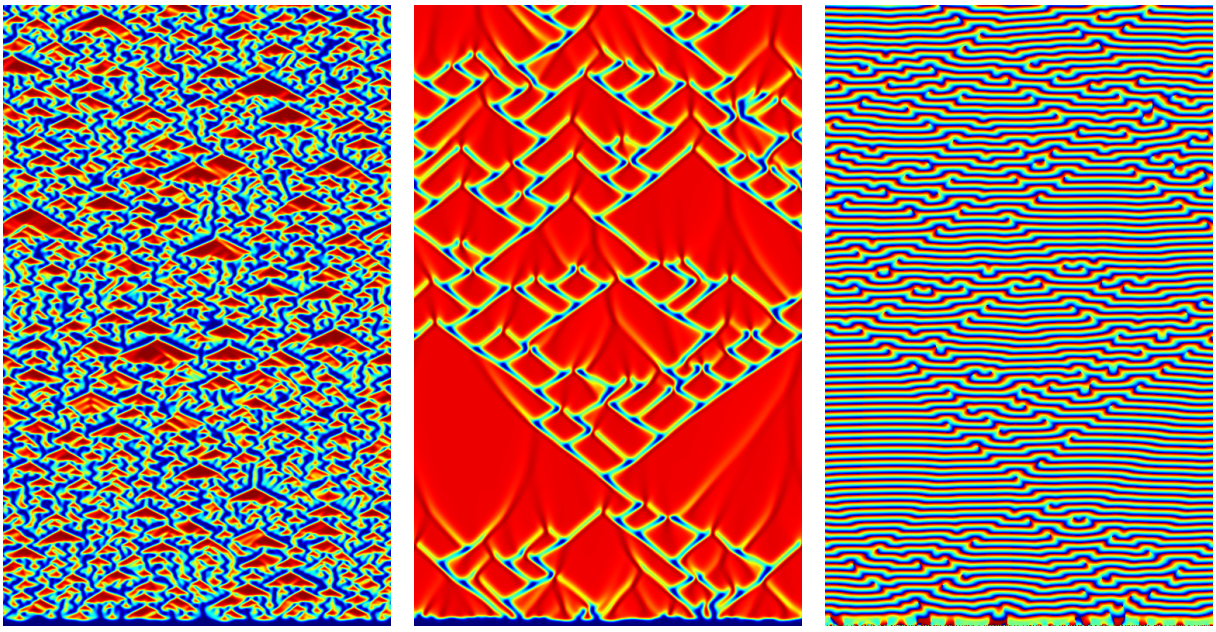

(a) (b) (c)

Figure 1.1: Spatio-temporal patterns in 1D. The horizontal axis is space x, and the vertical axis is time t. Values increases from blue to red. (a,b) Amplitude $A(x,t)$ of two systems. (c) Phase $\theta(x,t)$ of (b).

and conservative systems. The quantization of this NLHM is the Bose-Hubbard model [13] with nonlocal hopping, and there are likely interesting physics and quantum phases to be discovered.

In the remainder of this chapter, I will introduce the three main topics involved in this thesis: chimera states, cat states, and Bose-Einstein condensates. The theoretical background required to understand my results will be presented in the following chapter.

1.1 A new type of pattern - chimera states

Various interesting structures exist everywhere in nature, and easily recognizable structures are often referred to as patterns [3, 15, 16, 17]. A pattern may be considered as a high-level macroscopic description of the structures in different subparts of a given system. Patterns are usually visually distinct such as the spatio-temporal patterns in Fig. 1.1, or snapshots of spatial patterns in Fig. 1.2. These distinct features suggest that mathematical modeling is possible. For example, if the local dynamics of every spatial location $\mathbf{r}$ are oscillators, then the system may be described by two

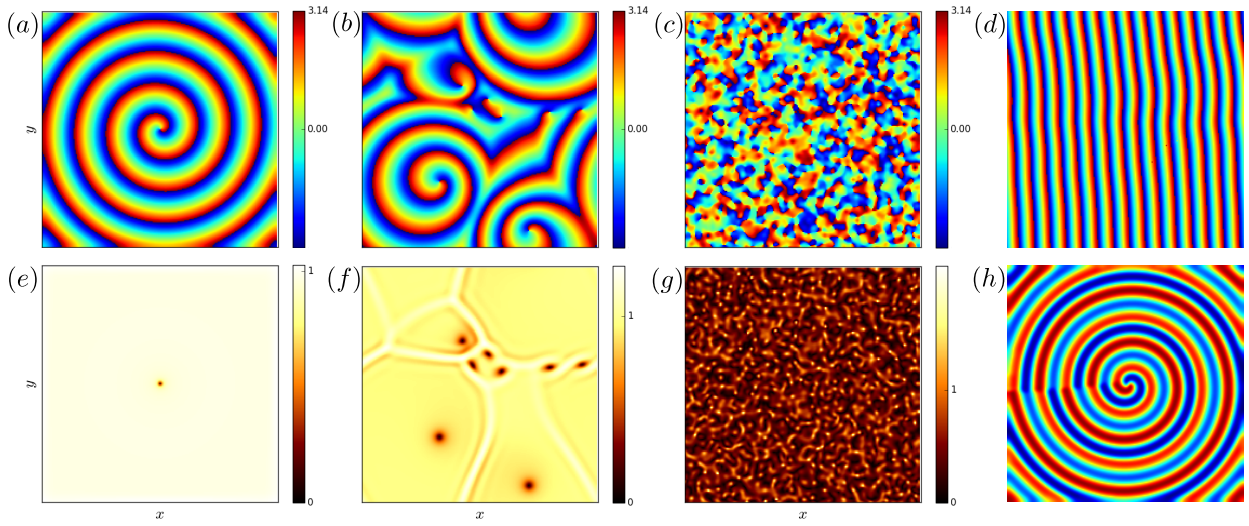

Figure 1.2: Snapshots of the patterns of in 2D. Amplitude $A(\mathbf{r},t)$ and phase $\theta(\mathbf{r},t)$ for (a,e) a single spiral, (b,f) multiple spirals, and (c,g) turbulence-like pattern. (d) Plane wave. (h) A line defect from the center to the left edge in Rössler model [14].

dynamical variables, the amplitude field $A(\mathbf{r},t)$ and the phase field $\theta(\mathbf{r},t)$. A new type of pattern called chimera states has been discovered recently, as shown Fig. 1.3a-e. The visual feature of this pattern is the coexistence of phase coherence in one region and phase incoherence in another region.

This chimera pattern is surprising because it can exist in a system with identical oscillators and identical coupling between oscillators. Before the discovery in 2002, for a long time, a network of identical oscillators was believed to be relatively boring with only two possibilities: Fully coherent or incoherent [5]. This viewpoint changed in 2002 when Yoshiki Kuramoto and his collaborator Dorjsuren Battogtokh were studying a ring of identically and nonlocally coupled phase oscillators [4]. They discovered that, for certain initial conditions, some of the oscillators can synchronize while the remaining oscillators are incoherent. This happens even in systems with translational and rotational symmetry in 2D studied in the follow-up studies [7, 18, 19]. The patterns include coherent and incoherent spots, stripes and spirals with randomized cores as shown in Fig. 1.3. The term chimera state was coined by Steve Strogatz [20] in 2004 because of the similarity with the Greek mythological creature composed of different animals.

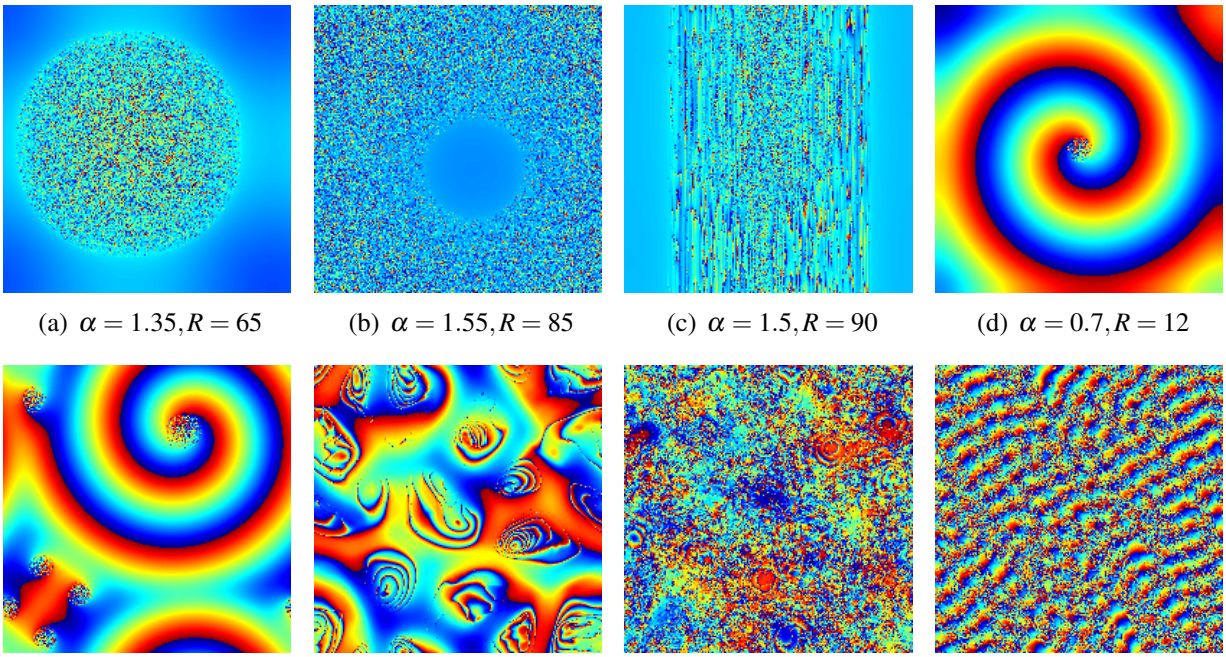

(a) $\alpha = 1.35, R = 65$ (b) $\alpha = 1.55, R = 85$ (c) $\alpha = 1.5, R = 90$ (d) $\alpha = 0.7, R = 12$

(e) $\alpha = 0.85, R = 12$ (f) $\alpha = 1.2, R = 12$ (g) $\alpha = 1.55, R = 12$ (h) $\alpha = 1.7, R = 12$

Figure 1.3: Snapshots of patterns observed in the nonlocal Kuramoto model (see Chapter 3). The plots are the phase $\theta(\mathbf{r},t)$ of oscillators. (a) Incoherent spot. (b) Coherent spot. (c) Chimera strip. (d) Incoherent core with a spiral. (e) Multiple incoherent cores. (f) Irregular pattern with the expansion of cores. (g) Near-random pattern. (h) Completing plane wave. Initial condition for all patterns are random phase, except (d) which starts from a spiral. Each direction has length $L = 200$ oscillators.

Only a decade later, in 2012, the existence of chimera states in experimental systems was confirmed in two demonstrations. The first one used photosensitive chemical oscillators with the light feedback coupling in a two-cluster setup [21], and later in a 1D ring [22]. The second experiment used a coupled map lattice with coupling through camera detections and light feedback [23]. The criticism of computer-controlled coupling was addressed by a third experiment using pure mechanical oscillators in 2013 [24]. The success of these experiments raises the interest of explaining physical phenomena in systems that resemble oscillator dynamics such as brains, hearts, and power grids [5].

As mentioned above, a chimera state is defined as a state with subpopulations that are mutually synchronized and the remaining populations unsynchronized. The term synchronization, as defined in [25], is the adjustment of rhythms of oscillating objects due to their weak interaction. A simple

harmonic oscillator is an example of an oscillating object. Most oscillators with multiple oscillating cycles need an input of energy to be self-sustained such as clocks, pendulum, lasers, chemical oscillation, pacemakers, and neuron activity. For these systems, a natural frequency ω_0 and phase θ can be defined. The coupling between oscillators change the rhythms, or the oscillating frequency and phase dynamics, of the oscillators. The synchronization of oscillators occurs when different natural frequencies that become locked to a common frequency due to weak coupling [26]. The simplest mathematical modeling for this phenomenon is the Kuramoto model [27].

The fact that coherent and incoherent regions can coexist in systems with completely identical oscillators is a prime example of the spontaneous breaking of synchrony. It is worth mentioning that with specially selected natural frequencies and couplings, patterns similar to chimera states may be created [5], which may not be considered as chimera states. Chimera states can appear as spatio-temporal patterns in 1D, 2D, two-cluster, and complex networks as listed in Ref. [5]. Numerical simulations suggest that most chimera states are stable, as well as robust against noises and perturbations. A few chimera states in 1D are known to be transient states with a long lifetime and become stable in the thermodynamic limit [28]. There are many classifications of chimera states. For example, stationary chimera patterns have a stationary boundary between coherence and incoherence regions as shown in Fig. 1.3(a-c), but still show phase randomness in time. In this case, an ansatz may be used to simplify the analysis of the stability [29, 30].

Oscillatory media are continuous media where each spatial point can be treated as an oscillator locally [16]. While in general continuous media $u(\mathbf{r},t)$ with space $\mathbf{r}$, time t, and field u continuum can be described by partial differential equations. Therefore, synchronization can exist in oscillatory media because oscillator dynamics exist locally and are coupled through, say, diffusion of the form $\nabla^2 u$. One of the most-studied and well-known equations for oscillatory media is the complex Ginzburg-Landau equation (CGLE) [1]. It is the normal form of all oscillatory media close to a supercritical Hopf bifurcation [17]. A Hopf bifurcation happens when tuning a control parameter causes a stable point in phase space to become a stable limit cycle oscillation.

The developments of CGLE can be traced back to the early work of Lev Davidovich Landau on phase transitions in 1937 [31, 32]. Later in 1950, together with Vitaly Lazarevich Ginzburg, they postulated the Ginzburg-Landau theory as a phenomenological description of superconductors [33]. Similar equations were eventually found to provide good descriptions of diverse phenomena including nonlinear waves, Rayleigh-Bénard convection, and Bose-Einstein condensates. An example of oscillatory media is reaction-diffusion systems where the local reactions behave like self-sustained oscillators and are coupled through spatial diffusion. Experimentally, it can be realized by chemical oscillations such as the Belousov-Zhabotinsky chemical reaction [2].

Nonlocal coupling plays a key role in most formations of spatial patterns of chimera states. As shown in the original works in 1D and 2D [4, 7], chimera states can be observed in the nonlocal CGLE where the typical diffusion term is replaced by a nonlocally coupled term, and later in the simplified nonlocal Kuramoto model [18]. A study of chimera states in 3D only happened recently [34]. In 3D, the point-like phase singularity in 2D at the center of Fig. 1.2a will become a line-like structure, often called a filament. The spiral wave in 2D becomes a scroll wave in 3D. Instead of a straight filament, filaments can also be closed like a ring. The stability of straight filaments, rings, and twisted filaments have been studied [35, 36]. However, no stable knots and links such as Hopf links (two intertwined rings) and trefoils have been observed. In contrast, stable knots and links exist in excitable media [37, 38]. The local dynamics of excitable media is normally in a stable non-oscillating state, and will only go through an oscillating cycle when the perturbation is large enough. Excitable media are very similar to oscillatory media and show many similar patterns, so it is surprising that knot structures are not stable in oscillatory media. On the other hand, the incoherent core in 2D in Fig. 1.3d should become a tube-like structure filled with incoherent oscillators in 3D. This suggests there are structures combining line-like topological structures with chimera structures in 3D, as studied in [34]. It is reasonable to expect that stable knots may also exist. The existence of stable chimera knots in oscillatory media with nonlocal coupling is the theme of Chapter 3.

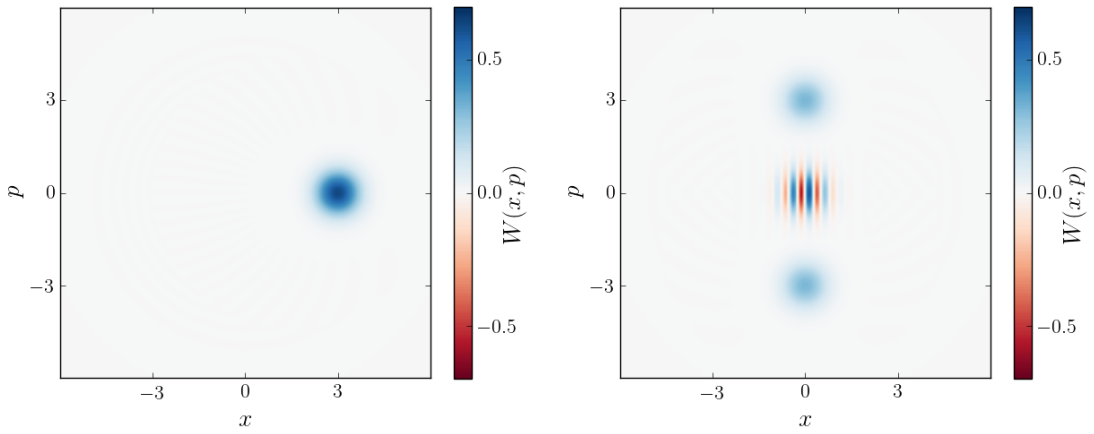

(a) A coherent state (b) A cat state

Figure 1.4: Quasi-probability distribution of (a) a coherent state, (b) and a cat state, which is the superposition of two coherent states. The negative values in the fringes indicate the non-classicality of the state.

As a new research field, there are still many open questions about the nature of chimera states as listed in a review paper [5] such as the stability criteria, the necessary conditions for chimera states, and their relationship with resonance. All chimera states studied until now occur in driven-dissipative systems that are out of equilibrium. In Chapter 5, I will present the existence of chimera states in conservative Hamiltonian systems. Moreover, there is evidence that chimera states may also exist in BECs with a mediated nonlocal hopping, which is an analogue of the nonlocal coupling in the CGLE.

1.2 Quantum effects in macroscopic systems - Schrödinger cat states

One of the most striking aspects of quantum mechanics is the superposition and entanglement of particles, which have no counterpart in classical systems. In particular, quantum nonlocality due to entanglement between particles has been conclusively proven in a series of recent experiments. Loophole free tests of the violation of Bell's inequality were finally performed by Ronald Hanson's group [39], shortly followed by Anton Zeilinger's group [40] and Lynden Shalm's group [41] in 2015. There is little doubt that quantum mechanics is the correct description of reality at the

microscopic level. However, it is still an open question if quantum mechanics is correct on all scales. After all, the current form of quantum mechanics is incompatible with general relativity.

The mathematical description of quantum systems has various interpretations that are not intuitive. To illustrate the counter-intuitive nature of applying quantum mechanics to macroscopic objects, in 1935, Schrödinger proposed a thought experiment now known as Schrödinger's cat [42]. In quantum mechanics, a quantum system can be in a superposition of two states, which can interact differently with a macroscopic object, say, a cat. Suppose the decay of a radioactive atom triggers a mechanism to kill the cat, while the non-decayed atom will do nothing. If quantum mechanics works on all scales, then the macroscopic cat will become a superposition of being dead and alive simultaneously, with the decayed and non-decayed atom respectively. However, when the chamber is opened, only one of the results can be observed, either an alive cat or a dead cat, but not both. Such superposition can happen between all kinds of objects, but we never observe them in our daily life. There are two main reasons for assuming quantum physics is universal. Firstly, decoherence of quantum systems is effectively a measurement which forces particles to follow classical mechanics [43, 44]. Hence, superpositions can be destroyed by decoherence due to interactions with the environment, such as radiation and collision with air molecules, so a large superposition will decay much faster [45]. Secondly, the required measurement precision grows as the size of the system grows in general [46], so it is extremely difficult to measure large systems. Hence, a carefully designed experiment with very high sensitivity is required for measuring any macroscopic, or even mesoscopic, quantum superposition.

A cat state is defined as a superposition of two macroscopically distinct quasi-classical states. However, macroscopicity of a state has no unique definition. It can refer to a large spatial extent, a large mass, or a large number of particles involved. One definition of cat states is the superposition of two, or more, coherent states in phase space (see Fig. 1.4b), where the coherent states are often considered to be the most classical particle-like states [47, 48, 49] (see Fig. 1.4a). This definition is commonly used in quantum optics, and the size of a cat depends on the number of particles. A

good quantification of macroscopicity for this definition is provided by Lee and Jeong [50] which measures the effective size and coherence at the same time. The size of a cat state can be as large as one hundred particles as achieved in a recent experiment using microwave photons [51].

Applications of cat states include quantum computation [52, 53], which treats a coherent state as a qubit so that a cat state corresponds to a qubit with a superposition of zero and one. In addition, cat states are useful in high-precision quantum metrology to bypass the standard quantum limit. For example, cat states in phase space can reduce the shot-noise of measurements. Cat states of massive objects can be used to improve the sensitivity of detection of the gravitational waves, which were recently experimentally confirmed [54]. Energy cat states and position cat states may be used to detect hypothetical collapse models [55].

Generation of cat states is no easy task. There are a few conceptually different schemes to generate cat states in phase space. One of the methods is based on bifurcation [56]. In classical systems, a particle located at an unstable point will go to one of the stable points upon a small perturbation. However, a corresponding quantum state that starts at the same unstable point will spread out due to quantum uncertainty, which will result in a superposition state at both stable points. A similar method allows cat states to be created in open systems [57, 58], which requires squeezing and two-particle loss to create an unstable point at the origin. A pure quantum mechanical approach was proposed by Yurke and Stoler [59, 60] using the third-order Kerr nonlinearity. Using this method, starting from a coherent state with the nonlinearity, a cat state will appear at a certain time because of the phase matching of all number states (see Chapter 2.1). After exactly the same amount of time, it will evolve back to the coherent state because of the recurrence. The nonlinearity in BECs takes a similar form of Kerr nonlinearity (see Chapter 2.3). Hence, with a special setting, atomic cat states involving hundreds of atoms can be created. The detailed analysis of my proposal will be presented in Chapter 4.

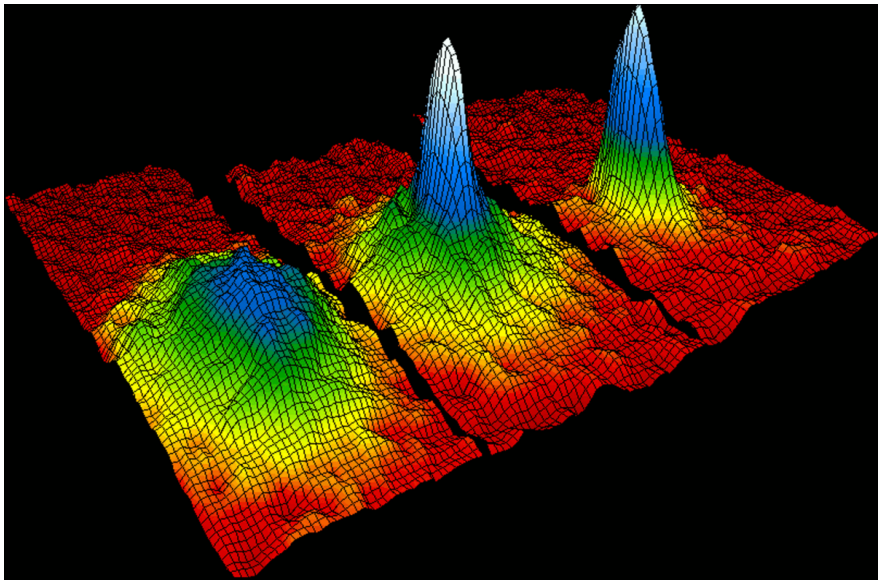

Figure 1.5: Velocity distribution of the Rubidium atoms undergoing a Bose-Einstein condensation. The temperature T decreases from left to right, $T \gg T_c$, $T < T_c$, and $T \ll T_c$, where T_c is the transition temperature. Thermal excitations disappear when the temperature is sufficiently low, so all particles are in the ground state with minimum uncertainty,which is displayed as a sharp peak. (E. Cornell [61]/ Creative Commons)

1.3 Simulating physical systems - Bose Einstein condensates

The experimental realization of Bose-Einstein condensation in ultracold atomic gases in 1995 has marked a new era of physics and opened up a whole new exciting field that continues to thrive. After the first realization, BECs quickly attracted lots of attention and were the subject of an explosion of research, with review articles on different aspects almost every year [9, 62, 63, 64, 65, 66, 67, 68, 69, 70, 71, 72, 73, 74], ranging from experimental techniques to the theory and applications of BECs. Now, after two decades of development, the relevant experimental techniques have become mature and are treated as basic tools for atomic physicists to study fundamental physics and simulate other physical systems.

The theoretical study of BECs dates back to 1924, when Satyendra Nath Bose re-derived the statistical distribution of photons in the black-body radiation by using the correct way of counting states of identical and indistinguishable particles, now called bosons. After the paper was rejected once, Bose sent it to Albert Einstein who agreed with the idea and helped with translating it into

German for publication [75]. Extending Bose's work in the following year, Einstein obtained the quantum statistical distribution for the non-interacting ideal gas [76], now known as BEC. This requires cooling the weakly interacting atoms to a temperature a billion times lower than room temperature and no technique for achieving it existed at the time. The invention of powerful laser cooling techniques for alkali atoms in the 1970s eventually made it possible to bring the temperature down to the order of $100\mu K$. The barrier of the remaining two orders of magnitude was eliminated by further evaporative cooling that let the high energy particles leave the system. Combining these techniques finally led to the groundbreaking observation of BEC (see Fig. 1.5), over 70 years after its first prediction [77, 78, 79]. The Nobel Prize in Physics was awarded to Eric Cornell, Carl Wieman, and Wolfgang Ketterle in 2001 for this achievement [80, 81].

A Bose-Einstein condensate is a state of matter with a macroscopic number of identical bosons occupying the same single-particle state. The phase transition towards a BEC happens when the system is cooled below a critical temperature T_c such that the temperature-dependent de Broglie wavelength becomes larger than the inter-particle separation. At such a low temperature, a macroscopic wavefunction forms due to the overlap of the individual wave packets, such that the bosons lose their distinguishability based on position. In the condensate, every atom behaves exactly the same. Hence, instead of describing the system by a quantum field $\hat{\psi}(\mathbf{r})$, a simple mean-field treatment $\hat{\psi}(\mathbf{r}) \rightarrow \langle\hat{\psi}(\mathbf{r})\rangle = \psi(\mathbf{r})$ may be used. This theoretical method was developed in the early 1960s independently by Eugene Gross and Lev Pitaevskii for weakly interacting BECs [82, 83, 84]. The mean-field macroscopic wavefunction obeys a Schrödinger-like equation with a third order nonlinear term, usually called Gross-Pitaevskii equation (GPE), which will be derived in Chapter 2.3.

The main advantages of BECs include a very good isolation from environmental influence, high tunability and very precise controllability of almost all parameters [85]. BECs are particularly good at simulating other physical systems, or quantum simulators as suggested by Feynman [86], and testbeds for diverse theories. For example, analogue black holes can be created in BECs [87]

and the corresponding Hawking radiation with phonon replacing photon can be observed [88, 89]. BECs in optical lattices can also simulate various condensed matter systems such as quantum phase transitions [90] and Anderson localizations [91]. Moreover, the nonlinearity in BECs allows the study of soliton dynamics [92, 93, 94]. An experimental test of BECs under microgravity in a drop tower [95] suggest the possibility of probing the boundary between general relativity and quantum mechanics. The potential of entangling large numbers of particles in BECs can find applications in quantum metrology such as using spin squeezing to surpass standard quantum limit [96, 97]. Mathematical models such as effective negative mass can also be engineered with spin-orbit coupling [98].

A reason for the high controllability is because of many available choices of BEC systems. Today, BEC has been realized in many different systems, including almost all alkali atoms, lithium (^{7}Li), sodium (^{23}Na), potassium (^{39}K, ^{41}K), rubidium (^{85}Rb, ^{87}Rb), caesium (^{133}Cs) [10]. Other atomic BECs include hydrogen (^{1}H), chromium (^{52}Cr), ytterbium (^{170}Yb, ^{174}Yb), the metastable excited state of helium (^{4}He*), Calcium (^{40}Ca), Strontium (^{84}Sr, ^{86}Sr, ^{88}Sr), Dysprosium (^{164}Dy), and Erbium (^{168}Er). It is also possible to have molecular BECs, for example, bosons formed by a pair of fermionic atoms, such as ^{6}Li and ^{40}K molecules. Since photons are also bosons, the BEC transition for photons can also be observed [99]. Room-temperature BECs can be created for exciton-polaritons because of their very low effective mass and resulting high transition temperature [100].

The typical scales of time, length, temperature, and energy of dilute atomic BECs can span several orders of magnitude. For atomic BECs, the lifetime τ can be as long as $\tau \sim 10\text{ms} - 100\text{s}$, where $\tau \sim 100$ms for most experiments. A typical experiment usually involves between 10^3 to 10^6 atoms, and the transition temperature T_c is between 100nK to 1000nK. Near T_c, only a small fraction of particles are in the condensate, while the other particles are in the thermal component. To have a pure condensate, a much lower temperature T must be used. For instance, at $T \sim 0.1T_c$, the thermal component will be about$\sim 0.1\%$ and can be ignored. It is worth emphasizing that no

cryogenic equipment is typically used in the experiments, so such cold condensates exist with a room temperature background. With alternative technique, the temperature of a condensate can be in the low picoKelvin regime [101]. The size of the condensates can be of order $\ell \sim 0.1\mu\text{m} - 10\mu\text{m}$ corresponding roughly to a trapping angular frequency $\omega \sim 10\text{Hz} - 10\text{kHz}$. The length can be adjusted independently in all directions, such that a strong trapping along one direction can reduce the system to an effective 2D BEC system of disk shape, and similarly for a 1D system with cigarette shape. This translates to a peak density $\rho \sim 10^{19}\text{m}^{-3} - 10^{22}\text{m}^{-3}$, which is much lower than the density of air $\sim 10^{25}\text{m}^{-3}$. Higher densities are hard to achieve because the loss from three-particle collisions grows as ρ^3, so the lifetime becomes short.

Atoms are particles with many internal states that can be controlled by light frequencies from optical to microwave, as well as electric and magnetic fields. For dilute atomic gases at such low density, the two-particle interactions can be well described by a single s-wave scattering length a_s that is independent of the details of the collision. The nonlinear interaction parameter U in the GPE is proportional to a_s, which can be controlled by Feshbach resonances in real time [69, 102]. By tuning the magnetic field near a Feshbach resonance, all values of a_s can be achieved theoretically, including positive $a_s > 0$ for repulsive interaction, negative $a_s < 0$ for attractive interaction, and $a_s = 0$ for no interaction. It has been demonstrated experimentally that this can be done over many orders of magnitude [103]. For Rubidium, $U/\hbar = 6 \times 10^{-17}\text{Hz/m}^3$, together with the density discussed above, $\rho U/\hbar \sim 10^3\text{Hz} - 10^6\text{Hz}$. The effect of nonlinearity is significant when the term is comparable or higher than the scale of the trapping frequency or other scale presented in the system such as kinetic energy.

Another setup typically considered is BECs with more than one type of boson created by mixing different types of atoms. Alternatively, atoms with different hyperfine states are distinguishable bosons, so creating two-component BECs with the same atoms is possible. In this setup, the atoms with different hyperfine states can be inter-convertible during experiments. Studying two-component BECs are the important part of my proposals as will be discussed in Chapter 2, Chapter

4, and Chapter 5.

1.4 Outline of the thesis

This thesis includes three main projects that I have studied. They are chimera knots in 3D, macroscopic spin cat states in BECs, and mediated nonlocal hopping in BECs. The first two projects provided me with the theoretical foundation for the last one. Since knowledge from several different fields is needed to understand the results, the relevant background is provided in Chapter 2. It includes the dynamics of various oscillators, including quantum, classical, and nonlinear. The two main differential equations, CGLE and GPE, are introduced. This is followed by the mechanism of the nonlocal diffusive coupling, the nonlocal hopping, and the basics of BECs.

In Chapter 3, I present the new discovery of stable chimera knot states as published in [8]. Prior to my work, knots were not known to be stable in oscillatory media, nor were such nontrivial chimera patterns known to exist in 3D. As my simulations show, the stability depends on the nonlocal coupling. I show the properties, structures, and dynamics for Hopf links and trefoils with good 3D visualization. The same conclusion holds for simple, complex, and chaotic oscillators. In complex oscillatory media, we can even observe the synchronization defect sheet for the first time.

In Chapter 4, I present my proposal for creating macroscopic cat states in two-component BECs using the Kerr nonlinearity as published in [12]. It was unclear how large cat states can be in such systems. In order to increase the nonlinearity and lifetime, we proposed to use strong trapping of the smaller BEC component and Feshbach resonance respectively. We analyzed the loss and other experimental imperfections and concluded that cat states involving hundreds of atoms should be possible.

In Chapter 5, I present a new mediating mechanism that can result in mediated nonlocal hopping, which is analogous to the effective nonlocal interaction between charged particles mediated by an electromagnetic field. In my scheme, due to the additional mediating channel without energy barrier, particles can bypass all energy barriers in the original system by jumping into the mediat-

ing channel, and can thus reach much further distances. My derivation shows that this approach allows independently adjustable on-site nonlinearity, hopping strength and range. This nonlocal hopping model is interesting also because further results show that it is the first known conservative Hamiltonian system showing chimera states. To show that it is more than a mathematical model, I also analyze the possibility of implementing mediated hopping in BECs and conclude that it can be done using current technology. Moreover, simulations show strong evidence of the presence of chimera states in the BEC system. The mechanism was discovered while I was attempting to search for chimera states in quantum systems. After dozens of trials of different dynamical equations, I found suitable equations and immediately realized that they correspond to a two-component GPE because of the similarity with diffusive coupling. I also recognized that they represent the Bose-Hubbard model [13, 104] with nonlocal hopping. A mean-field treatment is used in this thesis and the full quantum treatment will be the future work.

In Chapter 6, I summarize the main results presented in this thesis and discuss the possible future directions.

Chapter 2

Theoretical background

This chapter is comprised of three main sections with the theoretical background for the next three chapters. Sec. 2.1 is devoted to the basis of the nonlinear dynamic systems and formulation in phase spaces. I will review various types of oscillators, including both classical oscillators, quantum oscillators, and nonlinear oscillators. The mechanism of creating cat states based on Kerr nonlinearity will also be introduced. Sec. 2.2 introduces the diffusive coupling between oscillators which gives the complex Ginzburg-Landau equation (CGLE). I will then discuss the mechanism of the nonlocal diffusive coupling and introduce the nonlocal CGLE. The analogue mechanism of nonlocal hopping is derived. Sec 2.3 is dedicated to the Bose-Einstein Condensates. Starting from an interacting BEC, the Gross-Pitaevskii equation (GPE) is derived as the mean-field of a quantum field equation. Moreover, the nonlinear Kerr Hamiltonian of BECs can be obtained with a single-mode approximation of the same quantum field equation. Finally, I will give the mathematical formulation of two-component BECs, which will be used to derive the nonlocal hopping in Chapter 5.

2.1 Oscillators and phase space dynamics

Oscillators are one of the fundamental concepts across all branches of physics and describe many systems existing in nature with regular bounded motion. This is particularly true for the simple harmonic oscillator, which happens everywhere as a result of the linear approximation. In this section, various types of oscillators are introduced, including simple harmonic oscillators, nonlinear oscillators, and self-sustained oscillators. Both classical and quantum oscillators are discussed. Specifically, the nonlinear Kerr effect in quantum systems provides a method to create Schrödinger cat states, which will be used in Chapter 4.

2.1.1 Simple harmonic oscillators and nonlinear oscillators

Classical Harmonic Oscillator: A classical simple harmonic oscillator (SHO) is given by the Hamiltonian

$$\mathscr{H}(x,p) = \frac{1}{2m}p^2 + \frac{1}{2}m\omega_0^2 x^2, \tag{2.1}$$

where m is the mass and ω_0 is the natural angular frequency, with two canonical variables, canonical coordinate x and canonical momentum p. The corresponding dynamical equations can be found by the Hamilton's equation

$$\dot{x} = \frac{\partial \mathscr{H}}{\partial p} = \frac{p}{m}, \tag{2.2}$$

$$\dot{p} = -\frac{\partial \mathscr{H}}{\partial q} = -m\omega_0^2 x, \tag{2.3}$$

which is linear. The solution can be solved directly using the eigenvalue method, which shows a rotation around a circle with constant angular speed ω_0, as shown in Fig. 2.1. Alternatively, those two equations can be combined to a second order linear differential equation $\ddot{x} = -\omega_0^2 x$, which gives the same solution.

The same equation can be represented in a different canonical pair of action variable $I = \oint pdq/2\pi$ and angle variable θ [105]. The transformation for the SHO can be written as

$$I = \frac{1}{2m\omega_0}p^2 + \frac{1}{2}m\omega_0 x^2, \tag{2.4}$$

$$\theta = \tan^{-1}(m\omega_0 x/p), \tag{2.5}$$

and the Hamiltonian becomes

$$\mathscr{H}(I,\theta) = \omega_0 I. \tag{2.6}$$

Similarly, the dynamical equations can be obtained by using Hamilton's equation, which gives $\dot{I} = -\partial\mathscr{H}/\partial\theta = 0$ and $\dot{\theta} = \partial\mathscr{H}/\partial I = \omega_0$. Hence, $I(t)$ is a conserved quantity, which is proportional to the energy in this system, and the phase $\theta(t)$ is increasing over time. The quantity I is proportional to the number of particles in quantum mechanics, as will be clear soon.

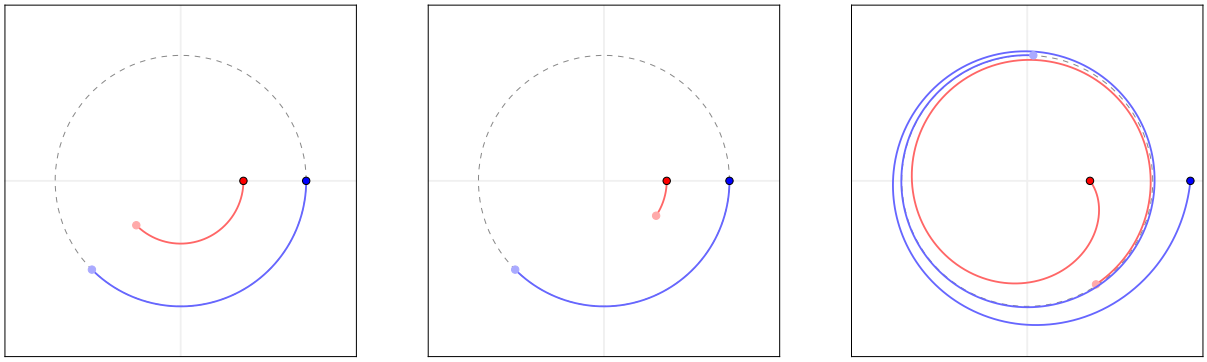

(a) Simple harmonic oscillator (b) Simple nonlinear oscillator (c) Self-sustained oscillator

Figure 2.1: Dynamics in a phase space with the bright spots indicate two different initial conditions, and the faint spots indicate the final states. (a) Simple harmonic oscillator. Phase gain is independent of the amplitude. (b) Simple nonlinear oscillator. The phase gain depends on the amplitude. (c) Self-sustained oscillator. Different initial conditions get closer and closer to the limit circle over time.

An alternative convenient representation is given by the transformation

$$z = \frac{1}{\sqrt{2}}(\sqrt{m\omega_0}x + i\frac{1}{\sqrt{m\omega_0}}p), \tag{2.7}$$

$$z^* = \frac{1}{\sqrt{2}}(\sqrt{m\omega_0}x - i\frac{1}{\sqrt{m\omega_0}}p). \tag{2.8}$$

The Hamiltonian can be rewritten as

$$\mathscr{H}(z, iz^*) = \omega_0|z|^2 = \omega_0 z^* z. \tag{2.9}$$

With z and iz^* treated similar to conjugate variables, the dynamic equation can be found by $\dot{z} = \partial\mathscr{H}/\partial(iz^*)$, giving

$$i\dot{z}(t) = \omega_0 z, \tag{2.10}$$

and the solution

$$z(t) = z(0)e^{-i\omega_0 t}. \tag{2.11}$$

This implies that the phase points with different initial conditions gain the same phase over time as shown in Fig. 2.1a.

Simple nonlinear oscillator: There are various types of nonlinear oscillators. The simplest nonlinear oscillator is given by the third order nonlinearity, or a quartic term in the Hamiltonian

$$\mathscr{H}(z, iz^*) = \frac{1}{2}\chi|z|^4. \tag{2.12}$$

Again, the dynamical equation can be obtained by using Hamilton's equation, as

$$i\dot{z}(t) = \chi|z|^2 z. \tag{2.13}$$

To solve this equation, we note that the action $I = |z|^2$ is time independent because

$$\frac{dI}{dt} = \frac{d}{dt}(z^* z) = \frac{dz^*}{dt}z + z^*\frac{dz}{dt} = \frac{1}{-i}(|z|^2 z^*)z + \frac{1}{i}(|z|^2 z)z^* = 0, \tag{2.14}$$

which means the energy $\mathscr{H} = \chi I^2/2$ is also conserved. Hence, using $|z(t)|^2 = |z(0)|^2$, the equation can be rewritten as

$$i\dot{z}(t) = \chi|z(0)|^2 z(t). \tag{2.15}$$

The solution is

$$z(t) = z(0)e^{-i\chi|z(0)|^2 t}, \tag{2.16}$$

which behaves the same as the SHO, except now the angular speed ω depends on the amplitude as $\omega = \chi|z(0)|^2$. Therefore, initial points with different amplitudes will lead to different phases at a later time as shown in Fig. 2.1b.

Typically, a linear term also exists in the system even when the expansion is done to the lowest order nonlinear as

$$i\dot{z}(t) = \omega_0 z + \chi|z|^2 z. \tag{2.17}$$

It can be shown easily that this equation reduces to Eq. (2.13) using the co-rotating frame as $z \to ze^{-i\omega_0 t}$. In such a frame, the constant rotation generated by the linear term can be eliminated.

The equation above is the simplest nonlinear oscillator because it has the lowest order nonlinear term for the system with the phase symmetry (or global $U(1)$-gauge symmetry) $z \to ze^{i\theta}$ for all θ. This is a symmetry that often exists in fundamental physics and conservative systems. Without

this symmetry, the second order nonlinearity can exist. To make it clear, if we assume a general Hamiltonian with the form

$$\begin{aligned} H(z,iz^*) &= \sum_{w_1=\{z,z^*\}} K_{w_1} w_1 + \sum_{w_1,w_2=\{z,z^*\}} K_{w_1 w_2} w_1 w_2 + \sum_{w_1,w_2,w_3=\{z,z^*\}} K_{w_1,w_2,w_3} w_1 w_2 w_3 \\ &+ \sum_{w_1,w_2,w_3,w_4=\{z,z^*\}} K_{w_1,w_2,w_3,w_4} w_1 w_2 w_3 w_4 + ..., \end{aligned} \tag{2.18}$$

substitute the symmetry above and compare with the original one, all odd power terms have to be zero. For each even power term, only one combination remains. Hence, the general Hamiltonian that preserves the phase symmetry is:

$$\mathscr{H} = \alpha|z|^2 + \frac{\beta}{2}|z|^4 + \frac{\gamma}{3}|z|^6..., \tag{2.19}$$

More generally, the system that preserves the gauge symmetry can be written as

$$\mathscr{H} = f(|z|^2). \tag{2.20}$$

Self-sustained oscillator: Instead of a pure nonlinear oscillator that conserves energy as discussed above, a simple non-conservative nonlinear system can be described by the normal form of a Stuart-Landau oscillator [2]

$$\dot{z}(t) = z - (1+ib)|z|^2 z. \tag{2.21}$$

It is a simple self-sustain oscillator representing a broad class of system with $\dot{z}(t) = (a_r + ia_i)z - (b_r + ib_i)|z|^2 z$ and $a_r, b_r > 0$. This equation can be reduced to the Eq. (2.21) by going into a co-rotating frame, rescaling the time t and rescaling the amplitude z. The dynamics are illustrated in Fig. 2.1c with all phase points trending towards the unit circle $|z| = 1$. It can be understood easily by rewriting the variable $z(t) = A(t)e^{i\theta(t)}$ in terms of amplitude $A(t)$ and phase $\theta(t)$. Substituting back, the resulting coupled equations are

$$\dot{A} = A - A^3, \tag{2.22}$$

$$\dot{\theta} = -bA^2, \tag{2.23}$$

If the amplitude is too small $A < 1$, then the amplitude will increase over time as $\dot{A} > 0$ and vice versa. So, the equilibrium condition $\dot{A} = 0$ gives $A = 1$. Any small perturbation will eventually disappear and the system is stable with small noise. Also, the phase advances depending on the amplitude. In the equilibrium system, it oscillates with a constant angular frequency $\omega = \dot{\theta} = -b$. Since the dynamics is always attracted to the unit circle $|z| = 1$ and is oscillating, hence, the name self-sustained oscillator. The closed loop attractor, $|z| = 1$ here, is referred as the limit circle. For the change of the quantity $I = |z|^2$, we have

$$\frac{dI}{dt} = \frac{dz^*}{dt} z + z^* \frac{dz}{dt} = 2|z|^2 - 2|z|^4 = 2I - 2I^2, \tag{2.24}$$

which is consistent with the amplitude equation above. The quantity I can be interpreted as the number of particles, so the first term corresponds to the pumping of particles into the system, and the second term corresponds to the nonlinear particle loss.

Complex oscillators: In general, oscillator dynamics exist in any systems with a well-defined phase θ. Consider a system with two bounded dynamic variables X and Y, then the phase may be defined as

$$\theta(t) = \tan^{-1}\left(\frac{Y(t) - Y_0}{X(t) - X_0}\right), \tag{2.25}$$

if $X(t) - X_0$ and $Y(t) = Y_0$ are not equal to zero simultaneously. (X_0, Y_0) is a reference point, which is a center in case of limit cycle dynamics. For the systems with more than two dynamic variables, there may have a two-dimensional submanifold that the dynamics behave in a way that θ is well defined, in particular, near the Hopf bifurcation point. An example is the specially designed Rössler model [106] with three variables $X(t)$, $Y(t)$, $Z(t)$ with differential equations

$$\begin{aligned} \dot{X}(t) &= -Y - Z, \\ \dot{Y}(t) &= X + aY, \\ \dot{Z}(t) &= b + Z(X - c), \end{aligned} \tag{2.26}$$

where a, b, c are the control variables and the phase can be defined in the XY plane with $(X_0, Y_0) = (0, 0)$. Therefore, in general, the phase can be well-defined for much broader systems such as the

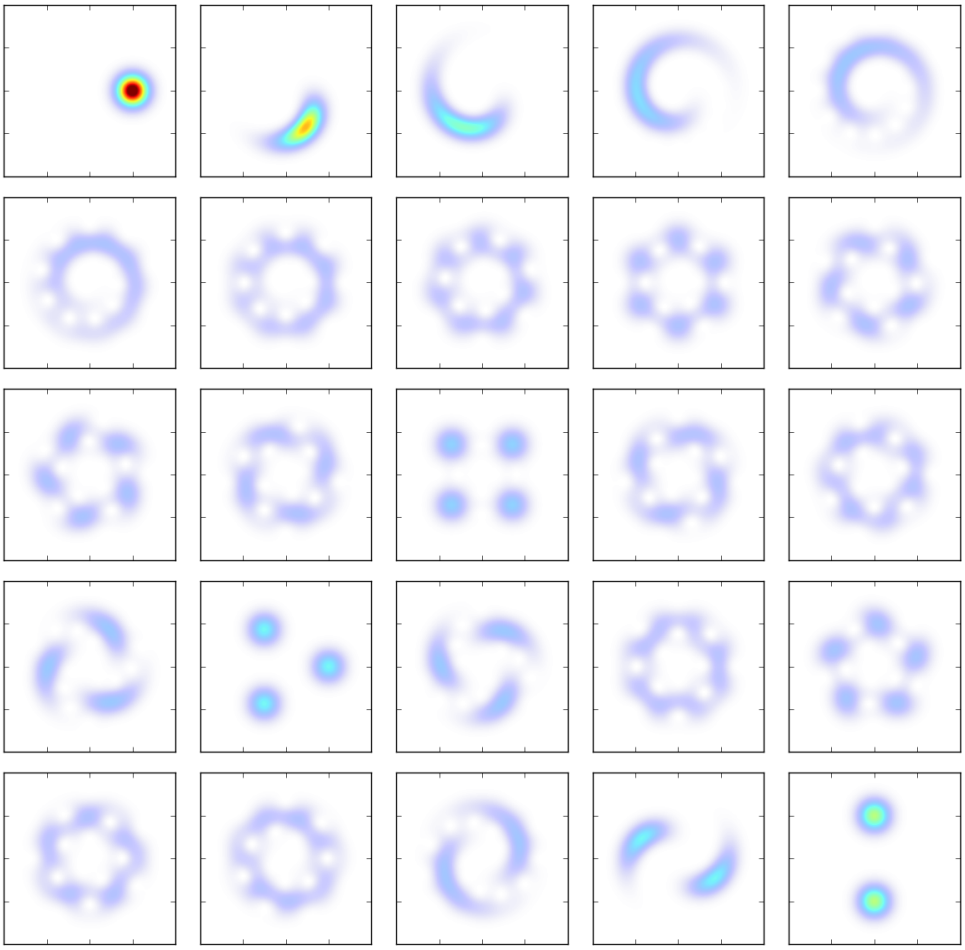

Figure 2.2: Formation of a cat state. The plots of Husimi Q-function of a coherent state under Kerr nonlinearity are shown. Time increase uniformly from $t = 0$ to $t = \tau_c$, from left to right and from top to bottom.

chemical, biological and neural systems [25]. If two or more such subsystems are put together with some form of coupling, then the relative phase dynamics can be interesting and allows the study of the synchronization between subsystems.

2.1.2 Quantum oscillators, Kerr nonlinearity and cat states

Quantum harmonic oscillator: The quantum harmonic oscillator behaves similarly to the classical counterpart in the limit with a large number of particles. The formulation can be done using the first quantization rules $x \to \hat{x}$, $p \to \hat{p} = -i\hbar\partial_x$, or replacing the Poisson bracket $\{x, p\} = 1$ by

commutator $[\hat{x},\hat{p}] = i\hbar$, or replacing $z \to \sqrt{\hbar}\hat{a}$ in the formulation in previous section. Or simply start with the commutation relation of annihilation operators $\hat{a}$ with commutator $[\hat{a},\hat{a}^\dagger] = 1$.

With this definition, we can write down the Hamiltonian for the quantum harmonic oscillator:

$$\hat{\mathscr{H}} = \left(\hat{n} + \frac{1}{2}\right)\hbar\omega, \tag{2.27}$$

with the Planck constant $\hbar$, the trapping frequency ω and the number operator $\hat{n} = \hat{a}^\dagger\hat{a}$. The dynamics is given by the Schrödinger equation

$$i\hbar\frac{\partial}{\partial t}|\psi\rangle = \hat{\mathscr{H}}|\psi\rangle, \tag{2.28}$$

which can be easily solved using the eigenvalue equation $\hat{n}|n\rangle = n|n\rangle$ with Fock basis $|n\rangle$, and the solution is

$$|\psi(t)\rangle = \sum_n c_n e^{-iE_n t/\hbar}|n\rangle, \tag{2.29}$$

with the eigenvalue $E_n = (n+1/2)\hbar\omega$. Note that the global phase is unimportant, so it can be written simply as

$$|\psi(t)\rangle = \sum_n c_n e^{-in\omega t}|n\rangle, \tag{2.30}$$

A special state called coherent state $|\alpha\rangle$ is known as the most classical state because the dynamics resemble the oscillatory behavior of the classical counterpart [47]. It is defined as the eigenstate of the annihilation operator as

$$\hat{a}|\alpha\rangle = \alpha|\alpha\rangle, \tag{2.31}$$

with associated eigenvalue $\alpha = |\alpha|e^{i\theta}$, which is a continuous complex number with amplitude $|\alpha|$ and phase θ. Hence, it gives a quantum-classical correspondence, say for the electromagnetic field, where the state $|\alpha\rangle$ has the corresponding amplitude α, phase θ and intensity $|\alpha|^2$. The coherent states are also states with the minimum uncertainty. It can be written in terms of the Fock basis as

$$|\alpha\rangle = e^{-|\alpha|^2/2}\sum_n \frac{\alpha^n}{\sqrt{n!}}|n\rangle, \tag{2.32}$$

which is normalized $\langle\alpha|\alpha\rangle = 1$. The probability of detecting n photons is therefore given by the Poisson distribution

$$P(n) = |\langle n|\alpha\rangle|^2 = e^{-|\alpha|^2}\frac{|\alpha|^{2n}}{n!}. \tag{2.33}$$

The dynamics of the coherent states can be found using the Heisenberg picture:

$$i\hbar\partial_t\hat{a} = -[\hat{\mathscr{H}}, \hat{a}] = \hbar\omega\hat{a}, \tag{2.34}$$

with solution

$$\hat{a}(t) = \hat{a}(0)e^{-i\omega t}, \tag{2.35}$$

and similarly for the eigenvalue

$$\alpha(t) = \alpha(0)e^{-i\omega t}, \tag{2.36}$$

So, the motion of the coherent state is periodic with angular frequency ω.

To compare the classical and quantum harmonic oscillator, a phase space representation of the states is required. One such common representation used in quantum optics is given by the Husimi Q-function:

$$Q(\beta) = \frac{1}{\pi}\langle\beta|\hat{\rho}|\beta\rangle, \tag{2.37}$$

with a complex number β and the corresponding coherent state $|\beta\rangle$. The density operator $\hat{\rho} = \sum_i p_i|\psi_i\rangle\langle\psi_i|$ with probability p_i describes the statistical mixture of quantum states, and takes the form $\hat{\rho} = |\psi\rangle\langle\psi|$ for a pure state $|\psi\rangle$. A density operator description is required if there is uncertainty about the quantum states such as decoherence or experimental uncertainty. The Q-function is essentially a measure of how close the state ρ is to the coherent state with β. It is normalized as $\int Q(\beta)d\beta = 1$, so $Q(\beta)$ may be interpreted as the probability to measure the state with value β. Note that β is a complex number and is not directly measurable, which corresponding to the fact that $|\beta\rangle$ forms an over-complete basis. Experimentally, $Q(\beta)$ can be reconstructed using tomographic techniques. In particular, the Q-function of the coherent state $\hat{\rho} = |\alpha\rangle\langle\alpha|$ is

$$Q(\beta) = \frac{1}{\pi}|\langle\alpha|\beta\rangle|^2 = \frac{1}{\pi}e^{-|\alpha-\beta|^2}, \tag{2.38}$$

which is Gaussian distributed as shown in the first plot in Fig. 2.2. The existence of the width of order 1 independent of $|\alpha|$ is due to the minimum uncertainty principle. Also, under the harmonic oscillator Hamiltonian $\hat{\mathscr{H}}$ above, the dynamics of the Q-function is

$$Q(\beta,t) = \frac{1}{\pi}|\langle\alpha(t)|\beta\rangle|^2 = \frac{1}{\pi}e^{-|\alpha(t)-\beta|^2} = \frac{1}{\pi}e^{-|\alpha e^{-i\omega t}-\beta|^2}. \tag{2.39}$$

It means that the Gaussian bump rotates along the circle with radius $|\alpha|$ with angular frequency ω in the phase space. If the amplitude $|\alpha|$ becomes large enough, the distribution may be treated as a point. Hence, the system behaves similarly to the classical harmonic oscillator.

Nonlinear Kerr effect: Similar to the classical system, the lowest order nonlinearity of the system preserving the gauge symmetry is given by

$$\hat{\mathscr{H}} = \hbar\chi\hat{n}^2. \tag{2.40}$$

where $\hat{n}$ is the number operator, and χ is the Kerr nonlinearity. This Hamiltonian is usually known as the Kerr Hamiltonian in quantum optics, which is originated from the refractive index change of the material when a light with strong intensity is passing through. Similarly, in BEC, similar term exist because of the two-particle interaction. A state evolves under this Hamiltonian as

$$|\psi(t)\rangle = \sum_n c_n e^{-iE_n t/\hbar}|n\rangle = \sum_n c_n e^{-in^2\chi t}|n\rangle, \tag{2.41}$$

which has a recurrence time $\chi t_r = 2\pi$ in which the state returns back to the same initial state because $e^{-in^2 2\pi} = 1$ for integer n.

This Hamiltonian can be used to generate a cat state $|CAT\rangle \sim |\alpha\rangle + i|-\alpha\rangle$, if the system starts with the coherent state $|\psi\rangle = |\alpha\rangle$ at $t = 0$, as originally proposed in [59]. At time $\chi t = \pi/2$, the factor becomes $e^{-in^2\chi t} = 1, -i, 1, -i, \ldots$ for $n = 0, 1, 2, 3, \ldots$. Multiplying by the global phase $e^{i\pi/4}$,

which rotates the phase space by $\pi/4$, the series becomes $e^{i\pi/4}e^{-in^2\chi t} = (1+(-i)^n)/\sqrt{2}$, and

$$
\begin{aligned}
|\psi(t)\rangle &= e^{-i\hat{\mathscr{H}}t/\hbar}|\alpha\rangle && (2.42)\\
&= e^{-|\alpha|^2/2}\sum_n \frac{\alpha^n}{\sqrt{n!}}\frac{(1+i(-1)^n)}{\sqrt{2}}|n\rangle && (2.43)\\
&= \frac{1}{\sqrt{2}}e^{-|\alpha|^2/2}\sum_n \left(\frac{\alpha^n}{\sqrt{n!}} + i\frac{(-\alpha)^n}{\sqrt{n!}}\right)|n\rangle && (2.44)\\
&= \frac{1}{\sqrt{2}}\left(|\alpha\rangle + i|-\alpha\rangle\right), && (2.45)
\end{aligned}
$$

The state becomes a cat state at a special time called cat time $\tau_c = \pi/(2\chi)$. The dynamics of a cat state formation can be visualized in the phase space using the Q-function as shown in Fig. 2.2. This construction mechanism is purely quantum mechanical and has no classical counter part.

2.2 Field equations and nonlocal coupling

Oscillations often refer to spatial motion, e.g. for a spring-mass system or a pendulum. But oscillators can also exist in phase space without any reference to spatial coordinates. For example, the electromagnetic field can oscillate in any spatial point. This leads to the concept of a physical field, which describes the assignment of quantities at all points in space and time, for example, the electromagnetic field and the gravitational field. Other systems can often be well approximated by field equations, when the scale of interest is much larger than the discreteness of the smallest system scale, such as the continuum approximation in fluid dynamics for the tiny particles. In this section, I introduce the field equations and the nonlocal coupling that will be used in Chapter 3 and Chapter 5. In particular, I try to emphasis the similarity between the nonlocal diffusive coupling and nonlocal hopping, which provides the motivation to study the nonlocal hopping in Chapter 5.

2.2.1 Local coupling and complex Ginzburg-Landau equation

A system with oscillators coupled locally with their nearest neighbor can be written as reaction-diffusion system [16]

$$\partial_t \mathbf{X}(\mathbf{r},t) = \mathbf{F}(\mathbf{X}) + \mathbf{D}\nabla^2\mathbf{X}, \tag{2.46}$$

for a dynamic variable $\mathbf{X}$. The vector field $\mathbf{F}$ represents a local limit-cycle oscillator of $\mathbf{X}$. The coupling of local oscillators is through the diffusion $\nabla^2\mathbf{X}$ with diffusion matrix $\mathbf{D}$. Note that $\mathbf{D}$ usually contains no imaginary part, but for, say, quantum systems, a similar term like this can have complex numbers. Suppose the self-sustained Stuart-Landau oscillators are used

$$\mathbf{F}(z) = z - (1+ib)|z|^2 z, \tag{2.47}$$

with z a complex number, then the field equation can become

$$\dot{z}(t) = z - (1+ib)|z|^2 z + (1+ic)\nabla^2 z, \tag{2.48}$$

with a choice on the diffusion. This is called the complex Ginzburg-Landau equation (CGLE) which describes a broad dissipative system near the Hopf bifurcation. The full derivation of CGLE for any oscillators near the Hopf bifurcation can be found in, say, [16]. Similar can be done in the Rössler model with the local oscillators given by Eq. (2.26). On the other hand, if non-dissipative isolated oscillators are used

$$\mathbf{F}(z) = -iu|z|^2 z, \tag{2.49}$$

then the field equation is

$$i\dot{z}(t) = u|z|^2 z - \kappa\nabla^2 z, \tag{2.50}$$

with a pure imaginary diffusion. It is often called the nonlinear Schrödinger equation. Note that this equation can be treated as a special case of the CLGE by setting $a \to -\infty$ and $b \to \infty$. In addition, it is also a special case of the Gross-Pitaevskii equation (GPE) with no trapping potential (see next section). In literature, GPE is sometimes mixed with nonlinear Schrödinger equation. In this thesis, I will refer GPE exclusively to the mean-field equations of BECs. Note that the properties of these equations are significantly different. CGLE describes an open system that the energy and particles can be exchanged, while nonlinear Schrödinger equation and GPE are conservative.

2.2.2 Nonlocal diffusive coupling

Similar to the direct local coupling discussed above, localized oscillators can be coupled with each other through a mediating channel. It can be illustrated by the following equation [6]

$$\partial_t \mathbf{X}(\mathbf{r},t) = \mathbf{F}(\mathbf{X}) + k\mathbf{g}(S), \tag{2.51}$$

$$\tau \partial_t S(\mathbf{r},t) = D\nabla^2 S - S + h(\mathbf{X}), \tag{2.52}$$

where $\mathbf{F}(\mathbf{X})$ describes a self-sustained oscillator with the dynamic variable $\mathbf{X}(\mathbf{r},t)$. k is the control parameter of the feedback strength from the the channel with the form $\mathbf{g}(S)$. $S(\mathbf{r},t)$ is a real variable that decays over time plus a source term $h(\mathbf{X})$. The spatial coupling dynamics is the diffusion in the mediating channel with diffusion constant $D > 0$. τ in the second equation sets the time scale. With a large separated time scales, adiabatic elimination can be used to derive the nonlocal diffusive coupling as done in [6].

Here, I will derive a similar alternative form which can highlight the similarity between the nonlocal diffusive coupling and the mediated nonlocal hopping derived in the next subsection. Let the local dynamic be the Stuart-Landau oscillator $\mathbf{F}(z)$, and the equations

$$\partial_t z(\mathbf{r},t) = z - (1+ib)|z|^2 z + k\xi, \tag{2.53}$$

$$\tau \partial_t \xi(\mathbf{r},t) = D\nabla^2 \xi - \xi + h_0 z, \tag{2.54}$$

where both z and ξ are complex dynamical variables. The second equation is a mediating channel that propagates the perturbation between oscillators and can be considered as two independent diffusion equations for the real and imaginary part of ξ. Note that the second equation is linear, so it has an exact solution. Here we consider only the adiabatic limit $\tau = 0$. In this limit, the mediating channel becomes

$$0 = D\nabla^2 \xi - \xi + h_0 z. \tag{2.55}$$

Suppose the Fourier transform of the dynamical variables are

$$\tilde{z}(\mathbf{q},t) = \mathscr{F}[z(\mathbf{r},t)] = (1/(2\pi)^d) \int d\mathbf{r} e^{-i\mathbf{q}\cdot\mathbf{r}} z(\mathbf{r},t) \tag{2.56}$$

and similar for $\tilde{\xi}(\mathbf{q},t) = \mathscr{F}[\xi(\mathbf{r},t)]$. So, the differential equation becomes an algebraic equation

$$0 = -q^2 D\tilde{\xi} - \tilde{\xi} + h_0\tilde{z}, \tag{2.57}$$

and the solution for $\tilde{\xi}$ is

$$\tilde{\xi} = h_0 \frac{1}{1+Dq^2}\tilde{z}. \tag{2.58}$$

The inverse Fourier transform gives the convolution

$$\xi = h_0 G(\mathbf{r}) * z(\mathbf{r},t) = h_0 \int d\mathbf{r}' G(\mathbf{r}-\mathbf{r}')z(\mathbf{r}',t), \tag{2.59}$$

assuming isotropic and translational invariant system with unbounded domain, where

$$G(\mathbf{r}) = \mathscr{F}^{-1}\left[\frac{1}{1+Dq^2}\right]. \tag{2.60}$$

The explicit solutions in different dimensions are

$$G_{1D}(\mathbf{r}) = \frac{1}{2R}e^{-r/R}, \tag{2.61}$$

$$G_{2D}(\mathbf{r}) = \frac{1}{2\pi R^2}K_0\left(\frac{r}{R}\right), \tag{2.62}$$

$$G_{3D}(\mathbf{r}) = \frac{1}{8\pi R^3}\frac{1}{r}e^{-r/R}, \tag{2.63}$$

where $r = |\mathbf{r}|$ and $R = \sqrt{D}$ is the effective radius and $r = |\mathbf{r}|$. K_0 is the modified Bessel function of the second kind. Substituting the solution back to Eq. (2.53), we have

$$\partial_t z(\mathbf{r},t) = z - (1+ib)|z|^2 z + kh_0 \int d\mathbf{r}' G(\mathbf{r}-\mathbf{r}')z(\mathbf{r}',t), \tag{2.64}$$

and can be rewritten as

$$\partial_t z(\mathbf{r},t) = z - (1+ib)|z|^2 z + K(1+ia)\int d\mathbf{r}' G(\mathbf{r}-\mathbf{r}')\left(z(\mathbf{r}',t) - z(\mathbf{r},t)\right). \tag{2.65}$$

This equation is called the nonlocal CGLE and can have stable chimera states. Specifically, the first observation of chimera core patterns appears in this model [7].

2.2.3 Nonlocal hopping with mediating channel

Considering a similar set of differential equations where simple nonlinear oscillators are used instead of self-sustained oscillators:

$$i\dot{\psi}_1(\mathbf{r},t) = U|\psi_1|^2\psi_1 + \Omega\psi_2, \tag{2.66}$$

$$i\dot{\psi}_2(\mathbf{r},t) = -\kappa\nabla^2\psi_2 + \Delta_2\psi_2 + \Omega\psi_1. \tag{2.67}$$

where ψ_1 and ψ_2 are dynamic variables representing wavefunctions. U is the nonlinear coefficient, Ω is the Rabi frequency, Δ_2 is the detuning, and κ is the inverse mass. All control variables are real numbers. The equations are related to mean-field GPE of two-component BEC which is derived in next section. Note that this model without kinetic energy term is just a mathematical model, and a realistic system will be considered in Chapter 5. It, however, greatly simplifies the detail and allows highlighting the mechanism for the effective nonlocality. The second equation is the mediating channel that propagates the perturbation and is similar to the equation in the previous section with an extra i in front of the time derivative. If adiabatic elimination is used $\tau = 1/\Delta_2 = 0$, then the mediating channel becomes

$$0 = -\kappa\nabla^2\psi_2 + \Delta_2\psi_2 + \Omega\psi_1. \tag{2.68}$$

Let $R = \sqrt{\kappa/\Delta_2}$ and use Fourier transform, so

$$0 = q^2R^2\tilde{\psi}_2 + \tilde{\psi}_2 + \frac{\Omega}{\Delta_2}\tilde{\psi}_1, \tag{2.69}$$

This equation is exactly the same as before, so it has the same solution as

$$\psi_2(\mathbf{r},t) = -\frac{\Omega}{\Delta_2}G(\mathbf{r}) * \psi_1(\mathbf{r},t), \tag{2.70}$$

with $G(\mathbf{r})$ is the same in previous section. Substituting back to the non-mediating channel, we have

$$i\dot{\psi}_1(\mathbf{r},t) = U|\psi_1|^2\psi_1 - \frac{\Omega^2}{\Delta_2}\int d\mathbf{r}G(\mathbf{r}-\mathbf{r}')\psi_1(\mathbf{r}',t) \tag{2.71}$$

Furthermore, this system has another set of solutions. Since the physical meaning of Δ_2 is the detuning, which can be negative. The mediating equation with adiabatical elimination can be

rewritten as

$$0 = -\nabla^2\psi_2 - \frac{1}{R_0^2}\psi_2 + \frac{\Omega}{\kappa}\psi_1, \tag{2.72}$$

where $R_0 = \sqrt{-\kappa/\Delta_2}$ and the corresponding solutions for the Sommerfeld radiation boundary condition are

$$G_{1D-}(\mathbf{r}) = \frac{iR_0}{2}e^{-ir/R_0}, \tag{2.73}$$

$$G_{2D-}(\mathbf{r}) = \frac{i}{4}H_0(r/R_0), \tag{2.74}$$

$$G_{3D-}(\mathbf{r}) = \frac{1}{4\pi r}e^{-ir/R_0}, \tag{2.75}$$

where $H_0^{(1)}$ is the Hankel function. These equations represent wave-like solutions for negative $\Delta_2 < 0$, while compared with the confined solutions for positive $\Delta_2 > 0$.

2.3 Bose-Einstein Condensates

Bose-Einstein Condensates are states of matter where all particles condense to the same single-particle state. This happens by cooling non-interacting systems below the BEC transition temperature. As long as the interaction is not too strong, BECs can still exist. Hence, the property that all particles are in the same single-particle state allows simple mathematical descriptions of the systems, in comparison with strongly interacting condensed matter systems. Depending on setups, BECs can be used to study a large variety of interesting physics. In this section, I introduce the weakly interacting BECs at zero temperature. The mathematical descriptions of two setups, the Kerr effects, and the two-component BECs, used in Chapter 4 and Chapter 5 are discussed.

2.3.1 Gross-Pitaevskii equation

We consider BECs at zero temperature so that all thermal excitations can be ignored. In the ideal situation without interaction, all bosons are in the same single-particle state. When the interaction is turned on, some particles may be kicked out from the condensates. The Hartree mean-field approach [10] can be used in the weak interaction regime by assuming that the full wavefunction

is the symmetrized product of a single-particle wavefunction $\phi(\mathbf{r})$. So the full wavefunction of N-particle system is

$$\Psi(\mathbf{r}_1, \mathbf{r}_2, ..., \mathbf{r}_N) = \prod_{i=1}^{N} \phi(\mathbf{r}_i), \tag{2.76}$$

with normalization

$$\int d\mathbf{r} |\phi(\mathbf{r})|^2 = 1. \tag{2.77}$$

For N identical non-interacting bosons, the Hamiltonian is

$$\mathscr{H}_0 = \sum_i^N \mathscr{H}_{0,i} = \sum_i^N \left[\frac{\mathbf{p}_i^2}{2m} + V(\mathbf{r}_i) \right], \tag{2.78}$$

where $\mathscr{H}_{0,i}$ is the Hamiltonian of an individual particle, $\mathbf{p}_i$ is the momentum operator, m is the mass of the particle, and $V(\mathbf{r}_i)$ is the external potential. The independence and additivity of Hamiltonian allow the use of separation of variables, so $\phi_{0,i}(\mathbf{r}_i)$ can be obtained by solving

$$\mathscr{H}_{0,i}\phi_{0,i} = \varepsilon_i \phi_{0,i}, \tag{2.79}$$

with the eigenenergy ε_i. Hence, the total wavefunction can be obtained by combining $\phi_{0,i}(\mathbf{r}_i)$. Since all single-particle wavefunction are the same, so $\phi_{0,i}(\mathbf{r}_i) = \phi_0(\mathbf{r}_i)$.

Now, suppose a dilute atomic gas of bosons is considered. In this system, the dominant interaction are the two-particle collisions of the form $U_0\delta(\mathbf{r} - \mathbf{r}')$ where $\delta(\mathbf{r})$ is the Dirac delta function. The interaction strength is $U_0 = 4\pi\hbar^2 a_s/m$ with the s-wave scattering length a_s. Therefore, the system is given by the Hamiltonian

$$\mathscr{H} = \mathscr{H}_0 + U_0 \sum_{i<j} \delta(\mathbf{r}_i - \mathbf{r}_j), \tag{2.80}$$

where the summation is taken over all pair of particles. The mean-field energy E of the state Ψ can be calculated as

$$E = \langle \Psi | \mathscr{H} | \Psi \rangle = N \int d\mathbf{r} \left[\frac{\hbar^2}{2m} |\nabla\phi|^2 + V|\phi|^2 + \frac{N-1}{2} U_0 |\phi|^4 \right]. \tag{2.81}$$

The term $N(N-1)/2$ counts the number of pair of particles and can be approximated by $N(N-1)/2 \approx N^2/2$, with the term of order $1/N$ being ignored.

The wavefunction of the condensate, which is sometimes referred to as the order parameter, can be defined as $\psi(\mathbf{r}) = \sqrt{N}\phi(\mathbf{r})$. Hence, the total number of particle is $N = \int d\mathbf{r}|\psi|^2$ and the particle density is $n(\mathbf{r}) = |\psi(\mathbf{r})|^2$. So the energy can be rewritten as

$$E[\psi] = \int d\mathbf{r}\left[\frac{\hbar^2}{2m}|\nabla\psi|^2 + V|\psi|^2 + \frac{1}{2}U_0|\psi|^4\right]. \tag{2.82}$$

By minimizing the $E - \mu N$ with respect to ψ^*, where μ is a Lagrange multiplier, we can obtain the time-independent Gross-Pitaevskii equation (GPE)

$$\mu\psi(\mathbf{r}) = -\frac{\hbar^2}{2m}\nabla^2\psi + V\psi + U_0|\psi|^2\psi. \tag{2.83}$$

This is basically the Schrödinger equation with an extra nonlinear term that originated from the two-particle collision. The eigenvalue μ has the meaning of chemical potential.

The corresponding time-dependent GPE is

$$i\hbar\partial_t\psi(\mathbf{r},t) = -\frac{\hbar^2}{2m}\nabla^2\psi + V\psi + U_0|\psi|^2\psi, \tag{2.84}$$

which describes the dynamics of the BEC in the mean-field limit. This equation can also be obtained by the variational derivative $\dot{\psi} = \delta E/\delta(i\hbar\psi^*)$. Note that some particles are in states that are different from the others due to interactions. So the dynamic equation above is true for the majority of the atoms except for a small number of particles of order $(na_s^3)^{1/2}$. The fact that not all particles are in the same state is referred as quantum depletion. For most experiments, it is of order one percent or less and can usually be ignored.

2.3.2 Kerr nonlinearity in BEC

Using Eq. (2.80), the second quantized Hamiltonian is

$$\hat{\mathscr{H}} = \int d\mathbf{r}\left[-\frac{\hbar^2}{2m}\hat{\psi}^\dagger\nabla^2\hat{\psi} + V\hat{\psi}^\dagger\hat{\psi} + \frac{1}{2}U_0\hat{\psi}^\dagger\hat{\psi}^\dagger\hat{\psi}\hat{\psi}\right], \tag{2.85}$$

where $\hat{\psi}(\mathbf{r})$ is the boson annihilation operator and $\hat{\psi}^\dagger(\mathbf{r})$ is the corresponding creation operator with the usual commutation relation $[\hat{\psi}(\mathbf{r}), \hat{\psi}^\dagger(\mathbf{r}')] = \delta(\mathbf{r} - \mathbf{r}')$. The time evolution of the field

$\hat{\psi}(\mathbf{r})$ operator can be obtained by using the Heisenberg equation of motion $i\hbar\partial_t\hat{\psi} = -[\hat{\mathscr{H}}, \hat{\psi}]$, which gives

$$i\hbar\partial_t\hat{\psi}(\mathbf{r},t) = -\frac{\hbar^2}{2m}\nabla^2\hat{\psi} + V\hat{\psi} + U_0\hat{\psi}^\dagger\hat{\psi}\hat{\psi}. \tag{2.86}$$

The field operator can be written as $\hat{\psi}(\mathbf{r}) = \psi(\mathbf{r}) + \delta\hat{\psi}(\mathbf{r})$, where $\psi(\mathbf{r})$ is the mean-field and $\delta\hat{\psi}(\mathbf{r})$ is the quantum fluctuation. In the mean-field limit $\hat{\psi}(\mathbf{r}) \to \langle\hat{\psi}(\mathbf{r})\rangle = \psi(\mathbf{r})$, where the quantum fluctuation is ignored, we can obtain the same GPE in Eq. (4.6).

If the interaction is weak and the quantum fluctuation can be ignored, then a BEC can be described by a single spatial wavefunction $\phi(\mathbf{r})$. In this case, the field operator can be rewritten as

$$\hat{\psi}(\mathbf{r}) = \hat{a}\phi(\mathbf{r}), \tag{2.87}$$

where $\hat{a}$ is the annihilation operator of the mode $\phi(\mathbf{r})$. Substituting this equation back to the Hamiltonian in Eq. (2.85) can be reduced to

$$\hat{\mathscr{H}} = \varepsilon_0\hat{n} + \frac{1}{2}U\hat{n}(\hat{n}-1), \tag{2.88}$$

with

$$\varepsilon_0 = \int d\mathbf{r}\left[\frac{\hbar^2}{2m}|\nabla\phi|^2 + V|\phi|^2\right], \tag{2.89}$$

$$U = U_0\int d\mathbf{r}|\phi|^4, \tag{2.90}$$

where $\hat{n} = \hat{a}^\dagger\hat{a}$ is the number operator. The linear term can be dropped in a rotating frame, so the Hamiltonian can be rewritten as

$$\hat{\mathscr{H}} = \frac{1}{2}U\hat{n}^2, \tag{2.91}$$

which is exactly the Kerr nonlinearity discussed before. It is the analogue of the optical Kerr effects in ultracold atoms. Hence, it provides a mechanism to create cat states in BECs.

2.3.3 Kerr nonlinearity in two-component BEC

The detection of the cat states requires a reference BEC to read out the phase information. So we may consider using a two-component BEC. To begin with, we consider a general two-component

model given by the Hamiltonian

$$\hat{\mathscr{H}} = \sum_{i=1,2} \left(\hat{\mathscr{H}}_i + \frac{1}{2} \hat{\mathscr{U}}_{ii} \right) + \hat{\mathscr{U}}_{12} + \hat{\mathscr{R}}, \tag{2.92}$$

with

$$\begin{aligned}
\hat{\mathscr{H}}_i &= \int d\mathbf{r} \left(\frac{\hbar^2}{2m_i} \nabla \hat{\psi}_i^\dagger(\mathbf{r}) \nabla \hat{\psi}_i(\mathbf{r}) + V_i(\mathbf{r}) \hat{\psi}_i^\dagger(\mathbf{r}) \hat{\psi}_i(\mathbf{r}) \right), && (2.93) \\
\hat{\mathscr{U}}_{ij} &= g_{ij} \int d\mathbf{r} \hat{\psi}_i^\dagger(\mathbf{r}) \hat{\psi}_j^\dagger(\mathbf{r}) \hat{\psi}_i(\mathbf{r}) \hat{\psi}_j(\mathbf{r}), && (2.94) \\
\hat{\mathscr{R}} &= \sum_{i=1,2} \hbar \Delta_i \int d\mathbf{r} \hat{\psi}_i^\dagger(\mathbf{r}) \hat{\psi}_i(\mathbf{r}) + \hbar \Omega \int d\mathbf{r} \left(\hat{\psi}_1^\dagger(\mathbf{r}) \hat{\psi}_2(\mathbf{r}) + \hat{\psi}_2^\dagger(\mathbf{r}) \hat{\psi}_1(\mathbf{r}) \right), && (2.95)
\end{aligned}$$

where m_i is the mass, $V_i(\mathbf{r})$ is the potential function, and g_{ij} is the two-particle collision energy density. The Rabi oscillation term $\hat{\mathscr{R}}$ represents the inter-conversion between the two components with Rabi frequency Ω and detuning Δ_i. The detuning is the frequency difference $\Delta_i = \omega_i - \omega$ between the driving frequency and the frequency of the target internal energy level.

We consider the setup with $\hat{\mathscr{R}} = 0$ here, which means that there is no conversion between the two components and the number of particles in each component is conserved. Again, assuming both the BEC components can be described by single-particle modes $\phi_i(\mathbf{r})$, so the field operator becomes

$$\hat{\psi}_i(\mathbf{r}) = \hat{a}_i \phi_i(\mathbf{r}). \tag{2.96}$$

Substituting back into the Hamiltonian above, we have [107]

$$\hat{\mathscr{H}} = \varepsilon_1 \hat{n}_1 + \varepsilon_2 \hat{n}_2 + \frac{1}{2} U_{11} \hat{n}_1^2 + \frac{1}{2} U_{22} \hat{n}_{22}^2 + U_{12} \hat{n}_1 \hat{n}_2, \tag{2.97}$$

with

$$\begin{aligned}
\varepsilon_i &= \int d\mathbf{r} \left[\frac{\hbar^2}{2m} |\nabla \phi_i|^2 + V |\phi_i|^2 \right], && (2.98) \\
U_{ij} &= g_{ij} \int d\mathbf{r} |\phi_i|^2 |\phi_j|^2. && (2.99)
\end{aligned}$$

Since the total number of particles $N = \hat{n}_1 + \hat{n}_2$ is conserved in the atomic system, so we can set it to a constant. The above equation can be rewritten in term of $\hat{n}_1$, with the constant and linear terms

dropped, as

$$\hat{\mathscr{H}} = \frac{1}{2}\left(U_{11} + U_{22} - 2U_{12}\right)\hat{n}_1^2. \tag{2.100}$$

So in this case, there is also Kerr nonlinearity that can generate a cat state. Note that ϕ_1 and ϕ_2 are usually different even in the ground state for few reasons. For example, the spatial mode of condensates with intra-atomic interactions can depend on the number of atoms. Also, the inter-atomic interaction changes the spatial modes of both of them. If all three scattering lengths a_{ij} are very close, such as for Rubidium atoms, and $N_1 \approx N_2$, then $\phi_1 \approx \phi_2$ [96] is a good assumption.

2.3.4 Mean-field equation of two-component BEC

The time evolution of the field operators in a two-component BEC can be found by Heisenberg equation $i\hbar\partial_t\hat{\psi}_i = -[\hat{\mathscr{H}}, \hat{\psi}_i]$ with $\hat{\mathscr{H}}$ in Eq. (2.92). If the mean field of the operators is taken, $\hat{\psi}_i(\mathbf{r}) \to \langle\hat{\psi}_i(\mathbf{r})\rangle = \psi_i(\mathbf{r})$, then the dynamic equations are

$$i\hbar\partial_t\psi_1(\mathbf{r},t) = \left(-\frac{\hbar}{2m}\nabla^2 + V_1 + g_{11}|\psi_1|^2 + g_{12}|\psi_2|^2 + \hbar\Delta_1\right)\psi_1 + \hbar\Omega\psi_2, \tag{2.101}$$

$$i\hbar\partial_t\psi_2(\mathbf{r},t) = \left(-\frac{\hbar}{2m}\nabla^2 + V_2 + g_{12}|\psi_1|^2 + g_{22}|\psi_2|^2 + \hbar\Delta_2\right)\psi_2 + \hbar\Omega\psi_1, \tag{2.102}$$

which gives the coupled two-component GPE. Note that the physics is invariant with a constant energy shift, so one of the detunings Δ_1 or Δ_2 can be eliminated, say, $\Delta_1 = 0$. The trapping potential V_1 and V_2 are usually the same, but can be different by using spin dependent potential. This can significantly change the relative density of both components and so the effective nonlinearity. The nonlinearity $g_{ij} = 4\pi\hbar^2 a_{ij}/m$ depends on the scattering a_{ij} between components i and j. Using Feshbach resonances, one of the scattering lengths a_{ij} can be usually adjusted freely. Depending on experiments, both large and small a_{ij} can be used. For large a_{ij}, the corresponding nonlinearity can be enhanced, while for small a_{ij}, the corresponding three-body loss can be suppressed.

Now, suppose we consider the system with no trapping on the second component, so $V_2 = 0$. Also, the nonlinear interaction involving ψ_2 is negligible, i.e. $g_{12} = g_{22} = 0$. Then the resulting

equations are

$$i\hbar\partial_t\psi_1(\mathbf{r},t) = \left(-\frac{\hbar}{2m}\nabla^2 + V_1 + g_{11}|\psi_1|^2\right)\psi_1 + \hbar\Omega\psi_2, \tag{2.103}$$

$$i\hbar\partial_t\psi_2(\mathbf{r},t) = \left(-\frac{\hbar}{2m}\nabla^2 + \hbar\Delta_2\right)\psi_2 + \hbar\Omega\psi_1, \tag{2.104}$$

which are the equations used in Chapter 5. Note that the equations describe a real BEC setup in experiment and should be implementable.

Chapter 3

Linked and knotted chimera filaments in oscillatory systems

3.1 Preface

While the existence of stable knotted and linked vortex lines has been established in many experimental and theoretical systems, their existence in oscillatory systems and systems with nonlocal coupling has remained elusive. Here, we present strong numerical evidence that stable knots and links such as trefoils and Hopf links do exist in simple, complex, and chaotic oscillatory systems if the coupling between the oscillators is neither too short ranged nor too long ranged. In this case, effective repulsive forces between vortex lines in knotted and linked structures stabilize curvature-driven shrinkage observed for single vortex rings. In contrast to real fluids and excitable media, the vortex lines correspond to scroll wave chimeras [synchronized scroll waves with spatially extended (tubelike) unsynchronized filaments], a prime example of spontaneous synchrony breaking in systems of identical oscillators. In the case of complex oscillatory systems, this leads to a novel topological superstructure combining knotted filaments and synchronization defect sheets.

The results in this chapter were part of my research and were published in [8]. This work was started by the observations of knots in 3D simulations of nonlocal Kuramoto model during the early stage of my PhD. To further study the phenomenon, I wrote the simulation and visualization programs specifically for this project. The manuscript was written with the guidance and criticism from Prof. Davidsen.

3.2 Introduction

In natural science, knots and linked structures have attracted attention in various branches as they are an essential part of many physical processes. This includes real fluids [108], liquid crys-

tals [109, 110], Bose-Einstein condensates [111, 112], electromagnetic fields and light [113, 114], superconductors [115], proteins [116] as well as excitable media [117, 118] and bistable media [119]. Stable knots and their topological invariants are of particular interest for both theory and experiments as they play an important role in characterizing and controlling different systems and their dynamics [120]. This is especially true in excitable media, where linked and knotted filaments of phase singularities can be essential to understand the nature of scroll wave propagation processes [117, 118, 3, 121], including nonlinear wave activity associated with ventricular fibrillation and sudden cardiac death [122, 123]. While the wave propagation processes in excitable and nonlinear oscillatory systems are very similar [16], the existence of such stable knotted and linked filaments in oscillatory systems has remained elusive. For example, to the best of our knowledge no corresponding parameter regime has been identified in the complex Ginsburg-Landau equation (CGLE), which is the normal form of oscillatory media close to the Hopf bifurcation [1, 36]. This is deeply unsatisfying as the collective behavior, spontaneous synchronization and wave propagation in oscillatory media and coupled systems of nonlinear oscillators are topics of general interest with applications across disciplines [16, 25], including the quantum regime [124, 125].

In this paper, we show for the first time that (i) stable knotted and linked filaments do exist in oscillatory systems, (ii) they do exist under non-local coupling in the underlying dynamical equations, and (iii) together with synchronization defect sheets they can form novel topological superstructures. From the Kuramoto model of simple phase oscillators and the CGLE to complex and chaotic oscillatory systems, we find in particular Hopf links and trefoils that persist over hundreds of thousands of scroll wave rotations for a wide range of parameters. Due to the non-local coupling, the filaments that make up the long-lived knotted structures are no longer simple phase singularities as is typical for scroll waves, but instead the filaments correspond to spatially extended regions in which the oscillators are unsynchronized. This is despite the fact that all oscillators are identical and uniformly coupled. The coexistence of these unsynchronized local regions with synchronized regions — exhibiting traveling waves in our specific case — is the hallmark of

a chimera state [4, 18, 20, 126, 5, 34]. While single ringlike chimera filaments shrink, knotted and linked filaments generate an effective repulsion that prevents shrinkage and stabilizes the pattern even in the presence of strong noise. We find that for coupling that is too short ranged (including local coupling) or coupling lag that is too small, the repulsion is too weak such that knotted structures collapse. This is despite the fact that phase twists along the filaments are present, which have been hypothesized to have a stabilizing effect by themselves [118]. If the coupling between oscillators is too long ranged and the coupling lag is too large, straight chimera filaments become unstable in a way reminiscent of negative line tension [123, 127, 128, 129, 130, 131, 132]. This leads to the breakup of the knotted structures as well.

3.3 Phase oscillators

As the simplest paradigmatic model of an oscillatory system, we first focus on the Kuramoto model [5, 2, 26]. In this model, $\theta(\mathbf{r},t) \in [-\pi,\pi)$ denotes the state of an oscillator at a spatial point $\mathbf{r}$ and time t. The evolution is governed by

$$\dot{\theta}(\mathbf{r},t) = \omega_0 + K\omega(\mathbf{r},t). \tag{3.1}$$

Here, ω_0 is the natural frequency of the oscillators and K is the coupling strength. Note that we can set $\omega_0 = 0$ and rescale time $Kt \to t$ without loss of generality. Thus, ω is the instantaneous angular frequency obeying

$$\omega(\mathbf{r},t) = \int_V G_0(\mathbf{r}-\mathbf{r}')\sin[\theta(\mathbf{r}',t) - \theta(\mathbf{r},t) - \alpha]d\mathbf{r}' \tag{3.2}$$

where $G_0(\mathbf{r})$ is a coupling kernel, α is the coupling lag or phase shift, and the integration is taken over the whole volume V. The kernel used is a top-hat kernel with coupling radius R

$$G_0(\mathbf{r}) \sim \begin{cases} 1, & r \le R \\ 0, & r > R \end{cases} \tag{3.3}$$

which is normalized as $\int_V G_0(\mathbf{r})d\mathbf{r} = 1$. In simulations, the spatial locations are discretized into $\mathbf{r} = (x_i, y_i, z_i)$ with $1 \leq x_i, y_i, z_i \leq L$ taking integer values in the system of linear length L such that $V = L^3$. Hence, the control parameters of the system are R and α, with finite size effects determined by L. Extensive simulations have been done using the Runge-Kutta scheme [1] with both random initial conditions (IC) and specific functions, see the Appendix for details. We use periodic boundary conditions (BC) here, yet our findings are quite independent of the BC.

The Kuramoto model with nonlocal coupling is known to exhibit chimera states, in which both synchronized and unsynchronized regions of oscillators can coexist in the same system even though all oscillators are identical and uniformly coupled. Most studies have been done on the one dimensional ring and complex networks [5]. In higher dimensions, two qualitatively different chimera regimes have been identified for the Kuramoto model given by Eqs. (3.1), (3.2), (3.3). For near global coupling with $R \sim L$ and large $\alpha \lesssim \pi/2$, various coherent and incoherent strip, spot, plane, cylinder, sphere and cross patterns have been observed in two and three dimensions (2D and 3D) [34, 133]. The other regime involves shorter range nonlocal coupling $L \gg R \gg 1$ with smaller α. In 2D geometries, synchronized spiral waves with unsynchronized chimera cores can appear. They behave like a normal spiral, yet the dynamics in the core is unsynchronized [133, 19, 134, 135]. Similarly, in 3D, regular scroll waves with chimera filaments (or chimera tubes) at their center — instead of the linelike filaments of phase singularity — have been observed [34].

3.4 Existence of knots

For $L \gg R \gg 1$ and large effective system size L/R, we observe different stable linked and knotted scroll waves in the Kuramoto model as shown in Figs. 3.1 and 3.2. To clearly visualize the chimera tubes and the knotted and linked structures (referred to as knots in the following), one has to take into account that both phase $\theta(\mathbf{r},t)$ and angular frequency $\omega(\mathbf{r},t)$ fluctuate a lot in

[1] We have tested different time steps using both explicit Runge-Kutta and Euler's method. The stable topological structures are preserved but the trajectories deviate after a long time. This is expected since a large time step introduces an effective noise. Similar observations have been mentioned in Ref. [118] for excitable media.

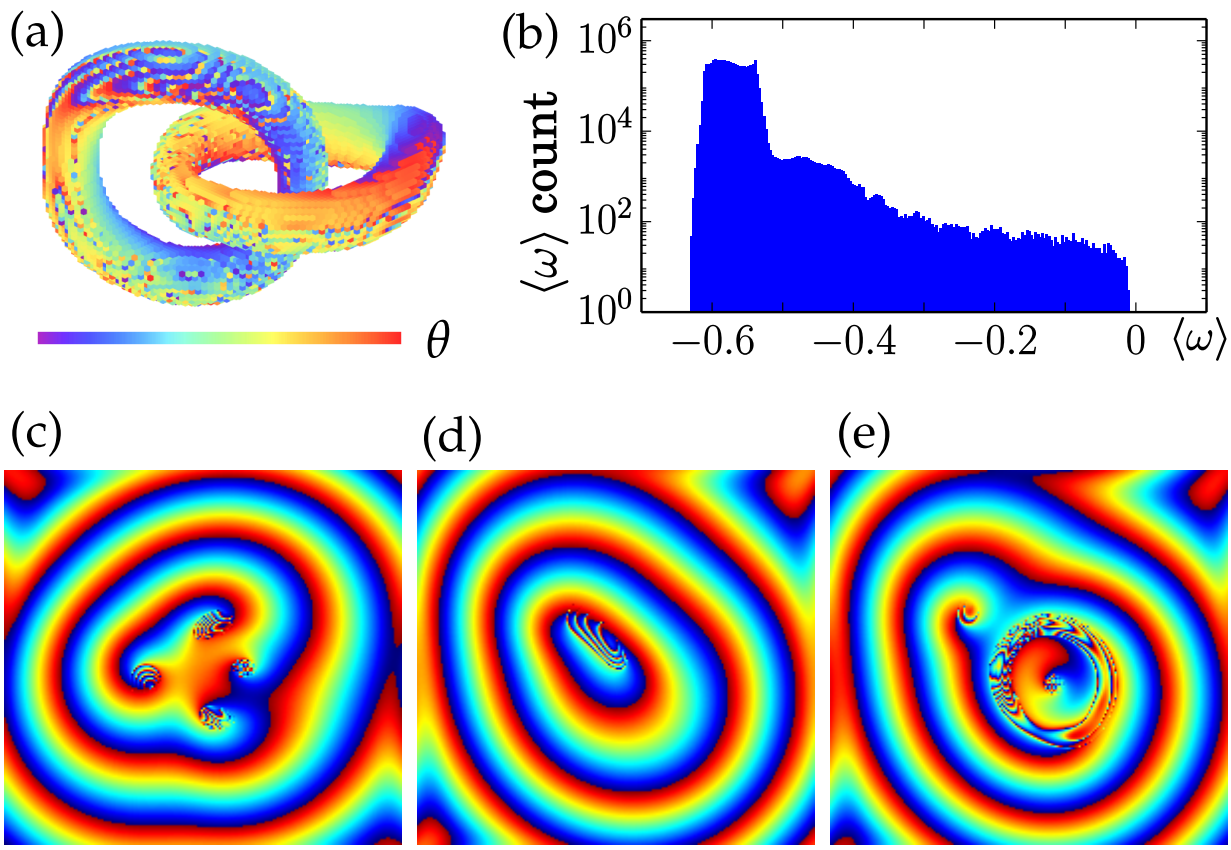

Figure 3.1: (color online) Chimera nature of knots ($\alpha = 0.8$, $R = 8$, $L = 200$). (a) Snapshot of a Hopf-link shows the unsynchronized phase $\theta(\mathbf{r},t)$ on the isosurface of spatially smoothed angular frequency $\tilde{\omega}(\mathbf{r},t)$. (b) Mean angular frequency distribution of $\langle\omega(\mathbf{r})\rangle$, averaged over approximately 10 periods. The tail to the right corresponds to unsynchronized oscillators. (c) Plot of 2D cross-section of $\theta(\mathbf{r})$ showing the chimera and spiral wave properties. A vertical cut through both rings in panel (a), showing four chimera cores. (d) A cut through the far edge of a ring. (e) Slicing of a ring, showing a ring chimera and two chimera cores of the other ring.

space as shown in Fig. 3.1b- 3.1e. Thus, it is helpful to define a local mean angular frequency $\tilde{\omega}(\mathbf{r},t) = \int_V G_0(\mathbf{r}-\mathbf{r}')\omega(\mathbf{r}',t)d\mathbf{r}$. Fig. 3.1a shows a snapshot of the chimera tubes by plotting the phases of the unsynchronized oscillators for $\tilde{\omega}(\mathbf{r},t) \geq$ const. The presence of scroll waves with chimera filaments can also be seen directly in the phase field. Selected 2D cross-sections of the phase field (Fig. 3.1c) show patterns similar to chimera spirals in 2D [19], while other cross-sections show features that are specific to 3D such as the chimera ring shown in Fig. 3.1e. Note that the Hopf link and other knots observed generate spherical wave in the far-field. Moreover, they are not stationary but keep rotating, drifting, and changing their shape over time as shown in

the Appendix.

As chimera filaments are associated with scroll waves, phase twists can be present along the filament [136]. This is visible in Fig. 3.1a, but can be better visualized by considering the local mean phase field $\tilde{\theta}(\mathbf{r},t)$, defined by

$$\tilde{\rho}(\mathbf{r},t)e^{i\tilde{\theta}(\mathbf{r},t)} = \int_V G_0(\mathbf{r}-\mathbf{r}')e^{i\theta(\mathbf{r}',t)}d\mathbf{r}'. \tag{3.4}$$

This is illustrated in Fig. 3.2, for example.

3.5 Phase diagram

For the Kuramoto model given by Eqs. (3.1), (3.2), and (3.3), our numerical simulations allow us to obtain a phase diagram as a function of α. This is plotted in Fig. 3.2 together with some of the asymptotic states. At small α, only relatively simple scroll wave structures with straight chimera tubes are stable. For $\alpha_K < \alpha < \alpha_0$, also knots such as 1 twist Hopf links and 3 twist trefoils (as shown in Fig. 3.2) are stable over hundreds of thousands of scroll wave rotation periods T [2]. More stable structures including helices, ring-tubes and linked triple rings are shown in the Appendix. For $\alpha > \alpha_0$, knots as well as simple straight tubes become unstable. The evolution in the former case is shown in Fig. 3.3b. In the latter case, the dynamics of the chimera filament indicates that a finite wavelength instability of the filament itself occurs such that the filament grows rapidly (see the Appendix). In both cases, the rapid growth of filaments is accompanied by fragmentation through collisions leading eventually to an irregular or turbulent-like behavior as shown in Fig. 3.2. Furthermore, in the same parameter regime near α_0 in 2D, chimera spirals are stable and no irregular pattern is present [19]. All this suggests that the underlying instability is truly 3D in nature as the negative line tension instability and similar filament instabilities that have been observed in excitable and oscillatory media [123]. Fig. 3.2 also shows that at even higher $\alpha \sim \pi/2$, no filament structures can be recognized.

[2]The stability of Hopf links and trefoils in the Kuramoto model has been tested for extended periods of time of at least $t = 1.2\times10^6$ (or period $T > 10^5$ where $T \approx 11$ at $\alpha = 0.8$) for $L = 100$ with $R = 4$, and $t = 1.2\times10^5$ for $L = 200$ with both $R = 4$ and $R = 8$.

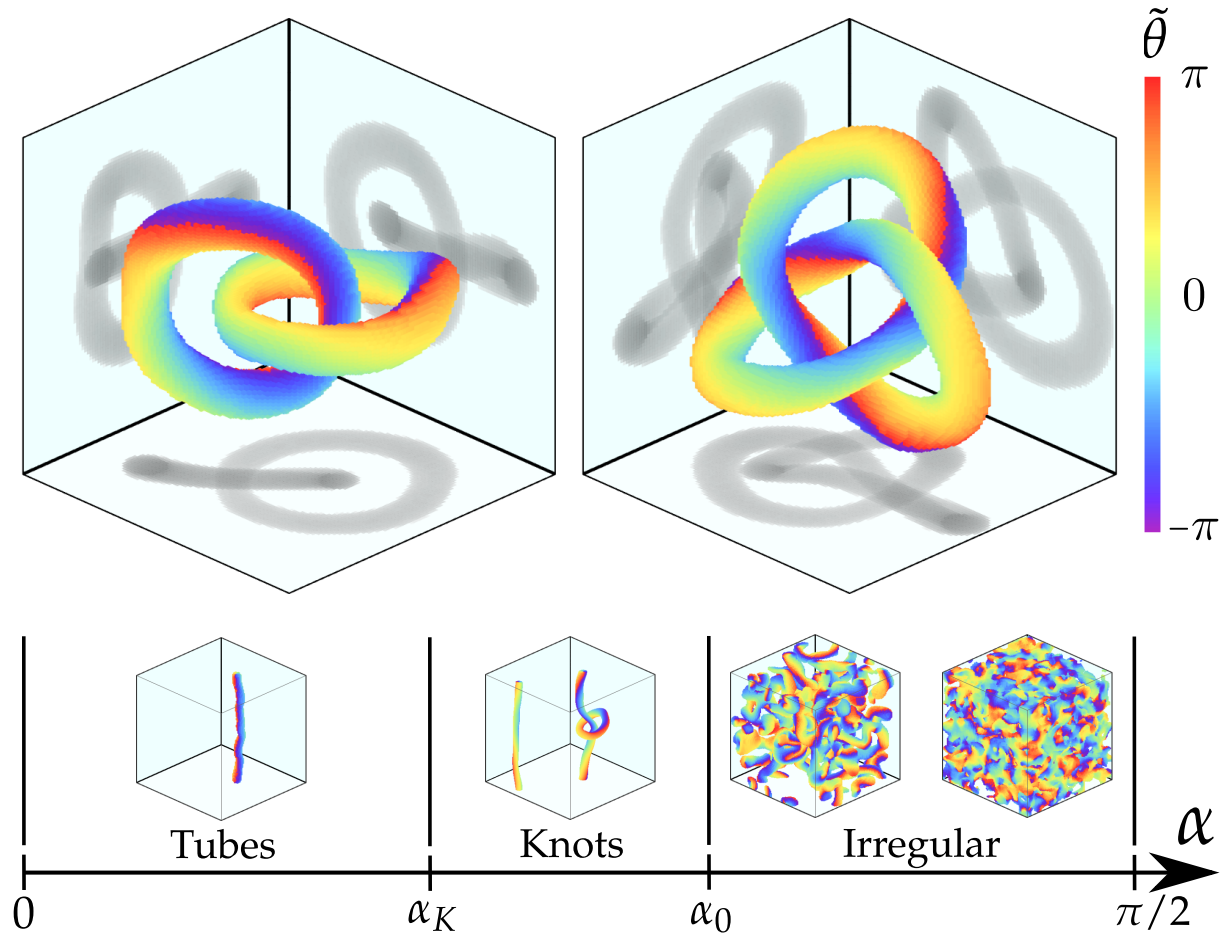

Figure 3.2: (color online) Phase diagram of the Kuramoto model in 3D as a function of α with nonlocal coupling $L \gg R \gg 1$. Various knots exist between α_K and α_0. Top panel shows stable Hopf-link (left), and trefoil (right) as examples. The plots are similar to those in Fig. 3.1a, but smoothed phases $\tilde{\theta}(\mathbf{r})$ are used instead. Shadows on the walls correspond to perpendicular projections of the structures.

The nature of the instability of knots at α_K and α_0 are significantly different. Below α_K, any knot transforms through one or multiple reconnections into a single untwisted ring which shrinks and disappears, leading to homogeneous oscillations. As we have tested, all single chimera rings with a radius of up to 80 shrink and eventually vanish for $0 \leq \alpha < \alpha_0$ with no-flux BC (see Appendix). This together with the stable knots for $\alpha_K < \alpha < \alpha_0$ indicates that there is an effective repulsion between filaments in knots that is sufficient to prevent curvature-driven shrinkage and stabilize these structures above α_K. Below α_K, the repulsion is too weak to prevent reconnections. This mechanism is similar to what has been observed for knots in bistable media [119] and plays

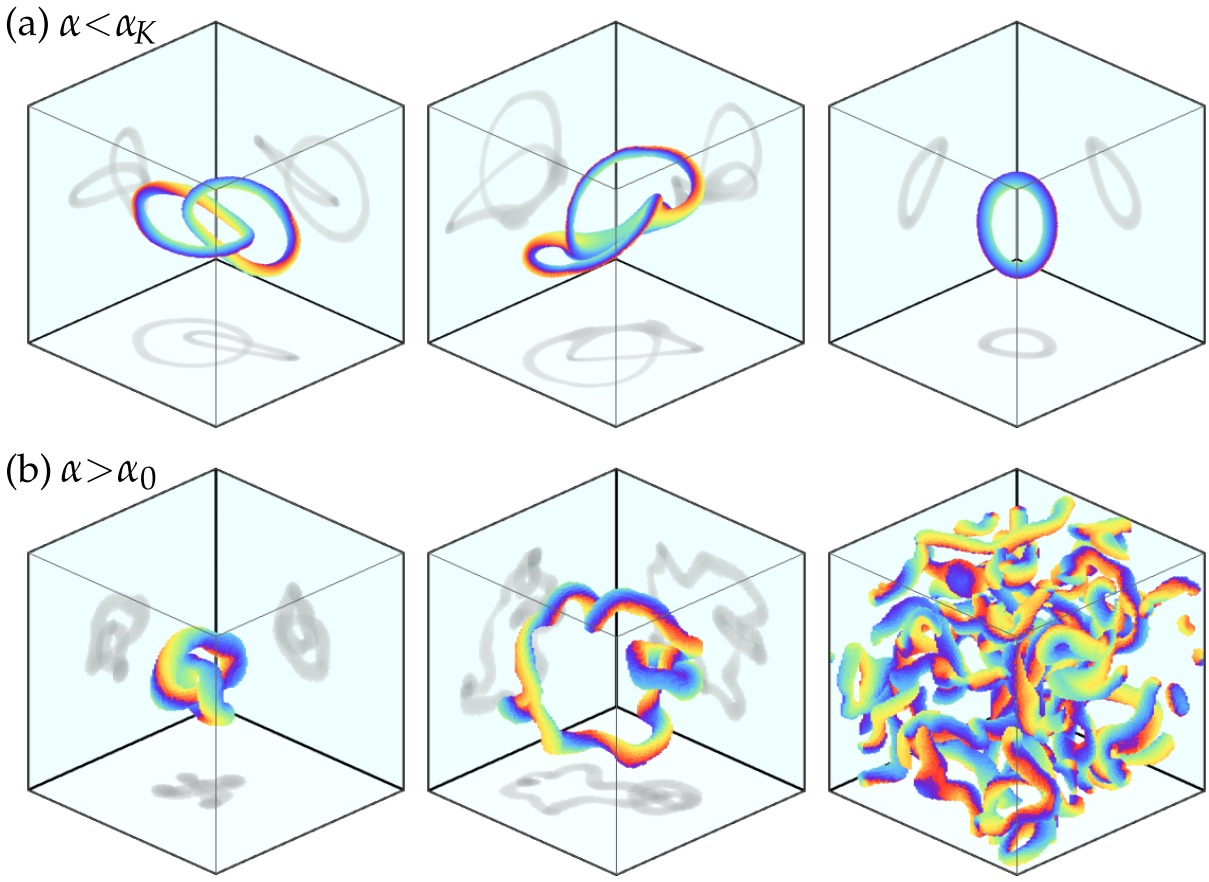

Figure 3.3: (color online) Time evolution of Hopf links outside their stability regimes near α_K and α_0, respectively. (a) $\alpha < \alpha_K$. After α is decreased slightly from above α_K to below, the two rings of the Hopf link merge resulting in a single ring which eventually vanishes. (b) $\alpha > \alpha_0$. After α is tuned slightly from below α_0 to above, one of the rings grows until it collides and reconnects, resulting in a turbulent-like pattern.

an important role in other situations as well [137]. Simulation results show that different knots have different stability regimes, especially Hopf links are stable over a broader range of α than trefoils. Therefore, we denote α_K in the following as the point at which Hopf links disappear.

3.6 Dependence on R, L, and geometry

Numerical simulations for $4 \leq R \leq 12$ and $64 \leq L \leq 300$ show that the phase diagram presented in Fig. 3.2 is independent of the specific choice of R and L as long as $L \gg R \gg 1$. Specifically, $\alpha_K \approx 0.61$ and $\alpha_0 \approx 0.90$ with uncertainty ± 0.02. The condition $L \gg R$ ensures that finite size

effects do not play a significant role as the size of stable knots and the wavelength scale with R [19, 134]. For example, we find that stable Hopf links cease to exist for $L/R \lesssim 16$. Also, if the effective system size is too small, more complex knots tend to decay into simpler ones (see the Appendix). The condition $R \gg 1$ is also crucial. We find that for shorter range couplings $R < 3$ the lifetime of knots is finite [3]. Specifically, no stable knots have been observed for local coupling, $R = 1$, independent of the IC used to generate Hopf links. This is a consequence of temporal fluctuations in the s hape of the individual rings within a Hopf link becoming comparable to the minimum separation between the rings such that the rings merge and disappear (see the Appendix) — the same behavior as for the instability at α_K. We observe qualitatively the same for trefoils.

3.7 Robustness with respect to noise

To further quantify the stability of different topological states, we examine them in noisy environments. This is modeled by an additional Gaussian phase noise $\xi(\mathbf{r},t)$ in the Kuramoto model

$$\dot{\theta}(\mathbf{r},t) = \omega(\mathbf{r},t) + D\xi(\mathbf{r},t) \tag{3.5}$$

where $\langle \xi(\mathbf{r},t) \rangle = 0$ and $\langle \xi(\mathbf{r},t)\xi(\mathbf{r}',t') \rangle = \delta(\mathbf{r}-\mathbf{r}')\delta(t-t')$. As shown in Fig. 3.4, Hopf links and trefoils can survive under noise magnitude as high as $D^* = 0.22$. This high robustness under noise signifies the topological protection of knots. Longer range coupling as quantified by R also increases the tolerance of local phase noise as shown in Fig. 3.4a.

3.8 Dependence on spatial kernel

In contrast to the top-hat kernel G_0, we did not observe stable knots for Gaussian kernels often considered in the context of chimera states. This together with the existence of a minimal R discussed above indicates that the range of the spatial kernel is crucial. To substantiate this further,

[3] For $R = 2$, the lifetime can vary significantly with the used time stepping of the integrator and becomes longer for shorter Δt. For example, the lifetime is about $t = \mathcal{O}(5000)$ and, thus, less than 1000 scroll wave rotations using 4th order Runge-Kutta with $\Delta t = 0.02$.

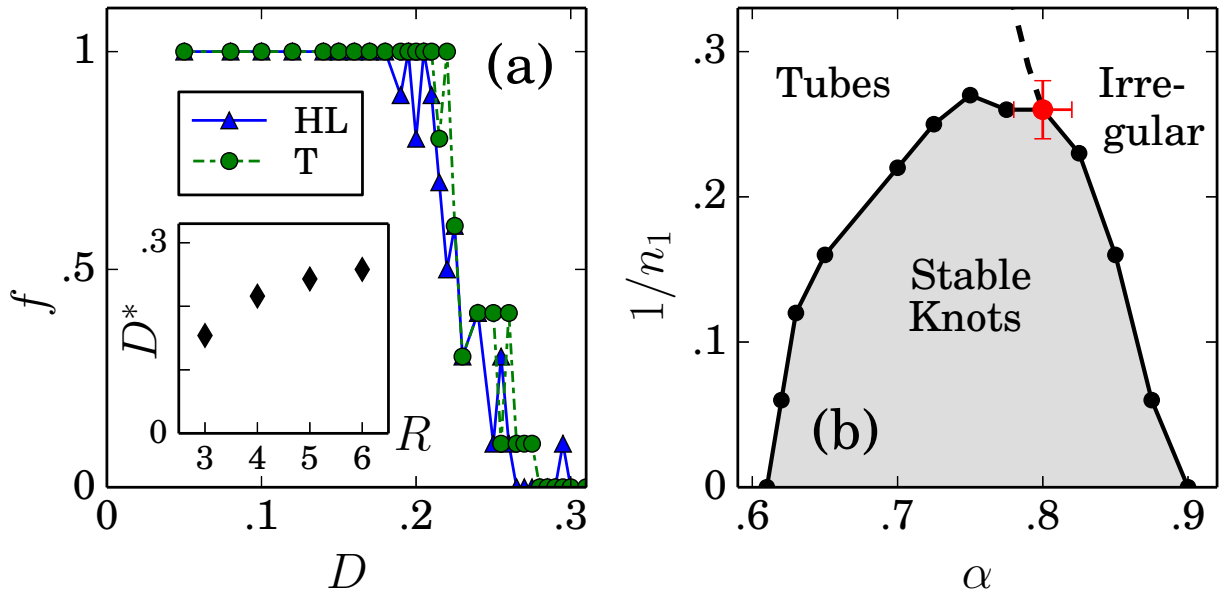

Figure 3.4: (color online) (a) The tolerable phase noise level for Hopf links (HL) and trefoils (T). f quantifies the fraction of structures persisting after $t = 5000$ (≈ 450 scroll wave rotations) under noise intensity D. Each point corresponds to an ensemble of 10 realizations. Here, $\alpha = 0.8$, $R = 4$, and $L = 100$. Inset: D^* denotes the point of $f = 0.5$ for a Hopf link as a function of R using $\alpha = 0.8$, $L/R = 16$. (b) Phase diagram showing the stable regime of Hopf links for kernel G_1 with $L \gg R \gg 1$. The red dot marks the triple point between all three phases where $\alpha_K = \alpha_0$. The error bars account for different $R \geq 4$ and L up to $L = 300$. Note that $1/n_1 = 0$ corresponds to the top-hat kernel G_0 used in Fig. 3.2.

let us consider the kernel $G_1(r) \sim e^{-(r/R)^{n_1}}$ such that $G_1 \to G_0$ when $n_1 \to \infty$ if $R < L$. Note that $n_1 = 2$ is a Gaussian, $n_1 = 1$ is an exponential, and $n_1 = 0$ gives global coupling. Simulations show that if G_1 becomes more long-ranged as n_1 decreases, the stable regime $\alpha_K < \alpha < \alpha_0$ of knots shrinks as shown in Fig. 3.4b. This is the only effect on the knots as the nature of the associated instabilities along the boundaries appears unchanged and follows the pattern shown in Fig. 3.3. The phenomenon is independent of the exact functional form of the kernel (see the Appendix).

3.9 Beyond phase oscillators

The nonlocal CGLE is given by [7]:

$$\dot{A}(\mathbf{r},t) = A - (1+ib)|A|^2 A + (1+ia)p_A, \tag{3.6}$$

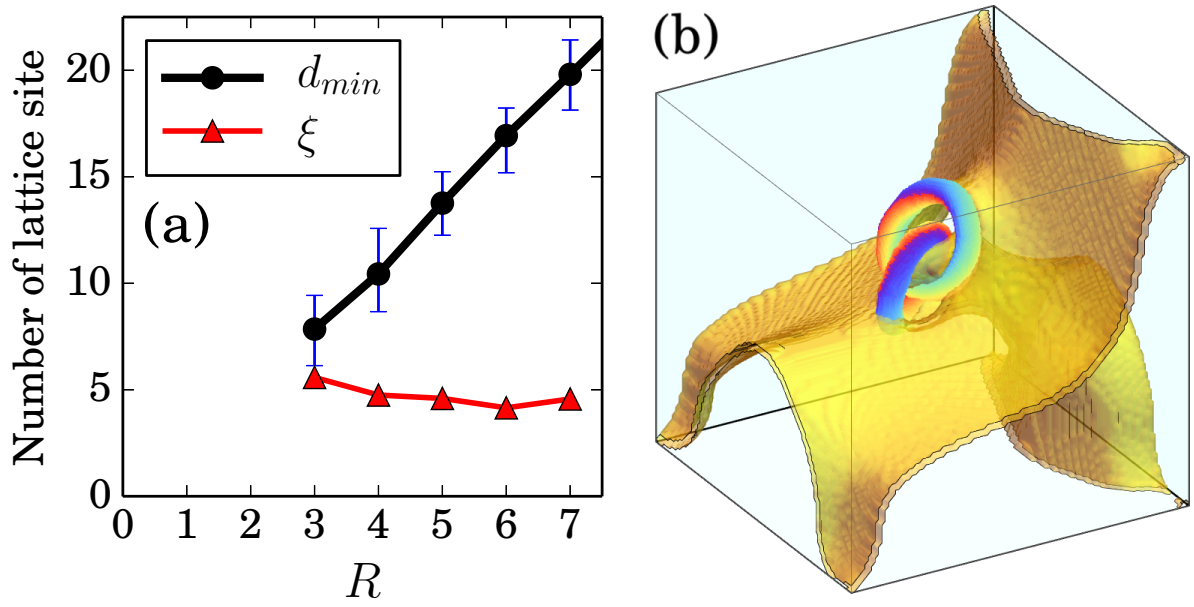

Figure 3.5: (color online) (a) CGLE [$(a,b) = (1,0)$, $K = 0.1$]: Comparison of minimum separation between rings in a Hopf link, d_{min}, and a measure of spontaneous fluctuations in the ring shape, ξ (see the Appendix for details). Bars indicate the 99% range. (b) Rössler model: Topological superstructure of a chimera Hopf link with an attached sychronization defect sheet in the period doubled regime (see the Appendix for more viewpoints and dynamics).

where the control parameters are (a,b). The nonlocal coupling p_A is given by

$$p_A(\mathbf{r},t) = K \int G_0(\mathbf{r}-\mathbf{r}')[A(\mathbf{r}',t) - A(\mathbf{r},t)]d\mathbf{r}', \tag{3.7}$$

and the coupling strength is K. Since the CGLE can be well approximated by the Kuramoto model in the weak-coupling limit independent of the specific coupling [18, 138], similar results are expected in certain parameter regimes. Indeed, stable chimera knots with *non-constant* amplitudes $|A|$ exist in the vicinity of the parameters $(a,b) = (1,0)$ [7] for $K = 0.1$ (see the Appendix) and larger values of K. The lifetimes of knots are longer than 6×10^5, provided that $R \gg 1$. All results discussed above for the Kuramoto model also hold qualitatively for the CGLE. This includes in particular the break-up of knots for small R. Fig. 3.5a provides a clear rationale why this happens: The separation between the rings in a Hopf link shrinks with decreasing R such that it eventually becomes comparable to the amplitude associated with the temporal fluctuations in the shape of individual rings. This offers an explanation of why no stable knots have been observed in the CGLE with local coupling. Our findings for the CGLE imply that *all* oscillatory systems with

appropriate nonlocal coupling should exhibit stable knots in some parameter regime near their Hopf bifurcation.

3.10 Complex oscillatory systems

We also observe stable chimera knots if the uncoupled oscillators are far from the Hopf bifurcation and undergo complex or even chaotic oscillations, requiring at least a three-dimensional local phase space. A specific example is the Rössler model with nonlocal coupling [139], which exhibits a phenomenology with many features in common with those observed in complex oscillatory systems including chemical experiments [140]. It is given by

$$\begin{aligned} \dot{X}(\mathbf{r},t) &= -Y - Z + p_X, \\ \dot{Y}(\mathbf{r},t) &= X + aY + p_Y, \\ \dot{Z}(\mathbf{r},t) &= b + Z(X - c), \end{aligned} \tag{3.8}$$

where the control parameters are (a,b,c) and the nonlocal coupling $p_X(\mathbf{r},t)$ and $p_Y(\mathbf{r},t)$ are defined analogously to Eq. (3.7). For $a = b = 0.2$, the effective α decreases as c increases [138]. For $R \gg 1$, we observe stable chimera knots in the period-doubled regime ($c = 3.6$) and in the chaotic regime ($c = 4.8$) with weak coupling $K = 0.05$ (see the Appendix). All findings described above for the other models hold qualitatively here as well. Stable knots only exist if the coupling between the oscillators is neither too short-ranged nor too long-ranged. For example, we did not observe stable Hopf links or trefoils for $R = 1$ or when the kernels were Gaussian in the parameter regimes given above. Moreover, in the period-doubled regime, synchronization defect sheets (SDS) — the analog of synchronization defect lines in 2D systems [139, 141] — can be observed for the first time and, more importantly, connect the different filaments (see Fig. 3.5b, the Appendix). This leads to another layer of topological structure associated with the knots, making this a unique phenomenon and adding potentially to their general robustness if multiple knots are present [140].

3.11 Discussion and conclusions

Our findings show that knots exist and are stable over a significant range of parameters in various oscillatory systems with nonlocal coupling as long as the characteristic coupling length of the kernel is sufficiently large and the tail of the kernel decays sufficiently fast. The variety of knots is also much higher compared to what has been reported for excitable media [118, 136]. For example, we have also observed other relevant unknotted structures such as stable double helices (see the Appendix) — a structure that has remained elusive in the CGLE with local coupling [35]. This suggests that the models considered here can serve as paradigmatic models to study various knotted and unknotted structures associated with scroll waves in general, including the novel topological superstructures of knots with SDSs. More specifically, it allows one to explore the topological constraints imposed by the phase field on the observable phase twists associated with a given knot — a field largely untouched [136] — as well as the effect of synchronization defect sheets on knots for the first time.

A remaining open question is to which extent the existence of stable knots in oscillatory systems depends on the presence of a chimera state. While our findings suggest that a chimera state is a necessary condition, there is no fundamental reason to substantiate this. However, our simulations indicate that the mobility of the scroll wave filaments plays an important role. If the filaments move or meander sufficiently fast (e.g. $R = 1$ or for a Gaussian kernel with large α), no chimera state can be numerically observed and stable knots are absent. This is similar to what has been reported for chimera spirals in 2D [134] and knots in excitable media [118]. One possible way forward is the recently proposed ansatz by Ott and Antonsen [29, 30], which has been successfully applied to study the existence and stability of chimera spirals [142].

In addition to the robustness of knots under dynamical noise, we also find that Hopf links and trefoils can emerge in a self-organized way from random IC with fair probability (see the Appendix). Both features indicate knots should be observable in real-world oscillatory systems that follow a dynamics similar to the models studied here, with most likely candidates to be chemical

systems [18, 139, 137, 143, 22]. Yet, the observation of chimera filaments in natural systems remains a challenge for the future.

3.12 Appendix A: Topological structures

Fig. 3.6 shows various long-lived (stable or metastable) topological structures in the non-local Kuramoto model within the regime $\alpha_K < \alpha < \alpha_0$. Note that knotted structures more complicated than simple Hopf links tend to have smaller stability regimes. An exception are (knotted) structures that require periodic boundary conditions (BC) *and* do not drift, which can be stable below α_K. This is shown, for example, in Fig. 3.7 and includes straight filaments. Simulations suggest that the multi-filament structure in Fig. 3.7c is stable for $\alpha > 0$.

3.13 Appendix B: Dynamics

In the non-local Kuramoto model, knotted structures that exist independent of the specific choice of BC (periodic vs. no-flux) are not stationary but drift, rotate and change their shape over time. As an example, Figs. 3.8(a) and 3.8(b) show a few snapshots for different structures. Note that for the system sizes studied, the center of mass motion is not straight over long time scales. The phase field away from these knotted structures takes on the form of spherical waves as shown in Fig. 3.9. In case of the ring-tube structure (which is specific to periodic BC), the ring propagates along the tube and keeps distorting the local part of the tube while it travels, see Fig. 3.8 (c). In all these cases, the direction of the filament motion can be deduced from the instantaneous angular frequency $\omega(x,y,z)$ shown in the rightmost column of Fig. 3.8.

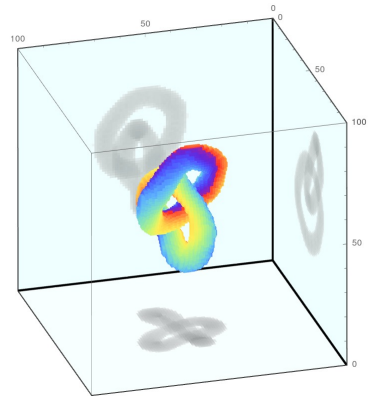

(a) $\tau > 1.2 \times 10^6$, $\alpha = 0.8$, $R = 4$

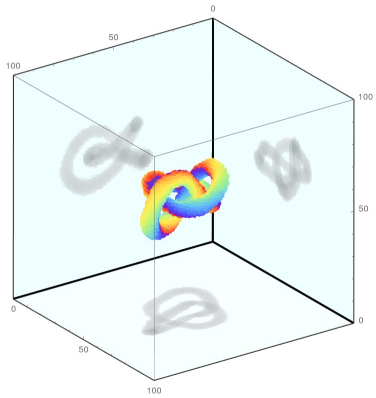

(b) $\tau > 1.2 \times 10^6$, $\alpha = 0.8$, $R = 4$

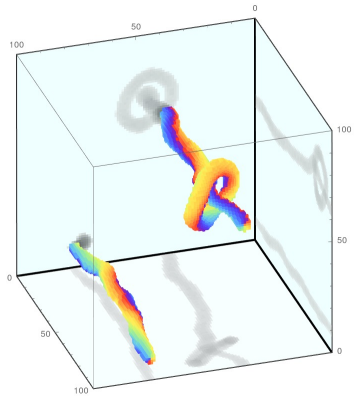

(c) $\tau > 250000$, $\alpha = 0.8$, $R = 4$

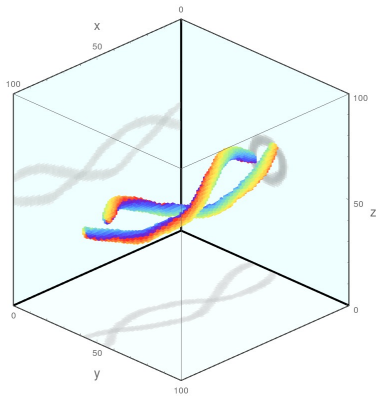

(d) $\tau > 200000$, $\alpha = 0.7$, $R = 4$

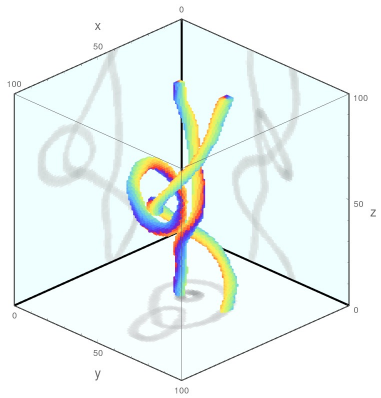

(e) $\tau > 200000$, $\alpha = 0.7$, $R = 4$

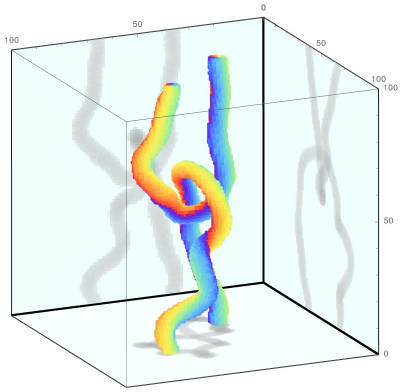

(f) $\tau \sim 70000$, $\alpha = 0.8$, $R = 4$

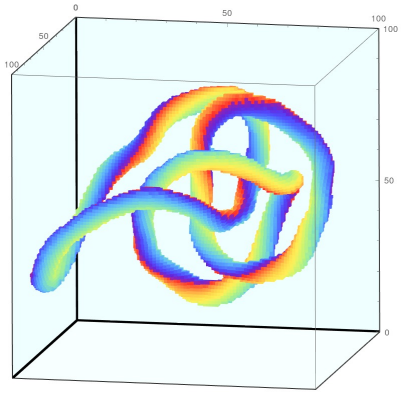

(g) $\tau \sim 5000$, $\alpha = 0.8$, $R = 4$

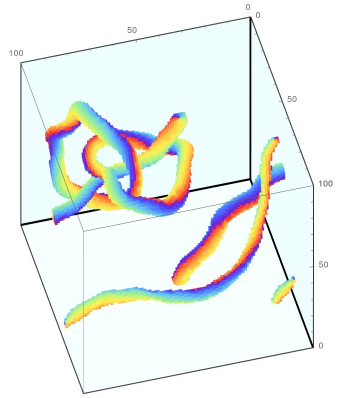

(h) $\tau \sim 5000$, $\alpha = 0.8$, $R = 4$

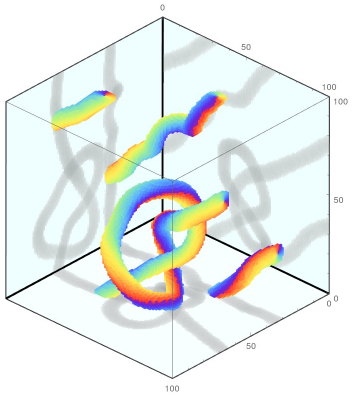

(i) $\tau \sim 5000$, $\alpha = 0.7$, $R = 5$

Figure 3.6: Non-trivial topological structures in the non-local Kuramoto model with periodic BC for $L = 100$. The lifetime τ and the corresponding parameters are given for each subfigure. $\tau > \tau_0$ means that the structure is stable within the testing time limit τ_0, while $\tau \sim \tau_0$ means the structure breaks down around τ_0 (order of magnitude). The period of the scroll waves is about $T \sim 11$ for $\alpha = 0.8$. This implies a lifetime of more than $10^5 T$ for Hopf links and trefoils. Together with the robustness in the presence of noise as established in the main text, this suggests that the lifetime $\tau \to \infty$ when $L \gg R$.

3.14 Appendix C: Creating chimera knots

3.14.1 Random initial condition

Knots and links can appear spontaneously from random initial conditions (IC). The transient time is of the order of one thousand scroll wave periods in the regimes being studied. A few snapshots of typical transient states are shown in Fig. 3.10. Using random IC, we can obtain all knotted structures shown in Figs. 3.6a-3.6f. The specific probabilities of generating Hopf links and trefoils from random IC are summarized in Table 3.1.

3.14.2 Algorithm to create rings and Hopf links

First, the phase field of a single ring is considered. Suppose the center of a ring is located at $\mathbf{r}_0 = (x_0, y_0, z_0)$ with radius R_0 and the normal vector of the ring is pointing in the positive $\hat{z}$ direction. A parameterization of the location of this ring using $\phi \in [0, 2\pi)$ is

$$\mathbf{r}(\phi) = (r_x, r_y, r_z) = (x_o + R_0 \cos\phi, y_0 + R_0 \sin\phi, z_0). \tag{3.9}$$

To create a ring shaped filament corresponding to phase singularities, the phase field needs to be specified in the whole domain such that it is smooth outside the ring but results in 2π phase difference while going around a point on the filament. This can be done by defining

$$\varphi = \tan^{-1}\left(\frac{z - z_0}{R_0 - f}\right) \tag{3.10}$$

$$f = \sqrt{(x - x_0)^2 + (y - y_0)^2} \tag{3.11}$$

for any spatial point $\mathbf{r} = (x, y, z)$. Then the phase of each oscillator $\theta(\mathbf{r})$ can be computed by $\theta(\mathbf{r}) = \psi(\mathbf{r})$, where

$$\psi(\mathbf{r}) = kd - \varphi - s\phi - \beta. \tag{3.12}$$

Here, k is the wavenumber, d is the distance to the closest point on the ring $d = \sqrt{(x - r_x)^2 + (y - r_y)^2 + (z - r_z)^2}$, φ is the angle between the plane consisting of the ring and the line to the closest point of the ring,

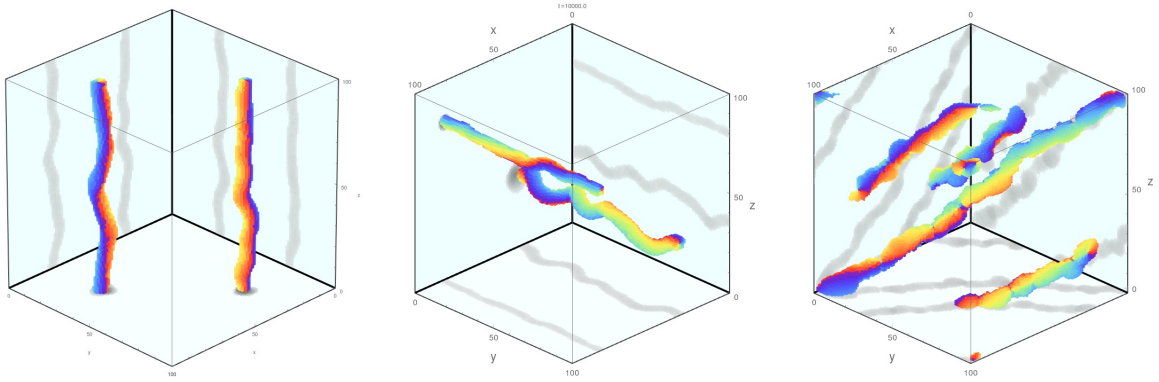

(a) Two simple filaments with no twist ($\alpha = 0.8$).

(b) Two simple filaments twisting once ($\alpha = 0.8$).

(c) Two twisted filaments passing through all three surfaces ($\alpha = 0.05$).

Figure 3.7: Various long-lived filaments with periodic BC, $L = 100$ and $R = 4$. (a-b) Each filament connects with itself through one of the surfaces. (c) Each filament passes through all three surfaces before connecting back to itself.

Table 3.1: Spontaneous formation of Hopf links and trefoils in simulations with random IC and periodic BC.

α	R	L	Number of simulations	Number of Hopf links	Number of trefoils
0.7	4	100	200	1	1
0.7	5	100	500	4	0
0.8	4	100	500	13	0
0.8	5	100	500	5	0
0.7	5	200	100	3	1
0.8	8	200	100	4	0

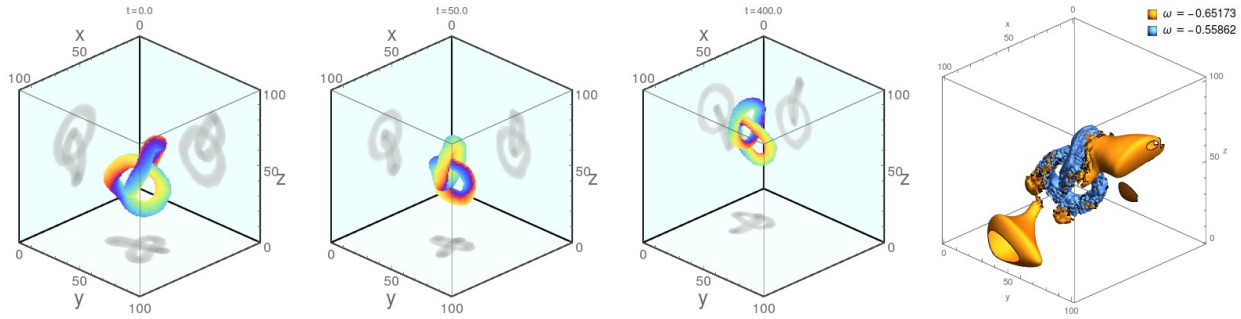

(a) Hopf link

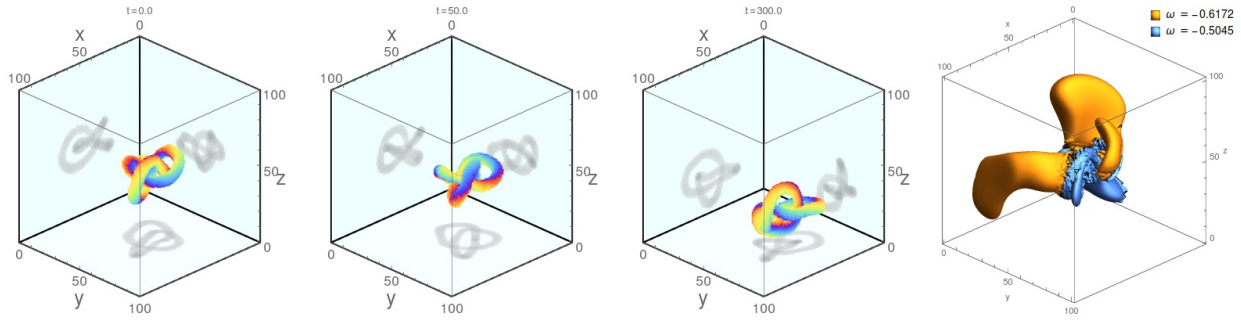

(b) Trefoil

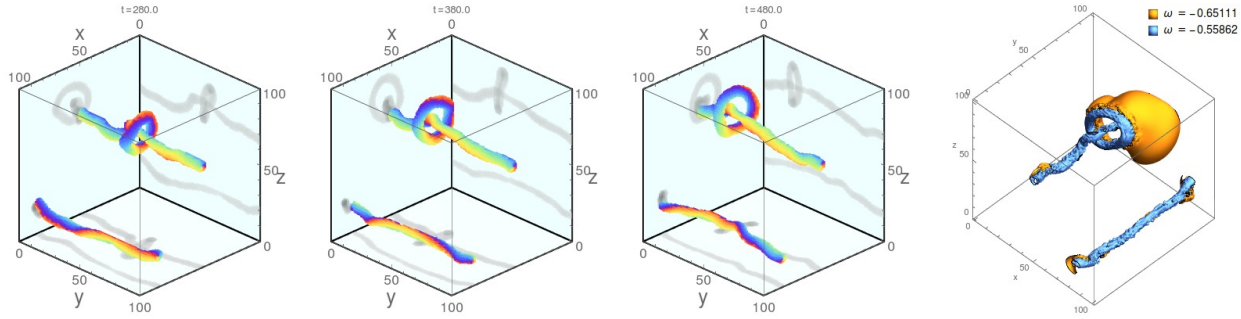

(c) Ring-tube

Figure 3.8: Dynamics of different topological structures ($\alpha = 0.8$, $R = 4$ and periodic BC). The first three columns are snapshots at three different instances in time. The rightmost column is the iso-surface plot of the instantaneous angular frequency ω of the last snapshot. Blue indicates the region with $|\omega| < |\bar{\omega}|$, while orange indicates the region $|\omega| > |\bar{\omega}|$. Filaments are moving away from the orange region.

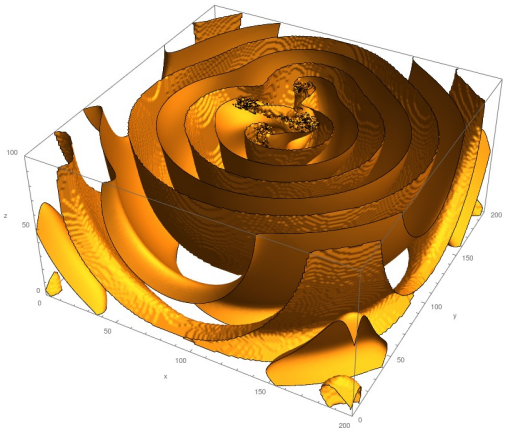

Figure 3.9: The spherical wave generated around a Hopf link is shown by plotting the iso-surface $\theta = 0$ ($\alpha = 0.8$, $R = 8$ and periodic BC). The irregular pattern at the center is the region with unsynchronized oscillators that form the filament. Note that only the lower half of the system is shown to highlight the structures near the center.

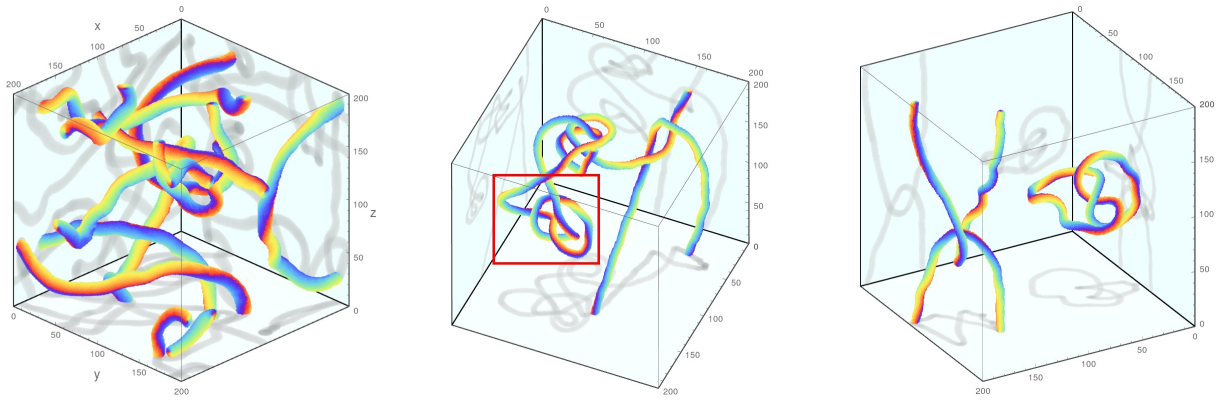

(a) A transient state for $R = 8$, $L = 200$.(b) A transient state for $R = 4$, $L = 200$. See Sec. 3.14.3 for a discussion of the significance of the red box.

(c) Same as in (b) at a later time.

Figure 3.10: Some snapshots of transient states ($\alpha = 0.8$ and periodic BC).

s is the twisting number, ϕ is the ring parameterization, and β is a constant phase shift. Examples are shown in Fig. 3.11.

The phase field of a Hopf link can be created by combining two rings, requiring a method to smoothly superimpose them. This can be achieved using a distance dependent phase:

$$\xi(\mathbf{r},\mathbf{r}_0,s,\beta) = \left(\frac{R}{d}\right)^2 e^{i\psi(\mathbf{r},s,\beta)}, \tag{3.13}$$

which is based on the inverse square distance. Then the phase field of a Hopf link $\theta(\mathbf{r})$ can be calculated by

$$\rho(\mathbf{r})e^{i\theta(\mathbf{r})} = \xi(x,y,z,x_0-R_0/2,y_0,z_0,s,\beta=0)+\xi(x,z,y,x_0+R_0/2,y_0,z_0,s,\beta=\pi) \tag{3.14}$$

with twisting number $s=1$. Examples are shown in Fig. 3.12. Note that a structure in a given system size L can be rescaled to L' using a simple scaling function of the form $\theta'(x',y',z') = \theta(\lfloor \frac{L}{L'}x' \rfloor, \lfloor \frac{L}{L'}y' \rfloor, \lfloor \frac{L}{L'}z' \rfloor)$, where $\lfloor\cdot\rfloor$ denotes the floor of the number (which is necessary since the oscillators are arranged on a discrete lattice) and the prime denotes the new phase and new location. This rescaling works quite well for the top-hat kernel as long as $R \sim R' \gg 1$. Also, if the smoothed phase $\tilde{\theta}$ of knots — see Eq. (4) in the main text — is used as IC, the unsynchronized region around the filaments can redevelop.

3.14.3 Reconnecting chimera filaments using random patches

A new structure can be obtained by reconnecting local filaments of a known structure. This reconnection requires a detailed specification of the whole local phase field that is smooth, without creating new filaments and while matching the desired filaments. This can be hard to do if the local filaments are obtained from a simulation. Alternatively, based on the observation that only simple straight filament can form in a small system size L/R from random IC, it suggests a way to transform a structure by randomizing a whole local region. Using this method, we have successfully created trefoils and a few other knots. To begin with, a structure that is similar to the desired knot is needed, with the region of reconnection close to each other. For example, the structure in

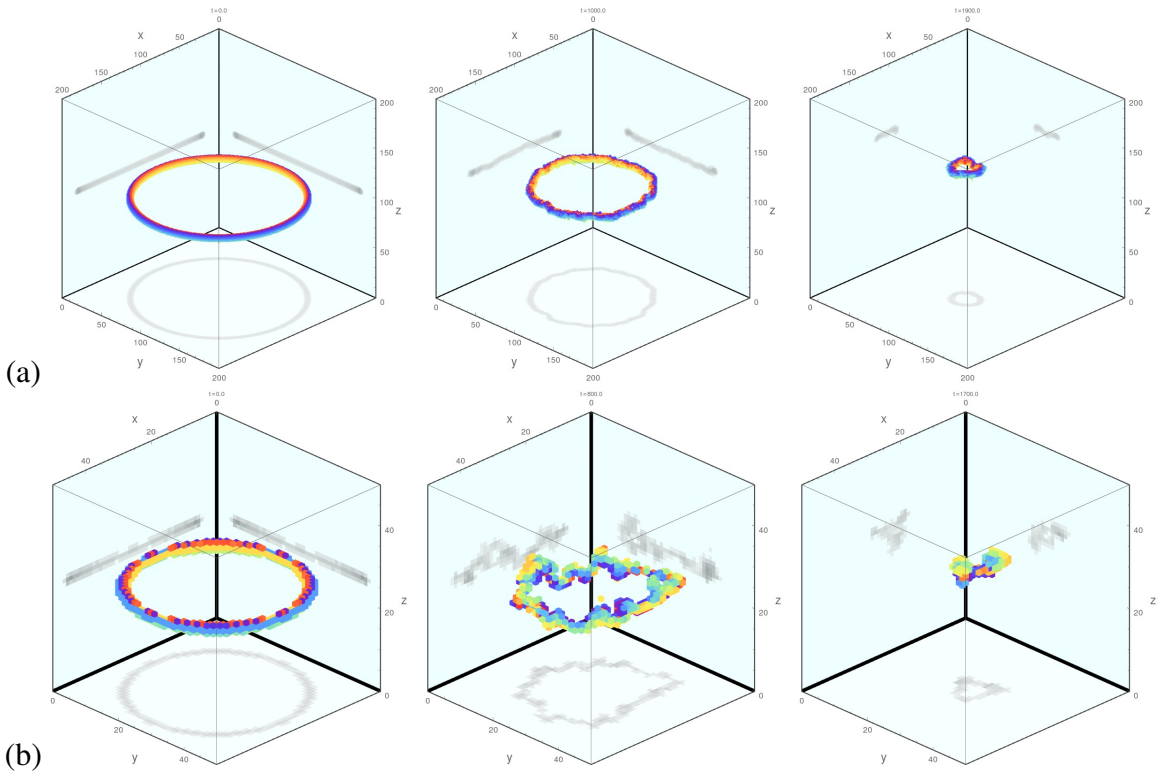

Figure 3.11: Shrinking rings with (a) non-local coupling $R = 4$, (b) nearest-neighbor coupling $R = 1$. Parameters: $L/R = 50$, $R_0/R = 20$, $\alpha = 0.8$ with no-flux BC.

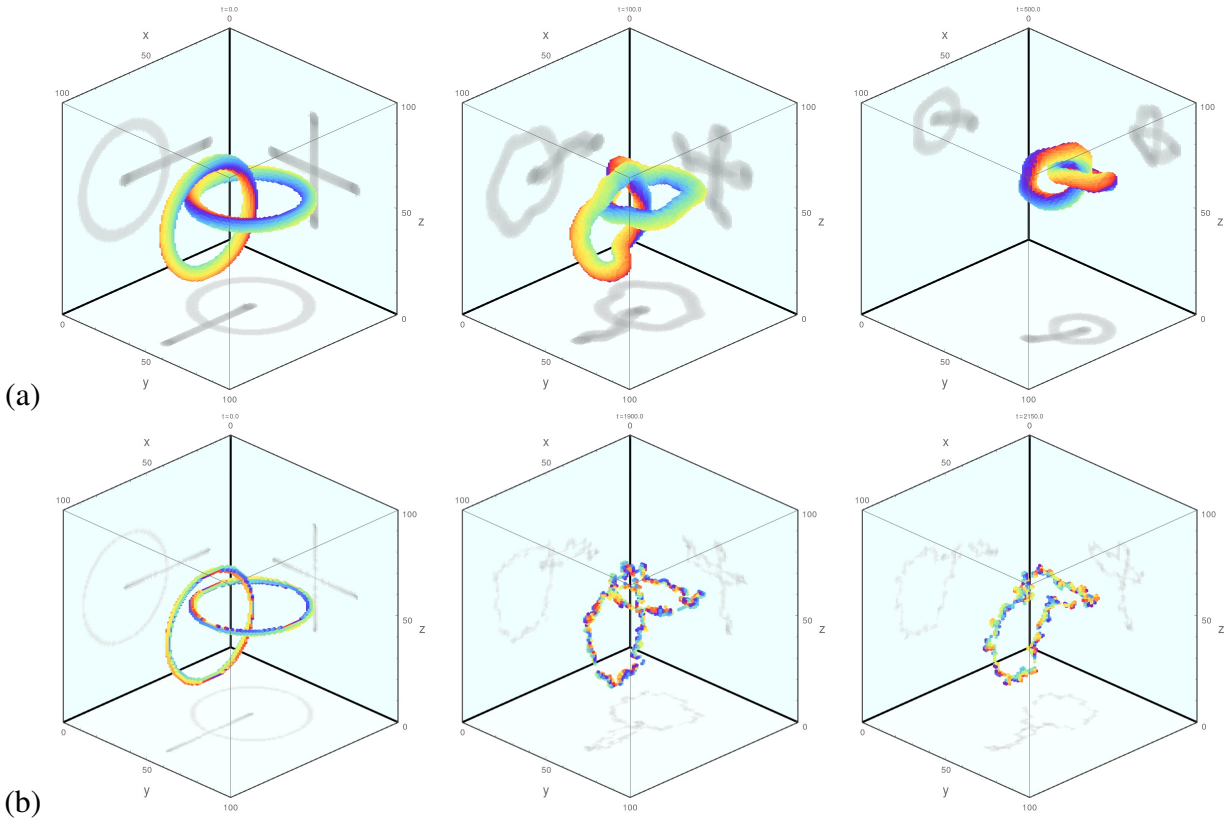

Figure 3.12: Formation of knots for (a) non-local coupling $R = 4$, (b) nearest neighbor coupling $R = 1$. Note that the IC are exactly the same in both cases. Parameters: $R_0 = 25$, $L = 100$, $\alpha = 0.8$ with no-flux BC.

the red box shown in Fig. 3.10 is a trefoil if the top parts are connected. After half a dozen trials using different shapes of the randomized region, we were indeed able to create a trefoil. Note that the region should be large enough to form a tube but not too large to form other structures. This method may suggest a similar way to create knots in real world experiment.

3.15 Appendix D: Instabilities

In the main text, the instabilities at α_K and α_0 of Hopf links in the Kuramoto model have been discussed. The instability near α_K is caused by a lack of repulsion to counter curvature-driven shrinkage, so knots collapse and disappear. On the other hand, the instability near α_0 originates from an instability of the filament where the filaments become longer and longer and eventually collide with themselves or other filaments. This effect is particularly clear in large domains as shown, for example, in Fig. 3.13. Note that an elongation also happens as a transient state when the parameters are suddenly changed or starting from a non-perfect IC. However, it will eventually shorten after refolding to an asymptotic state as also observed for other models [118]. Other instabilities are discussed below.

3.15.1 Instability of a single ring

Direct simulations show that rings are not stable for $\alpha < \alpha_0$ with no-flux BC. As shown in Fig. 3.11, all rings shrink in size and eventually vanish. The largest ring tested had radius $R_0 = 80$. This shrinkage process occurs for both nearest neighbor coupling $R = 1$ and non-local coupling $R = 4$. Note that the time it takes for a ring to disappear is approximately the same in both cases for the same effective radius R_0/R and effective system size L/R. Also, almost all transient (knotted) states resulting eventually in homogeneous oscillations become rings in their penultimate stage.

3.15.2 Instability of knots for $R = 1$

As shown in Fig. 3.12, using the IC for Hopf links described in Section 3.14.2 can result in a stable knot if $R \gg 1$. For the choice of R_0, the two rings initially shrink in size and then an effective repulsion prevents further shrinkage. At the same time, the center of the Hopf link starts moving. In contrast, if the same IC is used with nearest neighbor coupling $R = 1$, the two rings will eventually collide with each other and decay into a single ring, which in turn shrinks and vanishes.

3.15.3 Filament instability at α_0

As illustrated in Fig. 3.14, the instability at α_0 for simple straight chimera filaments is characterized by the emergence of secondary structures and the elongation of filaments. The same qualitative behavior is observed for knotted structures in the regime $\alpha > \alpha_0$ as shown in the main text. Nevertheless, the knotted structures can persist for thousands of scroll wave periods before they break up consistent with critical slowing down near a phase transition.

3.15.4 Instabilities from finite size effects

A stable knotted structure becomes unstable when it is confined in a small effective system L/R. While a Hopf link simply decays into a single ring which eventually vanishes, the situation is more complicated for larger and more complex knotted structures. One example is shown in Fig. 3.15 starting from a triple ring for $R = 4$ in $L = 100$, which decays into a ring knotted with 8-shape ring, and then transforms into a trefoil. Depending on the IC and the exact parameter regime, the decay path can be different. Note that even for the moderately larger system size $L = 150$, triple rings have significantly longer lifetimes ($\tau > 20000$) in some parameter regimes.

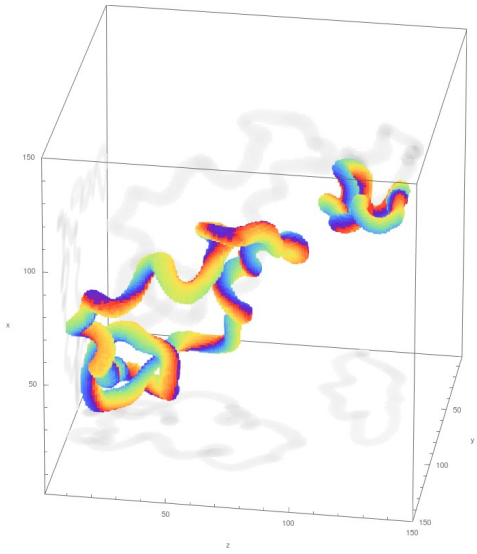

Figure 3.13: Instability of a trefoil near the transition point α_0 ($R = 4$, $L = 150$ and periodic BC). This snapshot shows the initial elongation of one branch of the trefoil, which has collided with itself and formed an extra ring.

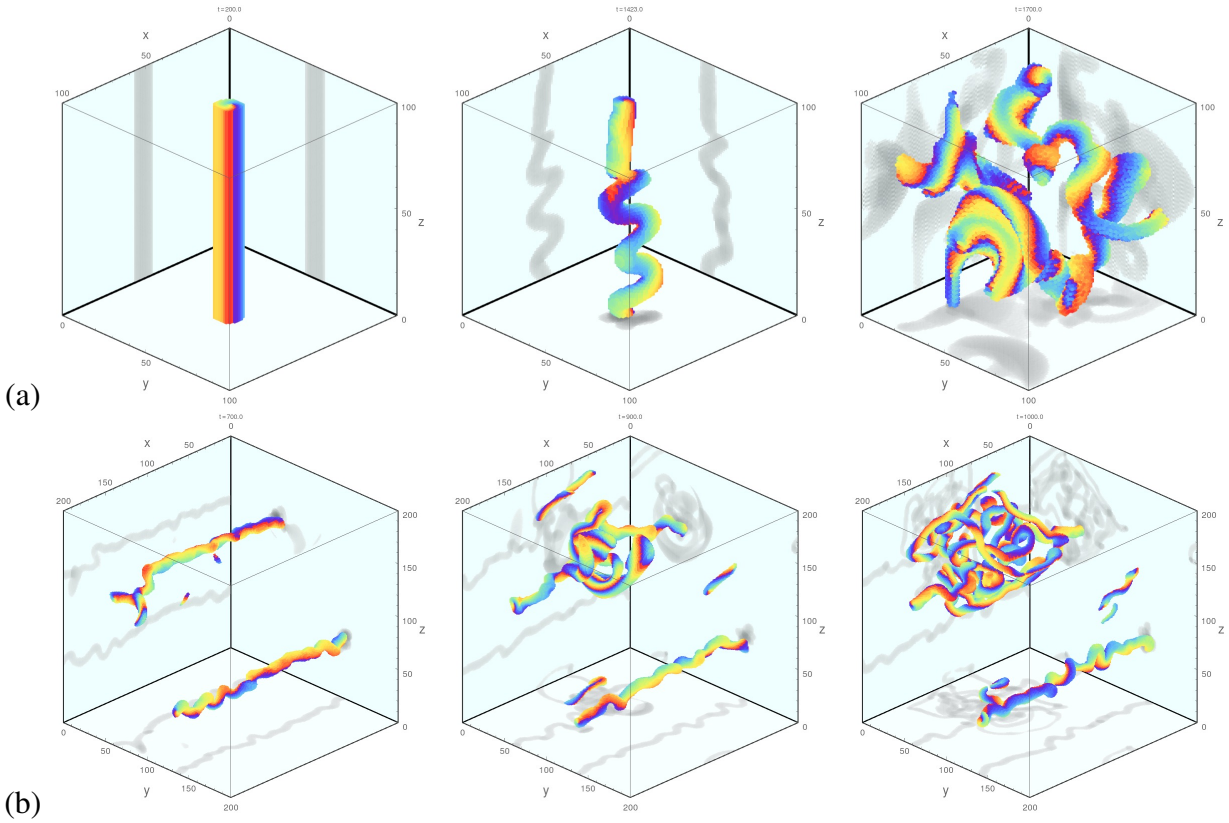

Figure 3.14: Snapshot series of the instability of straight filaments at $\alpha = 0.95 > \alpha_0$. (a) Single filament with $L = 100$, $R = 4$ and no-flux boundary conditions. Some secondary structures develop with local twisting before break-up. (b) Two filaments in a larger domain $L = 200$ and $R = 4$ with PBC. The rapid elongation of one of the filaments is evident.

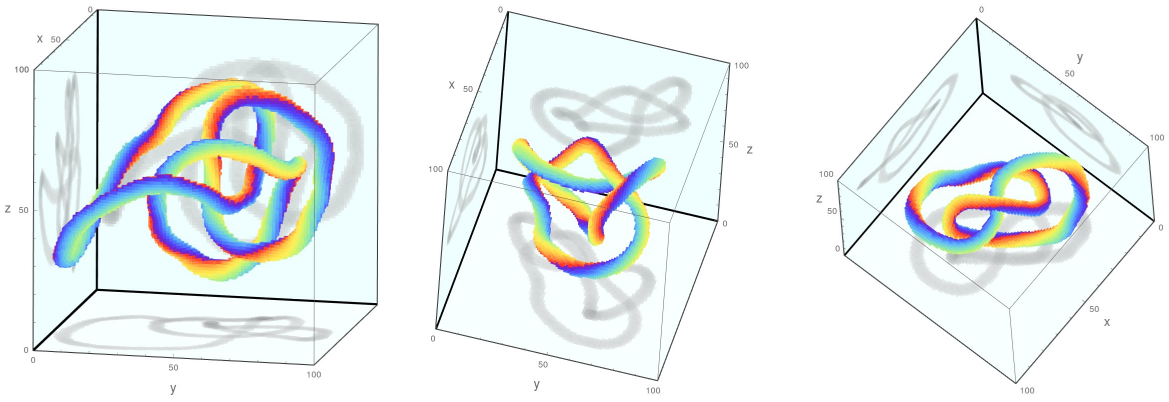

Figure 3.15: Decay of a triple ring for $L = 100$, $R = 5$, $\alpha = 0.7$ with PBC. (a) $t = 0$, triple rings. (b) $t = 15000$, decay into a ring knotted with an 8-shape ring. (d) $t = 20000$, further decay into a trefoil.

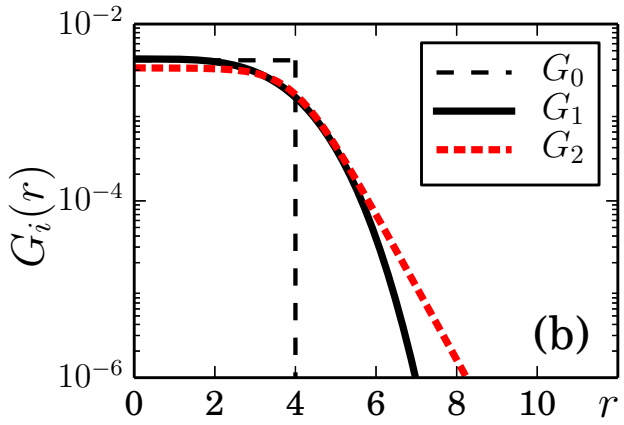

Figure 3.16: (color online) Plot of the localized kernels that can still result in a stable Hopf link, with estimated critical values $n_1 = 3.8$ and $n_2 = 1.9$ for $R = 4$ and $\alpha = 0.8$ of Kuramoto model. G_0 is shown for comparison.

3.16 Appendix E: Spatial kernels

As mentioned in the main text, our main findings do not depend qualitatively on the exact functional form of the considered kernels. For example, using the kernel

$$G_0'(\mathbf{r}) \sim \begin{cases} 1, & |x|,|y|,|z| \leq R \\ 0, & \text{otherwise} \end{cases} \tag{3.15}$$

instead of the top-hat kernel G_0 gives pretty much identical results for the stability of knots. As another example, using the kernel

$$G_2(\mathbf{r}) \sim (1+e^{n_2(r-R)})^{-1} \tag{3.16}$$

with an exponential tail instead of the kernel G_1 with super-exponential tail exhibits the same phenomenology: With decreasing n_2, the stable regime of knots shrinks. The shape of the kernels at the transition points of G_1 and G_2 for $R = 4$ and $\alpha = 0.8$ are shown in Fig. 3.16.

3.17 Appendix F: Other oscillatory models

3.17.1 Non-Local Complex Ginzburg-Landau equation (CGLE)

The non-local CGLE considered here is [7]:

$$\dot{A}(\mathbf{r},t) = A - (1+ib)|A|^2 A + K(1+ia)\int G(\mathbf{r}-\mathbf{r}')(A(\mathbf{r}')-A(\mathbf{r}))d\mathbf{r}', \tag{3.17}$$

where the control parameters are (a,b), the coupling strength is K and $G = G_0$ in the following. Under sufficiently weak coupling $K \to 0$, the local field oscillates with unit amplitude $|A| \approx 1$ and behaves like a simple phase oscillator in the non-local Kuramoto model. Therefore, we can use the knotted structures found in the Kuramoto model as IC by simply setting $A(\mathbf{r},t=0) = e^{i\theta(\mathbf{r})}$. We find that one of the regimes with stable Hopf links is $0.95 \lesssim a \lesssim 1.15$ for $b = 0$ and $K = 0.1$ provided that $L \gg R \gg 1$. In Fig. 3.17(a), the phase portrait shows that the magnitude of all oscillators only deviates slightly from $|A| = 1$ in this case. For stronger coupling $K = 0.2$, the deviations in

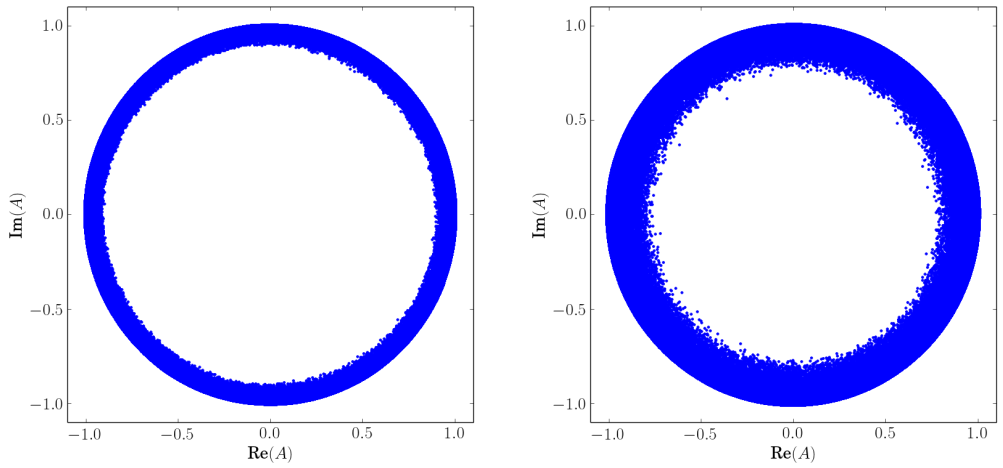

(a) $K = 0.1$ (b) $K = 0.2$

Figure 3.17: Snapshot of the states of the oscillators in phase space for a Hopf link in the non-local CGLE for $(a,b) = (1,0)$, $L = 200$, $R = 8$ and periodic BC.

A increase (see Fig. 3.17(b)) but stable knots still exist. In both cases, the phase $\theta(\mathbf{r}) = \arg(A(\mathbf{r}))$ behaves similar to the Kuramoto model as confirmed by Fig. 3.18(d). As Figs. 3.18(b) and 3.18(c) show, the chimera nature is also evident from the $\mathrm{Re}(A(x,y,z))$ and $\mathrm{Im}(A(x,y,z))$ fields. Using the local mean field $\tilde{\theta}(\mathbf{r})$, one can easily locate the unsynchronized filaments [4]. An example is shown in Fig. 3.18(a).

3.17.2 CGLE: Minimum separation & spontaneous fluctuations

When R becomes too small, knots are no longer stable. This instability can be characterized by the dynamics of the filament(s) that make up the knots. Even though the region around the filament is unsychronized, the filaments can be found by a filament detection algorithm [131] of the mean field (see Fig. 3.19(a)). The length of filament can therefore be defined as the number of occupied lattice sites. Denote the two rings or filaments of a Hopf link as F_1 and F_2 with circumference (or length) C_1 and C_2, respectively. As Fig. 3.19(c) shows, C_1 and C_2 fluctuate over time in a synchronous way. Fluctuations are also present in the minimum separation between F_1 and F_2,

[4] To identify the regions with unsynchronized phase, we consider the average of the absolute phase difference with its neighbors and select a suitable threshold.

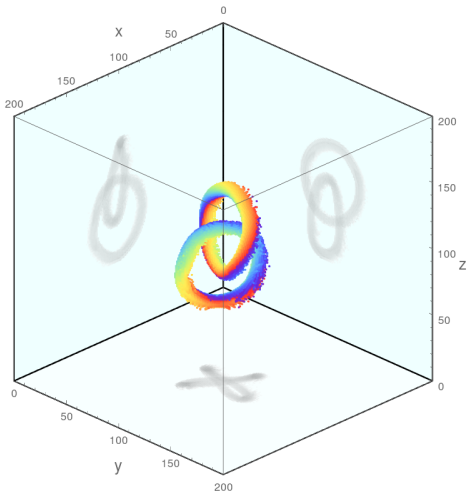

(a) Hopf link

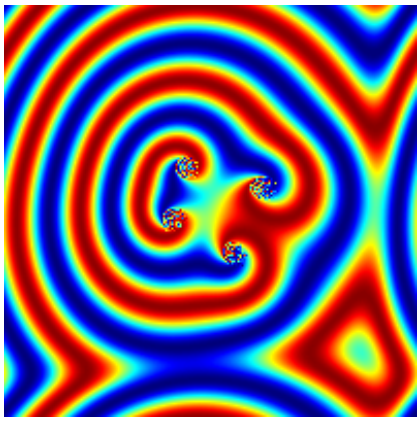

(b) Re(A)

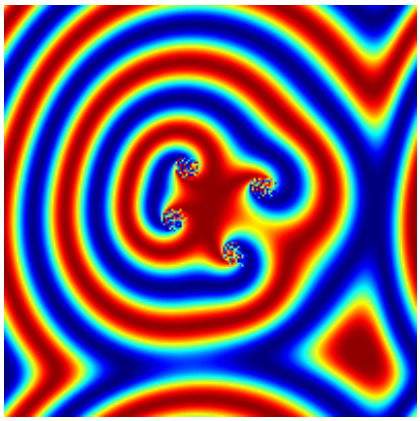

(c) Im(A)

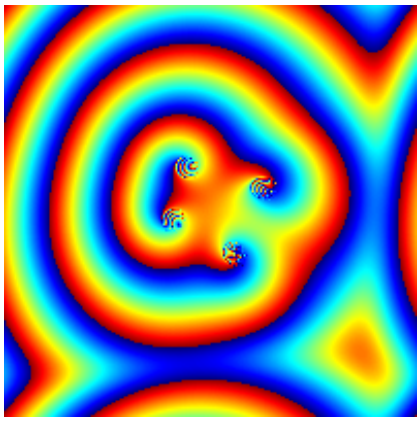

(d) $\theta = \arg(A)$

Figure 3.18: Snapshot of a Hopf link in the non-local CGLE corresponding to Fig. 3.17(a). (a) shows the unsynchronized region corresponding to the chimera knot. An x-y cross-section of the different fields at $z = 100$ is plotted in (b)-(d). In (b) and (c), the color map from deep blue to red corresponds to values from -1 to 1 in the respective field.

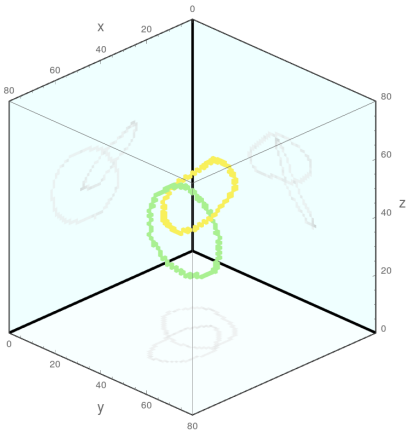

(a) Snapshot of the filaments of a Hopf link.

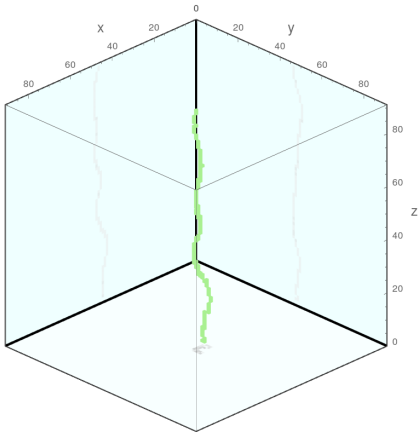

(b) Snapshot of a straight filament with no-flux BC.

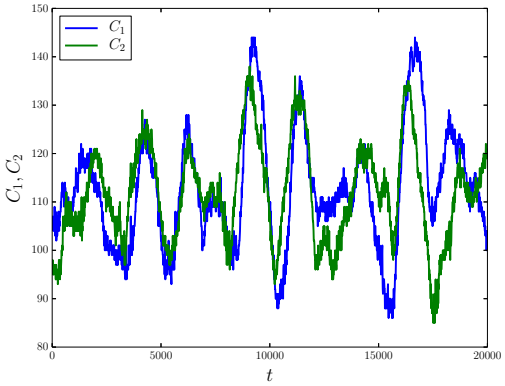

(c) Circumferences C_i of the two rings shown in (a) as a function of time.

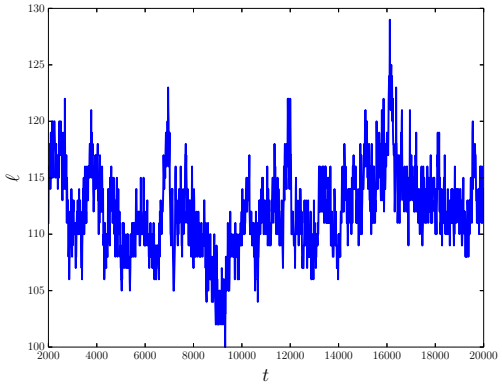

(d) Length of the filament ℓ shown in (b) as a function of time.

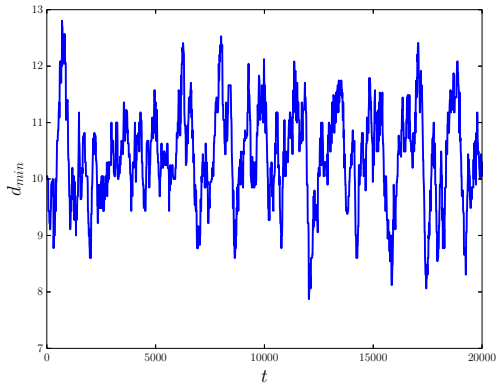

(e) Minimum separation between the two rings shown in (a) as a function of time.

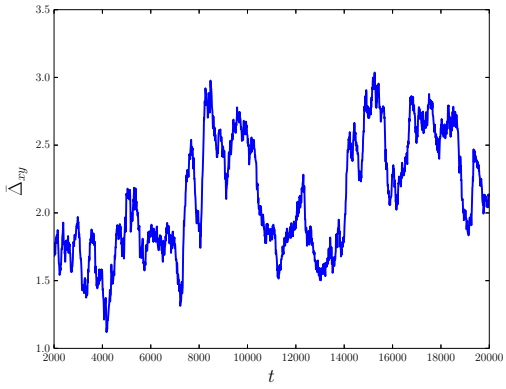

(f) Roughness of the filament shown in (b) as a function of time.

Figure 3.19: CGLE with $R = 4$, $a = 1$, $b = 0$, $K = 0.1$. (left) Temporal evolution of a Hopf link with $L = 80$. (right) Temporal evolution of a single filament oriented along the z-direction with $L = 91$ which results in a time average filament length $\langle \ell \rangle \approx 110$ that is approximately the same as the time average circumference $\langle C \rangle \approx 110$ of the rings in the left column.

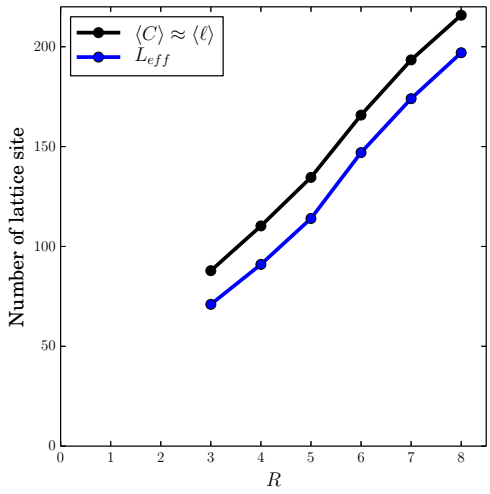

(a) Average circumference and effective system size L_{eff}.

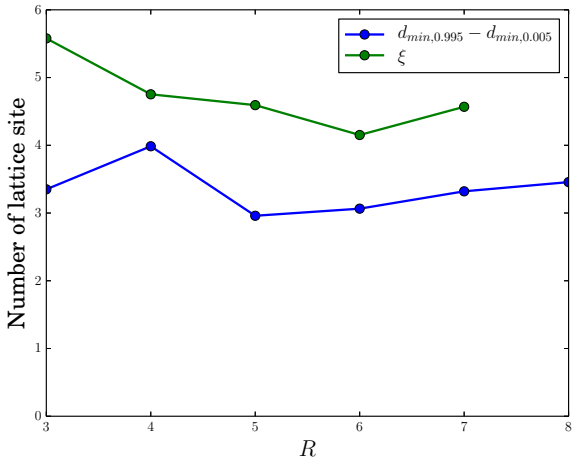

(b) Comparing different length scale of fluctuation.

Figure 3.20: CGLE with $a = 1$, $b = 0$, $K = 0.1$ as in Fig. 3.19. (a) System size, L_{eff}, for which a single filament has the same average length $\langle \ell \rangle$ as the average circumference $\langle C \rangle$ of a Hopf link. (b) Measures of fluctuations for the case of a Hopf link (spread in the minimum separation between the rings, $d_{min,99.5\%} - d_{min,0.5\%}$, see Fig. 3.19(e)) and for the case of a single filament (spread in the roughness, ξ, see Fig. 3.19(f)), both as a function of R.

defined as $d_{min} = \min_{\mathbf{r}_i \in F_i}(\mathbf{r}_1, \mathbf{r}_2)$, as shown in Fig. 3.19(e). To characterize these fluctuations statistically and identify an associated length scale, we consider the difference between the 99.5%-quantile and the 0.5%-quantile associated with d_{min}, corresponding to the error bars shown in Fig. 3.5(a) in the main text. As shown in Fig. 3.20(b), this difference is not varying much across the considered values of R. This is in sharp contrast to the linear scaling of d_{min} with R (see Fig. 3.5(a) in the main text).

To substantiate that the intrinsic length scales associated with filament fluctuations do not strongly vary with R, we further consider the fluctuations of a single straight filament (see Fig. 3.19(b)). To ensure a fair comparison with the fluctuations of Hopf links, we choose a system size $L = L_{eff}$ such that the average single filament length $\langle \ell \rangle$ equals the average circumference $\langle C \rangle = (\langle C_1 \rangle + \langle C_2 \rangle)/2$ of the filaments in the Hopf link (see Fig. 3.19(d)). The dependence of both these quantities as a function of R is shown in Fig. 3.20(a). To characterize the fluctuations of a single straight filament, we calculate its roughness. Due to the chosen initial conditions, the roughness is identical to the deviation from a straight filament oriented along the z-axis. Specifically, we define the deviation from the straight filament center $\bar{\mathbf{r}}_{xy} = (1/L)\sum_z \mathbf{r}_{xy}(z)$ to be

$$\Delta_{xy}(z) = |\mathbf{r}_{xy}(z) - \bar{\mathbf{r}}_{xy}|, \tag{3.18}$$

where $\mathbf{r}_{xy}(z)$ is the intersection point of the filament with the x-y plane for a given z. The roughness $\bar{\Delta}_{xy} = (1/L)\sum_z \Delta_{xy}(z)$ is now simply $\Delta_{xy}(z)$ averaged over z. As Fig. 3.19(f) shows, the roughness varies over time. To characterize these (non-negative) fluctuations in the roughness over time and within an ensemble and to identify an associated length scale, we consider the 99%-quantile and denote it by ξ. This is the quantity shown in Fig. 3.5(a) in the main text and again it does not vary much across the considered values of R. For a direct comparison with the length scale of fluctuations in the case of a Hopf link, please see Fig. 3.20(b).

3.17.3 Non-Local Rössler model

The non-local Rössler model considered here is [139]:

$$\dot{X}(\mathbf{r},t) = -Y - Z + K \int G(\mathbf{r}-\mathbf{r}') \big(X(\mathbf{r}') - X(\mathbf{r})\big)\, d\mathbf{r}', \tag{3.19}$$

$$\dot{Y}(\mathbf{r},t) = X + aY + K \int G(\mathbf{r}-\mathbf{r}') \big(Y(\mathbf{r}') - Y(\mathbf{r})\big)\, d\mathbf{r}', \tag{3.20}$$

$$\dot{Z}(\mathbf{r},t) = b + Z(X-c), \tag{3.21}$$

where the control parameters are (a,b,c) and the coupling strength is K. Again, we can use $(X,Y,Z) = (\cos\theta, \sin\theta, 0)$ with $\theta(\mathbf{r})$ from states with knotted structures generated by the Kuramoto model as IC. When $a = b = 0.2$, the effective $|\alpha|$ decreases as c increases [138]. We observe stable knots within $3.3 \lesssim c \lesssim 5$ for weak coupling $K = 0.05$ provided that $L \gg R \gg 1$. Note that as c increases the intrinsic dynamics of the oscillators also changes. Namely, the dynamics undergoes a period-doubling cascade to chaotic oscillations. In particular, we observe stable knots in the period-2 regime with $c = 3.6$ (Fig. 3.21), as well as in the chaotic regime with $c = 4.8$ (Fig. 3.22).

An additional feature of the wave dynamics in these regimes is evident from Fig. 3.21 and Fig. 3.22: The amplitudes are modulated. For example, in the period-2 regime alternating wave maxima are present. A topological consequence of such a behavior is that two dimensional structures exist such that the local dynamics has a lower period than that of the bulk. Specifically, these structures, called synchronization defect sheets (SDSs) in the following, separate domains of different oscillation phases and for periodic BC either originate from a filament or are closed. More importantly, every filament has an attached SDS such that they become part of any knotted structure. This can already be observed in the cross-sections shown in Fig. 3.21 and Fig. 3.22. To clearly identify SDSs, we use the detection algorithm developed for the lower dimensional case in Ref. [138]. A specific example of SDSs is shown in Fig. 3.23 and their subsequent motion is shown in the Supplementary Video.

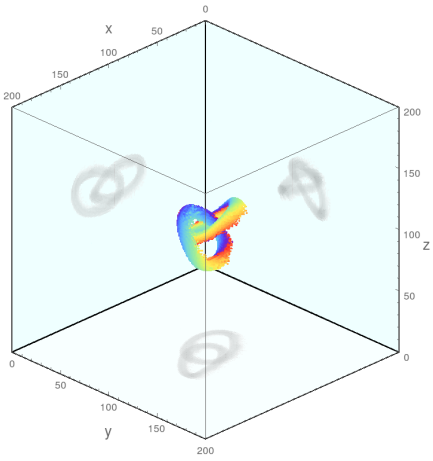

(a) Hopf link

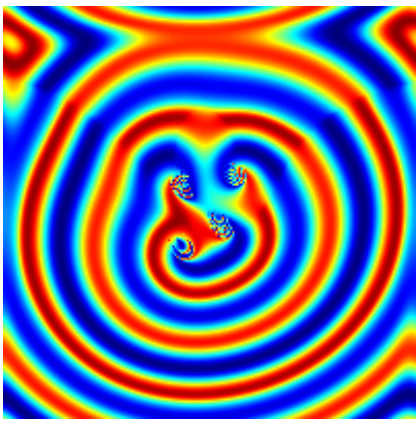

(b) X

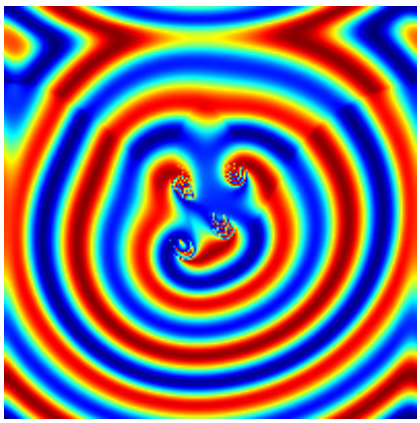

(c) Y

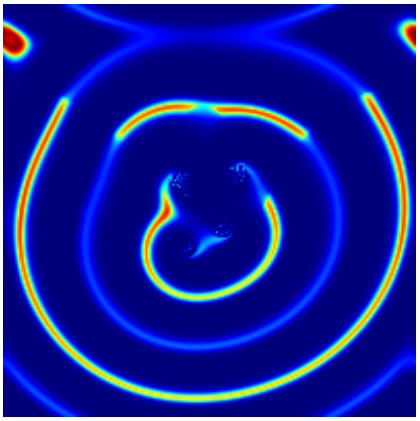

(d) Z

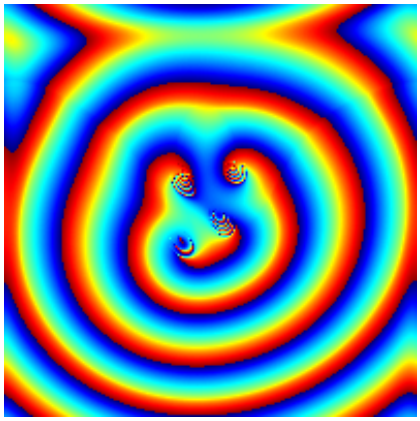

(e) $\theta = \tan^{-1}(Y/X)$

Figure 3.21: Snapshot of a Hopf link in the non-local Rössler model for $(a,b,c,K) = (0.2,0.2,3.6,0.05)$, corresponding to the period-2 regime. The lifetime of the knot is $\tau > 10^5$. The same 2D cross-sections of the Hopf link are shown in (b-e) for the different fields X, Y, Z and θ. The color scheme is such that deep blue represents the most negative value, and red represents the most positive value. The discontinuities of color along the wave fronts correspond to cross-sections of synchronization defect sheets. $L = 200$, $R = 8$ and periodic BC.

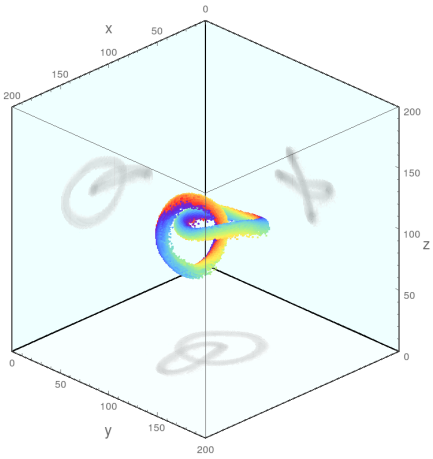

(a) Hopf link

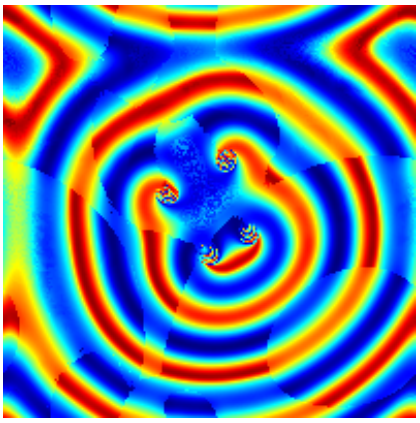

(b) X

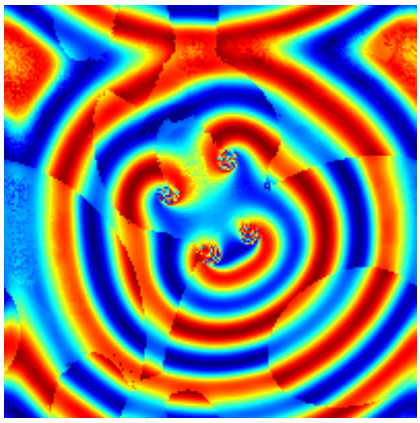

(c) Y

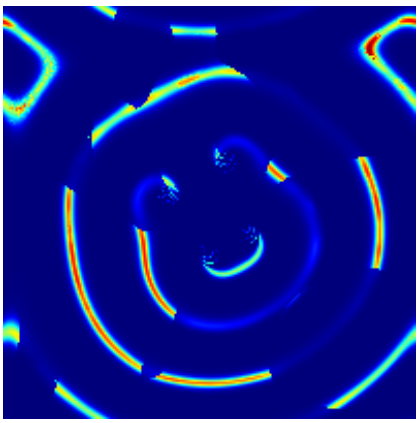

(d) Z

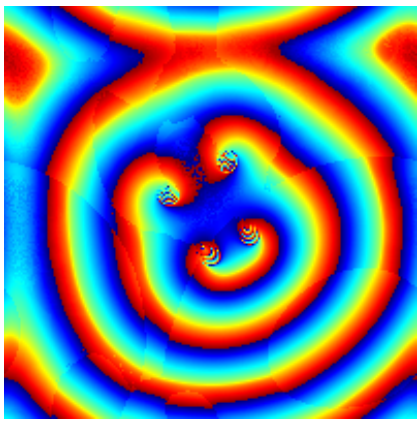

(e) $\theta = \tan^{-1}(Y/X)$

Figure 3.22: Similar to Fig. 3.21, but in the chaotic regime $(a,b,c,K) = (0.2, 0.2, 4.8, 0.05)$.

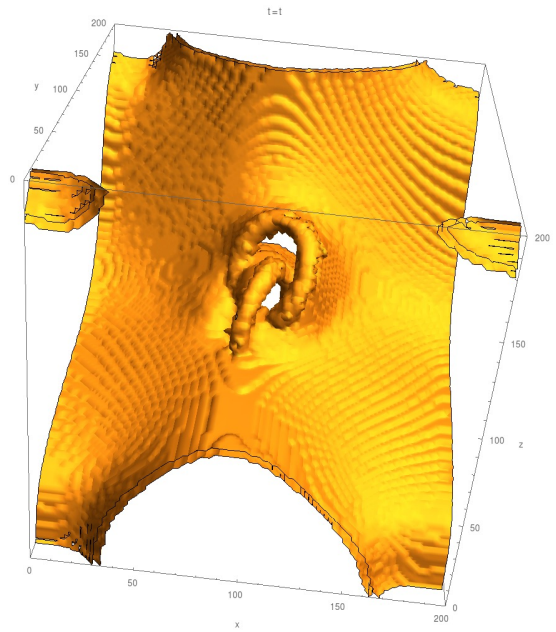

(a) Synchronization defect sheets

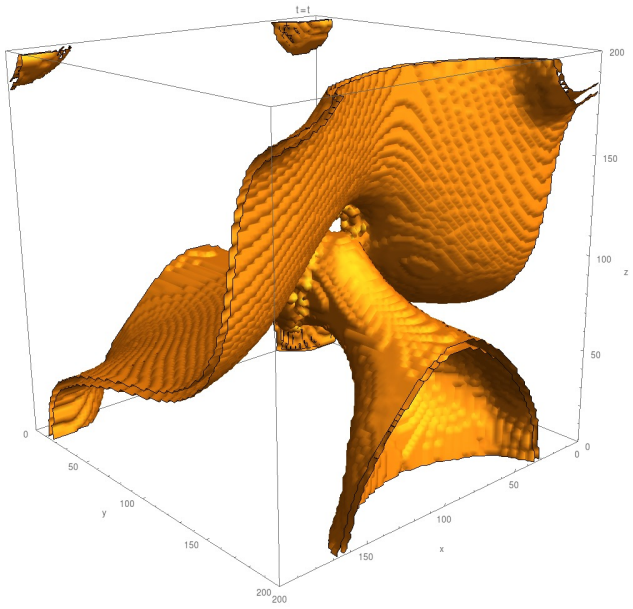

(b) Synchronization defect sheets (another view)

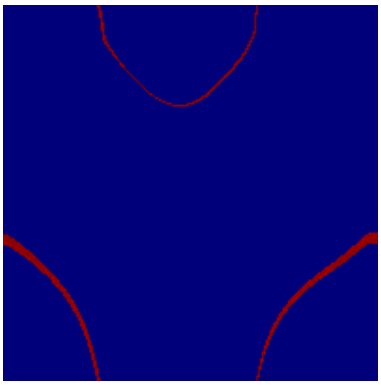

(c) $z = 50$

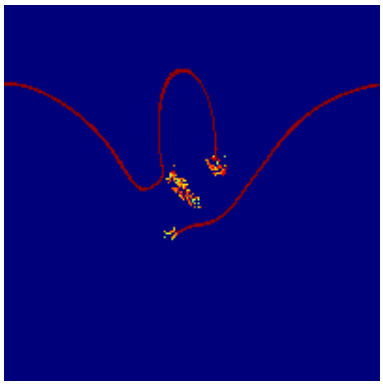

(d) $z = 85$

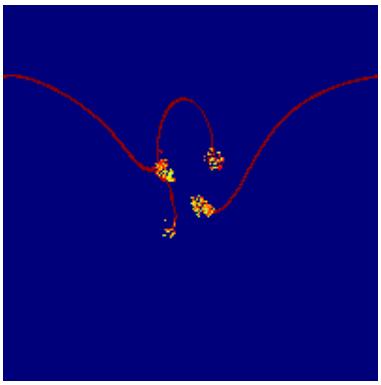

(e) $z = 93$

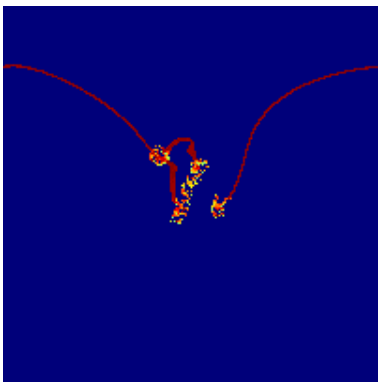

(f) $z = 109$

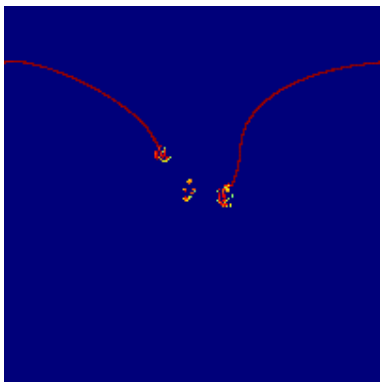

(g) $z = 118$

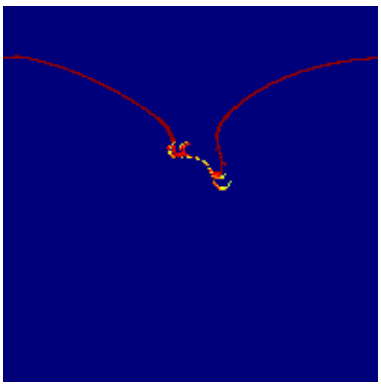

(h) $z = 130$

Figure 3.23: Visualization of the synchronization defect sheets (SDSs) present in Fig. 3.21. (a), (b): Different 3D plots of the SDSs. (c)-(h): 2D cross-sections at different values of z. The red lines represent the cross-sections of SDSs and the yellow-red dots indicate the unsynchronized regions. Note that the cross-section in (e) is the same cross-section as in Fig. 3.21 (b-e).

Chapter 4

Proposal for the Creation and Optical Detection of Spin Cat States in Bose-Einstein Condensates

4.1 Preface

We propose a method to create "spin cat states", i.e. macroscopic superpositions of coherent spin states, in Bose-Einstein condensates using the Kerr nonlinearity due to atomic collisions. Based on a detailed study of atom loss, we conclude that cat sizes of hundreds of atoms should be realistic. The existence of the spin cat states can be demonstrated by optical readout. Our analysis also includes the effects of higher-order nonlinearities, atom number fluctuations, and limited readout efficiency.

The work in this chapter was published in [12]. The detailed calculations in this chapter were the results of my own work. The original idea was proposed by Prof. Simon. Under his guidance, I was able to work out all the details of this proposal. During the development of this proposal, Dr. Zachary Dutton provided valuable suggestions thanks to his expertise in BECs. Another BEC expert I consulted is Dr. Rui Zhang. Their involvement made my proposal more realistic. Tian Wang was involved in the part related to the Kerr effect.

4.2 Introduction

Great efforts are currently made in many areas to bring quantum effects such as superposition and entanglement to the macroscopic level [144, 145, 146, 147, 148, 149, 150, 151, 97, 152, 153, 154, 155, 156, 157, 51]. A particularly dramatic class of macroscopic superposition states are so-called cat states, i.e. superpositions of coherent states where the distance between the two components in phase space can be much greater than their individual size [144, 145]. For example, the recent

experiment of [51] created a cat state of over one hundred microwave photons in a waveguide cavity coupled to a superconducting qubit. It was essential for the success of the latter experiment that the loss in that system is extremely small, since even the loss of a single particle from a cat state of this size will lead to almost complete decoherence.

Here we show that it should be possible to create cat states involving the spins of hundreds of atoms in another system where particle losses can be greatly suppressed, namely, Bose-Einstein condensates (BECs), where the spins correspond to different hyperfine states. We use the Kerr nonlinearity due to atomic collisions, which also played a key role in recent demonstrations of atomic spin squeezing [97, 152, 153]. In contrast to previous proposals [107, 158] we do not make use of Josephson couplings to create the cat state, but rely purely on the Kerr nonlinearity in the spirit of the well-known optical proposal of Ref. [59].

Our approach is inspired by the experiment of Ref. [159], which stored light in a BEC for over a second. Ref. [160] proposed to use collision-based interactions in this system to implement photon-photon gates, see also Ref. [161]. Here we apply a similar approach to the creation and optical detection of spin cat states. Because of the great sensitivity of these states, this requires a careful analysis of atom loss. Our theoretical treatment goes beyond that of Ref. [160], which was based on the Thomas-Fermi approximation (TFA). Our new approach allows us to study several key imperfections in addition to loss, including higher-order nonlinearities, atom number fluctuations, and inefficient readout, and we conclude that their effects should be manageable.

4.3 Spin cat states creation scheme

Our scheme is illustrated in Fig. 4.1. The setup is similar to the experiment of Ref. [159]; See also Ref. [164]. In particular, the light is converted into atomic coherences using a control beam ('slow' and 'stopped' light) [165, 159, 166, 167, 168, 169, 170]. We start with a ground state BEC with N atoms in internal states $|A\rangle$. To create a spin state, a coherent light pulse, $|\alpha\rangle_L = \sum_n c_n |n\rangle$ with mean photon number $\bar{n} = |\alpha|^2$ and $c_n = e^{-|\alpha|^2/2}(\alpha^n/\sqrt{n!})$, is sent into the BEC (see Fig. 4.1a).

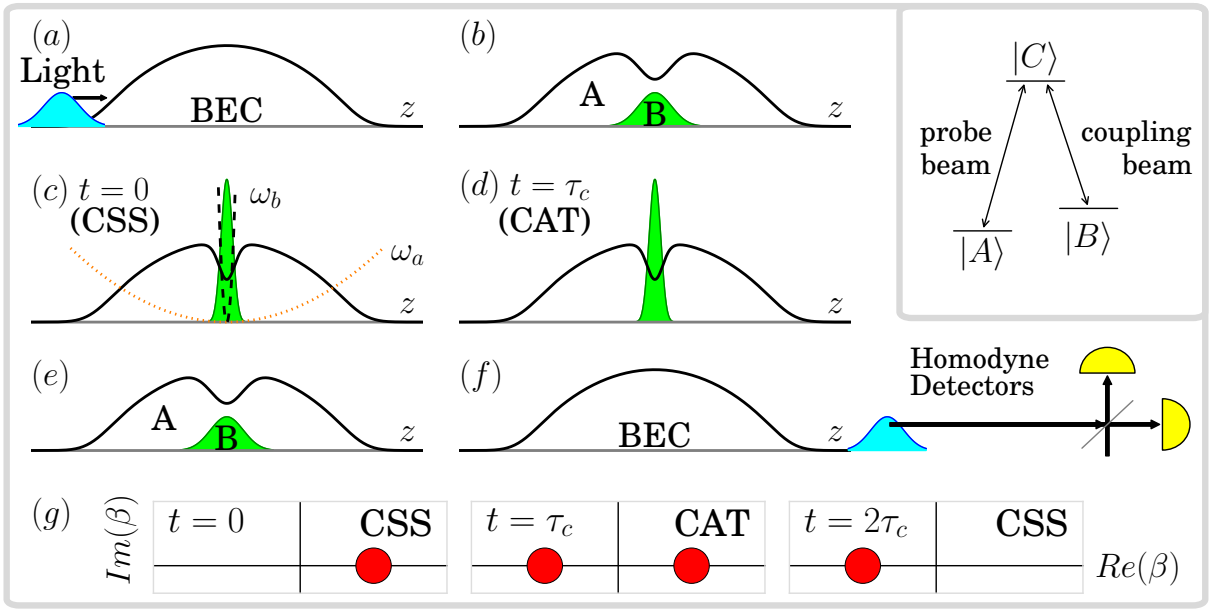

Figure 4.1: (color online) Spin cat state creation (a)-(d) and detection (e)-(g). In (a)-(f) the radially symmetric photons and spherically symmetric BECs are represented by spatial density distributions. (a) A coherent light pulse is sent into the BEC. (b) The light state is absorbed in the BEC (see inset), creating a CSS. The shape of the input pulse is chosen such that the two-component BEC is in its ground state after the absorption. (c) The trapping frequency ω_b for the small component is increased adiabatically. The density of the small component now exceeds that of the large component at the center. (d) The collision-induced Kerr nonlinearity drives the system into a spin cat state (CAT). (e) The trapping frequency is adiabatically reduced to its initial value. (f) The spin state is reconverted into light, whose Husimi Q function [47] is determined via homodyne detection [162]. (g) Expected shape of the $Q(\beta)$ function in phase space. The coherent state at $t = 0$ gives a single peak, while the cat state at $t = \tau_c$ yields two peaks. Further evolution for another interval τ_c returns the output light to a coherent state, yielding a single peak at $t = 2\tau_c$. This would not be possible if the two peaks at $t = \tau_c$ corresponded to an incoherent mixture, thus proving the existence of a coherent superposition of CSSs in the BEC at τ_c [163].

The light is absorbed by the BEC and some atoms are converted into internal states $|B\rangle$ as:

$$\sum_n c_n |n\rangle_L |N,0\rangle_S \rightarrow |0\rangle_L \sum_n c_n |N-n,n\rangle_S := |0\rangle_L |\alpha\rangle_S, \tag{4.1}$$

where the Fock state $|N_a,N_b\rangle_S$ represents N_a and N_b excitations of wavefunctions ψ_a and ψ_b in the A and B components respectively. Note that $|\alpha\rangle_S$ is an excellent approximation of a CSS [171] $\sum_{n=0}^{N} \sqrt{N!/(n!(N-n)!)}\alpha^n |N-n,n\rangle$ in the limit of $N \gg \bar{n}$ which is the case in this scheme.

The described absorption process should prepare the two-component BEC in its motional ground state to avoid the complication of unnecessary dynamics such as oscillations. This can

be achieved by matching the shape of the input pulse to the ground state of the effective trapping potential for the small component [160], provided that the effective trap is not too steep. Once the light has been absorbed, the trapping frequency ω_b is then increased adiabatically independently of ω_a, which can be achieved by combining optical and magnetic trapping. In the regime $\omega_b \gg \omega_a$, a narrow wavefunction ψ_b is formed at the center and its density can exceed the large component A, see Fig. 4.1c. This results in strong self-interaction and hence a large Kerr nonlinearity. On the other hand, keeping ω_a low reduces the unwanted effects due to collision loss involving the large component.

The spin state will now evolve with time according to

$$|\chi(t)\rangle_S = \sum_n c_n e^{-iE(N,n)t/\hbar} |N-n,n\rangle_S \tag{4.2}$$

with $|\chi(0)\rangle_S = |\alpha\rangle_S$. If the energy takes the Kerr nonlinear form $\hat{\mathscr{H}} = \hbar\eta_2\hat{n}^2$, then a spin cat state $|\chi(\tau_c)\rangle_S = (|\alpha\rangle_S + i|-\alpha\rangle_S)/\sqrt{2}$ is formed at the time $\tau_c = \pi/|2\eta_2|$ in full analogy with the proposal of Ref. [59]. The problem is thus reduced to the computation of the ground state energy $E(N,n)$.

4.4 Calculating energy

The energy of the system can be calculated by the following mean-field energy functional $E[\psi_a, \psi_b; N_a, N_b]$:

$$E = \sum_{i=a,b} N_i \left(\mathscr{K}_i + \mathscr{V}_i + \frac{1}{2}(N_i - 1)\mathscr{U}_{ii} \right) + N_a N_b \mathscr{U}_{ab} \tag{4.3}$$

where $\mathscr{K}_i$, $\mathscr{V}_i$, $\mathscr{U}_{ii}$ and $\mathscr{U}_{ab}$ are the kinetic energy, potential energy, intra- and inter-component interaction energy respectively, given by $\mathscr{K}_i = \int (\hbar^2/2m)|\nabla\psi_i|^2$, $\mathscr{V}_i = \int V_i|\psi_i|^2$ with spherically symmetric trapping $V_i = m\omega_i^2 r^2/2$, and $\mathscr{U}_{ij} = \int U_{ij}|\psi_i|^2|\psi_j|^2$ with interaction strength $U_{ij} = 4\pi\hbar^2 a_{ij}/m$. Here, ψ_i are single particle wavefunctions for i-th component with normalization $\int |\psi_i|^2 d^3r = 1$, a_{ij} are the scattering lengths, and m is the atom mass. The corresponding dynamic equation governing the system evolution is the Gross-Pitaevskii equation (GPE) [172, 173, 10]. With the restriction

$N_a = N - n$ and $N_b = n$ of spin states creation in Eq. (4.1), the nonlinearity in n can be obtained by the expansion of the energy $E(N,n) = \hbar\eta(N,n)$ around $n = 0$ as:

$$\eta(N,n) = \eta_0(N) + \eta_1(N)n + \eta_2(N)n^2 + \eta_3(N)n^3 + ... \tag{4.4}$$

where $\hbar\eta_0$ generates a global phase and $\hbar\eta_1 = -\mu_a + \mu_b$ with chemical potential μ_i ($i = a, b$) is the energy to remove one atom from $|A\rangle$ and add one atom to $|B\rangle$. $\hbar\eta_1$ generates a simple rotation in phase space $|\alpha\rangle \to |\alpha e^{-i\eta_1 t}\rangle$, which can be eliminated by a frame rotation. The term η_2 is the Kerr nonlinearity. We obtain these coefficients by fitting the total energy $E(N,n)$ with $n \in [0, 200]$ up to fourth orders in Eq. (4.4), where the numerical ground state ψ_i of GPE used in Eq. (4.3) is found by the imaginary time method [174]. This numerical approach is better than Ref. [160] because we can avoid the problems associated with the TFA of high densities [175]. Also, the high density for the small component at the center limits the negative effect of quantum fluctuations in the large component [176]. The latter are less important than the classical fluctuations in $\eta_k(N)$ due to uncertainty in N, whose effects will be discussed below. Moreover, we can now study the effects of higher-order nonlinearities (in particular η_3 and η_4).

4.5 Cat creation time

Fig. 4.2 shows our results for the spin cat creation time $\tau_c = \pi/|2\eta_2|$ and achievable cat size $\bar{n}$, taking into account the effects of atom loss. It is clear that the cat time τ_c decreases significantly as the trapping strength ω_b increases. Note that the Kerr effect disappears ($\eta_2 = 0$) around $\omega_b \approx 2\pi \times$ 55Hz, which may be used for long term storage. As mentioned above, the reason for the strong Kerr effect for large ω_b is that strong trapping potential forces ψ_b into a highly localized Gaussian $\phi_0(r) = (\frac{m\omega_b}{\pi\hbar})^{3/4} e^{-(m\omega_b r^2)/2\hbar}$. The radius of ψ_b is of the order of the characteristic length $s_b = \sqrt{\pi\hbar/(m\omega_b)}$, and the density $\rho_b(r) = n|\psi_b(r)|^2$ is peaked at the center $\rho_b(0) \approx n s_b^{-3}$ which can be much higher than $\rho_a(0)$ in our regime, see Fig. 4.1d. Therefore, the system can be effectively described by $\hat{\mathscr{H}} \approx \frac{1}{2}U_{bb}\hat{n}(\hat{n}-1)\int d^3r|\phi_0|^4$, and the second order term is approximately $\hbar\eta_2(N) \approx$

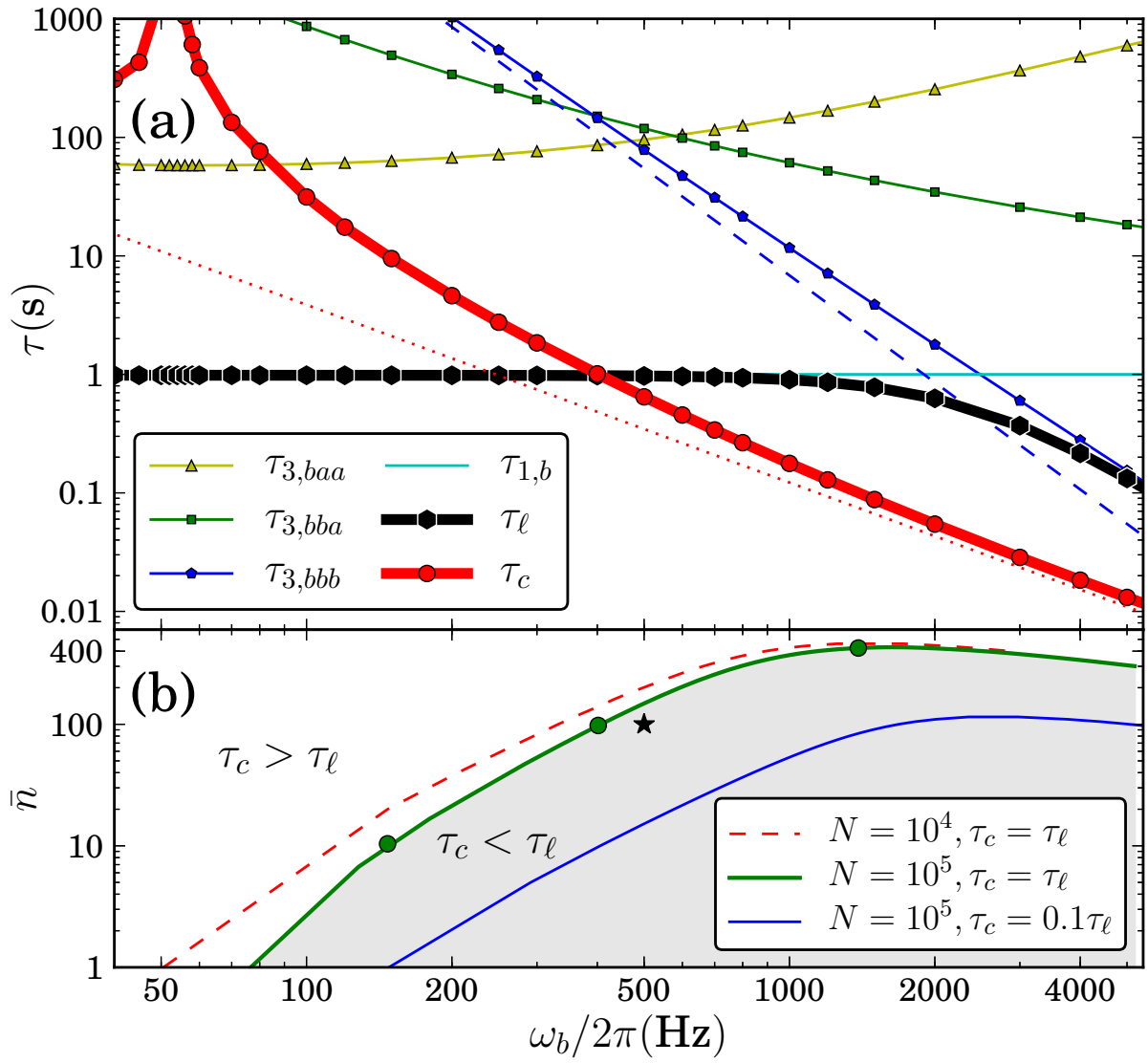

Figure 4.2: (color online) (a) The time to create a spin cat state $\tau_c = \pi/|2\eta_2|$ (thick red curve) versus the time to lose one atom τ_ℓ in component B (thick black curve) as a function of the trapping frequency for the small component ω_b. The size of the cat $\bar{n} = 100$ in this example. One sees that $\tau_c < \tau_\ell$ is possible for sufficiently large ω_b. The plot also shows the main individual loss channels contributing to the calculation of τ_ℓ, where $\tau_{m,c}$ is the individual time of losing one atom through m-body collision with particle combinations c. It furthermore shows analytic approximations for $\tau_c \sim \omega_b^{-3/2}$ (red dotted curve) and $\tau_{3,bbb} \sim \omega_b^{-3}$ (blue dashed curve), see text. (b) Achievable cat size $\bar{n}$ as a function of ω_b. The shaded region corresponds to $\tau_c < \tau_\ell$ for a condensate size $N = 10^5$ as in (a). The cat size can be increased somewhat by reducing N (dashed line). We also show that there is a region where $\tau_c < 0.1\tau_\ell$ so that loss should really be negligible. The green circles correspond to $\tau_c = 10, 1, 0.1$s (from left to right). The star corresponds to the values used in Fig. 3, and the corresponding density distributions are shown in Fig. 1(d). Both plots are for ^{23}Na with spin states $|A\rangle = |F = 1, m = 0\rangle$, $|B\rangle = |F = 2, m = -2\rangle$, scattering lengths $a_{aa} = 2.8$nm, $a_{bb} = a_{ab} = 3.4$nm [159], loss coefficients $L_1 = 0.01/$s, $L_2 = 0$, $L_3 = 2 \times 10^{-42}$m^6/s [177], and a trapping frequency $\omega_a = 2\pi \times 20$Hz for the large component.

$(U_{bb}/2)\int d^3r|\phi_0|^4 = U_{bb}2^{-5/2}s_b^{-3}$, which is consistent with the first order perturbation theory in the Appendix.

4.6 Atom loss

The phase between the two components of the spin cat state is flipped by losing just one atom (see the Appendix for more details on the effects of atom loss). This means that τ_c must be smaller than the time to lose one atom τ_ℓ, which depends on the density and thus $\bar{n}$. In our scheme, the loss of atoms in component A will not affect the cat states directly, so we focus on the loss of component B only, which can be estimated by the following loss rate equation [69, 178, 179]:

$$dn/dt = -\tau_\ell^{-1} = -(\mathscr{L}_1 + \mathscr{L}_2 + \mathscr{L}_3) \tag{4.5}$$

where $\tau_\ell = 1/(\mathscr{L}_1 + \mathscr{L}_2 + \mathscr{L}_3)$ is the approximate time to lose one atom through all possible loss channels if $n \gg 1$. The loss rates $\mathscr{L}_m$ correspond to the loss through m-body collisions involving particles in component B, where $\mathscr{L}_1 = L_1 n$ is due to collisions with the background gas, $\mathscr{L}_2 = \sum_j L_{2,bj}\int \rho_b\rho_j$ is due to spin exchange collisions, and $\mathscr{L}_3 = \sum_{j,k} L_3 \int \rho_b\rho_j\rho_k$ is due to three-body recombination [69]. It is known that the two-particle loss can be eliminated by certain choices of internal states and control methods such as applying a microwave field in [96], or a specific magnetic field as in Ref. [159]. The latter example motivates our choice of parameters in Fig. 4.2.

Fig. 4.2a shows the time to lose one atom through different channels: $\tau_1 = (L_1 n)^{-1}$ for one-body loss and $\tau_{3,ijk} = (L_3 \int d^3r \rho_i\rho_j\rho_k)^{-1}$ for three-body loss with different combination of collisions. It can be observed that the high ω_b regime is dominated by the loss of $\int \rho_b^3 \sim s_b^{-6}n^3$, which corresponds to $\tau_{3,bbb}$. For even larger values of ω_b than those shown in the figure, the three-body loss time $\tau_{3,bbb}$ becomes shorter than τ_c. The small ω_b regime is dominated by the effect of τ_1. See the Appendix for an approximate analytical treatment of atom loss. The desirable region for experiments is $\tau_c < \tau_\ell$ which also depends on $\bar{n}$. Therefore, we can draw a $\bar{n}$-ω_b phase diagram, which shows the achievable cat size as the shaded area in Fig. 4.2b.

4.7 Detection scheme

We now discuss how the existence of the spin cat states can be demonstrated via optical readout, see also Fig. 1(e) to 1(g). Our detection scheme is based on a revival argument and hence involves measurements at different times [163] (See also the related experiment of Ref. [180]). In all cases the readout process starts by reducing the trapping frequency adiabatically to its initial value. Then the spin state $|\chi(t)\rangle_S$ is reconverted into a state of light $|\chi(t)\rangle_L$, followed by homodyne detection on the output light. Using optical homodyne tomography [162], we can reconstruct the Husimi Q-function [47] $Q(\beta,t) = \frac{1}{\pi}\langle\beta|\hat{\rho}(t)|\beta\rangle$ with the density matrix $\hat{\rho}(t) = |\chi(t)\rangle_L\langle\chi(t)|$. The Q-function allows us to visualize the resulting spin states of BEC as a function of time.

Higher-order nonlinearities distort the cat state and shift the cat creation time from τ_c for a pure Kerr nonlinearity to a different observed value τ_c^*. Fig. 4.3(a) shows $Q(\beta,\tau_c^*)$ for $\omega_b = 2\pi\times 500$Hz including up to fourth-order nonlinear terms η_k. Two peaks at $t=\tau_c^*$ can be identified clearly. At the revival time $t=2\tau_c^*$, a single peak is recovered, which proves the existence of spin cat states in the BEC at τ_c^*, as described in Fig. 4.1(g). Note that the definition of τ_c^* used is the time at which the Q-function shows the two highest peaks. In general, $\eta_3<0$ and hence $\tau_c^*>\tau_c$ for $\omega_b \gg \omega_a$ since ψ_b is less localized than ϕ_0 due to the repulsive self-interaction. For the weakly phase separated regime ($a_{aa}a_{bb} \lesssim a_{ab}^2$) used in Fig. 4.2, the effective compression from component A on ψ_b can have the reverse effect. This gives $\eta_3 \approx 0$ and thus nearly perfect cat states at $\omega_b \approx 2\pi\times 400$ Hz. Further higher-order effects are shown in the Appendix.

In current experiments the light storage and retrieval process involves significant photon loss, e.g. about 90% loss in Ref. [159]. Its main effect is to move the peaks towards the origin, see Fig. 3b and Appendix. One important requirement for achieving high absorption and emission efficiency is high optical depth. For the example of Fig. 4.2, the optical depth can be estimated as $d \sim N\lambda^2/(\pi R^2) = 34$ with $N=10^5$, wavelength $\lambda = 590$nm and the BEC radius $R = 18\mu$m. This is in principle sufficient to achieve an overall efficiency close to 1 [181].

Another important experimental imperfection is the fact that the total atom number N cannot

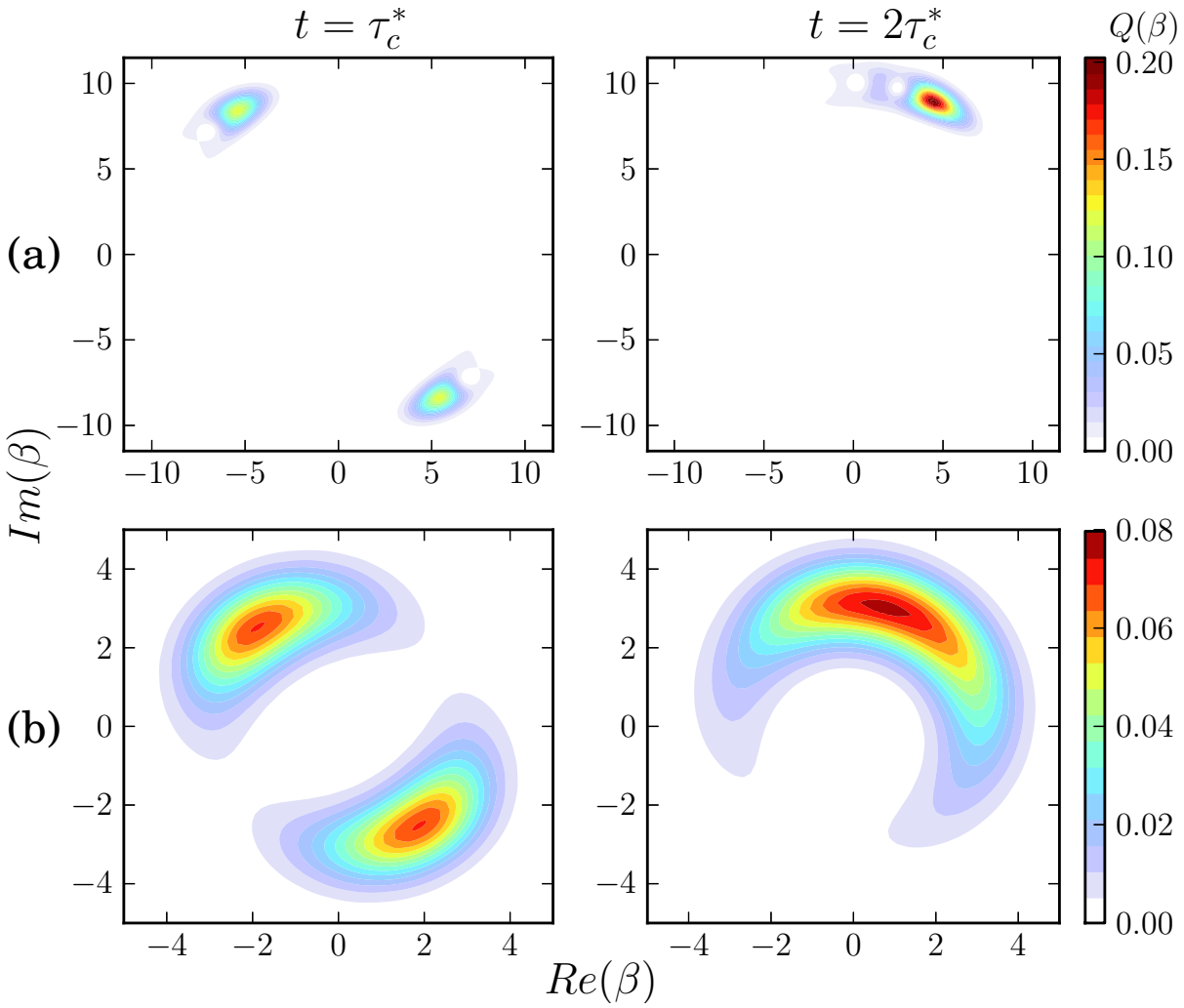

Figure 4.3: (color online) Optical demonstration of the spin cat state in the presence of various imperfections for the parameter values corresponding to the star in Fig. 2(b) ($\bar{n} = 100$ and $\omega_b = 2\pi \times 500$Hz). The spin state is reconverted into light and the Husimi phase space distribution function $Q(\beta)$ is determined via homodyne tomography. (a) Includes the effects of the higher-order nonlinearities η_3 and η_4. Two far separated peaks corresponding to the cat state are clearly visible at $\tau_c^* = 0.68$s, and one peak corresponding to the revived coherent state at $2\tau_c^*$. The shift of the cat creation time due to the higher-order terms is $\tau_c^*/\tau_c = 1.06$. (b) Furthermore includes 90% photon retrieval loss, which moves the peaks towards the origin, and 5% uncertainty in the total atom number, which spreads the peaks in the angular direction.

be precisely controlled from shot to shot. This leads to fluctuations in the nonlinear coefficients η_k. The most important negative effect of these fluctuations is dephasing, i.e. angular spreading of the peaks in Fig. 3 in phase space [46]. The magnitude of the angular spread at the time $\tau_c = \pi/|2\eta_2|$ of the cat state creation can be estimated as $\Delta\varphi = \frac{\pi\Delta N}{2\eta_2}\sum_k k\bar{n}^{k-1}\frac{\partial\eta_k}{\partial N}$, where ΔN is the uncertainty in N, as discussed in more detail in the Appendix. We find that the sensitivity of our scheme to atom number fluctuations is minimized for $\omega_b \approx 2\pi \times 600$Hz. Fig. 3b shows that a 5% uncertainty in N can be tolerated for $\omega_b = 2\pi \times 500$ Hz (even when occurring in combination with 90 % photon loss).

4.8 Summary

Two key ingredients for the success of the present scheme are the use of a high trapping frequency for the small component and the achievement of very low loss. The high trapping frequency enhances the strength of the Kerr nonlinearity, making it possible to create cat states without relying on a Feshbach resonance as proposed in Ref. [160]. This makes it possible to avoid the substantial atom loss typically associated with these resonances [69], and also allows one to use the magnetic field to eliminate two-body loss, which is critical. For example, the loss rates for the choice of Rubidium internal states discussed in Ref. [179] would only allow cat sizes of order ten atoms, see the Appendix. The high trapping frequency also helped us to suppress the unwanted effects of higher-order nonlinearities and atom number fluctuations. If the readout efficiency could be increased significantly, then the present scheme could also be used to create optical cat states. Besides their fundamental interest, both spin cat states and optical cat states are attractive in the context of quantum metrology [182].

4.9 Appendix A: Properties of two-component BEC

The most important results in the main text and these Appendixes are based on numerical methods. Therefore, the results can be considered exact within the domain of validity of the equations we

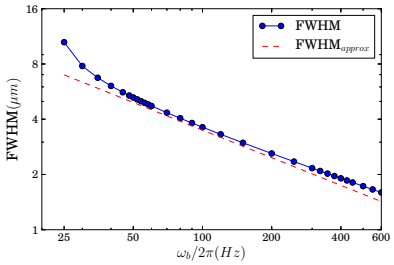

(a) Full width at half maximum (FWHM) for density ρ_b

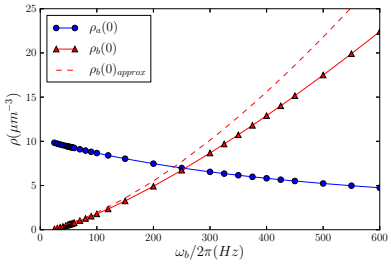

(b) Density distribution at center for both components

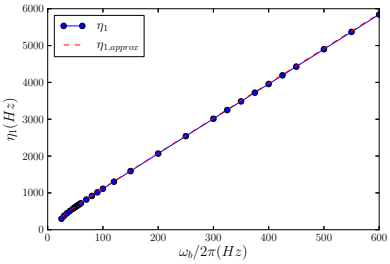

(c) Linear coefficient η_1 and its approximation Eq. (4.21)

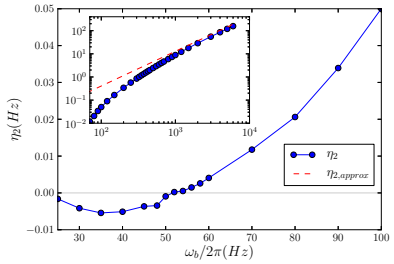

(d) Kerr coefficient η_2 and its approximation Eq. (4.23)

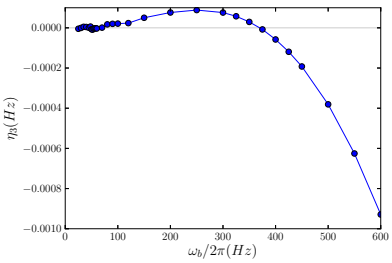

(e) Third order coefficient η_3

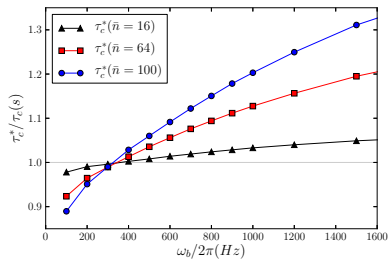

(f) The shift of the 'best' cat time τ_c^*/τ_c

Figure 4.4: Properties of spin states in the two-component BEC for the scheme with cat size $\bar{n} = 100$. (a) The width of component B becomes close to the width of a Gaussian as in Eq. (4.9) around $\omega_b \approx 2\pi 50$Hz (red dash curve). The deviation at high ω_b is because of self-repulsion in component B. Also, in this weakly phase separated regime $a_{aa}a_{bb} \lesssim a_{ab}^2$ with equal trapping $\omega_a = \omega_b = 2\pi 20$Hz, the component B is located outside of component A. The component B only peaks at the center with ω_b about 10% higher than ω_a. (b) Density $\rho_a(r=0)$ and $\rho_b(r=0)$ at the center of the trap. Note that the density $\rho_b(0)$ becomes greater than $\rho_a(0)$ around $\omega_b/2\pi \approx 250$Hz (see Fig. 4.5 for a spatial distribution). This suggests that most effects from the main BEC component A, including its quantum depletion, should be relatively small beyond $\omega_b/2\pi > 250$Hz. The red dashed curve is the density of the Gaussian approximation Eq. (4.9) (c) The numerical results for η_1 show a good agreement with first order perturbation theory. (d) The numerical solution for η_2 crosses zero around $\omega_b/2\pi \approx 55$Hz, which causes the cat time $\tau_c = \pi/|2\eta_2|$ to diverge around this point. The inset shows that the numerical results approach the simple scaling $\eta_2 \sim \omega_b^{3/2}$ at large ω_b. (e) The third order term η_3 also shows a zero-crossing point at around $\omega_b/2\pi \approx 375$Hz, which is a good region to observe nearly perfect cat states with small $\bar{n}$. (f) The relative change of the best real cat time τ_c^* from $\tau_c = \pi/|2\eta_2|$. The region with $\tau_c^*/\tau_c > 1$ is roughly $\omega_b/2\pi \gtrsim 375$Hz depending on $\bar{n}$, which corresponds roughly to the region $\eta_3 < 0$ in subfigure e, and vice versa. Note that the fourth order term is included when determining τ_c^*, see text for its definition and Fig. 4.6. The parameters used here are the same as in Fig. 2 in the main text: ^{23}Na with spin states $|A\rangle = |F=1, m=0\rangle$, $|B\rangle = |F=2, m=-2\rangle$, scattering lengths $a_{aa} = 2.8$nm, $a_{bb} = a_{ab} = 3.4$nm [159], loss coefficients $L_1 = 0.01/$s, $L_2 = 0$, $L_3 = 2\times 10^{-42}$m^6/s [177], and a trapping frequency $\omega_a = 2\pi \times 20$Hz for the large component.

used, without relying on analytic approximations. The two-component BEC can be described by the mean-field Gross-Pitaevskii equation (GPE) [172, 173, 10]. However, the typical analytical treatment, the Thomas-Fermi approximation (TFA), [183] which ignores the kinetic energy term, is not reliable in our case. It is known that TFA cannot be used in the case of high density [175], which is the case we are studying. Instead, we numerically solve the GPE:

$$i\hbar\frac{\partial}{\partial t}\psi_i = \left[-\frac{\hbar^2}{2m}\nabla^2 + V_i + \sum_{j=a,b} U_{ij}(N_i - \delta_{ij})|\psi_j|^2\right]\psi_i \tag{4.6}$$

where δ_{ij} is the Kronecker delta which cannot be ignored if N_i is of order one; ψ_i and N_i are the single mode wavefunction and the number of particles of the i-th BEC component respectively. The normalization is $\int d^3r|\psi_i|^2 = 1$ and the density is given by $\rho(r) = N_i|\psi_i(r)|^2$. The trapping potential is $V_i = m\omega_i^2 r^2/2$, with trapping strength ω_i, and the interaction strength is $U_{ij} = 4\pi\hbar^2 a_{ij}/m$, with scattering length a_{ij} between component i and j. Our target is to find the ground state energy and wavefunction, which can be done by using the imaginary time method [174]. First, we use a Wick rotation $t \to -it$ on Eq. (4.6) to obtain the corresponding diffusion equation, which is then reduced to two coupled 1D non-linear diffusion equations with the assumption of spherical symmetry. Finally, we let the system relax to the ground state with the fourth order Runge-Kutta method in time and finite difference method in space. After finding the ground state wavefunction, we can use it to calculate the mean-field energy functional:

$$E[\psi_a,\psi_b;N_a,N_b] = \sum_{i=a,b} N_i\int d^3r\left(\frac{\hbar^2}{2m}|\nabla\psi_i|^2 + V_i|\psi_i|^2 + \frac{1}{2}(N_i-1)U_{ii}|\psi_i|^4\right) + N_aN_b\int d^3rU_{ab}|\psi_a|^2|\psi_b|^2 \tag{4.7}$$

which depends on the spatial mode ψ_i and the number of particles N_i. Note that the spatial modes ψ_i depend implicitly on N_i through Eq. (4.6). In our scheme, the focus is the ground state energy $E(N,n)$ as a function of $N_a = N-n$ and $N_b = n$ because the total number of particles $N = N_a + N_b$ in the two-component BEC is fixed. After solving a set of BECs with different small component in the range $n \in [0,200]$, we fit the results up to fourth order to get the expansion coefficients

$$\frac{1}{\hbar}E(N,n) = \eta(N,n) = \eta_0(N) + \eta_1(N)n + \eta_2(N)n^2 + \eta_3(N)n^3 + \eta_4(N)n^4 + \ldots \tag{4.8}$$

Fig. 4.4 shows how the most relevant properties of the ground state of the two-component BEC change with ω_b. For the scheme described in the main text, the interesting regime is when component B is located at the center of the trap. This can be achieved with a slightly higher trapping for ω_b in this weakly phase separated regime as described in Fig. 4.4 with cat size $\bar{n} = 100$. Note that in the case of equal trapping $\omega_a = \omega_b$, the small component B will locate outside of component A because of the effective repulsion in this regime. As shown in Fig. 4.4a, the width of ρ_b is close to the width of a Gaussian at around $\omega_b/2\pi = 50$Hz, while at higher ω_b, the width is larger than the corresponding Gaussian because of the self-repulsion with other atoms in the same component B. The same effects can be observed for the real density $\rho_b(r = 0)$ at the center (Fig. 4.4b), which is lower than the corresponding Gaussian density with ω_b. When $\omega_b/2\pi \gg 250$Hz, the component B has higher density than the main component A. This allows us to ignore most effects of the component A, including the quantum depletion. Fig. 4.4c-e shows the expansion coefficients η_k. Note that both η_2 and η_3 have zero-crossing points. With zero Kerr coefficient, $\eta_2 = 0$, the system may be used to store spin states for a long time. Also, the zero third order, $\eta_3 = 0$, suggests a regime to create good small spin cat states. Fig. 4.4f shows the effects of the third order term on the shift of the "best" cat time τ_c^*, see definition below.

Qualitatively, the change in η_2 with respect to ω_b can be understood as follow. The contributions to the Kerr nonlinearity come from intra-species (aa, bb) and inter-species (ab) interactions, which have opposite sign to each other. When the trapping is weak and identical for both components, the Kerr nonlinearity is close to zero. Also, for the phase separated regime, the component B is staying in the outer region. When the trapping frequency ω_b for the B component is increased, the B component moves to the center and the overlap between A and B increases at first, which leads to an increase in the inter-species interaction term, resulting in a larger and negative Kerr nonlinearity. For very strong trapping of the B component, the overlap between A and B decreases again whereas the intra-species interaction for the B component increases strongly, leading to a large positive Kerr nonlinearity. This explains the crossover from negative to positive Kerr non-

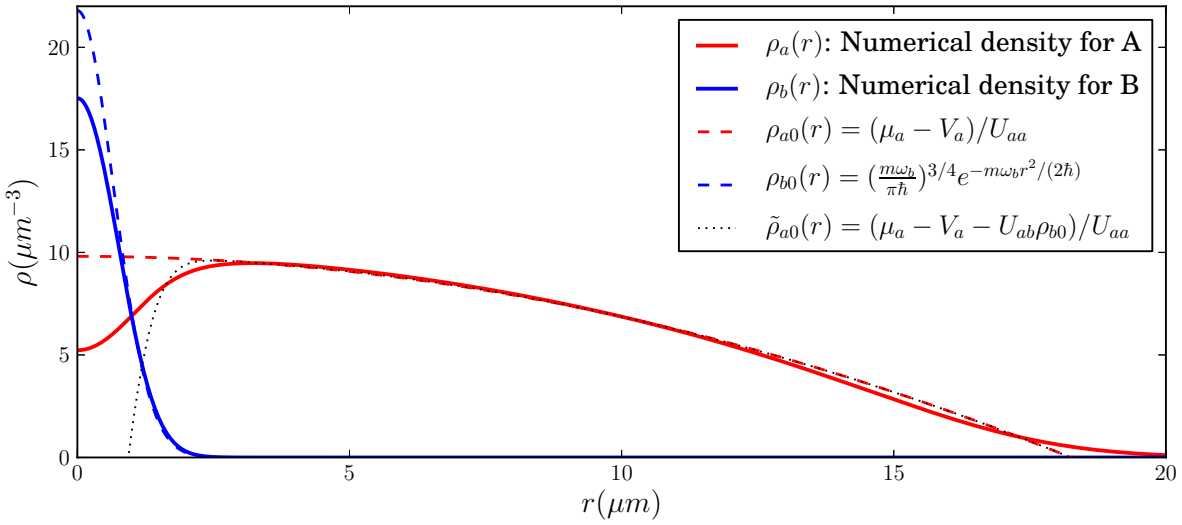

Figure 4.5: Numerical density distribution for both components (A and B) and its approximation with cat size $\bar{n} = 100$ and trapping strength $\omega_b/2\pi = 500$Hz. $\rho_{a0}(r)$ and $\rho_{b0}(r)$ are the unperturbed wavefunction used by the first order perturbation calculation. $\tilde{\rho_{a0}}(r)$ is another approximation. See text for details. Other parameters used are the same as in Fig. 4.4.

linearity as shown in Fig. S1d. In contrast, for the non-phase separated regime, the B component always stays inside the A component, and there is no crossover as discussed in Section IV (see Fig. S5).

4.10 Appendix B: Ground state energy from first order perturbation theory

The numerically obtained spatial density distribution ρ_i is shown in Fig. 4.5. The approximate solution of a harmonic oscillator ground state ρ_{b0} for B is good. If we follow a Thomas-Fermi approach similar to the one used in the previous paper [160] by dropping the kinetic energy term in Eq. (4.6), we will get $\tilde{\rho}_{a0} = (\mu_a - V_a - U_{ab}\rho_{b0})/U_{aa}$. As expected, this approximation is not good and gives a negative density as shown in Fig. 4.5. In contrast, the TFA solution for a single component BEC ρ_{a0} gives a fair approximation for A, given by [173, 10]:

$$\begin{aligned} \phi_{a0}(\mathbf{r};N_a) &= \sqrt{\frac{\mu_{a0}(N_a) - V_a}{N_a U_{aa}}}, \qquad \mu_{a0}(N_a) = \frac{1}{2}\hbar\omega_a \left(\frac{15a_a}{\sqrt{\hbar/(m\omega_a)}}\right)^{2/5} N_a^{2/5} \\ \phi_{b0}(\mathbf{r}) &= \left(\frac{m\omega_b}{\pi\hbar}\right)^{3/4} e^{-m\omega_b r^2/(2\hbar)}, \qquad \mu_{b0} = \frac{3}{2}\hbar\omega_b \end{aligned} \tag{4.9}$$

Therefore we perform first order perturbation theory with the following splitting for the GPE:

$$i\hbar\frac{\partial}{\partial t}\psi_a = (\underbrace{-\frac{\hbar^2}{2m}\nabla^2 + V_a + N_a U_{aa}|\phi_a|^2}_{H_{a0}} + \underbrace{N_b U_{ab}|\phi_b|^2}_{H_{a1}})\psi_a \tag{4.10}$$

$$i\hbar\frac{\partial}{\partial t}\psi_b = (\underbrace{-\frac{\hbar^2}{2m}\nabla^2 + V_b}_{\mathscr{H}_{b0}} + \underbrace{N_a U_{ab}|\phi_a|^2 + (N_b-1)U_{bb}|\phi_b|^2}_{\mathscr{H}_{b1}})\psi_b \tag{4.11}$$

where $\mathscr{H}_{i0}$ is the unperturbed Hamiltonian and the perturbation is given by $\mathscr{H}_{i1}$. Note that $N_a - 1 \approx N_a$ is used. The solutions of $\mathscr{H}_{i0}$ are given by Eq. (4.9).

To calculate the energy analytically, we expand the ground state energy $E(N_a, N_b)$ as the Taylor series:

$$E(N_a,N_b) = E(\bar{N}_a,\bar{N}_b) + \sum_{i=a,b}\frac{\partial E}{\partial N_i}\bigg|_{(\bar{N}_a,\bar{N}_b)}(N_i-\bar{N}_i) + \frac{1}{2}\sum_{j=a,b}\sum_{i=a,b}\frac{\partial}{\partial N_j}\frac{\partial E}{\partial N_i}\bigg|_{(\bar{N}_a,\bar{N}_b)}(N_i-\bar{N}_i)(N_j-\bar{N}_j) + \tag{4.12}$$

Note that the chemical potentials (energy change with respect to the number of particles) are given by $\mu_i(N_a,N_b) = \frac{\partial E}{\partial N_i}(N_a,N_b)$. Since the main component A in the scheme is much larger than the small component B, or $N-n \gg n$, the expansion can be carried out around the point $(N,0)$:

$$\hbar\eta_0(N) = E(N,0) \tag{4.13}$$

$$\hbar\eta_1(N) = -\mu_a(N,0) + \mu_b(N,0) \tag{4.14}$$

$$\hbar\eta_2(N) = \frac{1}{2}\left[\partial_{N_a}\mu_a(N,0) - \partial_{N_b}\mu_a(N,0) - \partial_{N_a}\mu_b(N,0) + \partial_{N_b}\mu_b(N,0)\right] \tag{4.15}$$

Note that the μ_i here denote the exact chemical potentials from the GPE, which can be approximated by the unperturbed μ_{i0} plus the perturbed chemical potential $\Delta\mu_i$:

$$\mu_i = \mu_{i0} + \Delta\mu_i \tag{4.16}$$

Using the unperturbed solutions Eq. (4.9), the chemical potential can be calculated as:

$$\Delta\mu_a = U_{ab}N_b\left\langle\phi_{a0}\left||\phi_{b0}|^2\right|\phi_{a0}\right\rangle \tag{4.17}$$

$$= \frac{N_b}{N_a}\left(\frac{U_{ab}}{U_{aa}}\mu_{a0}(N_a) - \frac{3}{4}\frac{U_{ab}\omega_a}{U_{aa}\omega_b}\hbar\omega_a\right) \tag{4.18}$$

$$\Delta\mu_b = U_{ab}N_a\left\langle\phi_{b0}\left||\phi_{a0}|^2\right|\phi_{b0}\right\rangle + U_{bb}(N_b-1)\left\langle\phi_{b0}\left||\phi_{b0}|^2\right|\phi_{b0}\right\rangle \tag{4.19}$$

$$= \left(\frac{U_{ab}}{U_{aa}}\mu_{a0}(N_a) - \frac{3}{4}\frac{U_{ab}\omega_a}{U_{aa}\omega_b}\hbar\omega_a\right) + U_{bb}(N_b-1)(\sqrt{2}s_b)^{-3} \tag{4.20}$$

where $s_i = \sqrt{\pi\hbar/(m\omega_i)}$ is the characteristic length of a Gaussian. Note that the perturbation involves an integration whose range is chosen to be the whole space for simplicity, which is justified by the fact that component B is much narrower than component A when $\omega_b \gg \omega_a$ (see Fig. 4.5). Substituting these results back into η_1 in Eq. (4.14), we have:

$$\hbar\eta_1(N) = -\mu_{a0}(N) + \underbrace{\frac{3}{2}\hbar\omega_b}_{\mu_{b0}} + \underbrace{\frac{U_{ab}}{U_{aa}}\mu_{a0}(N) - \frac{3}{4}\frac{U_{ab}\omega_a}{U_{aa}\omega_b}\hbar\omega_a - U_{bb}(\sqrt{2}s_b)^{-3}}_{\Delta\mu_b(N,0)} \tag{4.21}$$

The third and fourth terms on the right hand side are the effective interaction between the main BEC and the component B. The last term is the repulsion between the particles in component B. The fourth term is small when $\omega_b \gg \omega_a$ and can be ignored. This result gives a very good approximation as demonstrated in Fig. 4.4c.

Similarly, differentiating the chemical potential yields the second order term η_2 in Eq. (4.15):

$$\hbar\eta_2(N) = \frac{1}{2}\left[\underbrace{\frac{2}{5}\frac{\mu_{a0}(N)}{N}}_{\partial_{N_a}\mu_a(N,0)} - \underbrace{\left(\frac{U_{ab}}{U_{aa}}\mu_{a0}(N) - \frac{3}{4}\frac{U_{ab}\omega_a}{U_{aa}\omega_b}\hbar\omega_a\right)\frac{1}{N}}_{\partial_{N_b}\mu_a(N,0)} - \underbrace{\frac{2}{5}\frac{U_{ab}}{U_{aa}}\frac{\mu_{a0}(N)}{N}}_{\partial_{N_a}\mu_b(N,0)} + \underbrace{U_{bb}(\sqrt{2}s_b)^{-3}}_{\partial_{N_b}\mu_b(N,0)}\right] \tag{4.22}$$

The first three derivatives are smaller than the last term when $\omega_b \gg \omega_a$ and $N \to \infty$. Therefore, at high ω_b, the last term dominates $\eta_2(N)$, yielding

$$\hbar\eta_2(N) \approx \frac{U_{bb}}{2}(\sqrt{2}s_b)^{-3} = \frac{U_{bb}}{2}\left(\frac{m\omega_b}{2\pi\hbar}\right)^{3/2}. \tag{4.23}$$

As shown in Fig. 4.4b, Eq. (4.23) gives an order of magnitude estimation of $\eta_2(N)$. Note that we can also get the dominant term as calculated above by assuming component A to have a constant density distribution $|\psi(r)|^2 = \mu_{a0}/(N_a U_{aa})$, at $\omega_b \gg \omega_a$. A better approximation should take into account the change in density ρ_a as shown in Fig. 4.5.

4.11 Appendix C: Effects of higher-order nonlinearities

Cat states can be distorted by higher order nonlinearities. Thus we need to find out to what extent the cat states are distorted and whether the distortion is tolerable. Another practical problem is to

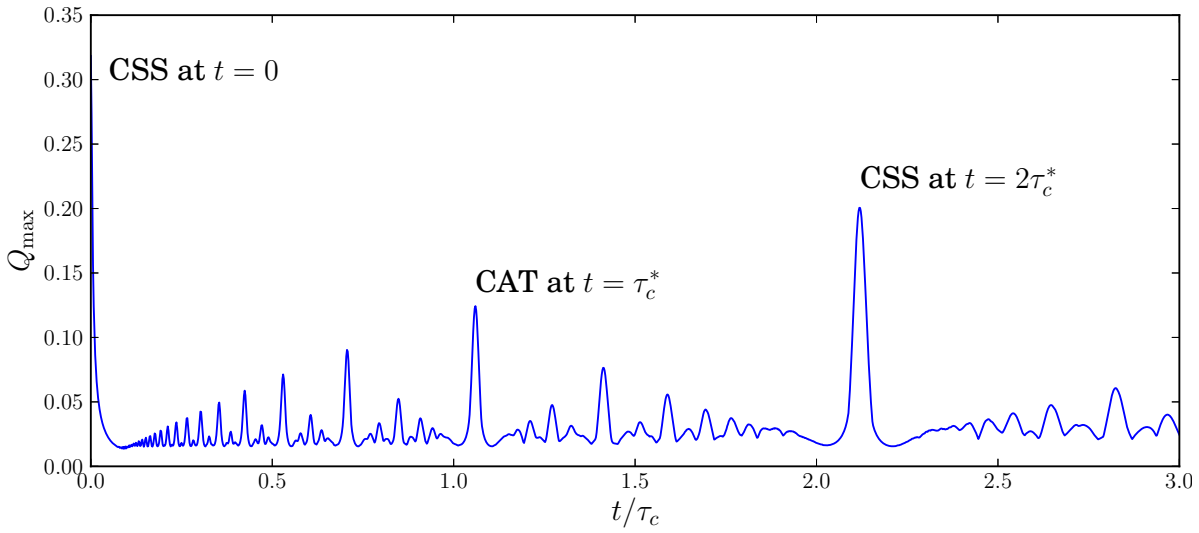

Figure 4.6: The maximum of the Q function, $Q_{\max}(\beta)$, as a function of the relative time t/τ_c. The "best" real cat time τ_c^* is defined as the time in which there are the two highest peaks in the Q-function. The leftmost peak corresponds to the initial coherent spin state (CSS), with a value $Q_{\max} = 1/\pi$. The peak at $\tau_c^*/\tau_c \approx 1.06$ corresponds to the spin cat state (CAT). The time at which the CAT state is observed is shifted with respect to the ideal case $\tau_c^*/\tau_c = 1$ because of the higher-order nonlinearities. The highest peak at $\tau_c^*/\tau_c \approx 2.12$ corresponds to the CSS at the revival time. Note that all fitting orders are included for determining τ_c^*. The CAT state at τ_c^* and CSS at $2\tau_c^*$ are plotted in Figs. 3a and 3b in the main text. The other parameters used are the same as in Fig. 4.4.

figure out the optimal time to observe a cat state in real experiments. We define the "best" cat time τ_c^* as the time with the two highest peaks in Q function. This definition is based on the feature of the cat states that two separated peaks in the Q function should be distinguished clearly.

This method is illustrated by Fig. 4.6 with the highest peak value Q_{max} plotted over time. It is clear that the peak for the cat state is located near $\tau_c^*/\tau_c = 1$ as expected. In practice, we search around the nearby region, say $\tau_c^*/\tau_c \in [0.8, 1.6]$, for the highest peak. The resulting τ_c^* corresponds to the best cat time. We further manually check that there are indeed only two opposite peaks in phase space. The resulting shift in the cat time is plotted in Fig. 4.4d. Note that the τ_c^* depends on $\bar{n}$, see also Fig. 4.4f.

In the scheme, the output light is of the form $|\chi(t)\rangle_L = \sum_n c_n e^{-i\eta(N,n)t}|n\rangle_L$ with the initial

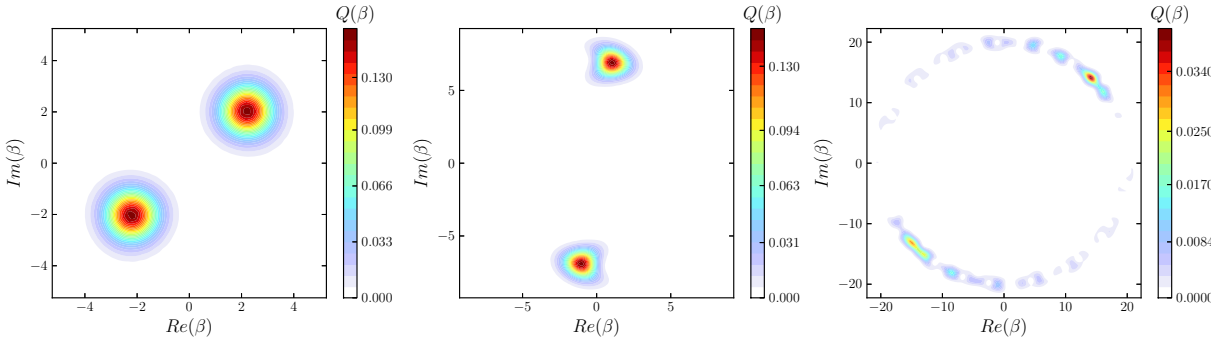

(a) $\bar{n} = 9$ and $\tau_c^* = 1.005\tau_c$ (b) $\bar{n} = 49$ and $\tau_c^* = 1.026\tau_c$ (c) $\bar{n} = 400$ and $\tau_c^* = 1.52\tau_c$

Figure 4.7: Plot of $Q(\beta, \tau_c^*)$ for different cat sizes $\bar{n}$. (a) $\bar{n} = 9$. The third order nonlinearity η_3 is weak, so the Q function looks like a perfect circle. (b) $\bar{n} = 49$. The effects of η_3 begin to appear and the cat state is distorted slightly. (c) $\bar{n} = 400$. Both η_3 and η_4 are significant. The two peaks are distorted and not symmetric. Note that τ_c^* is not quite well defined in this case. The case $\bar{n} = 100$ is plotted in Fig. 3a in the main text with $\omega_b = 2\pi 500$Hz and $\tau_c = 0.646$s. The other parameters used are the same as in Fig. 4.4.

condition $|\chi(0)\rangle_L = |\alpha\rangle_L$ and $\alpha = \sqrt{\bar{n}}$. Hence, the Q-function without loss is

$$Q(s,\theta,t) = \frac{1}{\pi} e^{-(\alpha-s)^2} \left| \sum_n \left(\frac{(\alpha s)^n}{n!} e^{-\alpha s} \right) e^{-in\theta} e^{-i\eta(N,n)t} \right|^2 \tag{4.24}$$

where the phase space is defined by $\beta = se^{i\theta}$. This equation is numerically evaluated to obtain the Q-function for given η_k, which are obtained by fitting the solutions of the GPE Eq. (4.6). A few more figures corresponding to Fig. 3a in main text are plotted in Fig. 4.7 for different cat sizes $\bar{n}$. One can see that the higher order effects ($k \geq 3$) are weak for small $\bar{n}$, but significant for larger $\bar{n}$.

4.12 Appendix D: Phase separated regime and non-phase separated regime

The scheme should also work in the non-phase separated regime $a_{ab}^2 < a_{aa}a_{bb}$. Fig. 4.8 shows the coefficients η_2, η_3, η_4 for different values of the inter-species scattering length a_{ab}, with $a_{aa} = 2.8$nm and $a_{bb} = 3.4$nm. The plots suggest that the Kerr effect is also strong in the non-phase separated regime, but the higher order terms might limit the resulting cat size $\bar{n}$. The main qualitative difference is that there are no zero-crossing points for η_k in the non-phase separated regime. These results further suggest that the weakly phase separated regime is advantageous because the higher-order terms are very small around $\omega_b/2\pi \approx 400$Hz.

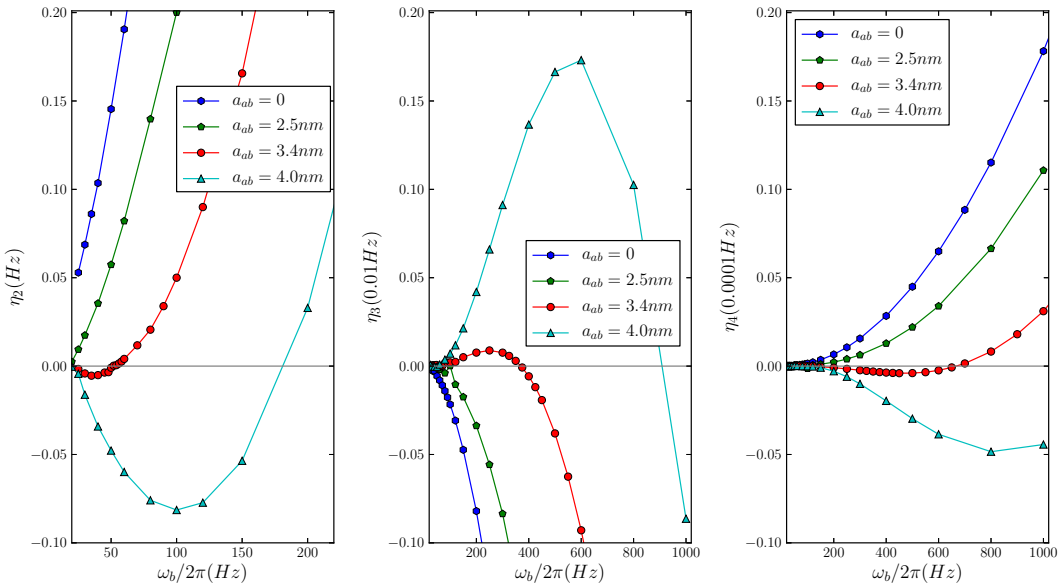

(a) $\eta_2(\omega_b)$ for different a_{ab} (b) $\eta_3(\omega_b)$ for different a_{ab} (c) $\eta_4(\omega_b)$ for different a_{ab}

Figure 4.8: Effects of the cross-scattering length a_{ab} on (a) η_2, (b) η_3, (c) η_4, with $a_{aa} = 2.8$nm and $a_{bb} = 3.4$nm (a_{ii} is the self-scattering length of component i). Both $a_{ab} = 0$ and $a_{ab} = 2.5$nm are in the non-phase separated regime $a_{ab}^2 < a_{aa}a_{bb}$, while $a_{ab} = 3.4$nm and $a_{ab} = 4.0$nm are in the phase separated regime $a_{ab}^2 > a_{aa}a_{bb}$. When a_{ab} is turned on gradually, the magnitude of all nonlinear coefficients η_k decreases at first because the effective scattering length for the two components decreases. All coefficients show a qualitative change, with a zero-crossing point in the phase separated regime. Compared with the non-phase separated regime, say, $a_{ab} = 0$, the phase separated regime can have a relatively weak higher-order effect even for high trapping frequencies, e.g. the small η_3 at $\omega_b/2\pi = 500$Hz which is used in Fig. 3 of the main text. Note that the y axis is rescaled by factors of 100 from left to right for easy comparison. The parameters used are the same as in Fig. 4.4, except a_{ab}.

4.13 Appendix E: Atom loss rates

The atom loss rate for component i is given by [69, 178, 179]:

$$\frac{dN_i}{dt} = -\tau_{i,\ell}^{-1} = -\left(L_{1,i}\int d^3r\rho_i + \sum_{j=a,b} L_{2,ij}\int d^3r\rho_i\rho_j + \sum_{j=a,b}\sum_{k=a,b} L_{3,ijk}\int d^3r\rho_i\rho_j\rho_k\right) \quad (4.25)$$

where $L_{1,i}$, $L_{2,ij}$, $L_{3,ijk}$ are the one, two and three particle collision loss rates. Note that the density $\rho_i = N_i|\psi_i|^2$ in the equation also depends on the numbers of particles N_i which decrease over time. As discussed in the main text, the individual times to lose one particle through an m-body process with particle combination c are defined as $\tau_{1,i} = (L_{1,i}\int d^3r\rho_i)^{-1}$, $\tau_{2,ij} = (L_{2,ij}\int d^3r\rho_i\rho_j))^{-1}$ and $\tau_{3,ijk} = (L_{3,ijk}\int d^3r\rho_i\rho_j\rho_k)^{-1}$, where $L_{3,i} = L_1$ and $L_{3,ijk} = L_3$ are used as an approximation. These

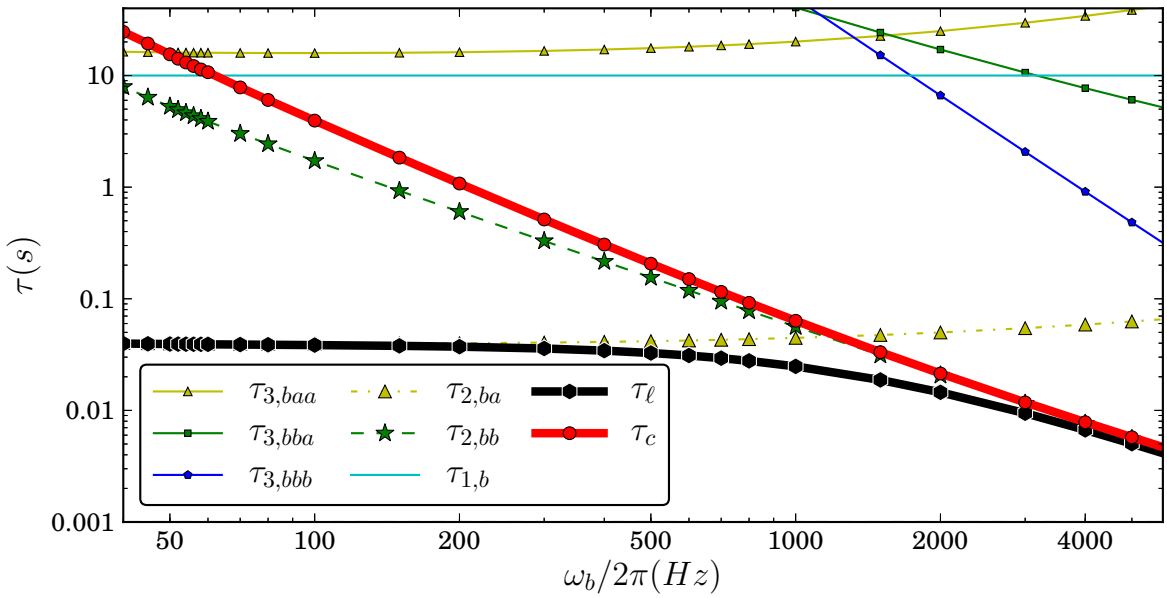

Figure 4.9: Cat time τ_c and one-atom loss time τ_ℓ for Rubidium with $\bar{n} = 10$, $N = 10^5$ and non-zero two-body loss rate $L_{2,ij}$. It is clear that the time to lose one atom through the two-body loss within the same component, $\tau_{2,bb}$, dominates at high ω_b, which has a similar scaling as the cat time $\tau_c \sim \omega_b^{-3/2}$. This limits the maximum $\bar{n}$ to around 10 atoms. Parameters: Rubidium atoms ^{87}Rb with scattering length $a_{aa} = 100.44 r_B$, $a_{bb} = 95.47 r_B$, $a_{ab} = 88.28 r_B$, where r_B is the Bohr radius. The atom loss rates are $L_1 = 0.01$/s, $L_{2,aa} = 0$, $L_{2,bb} = 119 \times 10^{-21} m^3$/s, $L_{2,ab} = 78 \times 10^{-21}$m^3/s, $L_3 = 6 \times 10^{-42}$m^6/s [179], and $\omega_a/2\pi = 20$Hz.

time scales can be evaluated using numerical integration for the ground state density distribution obtained from solving Eq. (4.6). Here, we further show the results for Rubidium atoms with non-zero two-body loss rate in Fig. 4.9. The loss due to two-body effects is significantly larger than that due to three-body effects in this case, which limits the maximum cat size to $\bar{n} = 10$ atoms, as compared to a few hundred atoms for the sodium example used in the main text. Note that this is only one possible choice of states for Rubidium. Large cats may still be possible if appropriate internal states and other conditions can be found such that two-body loss is suppressed.

For cat state creation, the maximum loss of atoms in the component B cannot be larger than one atom. Therefore, we are trying to give a conservative estimation. Since $|\psi_a(r)|^2 \leq |\psi_{a0}(0)|^2 = \mu_a/(N_a U_{aa})$ in the TFA, we can use the maximum $|\psi_{a0}(0)|$ for the main BEC, and the Gaussian

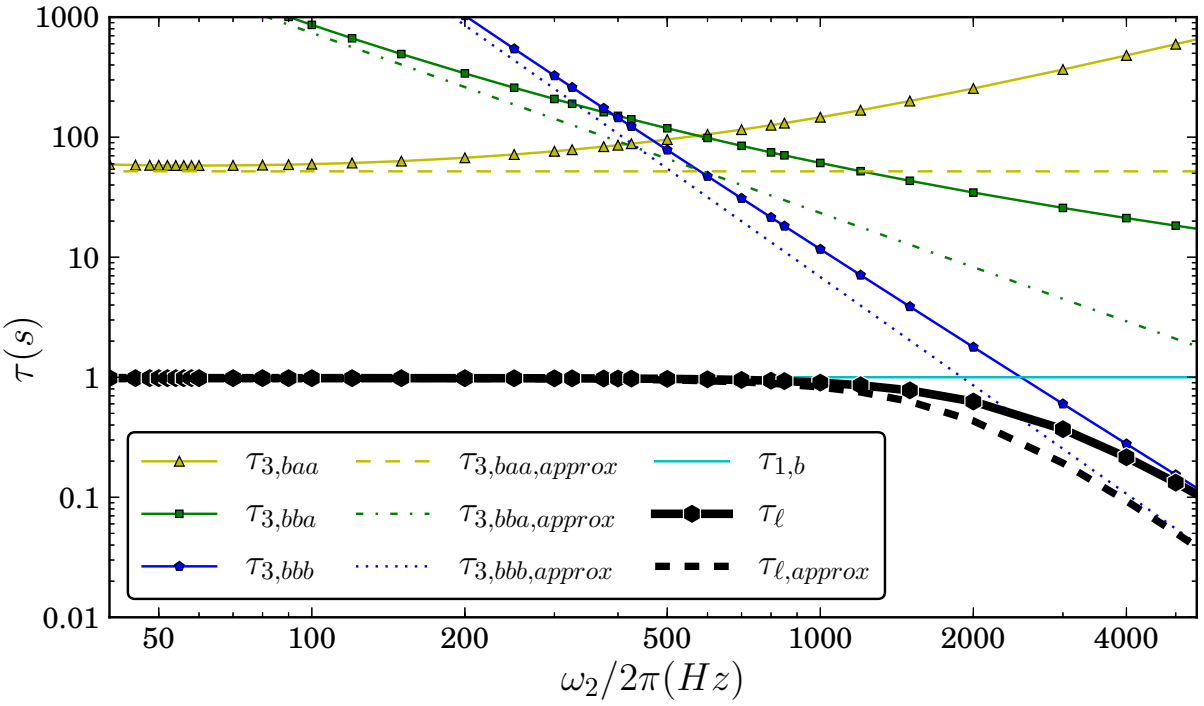

Figure 4.10: Comparison of the numerical and approximation results for all loss processes corresponding to Fig. 2a in the main text. The solid curves show the numerical solutions of the time to lose one atom $\tau_{m,c}$ through an m-body process with particle combination c, while the approximations are shown as dotted or dashed curves with the same color. The time to lose one atom through all processes is calculated by $\tau_\ell = (\tau_{1,b}^{-1} + \tau_{3,baa}^{-1} + \tau_{3,bba}^{-1} + \tau_{3,bbb}^{-1})^{-1}$. Note that the approximations here are essentially lower bounds for the numerical solutions, as shown in this figure. See text for details.

$\phi_{b0}(r)$ for component B in Eq. (4.9):

$$\int \rho_b d^3r = n \tag{4.26}$$

$$\int \rho_b^2 d^3r \approx \int d^3r |\phi_{b0}|^4 n^2 = (\sqrt{2}s_b)^{-3} n^2 \tag{4.27}$$

$$\int \rho_a \rho_b d^3r \approx \left(\frac{\mu_{a0}}{U_{aa}}\right) n = \frac{15^{2/5}\pi^{1/5}}{8} \frac{N^{2/5}}{a_a^{3/5} s_a^{12/5}} n \tag{4.28}$$

$$\int \rho_b^3 d^3r \approx \int d^3r |\phi_{b0}|^6 n^3 = 3^{-3/2} s_b^{-6} n^3 \tag{4.29}$$

$$\int \rho_a \rho_b^2 d^3r \approx \left(\frac{\mu_{a0}}{U_{aa}}\right) \int d^3r |\phi_{b0}|^4 n^2 = \frac{15^{2/5}\pi^{1/5}}{16\sqrt{2}} \frac{N^{2/5}}{a_{aa}^{3/5} s_a^{12/5} s_b^3} n^2 \tag{4.30}$$

$$\int \rho_a^2 \rho_b d^3r \approx \left(\frac{\mu_{a0}}{U_{aa}}\right)^2 n = \frac{15^{4/5}\pi^{2/5}}{64} \frac{N^{4/5}}{a_{aa}^{6/5} s_a^{24/5}} n \tag{4.31}$$

The estimations for three body loss are shown in Fig. 4.10, which suggests they are good lower

bounds for $\tau_{3,ijk}$ and the time to lose one atom through all loss channels $\tau_\ell = (\tau_{1,b}^{-1} + \tau_{3,baa}^{-1} + \tau_{3,bba}^{-1} + \tau_{3,bbb}^{-1})^{-1}$. The estimation is better at small ω_b, since the density of component A is not repelled away so that the approximation $|\psi_a(0)|^2 \approx |\psi_{a0}(0)|^2$ is good.

4.14 Appendix F: Readout loss

The readout loss from spin states to light is treated using the beam splitter model with a given loss rate $\mathfrak{r}^2$. The state passing through the beam splitter is $|\chi_{out}\rangle_L = \sum_{k=0}^{n} B_{nk} |n-k,k\rangle_L$ with $B_{nk} = \mathfrak{t}^{n-k}\mathfrak{r}^k n!/(k!(n-k)!)$, so the reduced density matrix $\hat{\rho}'$ is

$$\hat{\rho}' = Tr_2(\hat{\rho}) = \sum_i \langle i|\psi_{out}\rangle_L \langle \psi_{out}|i\rangle = \sum_{n,m} \sum_{k}^{\min(m,n)} B_{nk} B_{mk}^* c_n(t) c_m^*(t) |n-k\rangle \langle m-k| \tag{4.32}$$

Hence, the resulting Q function with loss $Q_{loss}(s,\theta,t)$ and initial coherent state $|\alpha\rangle_L$ can be written as:

$$Q_{loss}(s,\theta,t) = \frac{1}{\pi} e^{-(t\alpha - s)^2} \sum_{m,n} \left(\sum_{k=0}^{\min(m,n)} \frac{(\alpha^2\mathfrak{r}^2)^k (\mathfrak{t}\alpha s)^{n-k} (\mathfrak{t}\alpha s)^{m-k}}{k!(n-k)!(m-k)!} e^{-(\alpha^2\mathfrak{r}^2 + 2\mathfrak{t}\alpha s)} \right) e^{-i(n-m)\theta} e^{-i(\eta(n)-\eta(m))t} \tag{4.33}$$

The term inside the big bracket is the bivariate Poisson distribution so this summation is upper bounded by 1. Therefore the resulting $Q_{loss}(\beta)$ is confined to the annulus $|s - \mathfrak{t}\alpha| \sim 1$. Hence, the effect of photon loss is to move the peak of the Q-function toward the origin, as shown in Fig. 3c and 3d in the main text. This form of the Q-function can be evaluated fairly efficiently with time complexity of order $\mathcal{O}(\bar{n}^{3/2})$, which allows us to evaluate it for cat sizes of order a few hundred atoms.

4.15 Appendix G: Allowable uncertainty in atom number

Since all $\eta_k(N)$ depend on the total atom number N, the statistical fluctuations in N can cause dephasing (equivalent to angular spreading in phase space for the Q-function studied here), which can wash out all observable features of cat states (consider for example the N-dependent rotation

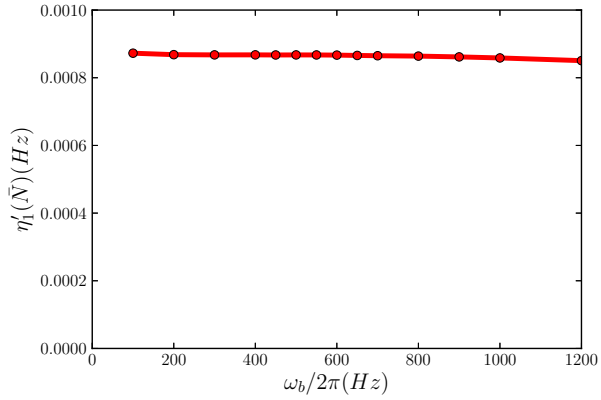

(a) $d\eta_1/dN$ vs ω_b

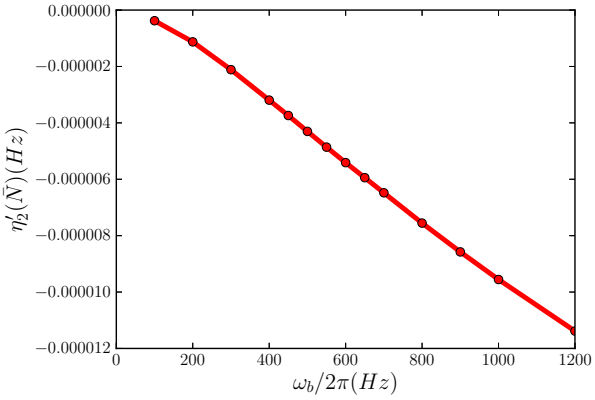

(b) $d\eta_2/dN$ vs ω_b

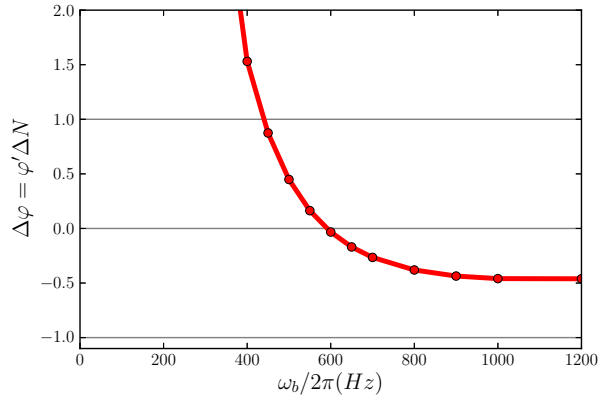

(c) Dephasing $\Delta\varphi$ with $\Delta N = 0.05N$, at τ_c

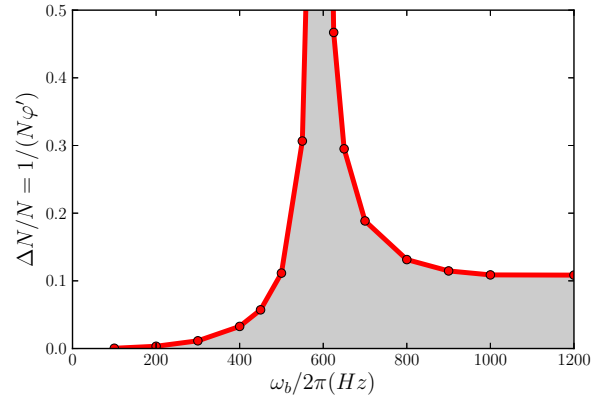

(d) Allowable range of uncertainty in $\Delta N/N$, at τ_c

Figure 4.11: Allowable range of atom number uncertainty with $\bar{N} = 10^5$ and $\bar{n} = 100$. (a) η_1' is basically constant over a large range of ω_b. (b) η_2' decreases with ω_b. (c) Total dephasing $\Delta\varphi = \varphi'\Delta N$, where $\varphi' = (\pi/2\eta_2)(\sum_k k\bar{n}^{k-1}\eta_k')$ includes up to fourth order terms from the GPE. $\Delta\varphi$ needs to be smaller than 1 to have two distinguishable peaks of cat states, see Fig 3c and 3d in main text for the Q-function for the case of $\Delta\varphi = 0.5$ at $\omega_b/2\pi = 500$Hz. (d) The gray region indicates the allowable uncertainty in atom number $\Delta N/N$. It shows that the uncertainty in N can be very large around $\omega_b/2\pi = 600$, and about 10% for high ω_b. The other parameters used are the same as in Fig. 4.4.

$e^{-i\eta_1(N)t}$ caused by $\eta_1(N)$). The dephasing is small if the derivatives of the coefficients with respect to N, $\eta_k'(N) = \partial_N \eta_k(N)$, are small. These quantities are plotted in Fig. 4.11a and 4.11b. Note that the constancy of η_1' in Fig. (4.11a) can be understood from Eq. (4.21) because $\eta_1' = (U_{ab}/U_{aa} - 1)\mu_{a0}'$ is independent of ω_b. Also, the dephasing is linear in time, hence, a short cat time τ_c can significantly reduce the dephasing effects. Moreover the rotation generated by $\eta_1(N)$ can be canceled by the opposite rotation generated by $\eta_2(N)$, as we derive below.

First considering the expansion of $n = \bar{n} + \Delta n$ around $\bar{n}$ the relevant terms become

$$\eta_1(N)n + \eta_2(N)n^2 = (\eta_1\bar{n} + \eta_2\bar{n}^2) + (\eta_1 + 2\eta_2\bar{n})\Delta n + \eta_2\Delta n^2 \tag{4.34}$$

On the right hand side, the first term gives a global phase which can be neglected. The second term leads to a rotation in phase space. Writing $N = \bar{N} + \Delta N$ and expanding the coefficients around $\bar{N}$ one has

$$\eta_k(N) = \eta_k(\bar{N}) + \eta_k'(\bar{N})\Delta N \tag{4.35}$$

where $\eta_k'(N) = \partial_N \eta_k(N)$. Note that $\Delta\eta_k(N) = \eta_k'(N)\Delta N$ is the fluctuation in η_k due to the uncertainty ΔN. Substituting these back into the second term in Eq. (4.34) yields the dephasing term $(\eta_1'\Delta N + 2\bar{n}\eta_2'\Delta N)\Delta n$. This dephasing term is the source of a ΔN dependent rotation in the β-plane, which is eliminated when the condition $\eta_1'(\bar{N}) + 2\bar{n}\eta_2'(\bar{N}) = 0$ is satisfied, see Fig. 4.11c. In particular, we want to find out the maximum allowable ΔN that still preserves an observable spin cat state at the cat time τ_c. Therefore, we define $\Delta\varphi = \varphi'\Delta N = \tau_c(\eta_1' + 2\bar{n}\eta_2')\Delta N$, and the condition $|\Delta\varphi| \lesssim 1$ should be satisfied, or

$$\Delta N \lesssim \frac{1}{\varphi'} \tag{4.36}$$

The higher order terms η_k can also be included, yielding

$$\varphi' = \frac{\pi}{2\eta_2}\left(\sum_k k\bar{n}^{k-1}\eta_k'\right) \tag{4.37}$$

Numerically, we find $\eta_k'(N)$ by taking the numerical derivative of $\eta_k(N)$. The results in Fig. 4.11d show that there is a large range of allowable uncertainty in atom number ΔN if ω_b is high enough.

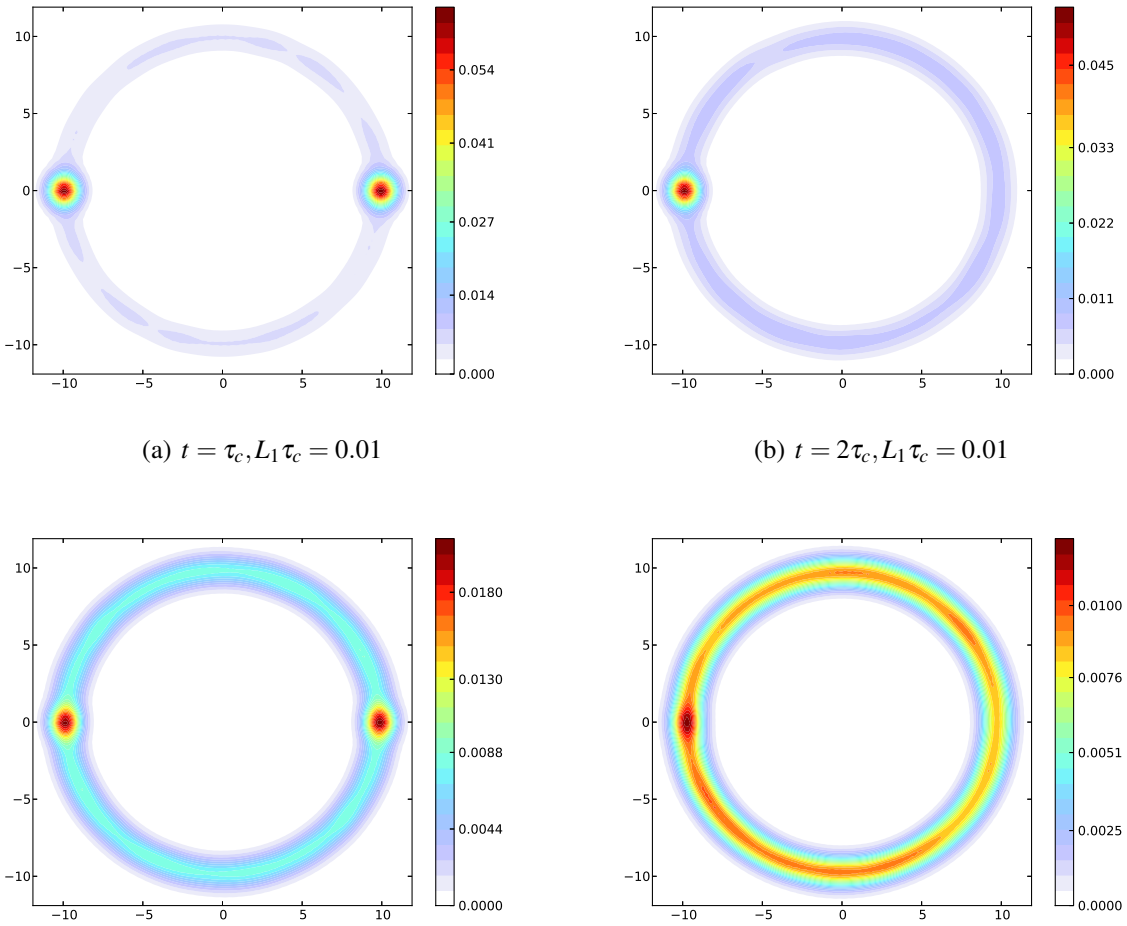

(a) $t = \tau_c, L_1\tau_c = 0.01$

(b) $t = 2\tau_c, L_1\tau_c = 0.01$

(c) $t = \tau_c, L_1\tau_c = 0.025$

(d) $t = 2\tau_c, L_1\tau_c = 0.025$

Figure 4.12: Q function of continuous atom loss for the standard Kerr effect with Hamiltonian $\hat{\mathscr{H}} = \hbar\eta_2\hat{n}^2$. (left column) At cat time $t = \tau_c = \pi/|2\eta_2|$, (right column) At revival time $t = 2\tau_c$. Mean photon number $\bar{n} = 100$ and 5000 samples.

Note that this range is an estimation since only the first order approximation of $\Delta\eta_k = \eta_k'(N)\Delta N$ is used. In contrast, the accuracy requirement $\Delta N/N$ at low trapping ω_b is even higher than the high resolution of counting cold atoms of 1 in 1200 in a recent experiment [184].

4.16 Appendix H: Atom loss

The continuous loss of atoms from the BEC can be described by the master equation:

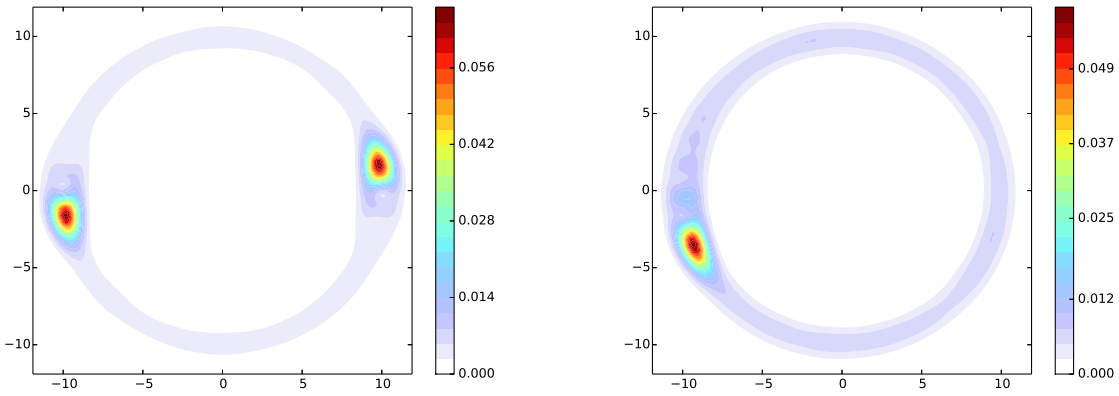

(a) (b)

Figure 4.13: Q function of continuous atom loss for η_k calculated from GPE for the parameters given in Fig. 2b in the main text ($\bar{n} = 100$, $\omega_b = 2\pi 500$). (a) $t = \tau_c^* = 1.06\tau_c = 0.68s$, $L_1 = 0.01/s$ corresponding to about 0.68 atom loss, (b) $t = 2\tau_c^*$, about 1.34 atom loss. No other effect is included. 5000 samples.

$$\dot{\rho} = -\frac{i}{\hbar}[\hat{\mathscr{H}}, \rho] + \sum_i (\hat{R}_i \rho \hat{R}_i^\dagger - \frac{1}{2}\hat{R}_i^\dagger \hat{R}_i \rho - \frac{1}{2}\rho \hat{R}_i^\dagger \hat{R}_i) \tag{4.38}$$

where ρ is the density operator, $\hat{\mathscr{H}}$ is the Hamiltonian of the system, $\hat{R}$ is the Lindblad operator for the loss channel in question, and the summation is over the different loss channels. In the main text, the 2-body loss is assumed to be zero and 3-body loss is much lower than the 1-body loss (see Fig. 3) in the regime considered. Therefore, only 1-body loss will be considered below to simplify the calculation. The loss atoms from the large component causes a change in N. The resulting effects are similar to the fluctuations in N considered in the previous section. Here we therefore focus on the small component. In this case one can effectively describe the system by the density operator $\rho = |\chi(t)\rangle\langle\chi(t)|$, with the initial state $|\chi(t=0)\rangle = |\alpha\rangle = \sum c_n |n\rangle$. Only one Lindblad operator $\hat{R} = \sqrt{L_1}\hat{a}$ is needed. The simplified master equation is:

$$\dot{\rho} = -\frac{i}{\hbar}[\hat{\mathscr{H}}, \rho] + L_1(\hat{a}\rho\hat{a}^\dagger - \frac{1}{2}\hat{a}^\dagger\hat{a}\rho - \frac{1}{2}\rho\hat{a}^\dagger\hat{a}) \tag{4.39}$$

with the Hamiltonian given by Eq. (4.8). The method used to simulate the system is the Quantum Jump Method [185, 186]. The results are shown in Fig. 4.12. For the standard Kerr effect without

higher-order terms, it can be observed that the creation of spin cat state still results in two clear peaks in the Q-function even when 2.5 atoms are lost on average. In fact, the cat state is still visible even for an average loss of 5 atoms. However, for the detection scheme, the system is required to evolve for $2\tau_c$, which limits the loss rate to $L_1\tau_c < 0.025$ as shown in the figure. For the parameters used in Fig. 2b in the main text (including higher-order nonlinearities), the average number of atoms lost is only 0.68 and the effect of the loss is small, see Fig. 4.13. The main effect of the loss is a fairly uniform background ring in the Q function.

4.17 Appendix I: Comparison with photon-photon gate proposal

Ref. [160] utilizes a similar collision induced cross-Kerr nonlinearity in BEC to implement photon-photon gates, while the current scheme uses a self-Kerr nonlinearity to create spin cat states. The Kerr effect in the previous scheme is enhanced by increasing both scattering length (through a Feshbach resonance) and the trapping frequency for both components. However, the Feshbach resonance induced atom loss can be very large [69], which will limit the maximum cat size. Not relying on a Feshbach resonance also makes it possible to use the magnetic field to further eliminate atom loss. Also, both trapping frequencies should not be increased at the same time because it will result in high atom loss through the collision with the main BEC. Instead, we suggest here to increase only the trapping frequency of small component. This results in a similarly strong Kerr effect, but with lower atom loss.

Moreover, the treatment in the previous paper, which used the quantized mean-field GPE with TFA and first order perturbation theory, does not allow the study of higher order nonlinearities or atom number fluctuations. Our present approach allows us to study both of these effects, and we show that they can be significant. The assumption of equal trapping frequencies also limits the previous treatment to the non-phase separated regime, which limits the choice of regimes with low atom loss, such as the sodium atom example used here. Furthermore, the density of the stored component in the previous scheme is much smaller (about four orders of magnitude) than the main

component. This raises the concern of other possible dominant effects on the same scale, such as quantum depletion [176]. As we have shown, these problem can be minimized in the current scheme by using a high enough ω_b so that the small component is located at the center with high density. Note that Eq. (4.23), which is obtained as a limiting case for high ω_b here, is basically equivalent to the results of the treatment in Ref. [160].

Chapter 5

Matter-wave mediated hopping in ultracold atoms: Chimera patterns in conservative systems

5.1 Preface

Physical systems can often be well described by instantaneous nonlocal theories, such as gravitational and Coulomb interactions, when the dynamics of the mediating field is orders of magnitude faster. Based on the same principle, here, I propose a new mediating mechanism that can achieve nonlocal spatial hopping for particles in systems with two inter-convertible states and very different time scales. Adiabatically eliminating the fast component results in an effective hopping model with independently adjustable nonlinearity, hopping strength and range. I show that the model can be implemented in Bose-Einstein Condensates mediated by matter waves with current technology. The results further show that the nonlocal hopping can result in non-trivial dynamical patterns known as chimera states, characterized by coexisting regions of phase coherence and incoherence. My analysis shows that chimera patterns can be observed in Bose-Einstein Condensates including the mean-field limit, hence, presenting the first known evidence of conservative Hamiltonian systems exhibiting chimera patterns.

This whole chapter contains my original work. I was attempting to find an analogue mechanism of diffusive coupling in BECs, as well as the existence of chimera patterns in BECs. With encouragement and guidance from both Prof. Simon and Prof. Davidsen, I was able to find the answers to the question.

5.2 Introduction

Locality is one of the basic principles of physics, which constrains the finite speed propagation of all perturbations and information. Despite this fact, a wide range of physical systems can be accurately and conveniently described by the instantaneous nonlocal coupling such as magnetic dipole interaction [187], Rydberg excitation [188], cavity-mediated coupling [71], and recent proposal for tunable long-range interaction [189, 190] mediated by light. The picture of particle-field-particle interaction can be reduced to an effective nonlocal particle-particle description when the mediating field has a much faster time scale such that the state, motion, and separation of the particles can be treated as constant.

Here, I introduce a new mediating mechanism to achieve the nonlocal spatial hopping, in which particles can jump not only to its nearest neighbor sites, such as Bose-Hubbard model [104, 190, 191], but much further away directly. This is possible if the particles can be converted into a mediating channel experiencing no energy barrier between the neighboring sites as shown Fig. 5.1a. Mathematically, the channel can be eliminated adiabatically, resulting in the nonlocal hopping model (NLHM) with independently adjustable on-site interaction, hopping strength, and hopping range. The mechanism is inspired by the diffusive coupling [6], but all physical process are required to be coherent. As far as we know, the mechanism and realization are not yet known.

The new length scale of hopping radius, as we show, can result in a non-trivial dynamical pattern with the phase coherent and incoherent region coexisting in the same state, generally known as chimera states [5, 126]. This pattern can appear in laser arrays, chemical reactions, mechanical, electronic, and neural networks. It is the result of the interplay between nonlinearity and nonlocal couplings, with nonlocal Kuramoto model as the representative model. Only few chimera patterns have been observed in experiments only recently [23, 21, 24], and they are less physical relevant. Though the Hamiltonian of Kuramoto model is known recently [192], no Hamiltonian showing chimera patterns are known. Here, we show three such Hamiltonians exhibiting chimera patterns. In particular, we show the existence of chimera core pattern composing incoherent cores near

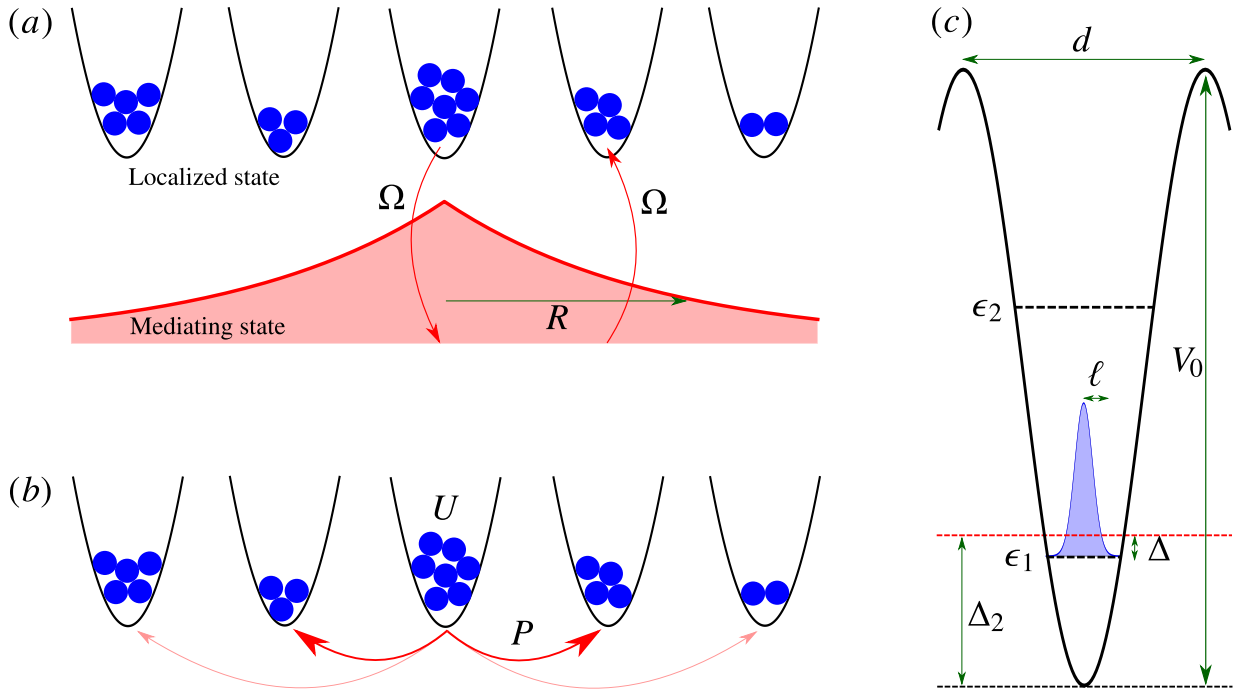

Figure 5.1: Illustration of nonlocal hopping. (a) Two-components model. Particles in traps are confined so there are no spatial dynamics. Localized particles can be converted into the mediating channel that can propagate freely. It is eventually converted back to the nearby sites. (b) Effective model. If the time scale of the mediating state is much faster than trapped state, the mediating component can be eliminated adiabatically and the hopping can be considered to be instantaneous and nonlocal with range R. (c) Periodic lattice with spacing d and depth V_0. Trapped bosonic particles can be described by the ground state wavefunction with width ℓ and energy ε_1 (with energy gap $\varepsilon_2 - \varepsilon_1$). The hopping strength P and the hopping radius R can be controlled by the Rabi frequency Ω and detuning $\Delta = \Delta_2 - \varepsilon_1$.

the spatial phase singularity in the coherent background [7, 18, 8], and properties unique to the Hamiltonian system.

The physically realizable implementation we propose is based on the two components inter-convertible Bose-Einstein Condensate (BEC) [9] in a spin-dependent trap [193], which is inspired by Ref. [104] of the Bose-Hubbard model in cold atoms. In this setup, the atomic hopping process is mediated by the matter wave itself in a way that the trapped component is isolated, while the untrapped component is treated as the mediating channel, as illustrated in Fig. 5.1. This spatial hopping is originated from the spreading in Schrödinger equation. Implementation in BECs has the advantage of studying both quantum and classical regimes, and high controllability of almost all

parameters to a certain degree [85, 64]. For example, loss is important issue for general quantum system [12] and limits the lifetime of system which turns out to limit the hopping range as we show. It may be reduced by lowering the density and Feshbach resonance [69] which can change both the nonlinear interaction and loss. We conclude that nonlocal hopping exists, and chimera patterns may be observed within certain parameter regimes.

5.3 Nonlocal hopping

The Hamiltonian of the NLHM is

$$\mathscr{H} \quad = \mathscr{U} + \mathscr{P} = \quad \frac{U}{2}\sum_i |a_i|^4 - P\sum_{i,j} G_{ij} a_i^* a_j \tag{5.1}$$

where $a_i = \sqrt{n_i}e^{i\theta_i}$ is a complex number representing the state of site i with the number of particle $n_i = |a_i|^2$ and the phase θ_i. $\mathscr{U}$ is the nonlinear energy with the on-site nonlinear interaction U, and $\mathscr{P}$ is the hopping energy with the hopping strength P. G_{ij} is the hopping kernel describing the hopping from site $\mathbf{r}_j$ to $\mathbf{r}_i$, with $G_{ij} = G_{ji}$ and normalization $\sum_j G_{ij} = 1$. In typical physical systems, G_{ij} decreases as the distance $|\mathbf{r}_j - \mathbf{r}_i|$ increases and may be characteristic by a hopping range R. For sufficiently small R, the hopping effectively becomes nearest neighbor. This Hamiltonian can also be expressed in the canonical coordinate and momentum $\{q_i, p_i\}$, as well as action and angle variable $\{n_i, \theta_i\}$ (see Appendix). The later one should be more suitable for the study of phase dynamics. Note that hopping is quadratic $a_i^* a_j$ in the Hamiltonian which is different from the usual quartic term of the particle-particle interaction $n_i n_j$ for, say, Coulomb interaction. Therefore, the corresponding dynamical equation contains the lowest order on-site nonlinearity and the nonlocal linear term:

$$i\hbar\dot{a}_i = U|a_i|^2 a_i - P\sum_j G_{ij} a_j \tag{5.2}$$

The nearest-neighbor variation of this equation is the discrete Gross-Pitaevskii equation [194] and the non-spatial variation is the discrete self-trapping equation [195].

Table 5.1: Hopping kernel $G_D(r)$ (to be normalized) with $r = |\mathbf{r}_j - \mathbf{r}_i|$ in D dimension. K_0 is the modified Bessel function of the second kind.

D	1	2	3
$G_D(r)$	$e^{-r/R}$	$K_0(r/R)$	$\frac{1}{r}e^{-r/R}$

5.4 Mediating mechanism

The simplest model captured the concepts of mediating channel in Fig. 5.1a takes the following form:

$$i\hbar\dot{\psi}_1(\mathbf{r},t) = U|\psi_1|^2\psi_1 + \hbar\Omega\psi_2 \tag{5.3}$$

$$i\hbar\dot{\psi}_2(\mathbf{r},t) = -\hbar\kappa\nabla^2\psi_2 + \hbar\Omega\psi_1 + \hbar\Delta\psi_2 \tag{5.4}$$

for the localized ψ_1 and mediating ψ_2 component respectively. Eq. (5.3) describes a localized component with nonlinear interaction U and Rabi frequency Ω for Rabi oscillation, which is a coherent conversion that conserves the particle numbers. Eq. (5.4) describes the mediating channel with inverse mass $\kappa = \hbar/(2m)$ and detuning Δ from the localized component. It is essentially the Schrdinger equation with a coherent conversion, so the spatial propagation is originated from the kinetic energy term. The additional detuning in the far-detuned regime $|\Delta| \gg |\Omega|$ ensures the mediating idea is well-defined: Number of particles $N_k = \int d\mathbf{r}|\psi_k|^2$ in the mediating channel $N_2 \ll N_1 \approx N$ can be neglected.

Suppose ψ_1 evolves much slower than ψ_2, then the adiabatic elimination can be used by setting $\dot{\psi}_2 = 0$ [196]. The solution of $-\kappa\nabla^2\psi_2 + \Omega\psi_1 + \Delta\psi_2 = 0$ in the unbounded isotropic space with translation invariant [6] is given by the convolution $\psi_2(\mathbf{r},t) = -(\Omega/\Delta)G_D(\mathbf{r}) * \psi_1(\mathbf{r},t)$ where $G_D(\mathbf{r})$ is the hopping kernels listed in Table 5.1, with hopping radius $R = \sqrt{\kappa/\Delta}$. Note that $\Delta > 0$ is required for the confined hopping kernels solution (see mediating state in Fig. 5.1a, while $\Delta < 0$ leads to a wave-like solution). Substituting this solution back to Eq. (5.3), we can get the continuum NLHM where the summation is replaced by integral with hopping strength $P = \hbar\Omega^2/\Delta$.

5.5 Implementation in ultracold atomic systems

The kinetic energy term in Eq. (5.3) cannot be ignored typically because coherent inter-convertible particles usually have the same mass m. Instead, the effective mass can be increased by using a periodic lattice. This can be done in ultracold atomic systems where the particles are forced to be localized with a sufficiently deep trap, described by:

$$i\hbar\dot{\psi}_1(\mathbf{r},t) = \left(-\hbar\kappa\nabla^2 + V_1 + g_{11}|\psi_1|^2\right)\psi_1 + \hbar\Omega\psi_2 \tag{5.5}$$

$$i\hbar\dot{\psi}_2(\mathbf{r},t) = \left(-\hbar\kappa\nabla^2 + \hbar\Delta_2\right)\psi_2 + \hbar\Omega\psi_1 \tag{5.6}$$

for the localized ψ_1 and mediating ψ_2 component respectively, where g_{ij} $(i,j=1,2)$ are the two particles collision constant. Here, we assume $g_{22} = g_{12} = 0$. V_i is the spin-dependent potential [193], with V_1 periodic and $V_2 = 0$. Even though it is similar to Eq. (5.18) with the extra kinetic and potential energy term, solving it is not straightforward because adiabatic elimination fails to work in the general form of Eq. (5.18). It is because the high energy level $\varepsilon_{i>1}$ is not evolving slowly comparing with the mediating component, and large $\Delta = \Delta_2 - \varepsilon_1$ can resonate with high energy level. This can be solved by confining the system to the local ground state ε_1 and suitable detuning $\varepsilon_2 - \varepsilon_1 \gg \Delta \gg |\Omega|$ as shown in Fig. 5.11c. Under these constraints, we can show that Eq. (5.18) and (5.19) reduce to the exact form of Eq. (5.2) with $P = \hbar\Omega^2/\Delta$, hopping kernel $G_D(r)$ in Table 5.1 and

$$R = C_D\left(\frac{d}{2\ell}\right)^{\frac{D}{2}}\sqrt{\frac{\kappa}{\Delta}} \tag{5.7}$$

where C_D is a constant (see Appendix for the proof). Since the effective conversion region has a characteristic length scale 2ℓ in a lattice units with length d, so scaling with $2\ell/d$ is expected when $d \gg 2\ell$. Indeed, we have the effective scaling $\Delta \to \Delta_{eff} = (2\ell/d)^D\Delta$. In this picture, a_i is the state variable of the localized wavepacket at site i. Hence, the kernel G_{ij} describes the matter-wave mediated hopping by annihilating a wavepacket at site j and creating a wavepacket at site i.

By further assuming the trapping potential to be sinusoidal $V_1(x) = V_0\sum_\sigma \sin^2(kx_\sigma)$ with wavelength λ, wavenumber $k = 2\pi/\lambda$, lattice spacing $d = \lambda/2$ and trap depth V_0. For sufficiently large

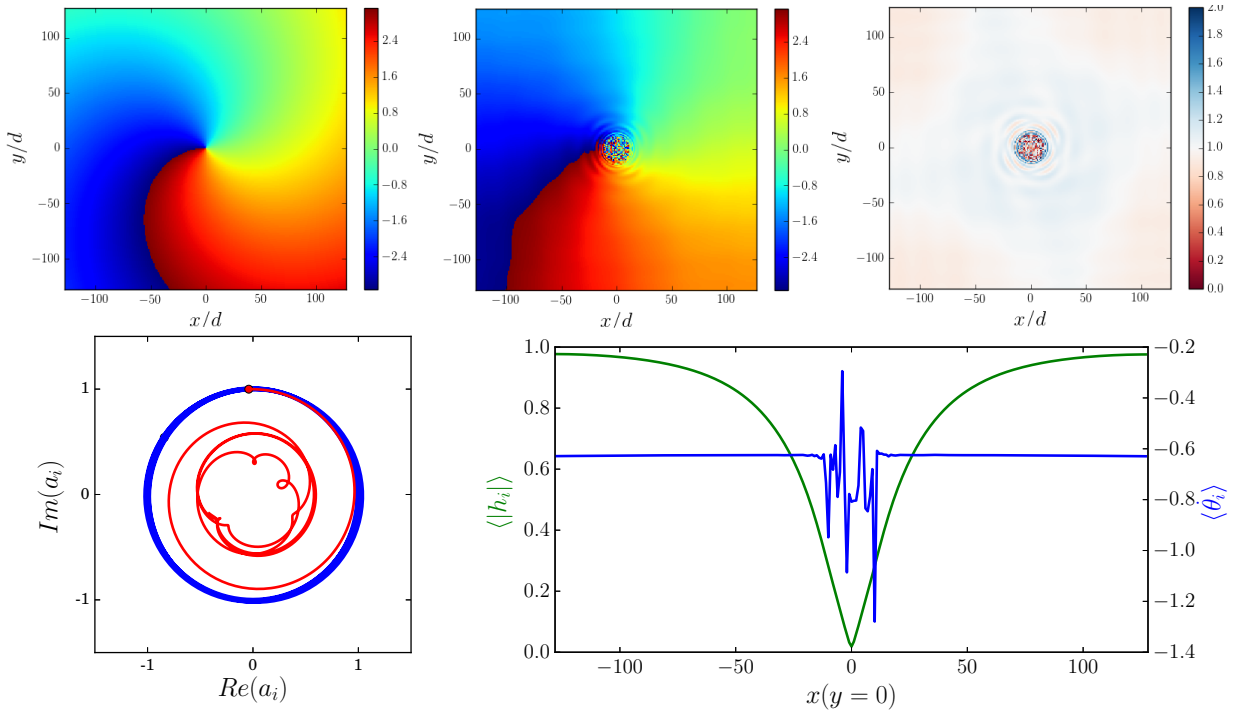

Figure 5.2: Chimera patterns in Hamiltonian system of NLHM. (a) Initial phase distribution with uniform density. (b) Phase $\theta_i(t = 100)$ over the 2D lattice. (c) Number of particle $n_i = |a_i|^2$ corresponds to (b). (d) Local phase space trajectory for $x = -100$ (blue) and $x = -4$ (red) at the cut $y = 0$. (e) Average hopping $\langle|h_i|\rangle$ and average angular $\langle\theta_i\rangle$ over time at the cut y=0. Hopping strength $P/Un_0 = 0.4$ with hopping radius $R = 16d$ after time $Un_0t = 100$.

V_0, the local ground states around trap minima can be approximated by a Gaussian $\phi_\sigma(x_\sigma) = e^{-\pi x^2/(2\ell_\sigma^2)}/\sqrt{\ell_\sigma}$ with $\ell_\sigma = \sqrt{\pi\hbar/(m\omega_\sigma)}$. In this setting, the nonlinearity is enhanced by the density as $U = g_{11}/V_{eff}$ with effective volume $V_{eff} = 2^{3/2}\ell_x\ell_y\ell_z$, and numerical fitting gives $C_D \approx 1$ (see Appendix).

5.6 Dynamics and chimera patterns

Here, we focus on the regime with simultaneous weak hopping $P \ll Un_0$ and long hopping range $R \gg d$, where n_0 is the average number of particles per site. This introduces a new length scale R to system which may show different dynamics [7, 6]. Starting from the initial condition (IC) of spiral phase as shown in Fig. 5.2a with uniform $n_i = n_0$ (see Appendix), the system evolves according to Eq. (5.1) into a state with phase incoherent near the center but coherent far away as shown in

Fig. 5.2b and 5.2c (see Appendix). The same pattern also exist with different IC such as a vortex with random phase near center (see Appendix). Also, when the hopping changes to the nearest neighbor, this localized disturbance quickly spreads and interferes with each other (see Appendix). It suggests the random core is a stable localized pattern. Moreover, the dynamics near the core are significantly different from the coherent background which is clear in Fig. 5.2d of the local phase space trajectories (more in Appendix). a_i is regular at the point far from the core, but is irregular near the core. Furthermore, the system is also scale invariant with a given R/L and the random core scales linear as R [134] (see Appendix). These results are similar to what is known about chimera cores, which exists in system with on-site nonlinearity for self-sustaining oscillators and diffusive coupling through nonlocal linear term [4, 7, 6, 134, 5]. In contrast, the mean angular frequency $\langle \dot{\theta}_i \rangle$ of undamped oscillators here are not regular, see 5.2d. On the other hand, the hopping term $h_i = \sum_j G_{ij} a_j$ is expected to have $h_i \approx 0$ near the center because of the randomness. Moreover, h_i is smooth for the spiral initial condition.

As a conservative Hamiltonian system, NLHM describes a closed system with both energy and the particle number $N = \sum_i n_i$ conserved, and display chimera properties. Also, the system has time reversal symmetry. These lead to persistent fluctuations or ripples as observed in 5.2 which would damp away in dissipative system quickly. In addition, the results of the backward time evolution of the core region is very delicate. With a small perturbation, the background can evolve back to nearly the same states at t = 0, but the core remain incoherent, which again signify the difference between two regions (see Appendix) In a realistic system, nonlinear loss can appear in a system which can be modeled by $U \to U - iU_{loss}$. As the simulation results suggest, chimera patterns can still be observed even with $U_{loss}/U = 0.02$ at $Un_0t = 100$.

5.7 Experimental settings

There are certain criteria that need to be satisfied by experiments in order to have a system described by NLHM. To summarize, these include the far detuning regime $\Delta \gg \Omega$ for the small

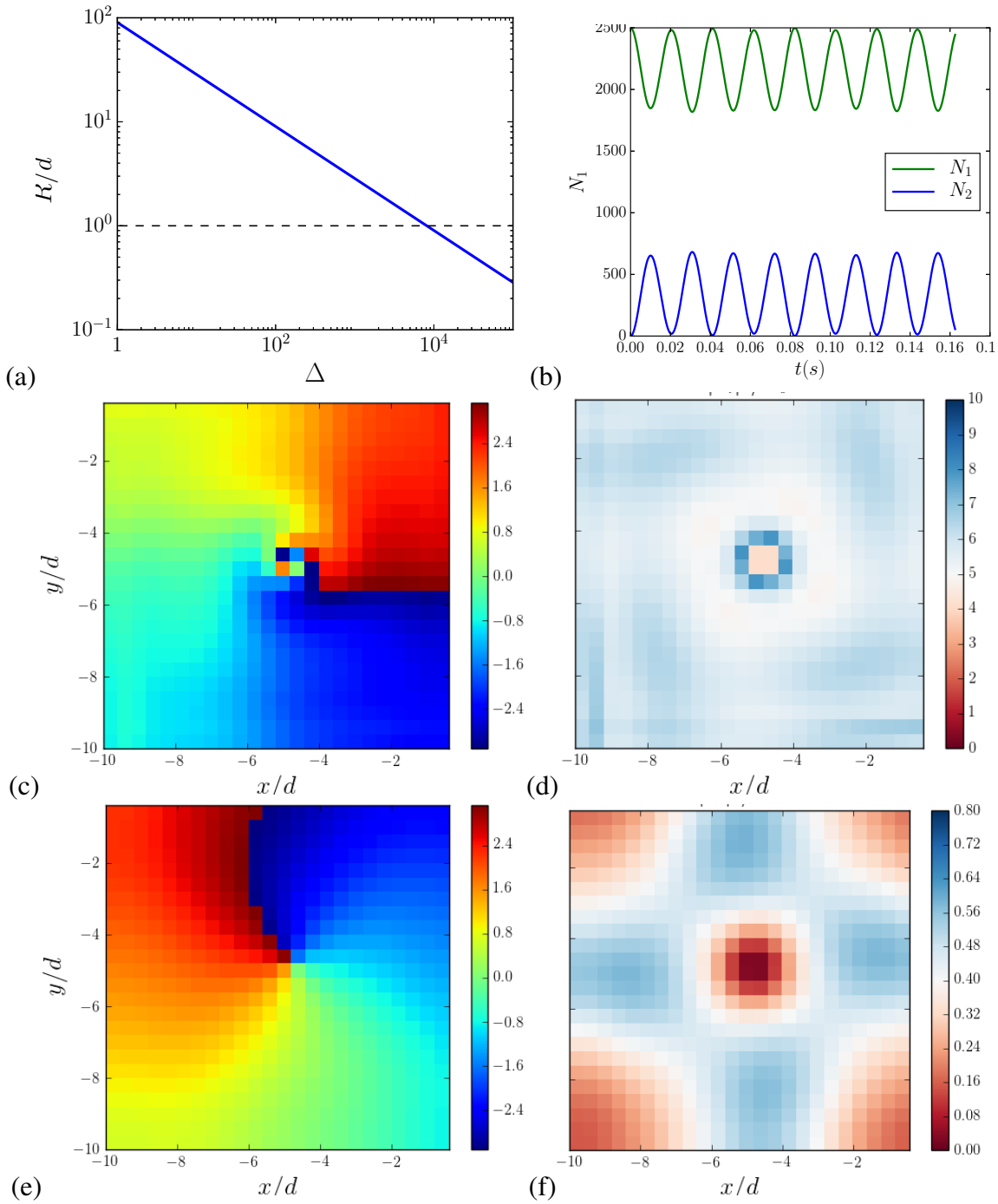

Figure 5.3: Chimera patterns in BEC. (a) Hopping radius R vs detuning Δ for ^{87}Rb with hyperfine states $|F=1,m_F=-1\rangle$, $|F=1,m_F=0\rangle$, optical lattice with $s=40$ and $\lambda=790$nm which gives $d=395$nm and $\ell_x=\ell_y=0.22d$. (b) Number of atoms in both components starting with an initial spiral (see Appendix). (c-f) State at $t=200ms$. (c) Phase and (d) density of localized component. (e) Phase and (f) density of mediating component. Loss is not included in the simulation and the lifetime is $\tau=1.4$s. Other parameters are $n_i(t=0)=10$, $\Delta=2\pi\times 64$Hz, $\Omega=2\pi\times 16$Hz, $g_{11}/\hbar=50\mu m^3/$s, $\ell_z=50\ell_x$, with predicted $Un_0/\hbar\approx 2\pi\times 24$Hz, $P=2\pi\times 16$Hz and $R\approx 5d$. No-flux condition.

number of particles in ψ_2, and $\Delta \ll \varepsilon_2 - \varepsilon_1$ to prevent excitation. A good adiabatic elimination needs a slow varying time scale for the localized component $\hbar\Delta \gg Un_0, P$ assuming all $n_i \sim n_0$. In addition, $R > d$ for the hopping to be considered nonlocal. All of Ω, Δ, U can be adjusted easily in experiments, so does P. Also, theoretically, $R \sim \Delta^{-1/2}$ can be arbitrary large by having particles staying in the mediating channel for long time. Therefore, the actual upper bound of R is set by the experimental lifetime τ and duration. Considering sufficiently deep optical dipole lattice with $s = 40$ (expressing $V_0 = sE_R$ in recoil energy $E_R = \hbar\kappa k^2$) so that the direct hopping can be ignored [104], the range of mediated hopping radius R for Rubidium is shown in Fig. 5.3a. Note that the lower bound of R is determined by the energy gap $\Delta \ll \omega = 2\pi \times 46$kHz.

The regime with competitive $P \sim Un_0$ is the most interesting. However, a BEC in 3D optical lattice is naturally in the very strong nonlinearity regime $Un_0 \gg P$, which is $U/\hbar = 2\pi \times 2.23$kHz with $g_{11} = 4\pi\hbar^2 a_{11}/m$ and natural s-wave scattering length a_{11}. It can be reduced by the use of both low density and Feshbach resonance, which can be adjusted by many orders of magnitude of a_{11} in experiments [69]. The former method is preferable to be used before the latter one because it can decrease both nonlinearity and two-particles collision loss at the same time. For a given λ, decreasing density cannot be done in 3D optical lattices. However, in a lower dimension, the non-lattice dimension (z-axis in our setting) can be weakly trapped to reduce the density, resulting in a lattice of cigarette shape wavefunction [92, 197]. The dominant loss is the two-particle loss in the localized component which gives an estimated $U_{loss} = \hbar L_{11}/V_{eff}$ and $\tau_{loss} = V_{eff}/L_{11}$ with a L_{11} two-particles loss rate (see Appendix) [12], so increasing ℓ_z can improve lifetime $\tau_{loss} \sim \ell_z$ in 2D.

The derivation of effective models implies that chimera patterns can also be observed in certain parameter regimes for NLHM and the Eqs. (5.2) and (5.3-5.4) (see Appendix). The problem is if such parameter regimes can be achieved experimentally. One such experimentally feasible regime has been identified as shown in Fig. 5.3. Nonlocal hopping induced chimera patterns can be observed, which are the results of full simulation of realistic Eqs. (5.18)-(5.19). With 10 atoms on

average, each site can be well described by amplitude and phase. The initial state can be prepared from a uniform BEC, with V_1 adiabatically turned on until the direct hopping is suppressed and taken over by mediated hopping. A short light pulse induced energy shift can then be used to create any desire initial phase, which is a spiral for Fig. 5.3. The system states and dynamics can be detected by standard time of flight technique [78], matter wave interference [198] or optical readout. As it is clear from simulations that random cores appear eventually. Similar patterns still exist even when the experimental time is longer than the lifetime, suggesting that chimera patterns should be observable in BEC.

5.8 Discussion and outlook

In brief, a new mediating mechanism of nonlocal spatial hopping is introduced, and the realization details in BEC with the current technology is given. All calculations are based on classical Hamiltonians. Since all the physical mechanism chosen are coherent, and conserve energy and particles, so the mediated hopping can happen in the quantum regime. Mathematically, all Hamiltonians and dynamic equations can be quantized, and Eq. (5.1) becomes Bose-Hubbard model with mediated hopping. At the single particle level, the loss problem is less important so the hopping range can be even larger and even global hopping when system size is less than R. Chimera patterns in open quantum system have been studied recently [199], and our results suggest the possibility that chimera patterns may even exist in closed quantum systems, which requires a better understanding of quantum synchronization [124, 200, 125]. Nonetheless, the correctness of our mean-field prediction of chimera patterns in ultracold atoms can be justified by the existence of slight loss, which causes the system to follow the classical trajectory [43]. The experimental technique can generalize the Bose-Hubbard model with tunable hopping from nearest-neighbor to infinite-range, which opens the door for the exploration of the new exotic condensed matter states similar to other long range effects [201]. We hope that the work here motivates further studies on the nonlocal hopping both experimentally and theoretically.

5.9 Appendix A: Hamiltonians

The Hamiltonian of the nonlocal hopping model (NLHM) is

$$H = \frac{U}{2}\sum_i |a_i|^4 - P\sum_{i,j} G_{ji} a_i^* a_j \tag{5.8}$$

which can be represented in few different canonical variables under different transformations (see [192, 202]). We can define the canonical coordinates and momenta to be q_i and p_i:

$$a_i = \frac{1}{\sqrt{2}}(q_i + ip_i) \tag{5.9}$$

$$a_i^* = \frac{1}{\sqrt{2}}(q_i - ip_i) \tag{5.10}$$

Hence, in the canonical coordinate and momentum $\{q_i, p_i\}$ system:

$$H = \frac{U}{8}\sum_i \left(q_i^2 + p_i^2\right)^2 - \frac{1}{2}P\sum_{i,j} G_{i,j}(q_i q_j + p_i p_j) \tag{5.11}$$

Similarly, we can define action n_i and angle θ_i such that $a_i = \sqrt{n_i}e^{i\theta_i}$, or

$$n_i = \frac{1}{2}\left(q_i^2 + p_i^2\right) \tag{5.12}$$

$$\theta_i = \tan^{-1}\left(p_i/q_i\right) \tag{5.13}$$

Hence, in the action-angle $\{n_i, \theta_i\}$ coordinate system:

$$H = \frac{U}{2}\sum_i n_i^2 - P\sum_{i,j} G_{i,j}\sqrt{n_i n_j}\cos(\theta_j - \theta_i) \tag{5.14}$$

Note that action n_ℓ can be interpret as the number of particles. The conservation of the total number of particles can be expressed as the constancy of the quantities $\sum_i |a_i|^2$, $\sum_i \left(q_i^2 + p_i^2\right)$ and $\sum_i n_i$. The energy is conserved as there are no explicit time dependence. Lastly, the global phase is irrelevant here, so the Hamiltonian is invariant under any global phase rotation $a_i \to a_i e^{i\theta_0}$.

In the continuum limit, such as the result from the simplified two-components model in the main text, the corresponding Hamiltonian can be obtained by replacing $a_i \to \psi(\mathbf{r})$, $\sum_i \to \int d\mathbf{r}$,

$\sum_{i,j} \to \int\int d\mathbf{r}d\mathbf{r}'$ and $G_{i,j} \to G(\mathbf{r},\mathbf{r}')$. Explicitly, those Hamiltonians become:

$$H = \frac{U}{2}\int d\mathbf{r}|\psi(\mathbf{r})|^4 - P\int\int d\mathbf{r}d\mathbf{r}'G(\mathbf{r},\mathbf{r}')\psi^*(\mathbf{r})\psi(\mathbf{r}') \quad (5.15)$$

$$H = \frac{U}{8}\int d\mathbf{r}\left(q(\mathbf{r})^2+p(\mathbf{r})^2\right)^2 - \frac{1}{2}P\int\int d\mathbf{r}d\mathbf{r}'G(\mathbf{r},\mathbf{r}')(q(\mathbf{r})q(\mathbf{r}')+p(\mathbf{r})p(\mathbf{r}')) \quad (5.16)$$

$$H = \frac{U}{2}\int d\mathbf{r}n(\mathbf{r})^2 - P\int\int d\mathbf{r}d\mathbf{r}'G(\mathbf{r},\mathbf{r}')\sqrt{n(\mathbf{r})n(\mathbf{r}')}\cos(\theta(\mathbf{r}')-\theta(\mathbf{r})) \quad (5.17)$$

5.10 Appendix B: Ultracold atom with periodic lattice

Starting from the equations describing the ultracold atomic system:

$$i\hbar\dot{\psi}_1(\mathbf{r},t) = \left(-\hbar\kappa\nabla^2 + V_1 + g_{11}|\psi_1|^2\right)\psi_1 + \hbar\Omega\psi_2 \quad (5.18)$$

$$i\hbar\dot{\psi}_2(\mathbf{r},t) = \left(-\hbar\kappa\nabla^2 + \hbar\Delta_2\right)\psi_2 + \hbar\Omega\psi_1 \quad (5.19)$$

Note that the reference energy is arbitrary, but it is well known that the adiabatic elimination works best when the first component evolves the slowest [196]. No such choice exists in the general form of Eq. (5.18), but it exists when we confine the dynamic to the ground state of individual traps.

There are no simultaneously good basis for both equation, though, the good basis for the localized and mediating equation are the Wannier basis and Fourier basis respectively. For the resonance dynamics, it is easier to understand in the Wannier basis [104] which are the orthonormal basis $\{w_{mn}(\mathbf{r})\}$ for the equation $\varepsilon_{mn}w_{mn}(\mathbf{r}) = -\hbar\kappa\nabla^2 w_{mn} + V_1 w_{mn}$ with periodic potential V_1, where n is the energy band index and m is the lattice site index. In this new basis, the wavefunctions are represented by $\psi_1(\mathbf{r},t) = \sum_{mn} a_{mn}(t)w_{mn}(\mathbf{r})$ and $\psi_2(\mathbf{r},t) = \sum_{mn} b_{mn}(t)w_{mn}(\mathbf{r})$ respectively. Substituting back to Eq. (5.18) and (5.19), we have

$$i\hbar\dot{a}_{mn}(t) = \varepsilon_{mn}a_{mn} + U|a_{mn}|^2 a_{mn} + \hbar\Omega b_{mn} \quad (5.20)$$

$$i\hbar\dot{b}_{mn}(t) = \hbar\sum_{kl} c_{mnkl}b_{kl} + \hbar\Delta_2 b_{mn} + \hbar\Omega a_{mn} \quad (5.21)$$

where

$$\begin{aligned}
\varepsilon_{mn} &= \int_V d\mathbf{r}\left(\hbar\kappa|\nabla w_{mn}|^2 + V_1|w_{mn}|^2\right) && (5.22)\\
U &= g_{11}\int_V d\mathbf{r}|w_{mn}|^4 && (5.23)\\
c_{mnkl} &= \kappa\int_V d\mathbf{r}\nabla w^*_{mn}(\mathbf{r})\nabla w_{kl}(\mathbf{r}) && (5.24)
\end{aligned}$$

In a periodic lattice V_1, the eigenenergy $\varepsilon_{m1} = \varepsilon_0$ is a constant in the lowest band $n = 1$ if the trap are sufficiently deep or there are no overlap between the Wannier function of the nearest neighbor site. Hence, we can shift the energy $\Delta_2 \to \Delta := \Delta_2 - \varepsilon_0$ using the transformation $a_{mn} \to a_{mn}e^{-i\varepsilon_0 t}$. If the energy gap is large $\varepsilon_{m2} - \varepsilon_{m1} \gg \Delta$, then we can ignore the resonance with the higher band index $n > 1$. Furthermore, suppose initially there are no excited states, i.e. $a_{mn}(t = 0) = 0$ for $n > 1$, then no excited states will be populated because there are no resonance with those states, written explicitly:

$$\begin{aligned}
i\hbar\dot{a}_{m1}(t) &= U|a_{m1}|^2 a_{m1} + \hbar\Omega b_{m1} && (5.25)\\
i\hbar\dot{b}_{m1}(t) &= \hbar\sum_{kl} c_{m1kl}b_{kl} + \hbar\Delta b_{m1} + \hbar\Omega a_{m1} && (5.26)\\
i\hbar\dot{b}_{mn}(t) &= \hbar\sum_{kl} c_{mnkl}b_{kl} \qquad \text{for } n > 1 && (5.27)
\end{aligned}$$

In this form, all important dynamics are captured, and the localized component can be slow relative to the mediating component.

5.11 Appendix C: Hopping Kernel

The adiabatic elimination of the mediating channel can be obtained by setting $\dot{b}_{mn} = 0$. Therefore, we can find the hopping kernel by solving b_{m1} in the following equation

$$\begin{aligned}
0 &= \sum_{kl} c_{m1kl}b_{kl} + \Omega a_{m1} + \Delta b_{m1} && (5.28)\\
0 &= \sum_{kl} c_{mnkl}b_{kl} \qquad \text{for } n > 1
\end{aligned}$$

self-consistently by setting $a_{m1} = 1$ at the center. This draw a direct analogue of finding the continuum hopping kernel $G_D(\mathbf{r})$ as described in the main text by setting $\psi_1(\mathbf{r}) = \delta(\mathbf{r})$. The effective

conversion region have length scale 2σ of the localized package, in each lattice unit with length d. Therefore, it is expected that the only difference for the solution is with the effective scaling $\Delta \to \Delta_{eff} = (2\sigma/d)^D \Delta$. So, the solution is $b_{i1} = \frac{\Omega}{\Delta} G_{ij} * a_{j1}$ and substituting back to first component, we have the hopping strength

$$P = \hbar \frac{\Omega^2}{\Delta} \tag{5.29}$$

and G_{ij} takes the same form in the Table 1 in the main text with discrete normalization, and the effective hopping radius as

$$R = C_D \left(\frac{d}{2\sigma} \right)^{\frac{D}{2}} \sqrt{\frac{\kappa}{\Delta}} \tag{5.30}$$

where D is the dimension and C_D is a constant.

The above result can be verified numerically. For the method to find to hopping kernel in an optical lattice self-consistently, we solve the corresponding time dependent equation and find the equilibrium solution. Hence, Eq. (5.28) with a time splitting method becomes

$$\dot{b}_{m1}(t) = - \Omega a_{m1} - \Delta b_{m1} \tag{5.31}$$

$$\dot{\tilde{\psi}}_2(\mathbf{q},t) = - \frac{\hbar q^2}{2m} \tilde{\psi}_2 \tag{5.32}$$

for the conversion step and propagation step respectively. Both of them have exact solutions and the basis change is preformed between each step. The hopping kernel G_{ij} can be found by setting $a_{m1} = \delta_{mj}$, where j is the source lattice site (chosen to be the center of the lattice), and obtained the equilibrium solution b^*_{i1}, which gives $G_{ij} = b_{i1}$. The Gaussian is used to approximate the lowest band Wannier function as

$$w_{m1}(\mathbf{r}) = \phi(\mathbf{r} - \mathbf{r}_m) \sim e^{-\frac{|\mathbf{r}-\mathbf{r}_m|^2}{2\sigma^2}} \tag{5.33}$$

where σ defines a characteristic length of the Gaussian function. This describes the local ground state that can be approximated by a harmonic oscillator, such as a deep sinusoidal trap. And the transformation between the real space and the Wannier basis are given by

$$b_{m1} = \langle w_{m1}(\mathbf{r}) | \psi_2(\mathbf{r}) \rangle = \int_V d^3\mathbf{r} \phi(\mathbf{r}) \psi_2(\mathbf{r}) \tag{5.34}$$

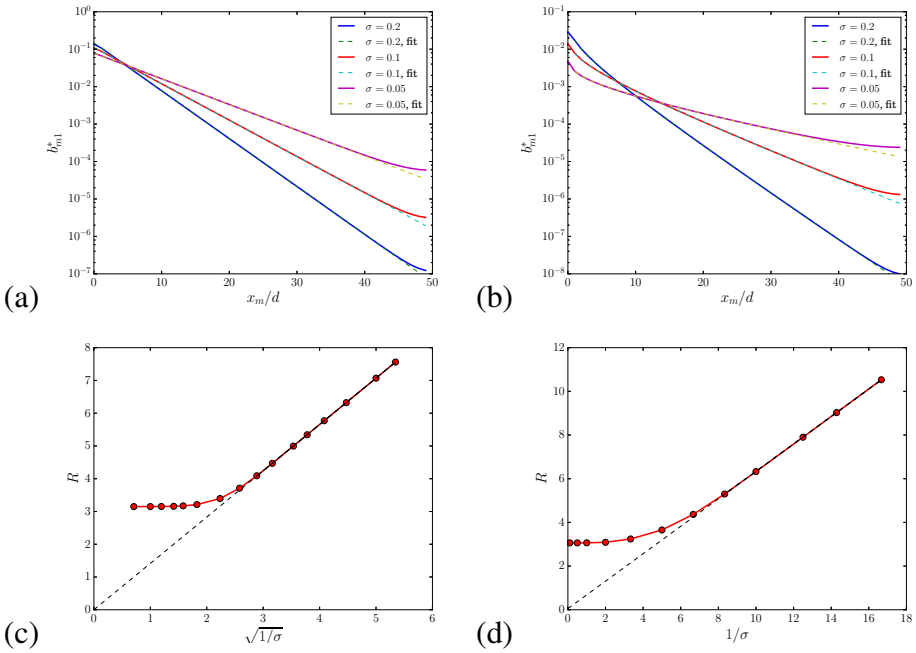

Figure 5.4: Discrete hopping kernel G_{ij}. (a) Comparing $b^*_{m1} \sim G_{mj}$ with exponential fitting in 1D. $\kappa = 100$, $\Omega = 10$, $\Delta = 10$. (b) Comparing b^*_{m1} with K_0 fitting in 2D. (c) The scaling of the of the hopping radius $R \sim \sigma^{-1/2}$ in 1D vs the width of the Gaussian σ. (d) The scaling of the of the hopping radius $R \sim \sigma^{-1}$ in 2D vs the width of the Gaussian σ.

where V is the confined volume around the lattice minimum $[-d/2, d/2]^D$ with a finite cutoff of lattice spacing d.

The numerical results fit perfectly for the kernel $G_D(r)$ as shown in Fig. 5.4. With sufficiently narrow Gaussian $\sigma \ll d$, the predicted hopping radius R fits perfectly with Eq. 5.30.

5.12 Appendix D: Chimera patterns

The dynamic equation of NLHM can be rewritten in the dimensionless form using the rescaling $\tilde{a}_i = a_i/\sqrt{n_0}$, $\tilde{t} = (Un_0/\hbar)t$, and $\tilde{P} = P/(Un_0)$ where n_0 is the average particle number per site. The equation becomes, after dropping the tilde,

$$i\partial_t a_i(t) = |a_i|^2 a_i - P\sum_j G_{ij} a_j \tag{5.35}$$

which depends on the control parameters of rescaled hopping strength $\tilde{P}$ and rescaled hopping radius $\tilde{R} = R/d$. Without the hopping term, the system is decoupled and evolves locally as $a_i(t) =$

$e^{-i|a_i(0)|^2 t} a_i(0)$. The dynamics may be clear if the rotation is eliminated by shifting the reference energy as:

$$i\partial_t a_i(t) = -a_i + |a_i|^2 a_i - P\sum_j G_{ij} a_j \tag{5.36}$$

which gives a solution $a_i(t) = e^{-i(|a_i(0)|^2-1)t} a_i(0)$ with the extra global phase e^{it} when $P = 0$. If the system is uniformly distributed $|a_i(0)|^2 = 1$, then $a_i(t) = a_i(0)$. Hence, the oscillation dynamics can be eliminated in this reference frame, which is used in all simulation for NLHM. The simulation is done in the square lattice with size L with no-flux boundary condition. The numerical method used is the 4-th order Runge-Kutta method.

For the spiral initial condition, uniform density $a_i = \sqrt{n_0}$ is used and the state is given by

$$a_i(t=0) = \sqrt{n_0} e^{i(k_s r - \tan^{-1}(y/x))} \tag{5.37}$$

with $r = \sqrt{x^2+y^2}$ and spiral wavelength k_s. The dynamics is shown in Fig. 5.5. As shown in the figure, the chimera core formed near the spatial phase singularity. This pattern is similar as the system scaled up with R/L fixed as shown in Fig. 5.7 with 4 times larger system. The dynamics outside the core is the same as clear indicated by the ripple near the core, but the core now becomes 4 times larger with random phase. This chimera core pattern can exist with alternative initial condition such as a vortex with a randomized core of size radius R_{rc} as shown in Fig. 5.8. Note that with large k_s, a new pattern of chimera rings in 2D can be formed that surrounds the center core as shown in Fig. 5.10.

The chimera core pattern depends on the nonlocal hopping range $R \gg d$, whose dynamics are very different from $R \sim d$. The difference is very clear when the system starts from the random core vortex with nearest neighbor hopping as shown in Fig. 5.9. The random phase near the core is a highly localized disturbance that are eventually propagating outward and interferes with each other. No localized chimera core pattern appears and the dynamic is different.

The inverse time propagation can go back to the initial condition by reversing the parameters. Using the state in Fig. 5.5f as the initial condition, the system is propagated by the same amount of the time t. As shown in 5.11a, it can perfectly go back to a spiral as expected. The chaotic nature

of the core can be shown by adding a single shot phase noise to the system state in Fig. (5.5)f as a perturbation before the inverting time propagation occurs, given by

$$\theta_i \to \theta_i + \chi_{noise}\xi_i \tag{5.38}$$

where the noise is Gaussian with $\langle \xi_i \rangle = 0$, $\langle Re(\xi_i)Re(\xi_{i'})\rangle = \delta_{i,i'}$, and $\langle Im(\xi_i)Im(\xi_{i'})\rangle = \delta_{i,i'}$, with amplitude χ_{noise}. As shown in Fig. 5.11b and 5.11c, the system cannot go back to the spiral with noise as low as $\chi_{noise} = 10^{-11}$. This suggest that the core regions are very sensitive to the initial condition. This is in stark contrast with the coherent background which has almost the same values as the noiseless case. It indicates that the system behaves differently in the core region and the non-core which is the important property of chimera states.

As shown above, the minimal two-component model can be reduced to the effective NLHM. The accuracy of the parameters mapping is tested and shown in Figs. 5.12 and 5.13 for 1D and 2D system. The results are already very good for the short time scale. The accuracy can be further increases by increasing the detuning Δ, and decreasing the spacing dx.

5.13 Appendix E: Numerical methods

For the full simulation of the BEC in an optical lattice, Eq. (5.18) and (5.19), we use the time-split spectral method for the two components Gross-Pitaevskii equation [203], with a 4-th order time splitting scheme. For the simulation of the effective NLHM, Eq. (5.2), we use the 4-th order Runge-Kutta scheme with a convolution in the Fourier space.

5.13.1 Split method

A two step time split method for the differential equation of the form

$$\dot{\psi} = (\hat{A} + \hat{B})\psi, \tag{5.39}$$

with operator $\hat{A}$ and $\hat{B}$ is given by

$$\psi(\mathbf{r}, t + \Delta t) = e^{b_s \Delta t \hat{B}} e^{a_s \Delta t \hat{A}} \ldots e^{b_1 \Delta t \hat{B}} e^{a_1 \Delta t \hat{A}} \psi(\mathbf{r}, t), \tag{5.40}$$

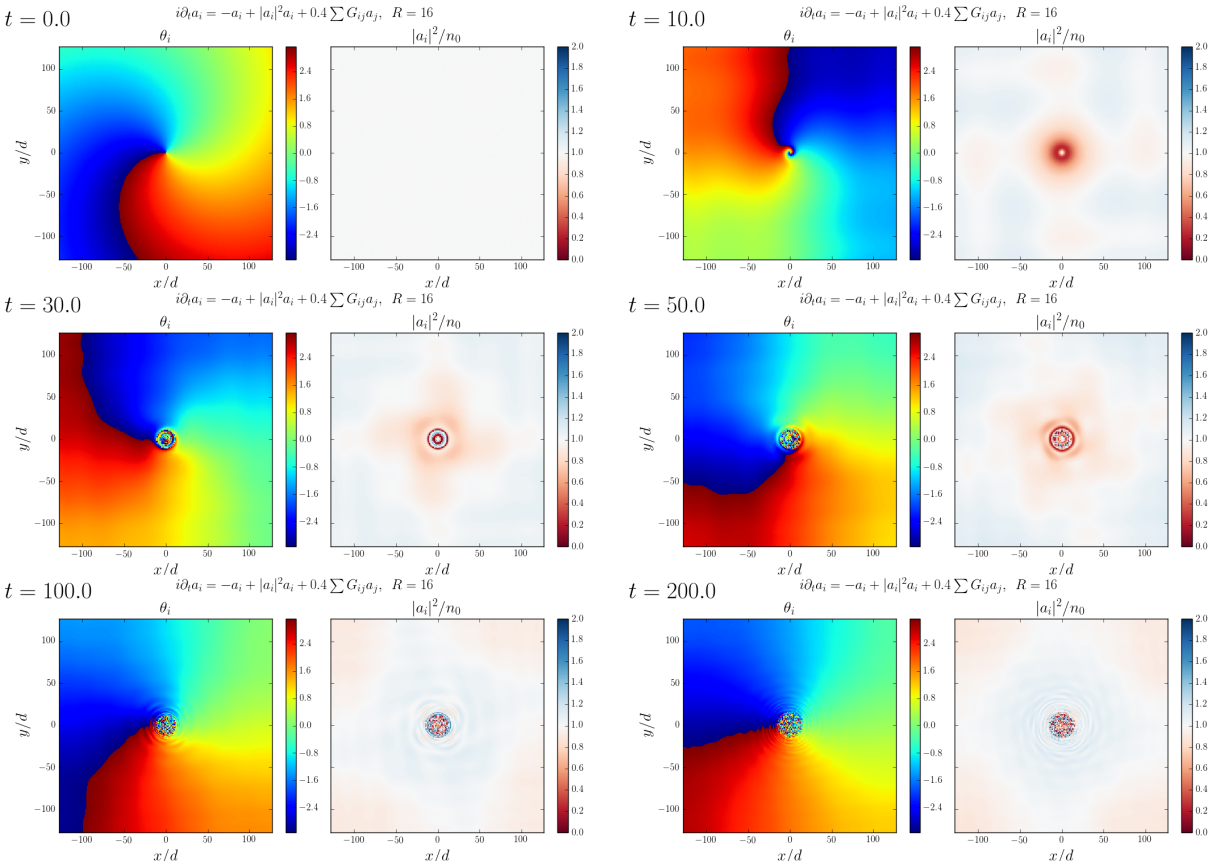

Figure 5.5: Time evolution of initial spiral with spiral wavelength $k_s d = 0.01$ with length $L = 256d$. Nonlocal hopping $P/(Un_0) = 0.4$ and $R = 16d$ in $L = 256d$.

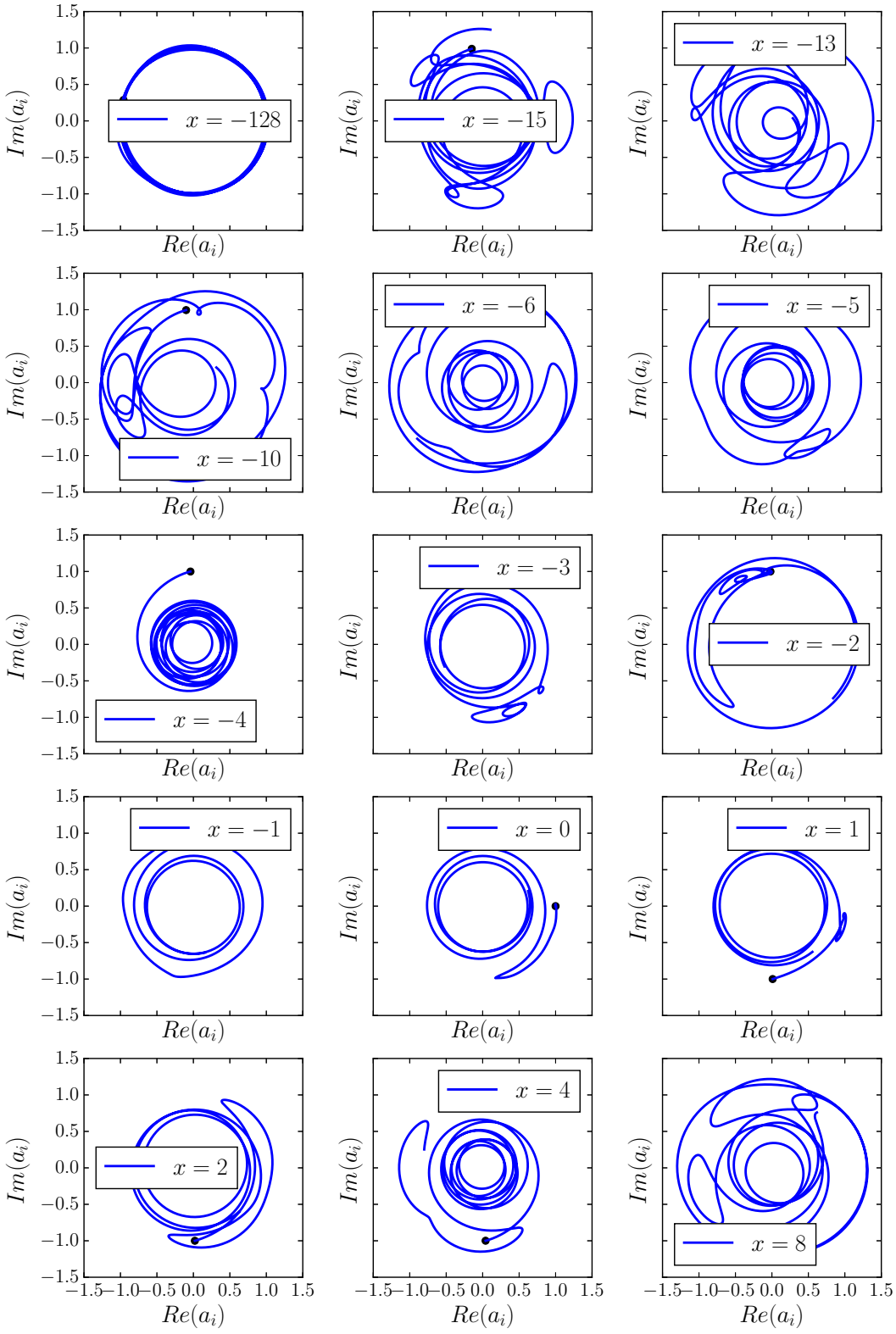

Figure 5.6: The local trajectory of a_i for Fig. 5.5 at different sites at $y = 0$. Time between $t = 0$ and $t = 100$.

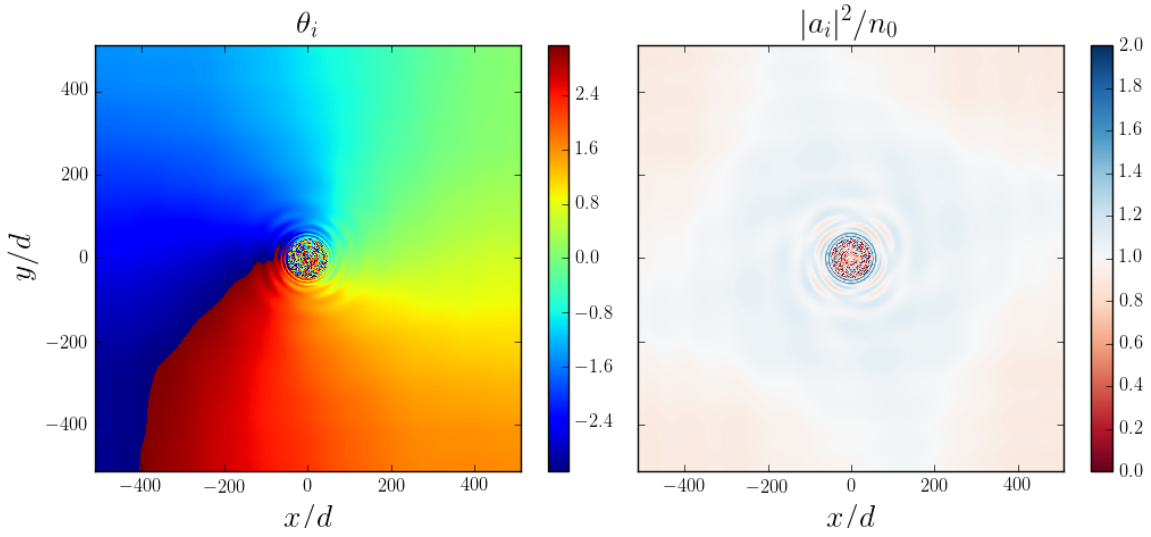

Figure 5.7: Similar to Fig. 5.5 in a larger system $P/(Un_0) = 0.4$ and $R = 64d$ in $L = 1024d$ at $t = 100$.

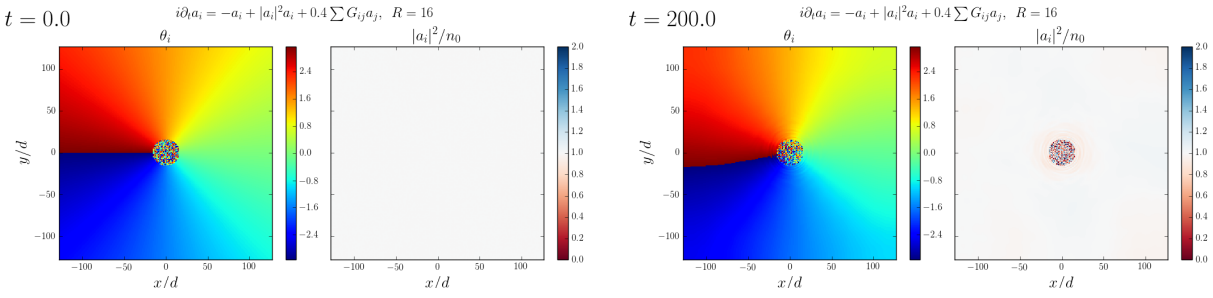

Figure 5.8: Time evolution of initial vortex with random core $R_{rc} = 16d$ with nonlocal hopping $P/(Un_0) = 0.4$ and $R = 16d$ in $L = 256d$.

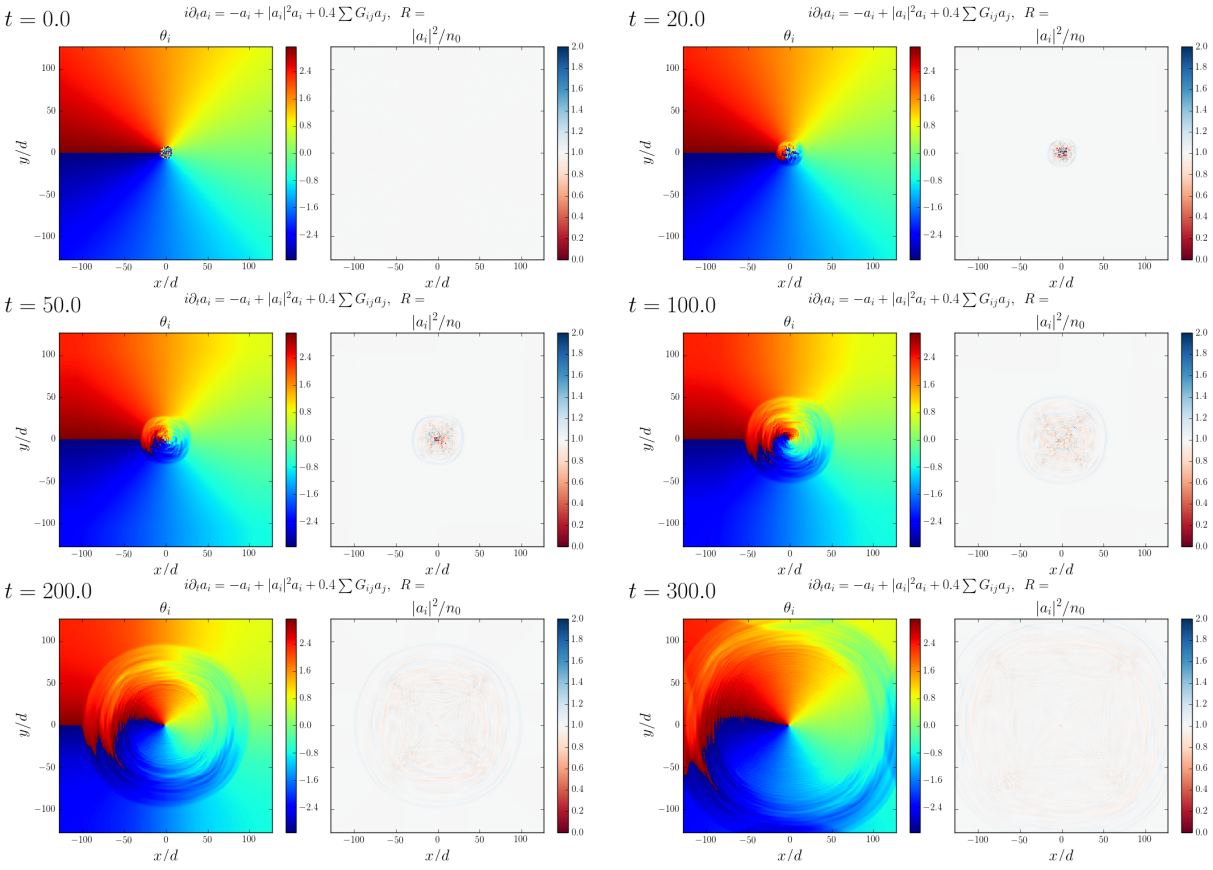

Figure 5.9: Time evolution of initial vortex with random core $R_{rc} = 8$ with nearest neighbor hopping, $P/(Un_0) = 0.4$.

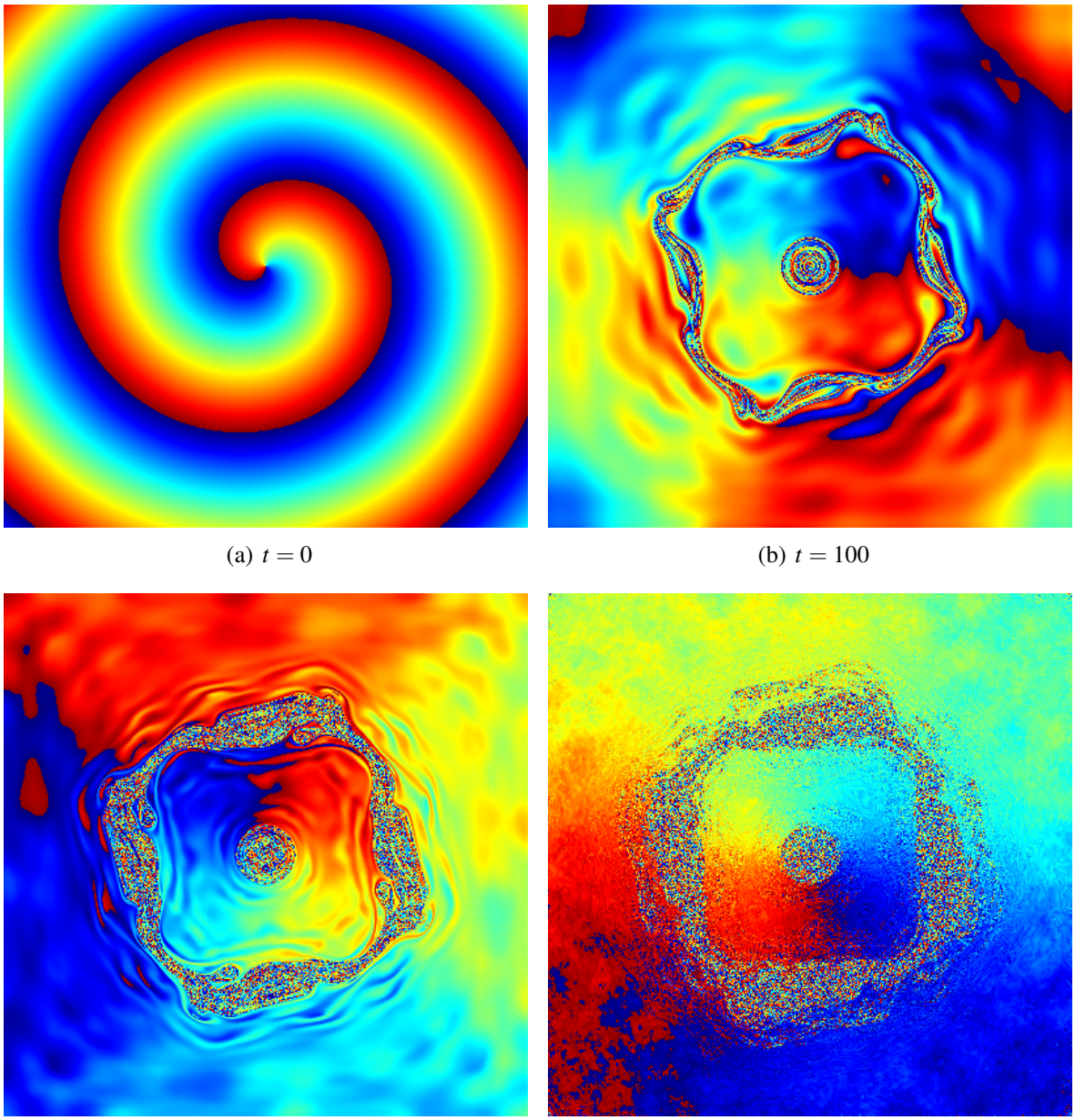

(a) $t = 0$ (b) $t = 100$

(c) $t = 220$ (d) $t = 4000$

Figure 5.10: Time evolution of NLHM with a spiral IC and wavenumber $k_s = 0.05$. $P/(Un_0) = 0.1$ and $R = 40d$ in $L = 400d$. BC: no-flux, kernel: top-hat.

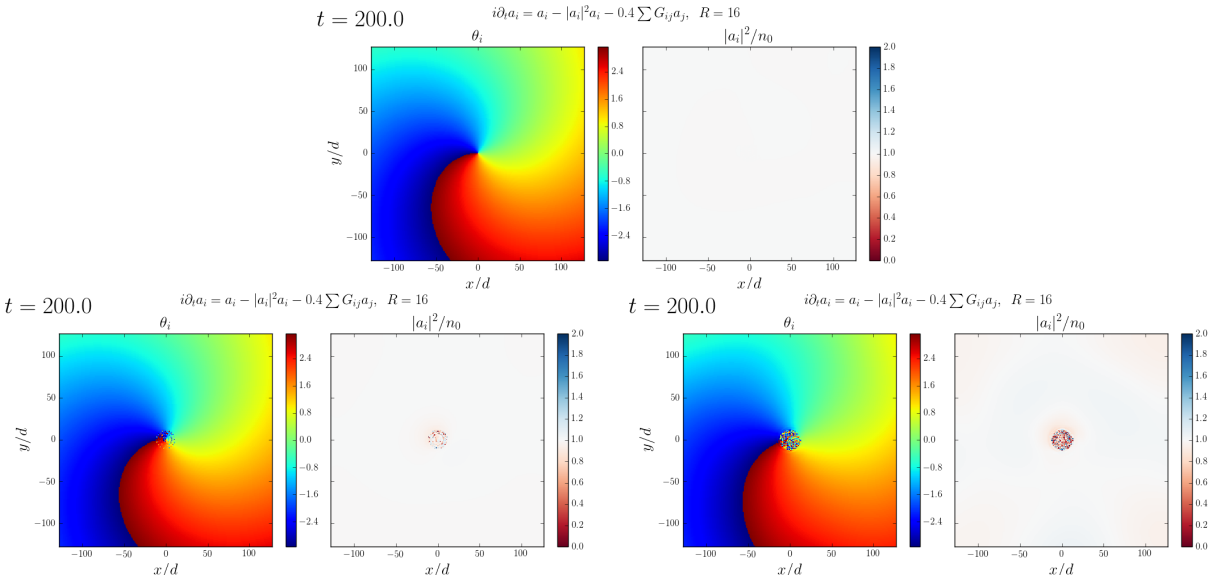

Figure 5.11: Inverse the time simulation with initial condition given by Fig. 5.5f. (a) No noise, (b) $\chi_{noise} = 10^{-11}$, (c) $\chi_{noise} = 10^{-10}$, where a single shot noise is add at $t = 0$.

Table 5.2: Time splitting: First order coefficients

step i	a_i	b_i
1	1	1

where a_i, b_i are coefficients satisfied $\sum_i a_i = \sum_i b_i = 1$. The $e^{a_s \Delta t \hat{A}}$ and $e^{b_s \Delta t \hat{B}}$ in the equation are the formal solution to the differential equations

$$\dot{\psi} = \hat{A}\psi, \tag{5.41}$$

$$\dot{\psi} = \hat{B}\psi, \tag{5.42}$$

respectively. For the coefficients of the first order, the second order Strang splitting, and a fourth order method, see the Table 5.2, 5.3 and 5.4. Note that the time split method with negative coefficients, such as the one in Table 5.4, requires the differential equation to be time reversed.

Table 5.3: Time splitting: Second order Strang splitting coefficients

step i	a_i	b_i
1	0.5	1
2	0.5	0

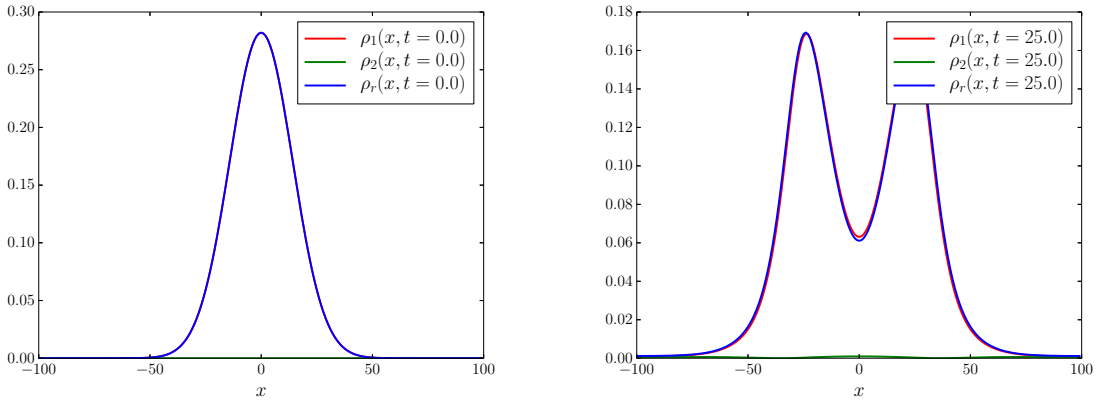

(a) $t = 0$

(b) $t = 25$

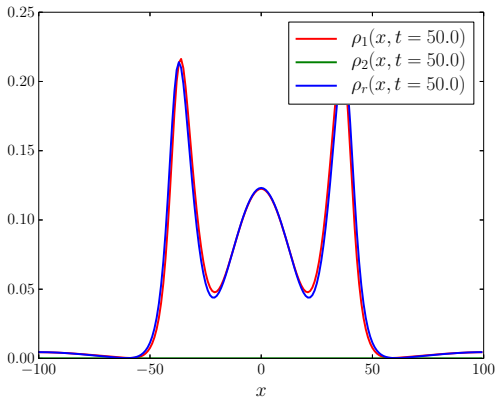

(c) $t = 50$

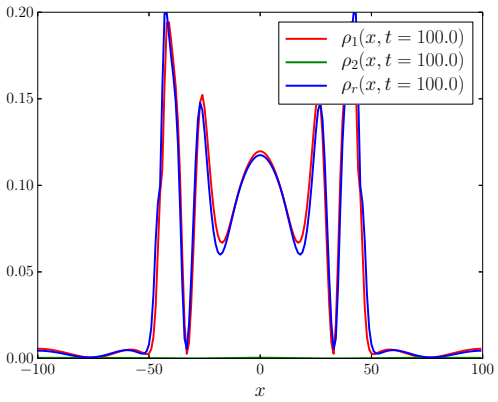

(d) $t = 100$

Figure 5.12: Comparison of NLHM and the minimal two-component model in 1D. Time evolution of a initial Gaussian state with wide 20 for the minimal model (ρ_1 and ρ_2) and the NLHM (ρ_r). Common parameter for both model: $N_{atom} = 10$, $U = 1$ with spatial discretization $x = [-100, 100]$, $dx = 1$. For minimal model, $\kappa = 4000$, $\Omega = 1$, $\Delta = 10$, resulting in effective hopping range $R_0 = \sqrt{\kappa_2/\Delta} = 20$, $P = \Omega^2/\Delta = 0.1$.

Table 5.4: Time splitting: Fourth order coefficients (Emb 4/3 BM PRK/A [204])

step i	a_i	b_i
1	0.0792036964311954608	0.209515106613361891
2	0.353172906049773948	-0.143851773179818077
3	-0.0420650803577191948	0.434336666566456186
4	0.219376955753499572	0.434336666566456186
5	-0.0420650803577191948	-0.143851773179818077
6	0.353172906049773948	0.209515106613361891
7	0.0792036964311954608	0

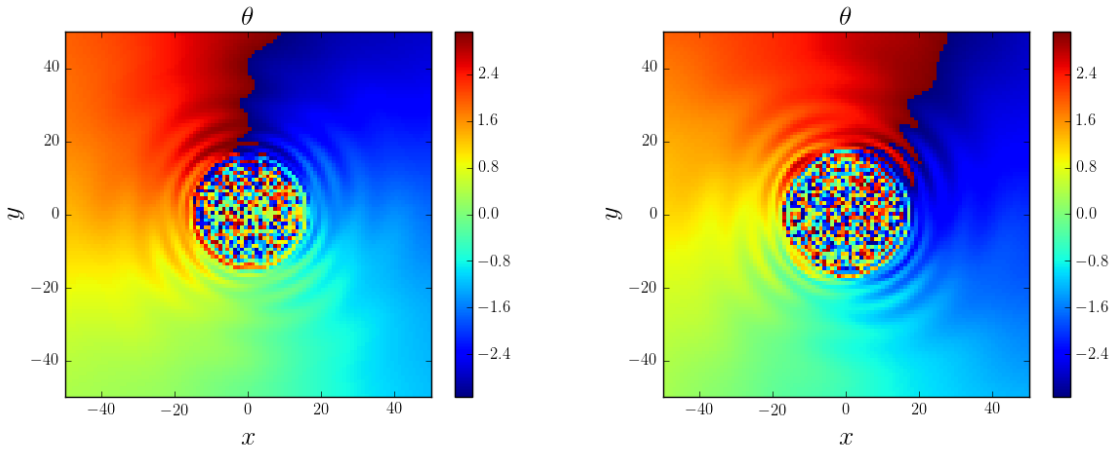

(a) NLHM (b) Minimal model

Figure 5.13: Comparison of NLHM and the minimal two-component model in 2D. The phases at $t = 100$ are shown with the same initial spiral $k_s = 0.01$. Parameters for NLHM are $Un_0 = 1$, $P = 0.5$, $R = 16$, and size $L = 256$ with no-flux boundary condition. Parameters for minimal model are $\Delta = 8$, $\Omega = 2$, $U = 1$, and $\kappa = 2048$, with $dx = 1$.

5.13.2 Time split method for the one-component GPE

A one component GPE is given by

$$i\hbar\dot{\psi}(\mathbf{r},t) = -\frac{\hbar^2}{2m}\nabla^2\psi + V(\mathbf{r})\psi + U|\psi|^2\psi. \tag{5.43}$$

The splitting used is chosen to be

$$i\hbar\dot{\psi}(\mathbf{r},t) = -\frac{\hbar^2}{2m}\nabla^2\psi, \tag{5.44}$$

$$i\hbar\dot{\psi}(\mathbf{r},t) = V(\mathbf{r})\psi + U|\psi|^2\psi. \tag{5.45}$$

The second equation is a pure local phase evolution without change in the local amplitude $|\psi(\mathbf{r},t)|$ or, similarly, the local density $|\psi(\mathbf{r},t)|^2$, because

$$i\hbar\dot{\rho}(\mathbf{r},t) = i\hbar(\dot{\psi}^*\psi + \psi^*\dot{\psi}) = 0. \tag{5.46}$$

Hence, the exact solution at the subsequent time t starting from $t = 0$ is given by

$$\psi(\mathbf{r},t) = \psi(\mathbf{r},0)e^{-i(V(\mathbf{r})+U|\psi(\mathbf{r},0)|^2)t/\hbar}. \tag{5.47}$$

The first equation can also be solved exactly, by transforming it in the Fourier space:

$$i\hbar\dot{\tilde{\psi}}(\mathbf{q},t) = \frac{\hbar^2 q^2}{2m}\tilde{\psi}, \tag{5.48}$$

which has an exact solution

$$\psi(\tilde{\mathbf{q}},t) = e^{-i\frac{\hbar q^2}{2m}t}\tilde{\psi}(\tilde{\mathbf{q}},0). \tag{5.49}$$

The real space solution can be obtained by the inverse Fourier transform.

5.13.3 Time split method for the two-component GPE

The two-component GPE considered is

$$i\hbar\dot{\psi}_i(\mathbf{r},t) = -\frac{\hbar^2}{2m_i}\nabla^2\psi_i + V_i\psi_i + \sum_j g_{ij}|\psi_j|^2\psi_i + \hbar\Omega\psi_{3-i} + \hbar\Delta_i\psi_i, \tag{5.50}$$

with $i = 1,2$. Here, we only consider the equation without cross nonlinearity $g_{12} = 0$, as it is easier to have an exact solution in the time split method. Otherwise, it can be solved by a three-step time-split method in this case, or one can use a higher order numerical approximation for each individual step. The following splits are considered

$$i\hbar\dot{\psi}_1 = -\frac{\hbar^2}{2m_1}\nabla^2\psi_1 + \hbar\Omega\psi_2, \tag{5.51}$$

$$i\hbar\dot{\psi}_2 = -\frac{\hbar^2}{2m_2}\nabla^2\psi_2 + \hbar\Omega\psi_1, \tag{5.52}$$

$$i\hbar\dot{\psi}_1 = V_1(\mathbf{r})\psi_1 + g_{11}|\psi_1|^2\psi_1 + \hbar\Delta_1\psi_1, \tag{5.53}$$

$$i\hbar\dot{\psi}_2 = V_2(\mathbf{r})\psi_2 + g_{22}|\psi_2|^2\psi_2 + \hbar\Delta_2\psi_2, \tag{5.54}$$

Similarly to the one component equation, the exact solutions to the second set of equations are

$$\psi_i(\mathbf{r},t) = e^{-i(V_i(\mathbf{r})+g_{ii}|\psi_i(\mathbf{r},0)|^2+\hbar\Delta_i)t/\hbar}\psi_i(\mathbf{r},0). \tag{5.55}$$

The first equation in the Fourier space takes the form

$$i\dot{\tilde{\Psi}}(\mathbf{q},t) = \hat{M}\tilde{\Psi}, \tag{5.56}$$

where M is a symmetric matrix given by

$$\hat{M} = \begin{pmatrix} \frac{\hbar q^2}{2m_1} & \Omega \\ \Omega & \frac{\hbar q^2}{2m_2} \end{pmatrix} \qquad \tilde{\Psi}(\mathbf{q},t) = \begin{pmatrix} \tilde{\psi}_1(\mathbf{q},t) \\ \tilde{\psi}_2(\mathbf{q},t) \end{pmatrix}, \tag{5.57}$$

which can be diagonalized. Hence the solution is

$$\tilde{\Psi}(\mathbf{q},t) = e^{-i\hat{M}t}\tilde{\Psi}(\mathbf{q},0). \tag{5.58}$$

These solutions can then be used in the time split method.

Chapter 6

Conclusion and future work

6.1 Conclusion

In this thesis, I have presented my studies on three nonlinear effects and attempted to propose implementations using ultracold atoms. After studying chimera knot states in 3D and cat states in Bose-Einstein Condensates, I intended to find an analogue for diffusive coupling in BECs. This led to my discovery of a new matter-wave mediated nonlocal hopping mechanism.

In chapter 3, I have presented strong numerical evidence that stable knots and links can exist in oscillatory systems and systems with nonlocal coupling. These include structures such as trefoils, Hopf links, and more. The same conclusion holds in simple, complex and chaotic oscillatory systems, if the coupling between the oscillators is neither too short-ranged nor too long-ranged. In the case of complex oscillatory systems, I have also discerned a novel topological superstructure combining knotted filaments and synchronization defect sheets.

In chapter 4, I proposed a method to create spin cat states, which are macroscopic superpositions of coherent spin states, in BECs, using the Kerr nonlinearity due to atomic collisions. This proposal includes an enhancement of the nonlinearity through the strong trapping of the small BEC component, and an enhancement of the lifetime using a Feshbach resonance. Based on a detailed study of atom loss, I concluded that cat sizes of hundreds of atoms should be realistic. The detailed analysis I presented also includes the effects of higher-order nonlinearities, atom number fluctuations, and limited readout efficiency.

In chapter 5, I proposed a new mediating mechanism that can achieve nonlocal spatial hopping for particles in systems with two inter-convertible states and very different time scales. Adiabatically eliminating the fast component results in an effective hopping model with independently adjustable nonlinearity, hopping strength, and hopping range. I showed that this model can be im-

plemented in BECs using current technology. My results further show that the nonlocal hopping can lead to chimera states, which should be observable in BECs experimentally.

6.2 Future work

My results in Chapter 3 suggest that the nonlocal diffusive coupling can stabilize the knot structures in oscillatory media, and, in Chapter 5, nonlocal hopping is an analogue to the nonlocal diffusive coupling. Technically, the Gross-Pitaevskii equation can be considered as describing a special case of oscillatory media with energy and particle conservation, so it is natural to speculate that chimera knots can also exist in systems with nonlocal hopping. The simulations, however, will take much longer, because of high accuracy requirements for conservative systems, and will require detailed planning on how to use the available computational resources as efficiently as possible.

For the spin cat states in BEC studied in Chapter 4, it will be interesting to really see it implemented in an experimental system. Since the paper was published, we have been in contact with experimental groups to see if it is feasible with their experimental setups. We have learned that not many groups have exactly the same setting used in my paper, but that there should be no real obstacle from the experimental point of view. However, research groups will need time to adapt their experimental systems.

The study of mediated nonlocal hopping and the proposed implementation in BEC brings up many questions. There are two main future directions for the mediated hopping. The first direction is the search for alternative experimental implementations. The scheme proposed in Chapter 5 is only one of the promising implementations found during my research. For example, an alternative proposal might replace hyperfine states with a double well potential, which has the same mathematical description. However, it requires one spatial dimension for the double well control, so it will be harder to control loss. Another example might be a adiabatically and periodically varying trapping, which will likely require a longer experimental time, and whose side effects are harder to analyze. There are two other promising setups that I would like to study. My preliminary analysis

suggests that photon mediated nonlocal hopping with BEC in multiple traps should be possible. This setup should have a faster time scale with no requirement of spin dependent traps, but it relies on recently developing trapping technology [189, 190]. Another approach is a purely photonic system using an optical-fiber based implementation, this is only possible if the nonlinearity is strong enough compared with the loss.

Another direction is the study of the nonlocal hopping model itself. It is interesting to study the dynamics of chimera states in conservative systems. Preliminary results show that there are more spatial-temporal chimera patterns in BECs that have not been reported elsewhere, such as stable chimera rings in 2D. There may be even more patterns in other parameter regimes that are yet to be explored. The existence of chimera states in conservative systems also suggests a relation with chaotic dynamics in conservative Hamiltonian systems [205, 206] confined to a spatial region. The incoherent region shows some properties of superfluid turbulence. Further simulations also suggest the existence of certain localization effects in systems with the nonlocal hopping. Further work will be required to fully quantify these observations.

The effective model used in my analysis is the mean-field of the Bose-Hubbard model [13] with nonlocal hopping. This raises questions related to condensed matter physics. In the standard Bose-Hubbard model with strong hopping, the system is in the superfluid state with particles freely moving, and is described by a macroscopic wavefunction. My scheme further constrains the wavefunction to exhibit periodically localized structures. This order is generally known as the lattice supersolid state [191, 207, 208]. The current system in Chapter 5 is in the mean-field limit, so a quantum treatment will be needed to quantify and prove the existence of the supersolid state.

For conservative Hamiltonian systems, eigenstates, and in particular the ground state, are well-defined. This is generally not the case for chimera states in open systems. For the eigenstates, the time evolution involves a time-dependent global phase with a spatial structure $\psi(x)$. So it will be interesting to study if such pure spatial chimera patterns can exist too, in addition to the typical chimera states of spatio-temporal patterns.

Bibliography

[1] I. S. Aranson and L. Kramer, "The world of the complex Ginzburg-Landau equation," *Rev. Mod. Phys.*, vol. 74, no. 1, pp. 99–143, 2002.

[2] Y. Kuramoto, "Chemical Oscillations, Waves, and Turbulence," No. 19 in Springer Series in Synergetics, pp. 1–4, Springer Berlin Heidelberg, 1984.

[3] R. Kapral and K. Showalter, *Chemical Waves and Patterns*. Springer Science & Business Media, 2012.

[4] Y. Kuramoto and D. Battogtokh, "Coexistence of Coherence and Incoherence in Nonlocally Coupled Phase Oscillators," *Nonlinear Phenom. Complex Syst*, vol. 5, no. 4, pp. 380–385, 2002.

[5] M. J. Panaggio and D. M. Abrams, "Chimera states: coexistence of coherence and incoherence in networks of coupled oscillators," *Nonlinearity*, vol. 28, no. 3, p. R67, 2015.

[6] D. Tanaka and Y. Kuramoto, "Complex Ginzburg-Landau equation with nonlocal coupling," *Phys. Rev. E*, vol. 68, no. 2, p. 026219, 2003.

[7] Y. Kuramoto and S.-i. Shima, "Rotating Spirals without Phase Singularity in Reaction-Diffusion Systems," *Prog. Theor. Phys. Supplement*, vol. 150, pp. 115–125, 2003.

[8] H. W. Lau and J. Davidsen, "Linked and knotted chimera filaments in oscillatory systems," *Phys. Rev. E*, vol. 94, no. 1, p. 010204, 2016.

[9] F. Dalfovo, S. Giorgini, L. P. Pitaevskii, and S. Stringari, "Theory of Bose-Einstein condensation in trapped gases," *Rev. Mod. Phys.*, vol. 71, no. 3, pp. 463–512, 1999.

[10] C. J. Pethick and H. Smith, *Bose-Einstein Condensation in Dilute Gases*. Cambridge University Press, 2 ed., 2008.

[11] M. Khazali, H. W. Lau, A. Humeniuk, and C. Simon, "Large energy superpositions via Rydberg dressing," *Phys. Rev. A*, vol. 94, no. 2, p. 023408, 2016.

[12] H. W. Lau, Z. Dutton, T. Wang, and C. Simon, "Proposal for the Creation and Optical Detection of Spin Cat States in Bose-Einstein Condensates," *Phys. Rev. Lett.*, vol. 113, no. 9, p. 090401, 2014.

[13] M. P. A. Fisher, P. B. Weichman, G. Grinstein, and D. S. Fisher, "Boson localization and the superfluid-insulator transition," *Phys. Rev. B*, vol. 40, no. 1, pp. 546–570, 1989.

[14] A. Goryachev, H. Chaté, and R. Kapral, "Synchronization Defects and Broken Symmetry in Spiral Waves," *Phys. Rev. Lett.*, vol. 80, no. 4, pp. 873–876, 1998.

[15] P. Ball and N. R. Borley, *The self-made tapestry: pattern formation in nature*, vol. 198. Oxford University Press Oxford, 1999.

[16] R. C. Desai and R. Kapral, *Dynamics of Self-organized and Self-assembled Structures*. Cambridge University Press, 2009.

[17] M. Cross and H. Greenside, *Pattern Formation and Dynamics in Nonequilibrium Systems*. Cambridge University Press, 1 ed., 2009.

[18] S.-i. Shima and Y. Kuramoto, "Rotating spiral waves with phase-randomized core in nonlocally coupled oscillators," *Phys. Rev. E*, vol. 69, no. 3, p. 036213, 2004.

[19] P.-J. Kim, T.-W. Ko, H. Jeong, and H.-T. Moon, "Pattern formation in a two-dimensional array of oscillators with phase-shifted coupling," *Phys. Rev. E*, vol. 70, no. 6, p. 065201, 2004.

[20] D. M. Abrams and S. H. Strogatz, "Chimera States for Coupled Oscillators," *Phys. Rev. Lett.*, vol. 93, no. 17, p. 174102, 2004.

[21] M. R. Tinsley, S. Nkomo, and K. Showalter, "Chimera and phase-cluster states in populations of coupled chemical oscillators," *Nature Physics*, vol. 8, no. 9, pp. 662–665, 2012.

[22] S. Nkomo, M. R. Tinsley, and K. Showalter, "Chimera States in Populations of Nonlocally Coupled Chemical Oscillators," *Phys. Rev. Lett.*, vol. 110, no. 24, p. 244102, 2013.

[23] A. M. Hagerstrom, T. E. Murphy, R. Roy, P. Hövel, I. Omelchenko, and E. Schöll, "Experimental observation of chimeras in coupled-map lattices," *Nature Physics*, vol. 8, no. 9, pp. 658–661, 2012.

[24] E. A. Martens, S. Thutupalli, A. Fourrière, and O. Hallatschek, "Chimera states in mechanical oscillator networks," *PNAS*, vol. 110, no. 26, pp. 10563–10567, 2013.

[25] A. Pikovsky, M. Rosenblum, and J. Kurths, *Synchronization: A Universal Concept in Nonlinear Sciences*. Cambridge: Cambridge University Press, 1 edition ed., 2003.

[26] J. A. Acebrón, L. L. Bonilla, C. J. Pérez Vicente, F. Ritort, and R. Spigler, "The Kuramoto model: A simple paradigm for synchronization phenomena," *Rev. Mod. Phys.*, vol. 77, no. 1, pp. 137–185, 2005.

[27] Y. Kuramoto, "Self-entrainment of a population of coupled non-linear oscillators," in *International symposium on mathematical problems in theoretical physics*, pp. 420–422, Springer, 1975.

[28] M. Wolfrum and O. E. Omel'chenko, "Chimera states are chaotic transients," *Phys. Rev. E*, vol. 84, no. 1, p. 015201, 2011.

[29] E. Ott and T. M. Antonsen, "Low dimensional behavior of large systems of globally coupled oscillators," *Chaos: An Interdisciplinary Journal of Nonlinear Science*, vol. 18, no. 3, p. 037113, 2008.

[30] E. Ott and T. M. Antonsen, "Long time evolution of phase oscillator systems," *Chaos: An Interdisciplinary Journal of Nonlinear Science*, vol. 19, no. 2, p. 023117, 2009.

[31] L. D. Landau, "On the theory of phase transitions. I.," *Zh. Eksp. Teor. Fiz.*, vol. 11, p. 19, 1937.

[32] L. D. Landau, "On the theory of phase transitions. II.," *Zh. Eksp. Teor. Fiz.*, vol. 11, p. 627, 1937.

[33] L. D. Landau and V. L. Ginzburg, "On the theory of superconductivity," *Zh. Eksp. Teor. Fiz.*, vol. 20, p. 1064, 1950.

[34] Y. Maistrenko, O. Sudakov, O. Osiv, and V. Maistrenko, "Chimera states in three dimensions," *New J. Phys.*, vol. 17, no. 7, p. 073037, 2015.

[35] I. S. Aranson, A. R. Bishop, and L. Kramer, "Dynamics of vortex lines in the three-dimensional complex Ginzburg-Landau equation: Instability, stretching, entanglement, and helices," *Phys. Rev. E*, vol. 57, no. 5, pp. 5276–5286, 1998.

[36] G. Rousseau, H. Chaté, and R. Kapral, "Twisted vortex filaments in the three-dimensional complex Ginzburg-Landau equation," *Chaos: An Interdisciplinary Journal of Nonlinear Science*, vol. 18, no. 2, pp. 026103–026103–21, 2008.

[37] A. N. Zaikin and A. M. Zhabotinsky, "Concentration wave propagation in two-dimensional liquid-phase self-oscillating system," *Nature*, vol. 225, no. 5232, pp. 535–537, 1970.

[38] A. T. Winfree, "Spiral Waves of Chemical Activity," *Science*, vol. 175, no. 4022, pp. 634–636, 1972.

[39] B. Hensen, H. Bernien, A. E. Dréau, A. Reiserer, N. Kalb, M. S. Blok, J. Ruitenberg, R. F. L. Vermeulen, R. N. Schouten, C. Abellán, W. Amaya, V. Pruneri, M. W. Mitchell, M. Markham, D. J. Twitchen, D. Elkouss, S. Wehner, T. H. Taminiau, and R. Hanson, "Loophole-free Bell inequality violation using electron spins separated by 1.3 kilometres," *Nature*, vol. 526, no. 7575, pp. 682–686, 2015.

[40] M. Giustina, M. A. Versteegh, S. Wengerowsky, J. Handsteiner, A. Hochrainer, K. Phelan, F. Steinlechner, J. Kofler, J.-Å. Larsson, C. Abellán, W. Amaya, V. Pruneri, M. W. Mitchell, J. Beyer, T. Gerrits, A. E. Lita, L. K. Shalm, S. W. Nam, T. Scheidl, R. Ursin, B. Wittmann, and A. Zeilinger, "Significant-Loophole-Free Test of Bell's Theorem with Entangled Photons," *Phys. Rev. Lett.*, vol. 115, no. 25, p. 250401, 2015.

[41] L. K. Shalm, E. Meyer-Scott, B. G. Christensen, P. Bierhorst, M. A. Wayne, M. J. Stevens, T. Gerrits, S. Glancy, D. R. Hamel, M. S. Allman, K. J. Coakley, S. D. Dyer, C. Hodge, A. E. Lita, V. B. Verma, C. Lambrocco, E. Tortorici, A. L. Migdall, Y. Zhang, D. R. Kumor, W. H. Farr, F. Marsili, M. D. Shaw, J. A. Stern, C. Abellán, W. Amaya, V. Pruneri, T. Jennewein, M. W. Mitchell, P. G. Kwiat, J. C. Bienfang, R. P. Mirin, E. Knill, and S. W. Nam, "Strong Loophole-Free Test of Local Realism," *Phys. Rev. Lett.*, vol. 115, no. 25, p. 250402, 2015.

[42] E. Schrödinger, "Die gegenwärtige Situation in der Quantenmechanik," *Naturwissenschaften*, vol. 23, no. 48, pp. 807–812, 1935.

[43] S. Habib, K. Shizume, and W. H. Zurek, "Decoherence, Chaos, and the Correspondence Principle," *Phys. Rev. Lett.*, vol. 80, no. 20, pp. 4361–4365, 1998.

[44] W. H. Zurek, "Decoherence, einselection, and the quantum origins of the classical," *Rev. Mod. Phys.*, vol. 75, no. 3, pp. 715–775, 2003.

[45] T. Wang, H. W. Lau, H. Kaviani, R. Ghobadi, and C. Simon, "Strong micro-macro entanglement from a weak cross-Kerr nonlinearity," *Phys. Rev. A*, vol. 92, no. 1, p. 012316, 2015.

[46] T. Wang, R. Ghobadi, S. Raeisi, and C. Simon, "Precision requirements for observing macroscopic quantum effects," *Physical Review A*, vol. 88, no. 6, p. 062114, 2013.

[47] C. Gerry and P. Knight, *Introductory quantum optics*. Cambridge university press, 2005.

[48] U. Leonhardt, *Measuring the quantum state of light*. Cambridge, N.Y.: Cambridge University Press, 2005.

[49] D. F. Walls and G. J. Milburn, *Quantum Optics*. Berlin: Springer, 2nd edition ed., 2008.

[50] C.-W. Lee and H. Jeong, "Quantification of Macroscopic Quantum Superpositions within Phase Space," *Phys. Rev. Lett.*, vol. 106, no. 22, p. 220401, 2011.

[51] B. Vlastakis, G. Kirchmair, Z. Leghtas, S. E. Nigg, L. Frunzio, S. M. Girvin, M. Mirrahimi, M. H. Devoret, and R. J. Schoelkopf, "Deterministically Encoding Quantum Information Using 100-Photon Schrödinger Cat States," *Science*, vol. 342, no. 6158, pp. 607–610, 2013.

[52] T. C. Ralph, W. J. Munro, and G. J. Milburn, "Quantum Computation with Coherent States, Linear Interactions and Superposed Resources," *arXiv:quant-ph/0110115*, 2001.

[53] T. C. Ralph, A. Gilchrist, G. J. Milburn, W. J. Munro, and S. Glancy, "Quantum computation with optical coherent states," *Physical Review A*, vol. 68, no. 4, p. 042319, 2003.

[54] LIGO Scientific Collaboration and Virgo Collaboration, "Observation of Gravitational Waves from a Binary Black Hole Merger," *Phys. Rev. Lett.*, vol. 116, no. 6, p. 061102, 2016.

[55] A. Bassi, K. Lochan, S. Satin, T. P. Singh, and H. Ulbricht, "Models of wave-function collapse, underlying theories, and experimental tests," *Rev. Mod. Phys.*, vol. 85, no. 2, pp. 471–527, 2013.

[56] A. Micheli, D. Jaksch, J. I. Cirac, and P. Zoller, "Many-particle entanglement in two-component Bose-Einstein condensates," *Phys. Rev. A*, vol. 67, no. 1, p. 013607, 2003.

[57] L. Gilles, B. M. Garraway, and P. L. Knight, "Generation of nonclassical light by dissipative two-photon processes," *Phys. Rev. A*, vol. 49, no. 4, pp. 2785–2799, 1994.

[58] L. Gilles and P. Knight, "Two-photon absorption and nonclassical states of light," *Phys. Rev. A*, vol. 48, no. 2, pp. 1582–1593, 1993.

[59] B. Yurke and D. Stoler, "Generating quantum mechanical superpositions of macroscopically distinguishable states via amplitude dispersion," *Phys. Rev. Lett.*, vol. 57, no. 1, pp. 13–16, 1986.

[60] B. Yurke and D. Stoler, "The dynamic generation of Schrödinger cats and their detection," *Physica B+C*, vol. 151, no. 1-2, pp. 298–301, 1988.

[61] E. Cornell, "Very cold indeed: The nanokelvin physics of Bose-Einstein condensation," *Journal of research of the National Institute of Standards and Technology*, vol. 101, no. 4, p. 419, 1996.

[62] A. J. Leggett, "Bose-Einstein condensation in the alkali gases: Some fundamental concepts," *Rev. Mod. Phys.*, vol. 73, no. 2, pp. 307–356, 2001.

[63] R. Ozeri, N. Katz, J. Steinhauer, and N. Davidson, "Colloquium: Bulk Bogoliubov excitations in a Bose-Einstein condensate," *Rev. Mod. Phys.*, vol. 77, no. 1, pp. 187–205, 2005.

[64] O. Morsch and M. Oberthaler, "Dynamics of Bose-Einstein condensates in optical lattices," *Rev. Mod. Phys.*, vol. 78, no. 1, pp. 179–215, 2006.

[65] J. Fortágh and C. Zimmermann, "Magnetic microtraps for ultracold atoms," *Rev. Mod. Phys.*, vol. 79, no. 1, pp. 235–289, 2007.

[66] I. Bloch, J. Dalibard, and W. Zwerger, "Many-body physics with ultracold gases," *Rev. Mod. Phys.*, vol. 80, no. 3, pp. 885–964, 2008.

[67] S. Giorgini, L. P. Pitaevskii, and S. Stringari, "Theory of ultracold atomic Fermi gases," *Rev. Mod. Phys.*, vol. 80, no. 4, pp. 1215–1274, 2008.

[68] A. L. Fetter, "Rotating trapped Bose-Einstein condensates," *Rev. Mod. Phys.*, vol. 81, no. 2, pp. 647–691, 2009.

[69] C. Chin, R. Grimm, P. Julienne, and E. Tiesinga, "Feshbach resonances in ultracold gases," *Rev. Mod. Phys.*, vol. 82, no. 2, pp. 1225–1286, 2010.

[70] H. Deng, H. Haug, and Y. Yamamoto, "Exciton-polariton Bose-Einstein condensation," *Rev. Mod. Phys.*, vol. 82, no. 2, pp. 1489–1537, 2010.

[71] H. Ritsch, P. Domokos, F. Brennecke, and T. Esslinger, "Cold atoms in cavity-generated dynamical optical potentials," *Rev. Mod. Phys.*, vol. 85, no. 2, pp. 553–601, 2013.

[72] D. M. Stamper-Kurn and M. Ueda, "Spinor Bose gases: Symmetries, magnetism, and quantum dynamics," *Rev. Mod. Phys.*, vol. 85, no. 3, pp. 1191–1244, 2013.

[73] V. Zapf, M. Jaime, and C. Batista, "Bose-Einstein condensation in quantum magnets," *Rev. Mod. Phys.*, vol. 86, no. 2, pp. 563–614, 2014.

[74] A. Eckardt, "Colloquium: Atomic quantum gases in periodically driven optical lattices," *Rev. Mod. Phys.*, vol. 89, no. 1, p. 011004, 2017.

[75] S. N. Bose, "Plancks gesetz und lichtquantenhypothese," *Z. phys*, vol. 26, no. 3, p. 178, 1924.

[76] A. Einstein, *Quantentheorie des einatomigen idealen Gases*. Akademie der Wissenshaften, in Kommission bei W. de Gruyter, 1924.

[77] M. H. Anderson, J. R. Ensher, M. R. Matthews, C. E. Wieman, and E. A. Cornell, "Observation of Bose-Einstein Condensation in a Dilute Atomic Vapor," *Science*, vol. 269, no. 5221, pp. 198–201, 1995.

[78] K. B. Davis, M. O. Mewes, M. R. Andrews, N. J. van Druten, D. S. Durfee, D. M. Kurn, and W. Ketterle, "Bose-Einstein Condensation in a Gas of Sodium Atoms," *Phys. Rev. Lett.*, vol. 75, no. 22, pp. 3969–3973, 1995.

[79] C. C. Bradley, C. A. Sackett, J. J. Tollett, and R. G. Hulet, "Evidence of Bose-Einstein Condensation in an Atomic Gas with Attractive Interactions," *Phys. Rev. Lett.*, vol. 75, no. 9, pp. 1687–1690, 1995.

[80] E. A. Cornell and C. E. Wieman, "Nobel Lecture: Bose-Einstein condensation in a dilute gas, the first 70 years and some recent experiments," *Rev. Mod. Phys.*, vol. 74, no. 3, pp. 875–893, 2002.

[81] W. Ketterle, "Nobel lecture: When atoms behave as waves: Bose-Einstein condensation and the atom laser," *Rev. Mod. Phys.*, vol. 74, no. 4, pp. 1131–1151, 2002.

[82] E. P. Gross, "Structure of a quantized vortex in boson systems," *Il Nuovo Cimento (1955-1965)*, vol. 20, no. 3, pp. 454–477, 1961.

[83] E. P. Gross, "Hydrodynamics of a Superfluid Condensate," *Journal of Mathematical Physics*, vol. 4, no. 2, pp. 195–207, 1963.

[84] L. P. Pitaevskii, "Vortex lines in an imperfect Bose gas," *Sov. Phys. JETP*, vol. 13, no. 2, pp. 451–454, 1961.

[85] D. Jaksch and P. Zoller, "The cold atom Hubbard toolbox," *Annals of Physics*, vol. 315, no. 1, pp. 52–79, 2005.

[86] R. P. Feynman, "Simulating physics with computers," *Int J Theor Phys*, vol. 21, no. 6-7, pp. 467–488, 1982.

[87] O. Lahav, A. Itah, A. Blumkin, C. Gordon, S. Rinott, A. Zayats, and J. Steinhauer, "Realization of a Sonic Black Hole Analog in a Bose-Einstein Condensate," *Phys. Rev. Lett.*, vol. 105, no. 24, p. 240401, 2010.

[88] J. Steinhauer, "Observation of self-amplifying Hawking radiation in an analogue black-hole laser," *Nat Phys*, vol. 10, no. 11, pp. 864–869, 2014.

[89] G. Modugno, "Ultracold atoms: A black-hole laser," *Nat Phys*, vol. 10, no. 11, pp. 793–794, 2014.

[90] M. Greiner, O. Mandel, T. Esslinger, T. W. Hänsch, and I. Bloch, "Quantum phase transition from a superfluid to a Mott insulator in a gas of ultracold atoms," *Nature*, vol. 415, no. 6867, pp. 39–44, 2002.

[91] G. Roati, C. D'Errico, L. Fallani, M. Fattori, C. Fort, M. Zaccanti, G. Modugno, M. Modugno, and M. Inguscio, "Anderson localization of a non-interacting Bose-Einstein condensate," *Nature*, vol. 453, no. 7197, pp. 895–898, 2008.

[92] S. Burger, K. Bongs, S. Dettmer, W. Ertmer, K. Sengstock, A. Sanpera, G. V. Shlyapnikov, and M. Lewenstein, "Dark Solitons in Bose-Einstein Condensates," *Phys. Rev. Lett.*, vol. 83, no. 25, pp. 5198–5201, 1999.

[93] J. Denschlag, J. E. Simsarian, D. L. Feder, C. W. Clark, L. A. Collins, J. Cubizolles, L. Deng, E. W. Hagley, K. Helmerson, W. P. Reinhardt, S. L. Rolston, B. I. Schneider, and W. D. Phillips, "Generating Solitons by Phase Engineering of a Bose-Einstein Condensate," *Science*, vol. 287, no. 5450, pp. 97–101, 2000.

[94] B. P. Anderson, "Watching Dark Solitons Decay into Vortex Rings in a Bose-Einstein Condensate," *Phys. Rev. Lett.*, vol. 86, no. 14, pp. 2926–2929, 2001.

[95] T. v. Zoest, N. Gaaloul, Y. Singh, H. Ahlers, W. Herr, S. T. Seidel, W. Ertmer, E. Rasel, M. Eckart, E. Kajari, S. Arnold, G. Nandi, W. P. Schleich, R. Walser, A. Vogel, K. Sengstock, K. Bongs, W. Lewoczko-Adamczyk, M. Schiemangk, T. Schuldt, A. Peters, T. Könemann, H. Müntinga, C. Lämmerzahl, H. Dittus, T. Steinmetz, T. W. Hänsch, and J. Reichel, "Bose-Einstein Condensation in Microgravity," *Science*, vol. 328, no. 5985, pp. 1540–1543, 2010.

[96] A. Sørensen, L.-M. Duan, J. I. Cirac, and P. Zoller, "Many-particle entanglement with Bose-Einstein condensates," *Nature*, vol. 409, no. 6816, pp. 63–66, 2001.

[97] J. Estève, C. Gross, A. Weller, S. Giovanazzi, and M. K. Oberthaler, "Squeezing and entanglement in a Bose-Einstein condensate," *Nature*, vol. 455, no. 7217, pp. 1216–1219, 2008.

[98] M. Khamehchi, "Negative-Mass Hydrodynamics in a Spin-Orbit-Coupled Bose-Einstein Condensate," *Phys. Rev. Lett.*, vol. 118, no. 15, 2017.

[99] J. Klaers, J. Schmitt, F. Vewinger, and M. Weitz, "Bose-Einstein condensation of photons in an optical microcavity," *Nature*, vol. 468, no. 7323, pp. 545–548, 2010.

[100] J. D. Plumhof, T. Stöferle, L. Mai, U. Scherf, and R. F. Mahrt, "Room-temperature Bose-Einstein condensation of cavity exciton-polaritons in a polymer," *Nat Mater*, vol. 13, no. 3, pp. 247–252, 2014.

[101] T. Kovachy, J. M. Hogan, A. Sugarbaker, S. M. Dickerson, C. A. Donnelly, C. Overstreet, and M. A. Kasevich, "Matter Wave Lensing to Picokelvin Temperatures," *Phys. Rev. Lett.*, vol. 114, no. 14, p. 143004, 2015.

[102] S. Inouye, M. R. Andrews, J. Stenger, H.-J. Miesner, D. M. Stamper-Kurn, and W. Ketterle, "Observation of Feshbach resonances in a Bose-Einstein condensate," *Nature*, vol. 392, no. 6672, pp. 151–154, 1998.

[103] S. E. Pollack, D. Dries, and R. G. Hulet, "Universality in Three- and Four-Body Bound States of Ultracold Atoms," *Science*, vol. 326, no. 5960, pp. 1683–1685, 2009.

[104] D. Jaksch, C. Bruder, J. I. Cirac, C. W. Gardiner, and P. Zoller, "Cold Bosonic Atoms in Optical Lattices," *Phys. Rev. Lett.*, vol. 81, no. 15, pp. 3108–3111, 1998.

[105] L. D. Landau and E. M. Lifshitz, *Mechanics: Volume 1*. Amsterdam u.a: Butterworth-Heinemann, 3 edition ed., 1976.

[106] O. E. Rössler, "An equation for continuous chaos," *Physics Letters A*, vol. 57, no. 5, pp. 397–398, 1976.

[107] J. I. Cirac, M. Lewenstein, K. Mølmer, and P. Zoller, "Quantum superposition states of Bose-Einstein condensates," *Phys. Rev. A*, vol. 57, no. 2, pp. 1208–1218, 1998.

[108] D. Kleckner and W. T. M. Irvine, "Creation and dynamics of knotted vortices," *Nat Phys*, vol. 9, no. 4, pp. 253–258, 2013.

[109] T. Machon and G. P. Alexander, "Knotted Defects in Nematic Liquid Crystals," *Phys. Rev. Lett.*, vol. 113, no. 2, p. 027801, 2014.

[110] S. Čopar, U. Tkalec, I. Muševič, and S. Žumer, "Knot theory realizations in nematic colloids," *PNAS*, vol. 112, no. 6, pp. 1675–1680, 2015.

[111] Y. Kawaguchi, M. Nitta, and M. Ueda, "Knots in a Spinor Bose-Einstein Condensate," *Phys. Rev. Lett.*, vol. 100, no. 18, p. 180403, 2008.

[112] D. Proment, M. Onorato, and C. F. Barenghi, "Vortex knots in a Bose-Einstein condensate," *arXiv:1110.5757*, 2011.

[113] M. R. Dennis, R. P. King, B. Jack, K. O'Holleran, and M. J. Padgett, "Isolated optical vortex knots," *Nat Phys*, vol. 6, no. 2, pp. 118–121, 2010.

[114] H. Kedia, I. Bialynicki-Birula, D. Peralta-Salas, and W. T. M. Irvine, "Tying Knots in Light Fields," *Phys. Rev. Lett.*, vol. 111, no. 15, p. 150404, 2013.

[115] E. Babaev, "Non-Meissner electrodynamics and knotted solitons in two-component superconductors," *Phys. Rev. B*, vol. 79, no. 10, p. 104506, 2009.

[116] T. Wüst, D. Reith, and P. Virnau, "Sequence Determines Degree of Knottedness in a Coarse-Grained Protein Model," *Phys. Rev. Lett.*, vol. 114, no. 2, p. 028102, 2015.

[117] A. T. Winfree and S. H. Strogatz, "Singular filaments organize chemical waves in three dimensions: I. Geometrically simple waves," *Physica D: Nonlinear Phenomena*, vol. 8, no. 1-2, pp. 35–49, 1983.

[118] P. M. Sutcliffe and A. T. Winfree, "Stability of knots in excitable media," *Phys. Rev. E*, vol. 68, no. 1, p. 016218, 2003.

[119] A. Malevanets and R. Kapral, "Links, Knots, and Knotted Labyrinths in Bistable Systems," *Phys. Rev. Lett.*, vol. 77, no. 4, pp. 767–770, 1996.

[120] E. V. Goldstein, M. G. Moore, H. Pu, and P. Meystre, "Eliminating the Mean-Field Shift in Two-Component Bose-Einstein Condensates," *Phys. Rev. Lett.*, vol. 85, no. 24, pp. 5030–5033, 2000.

[121] T. Bánsági and O. Steinbock, "Negative filament tension of scroll rings in an excitable system," *Phys. Rev. E*, vol. 76, no. 4, p. 045202, 2007.

[122] F. H. Fenton, E. M. Cherry, H. M. Hastings, and S. J. Evans, "Multiple mechanisms of spiral wave breakup in a model of cardiac electrical activity," *Chaos: An Interdisciplinary Journal of Nonlinear Science*, vol. 12, no. 3, pp. 852–892, 2002.

[123] G. St-Yves and J. Davidsen, "Influence of the medium's dimensionality on defect-mediated turbulence," *Phys. Rev. E*, vol. 91, no. 3, p. 032926, 2015.

[124] A. Mari, A. Farace, N. Didier, V. Giovannetti, and R. Fazio, "Measures of Quantum Synchronization in Continuous Variable Systems," *Phys. Rev. Lett.*, vol. 111, no. 10, p. 103605, 2013.

[125] S. Walter, A. Nunnenkamp, and C. Bruder, "Quantum Synchronization of a Driven Self-Sustained Oscillator," *Phys. Rev. Lett.*, vol. 112, no. 9, p. 094102, 2014.

[126] A. E. Motter, "Nonlinear dynamics: Spontaneous synchrony breaking," *Nat Phys*, vol. 6, no. 3, pp. 164–165, 2010.

[127] A. T. Winfree, "Electrical turbulence in three-dimensional heart muscle," *Science*, vol. 266, no. 5187, pp. 1003–1006, 1994.

[128] V. N. Biktashev, "A Three-Dimensional Autowave Turbulence," *Int. J. Bifurcation Chaos*, vol. 08, no. 04, pp. 677–684, 1998.

[129] S. Alonso, F. Sagués, and A. S. Mikhailov, "Taming Winfree Turbulence of Scroll Waves in Excitable Media," *Science*, vol. 299, no. 5613, pp. 1722–1725, 2003.

[130] J. Davidsen, M. Zhan, and R. Kapral, "Filament-induced surface spiral turbulence in three-dimensional excitable media," *Physical review letters*, vol. 101, no. 20, p. 208302, 2008.

[131] J. C. Reid, H. Chaté, and J. Davidsen, "Filament turbulence in oscillatory media," *EPL*, vol. 94, no. 6, p. 68003, 2011.

[132] H. Dierckx, H. Verschelde, Ö. Selsil, and V. N. Biktashev, "Buckling of Scroll Waves," *Phys. Rev. Lett.*, vol. 109, no. 17, p. 174102, 2012.

[133] O. E. Omel'chenko, M. Wolfrum, S. Yanchuk, Y. L. Maistrenko, and O. Sudakov, "Stationary patterns of coherence and incoherence in two-dimensional arrays of non-locally-coupled phase oscillators," *Phys. Rev. E*, vol. 85, no. 3, p. 036210, 2012.

[134] E. A. Martens, C. R. Laing, and S. H. Strogatz, "Solvable Model of Spiral Wave Chimeras," *Phys. Rev. Lett.*, vol. 104, no. 4, p. 044101, 2010.

[135] M. J. Panaggio and D. M. Abrams, "Chimera states on the surface of a sphere," *Phys. Rev. E*, vol. 91, no. 2, p. 022909, 2015.

[136] A. T. Winfree, "Stable Particle-Like Solutions to the Nonlinear Wave Equations of Three-Dimensional Excitable Media," *SIAM Review*, vol. 32, no. 1, pp. 1–53, 1990.

[137] Z. A. Jiménez and O. Steinbock, "Stationary Vortex Loops Induced by Filament Interaction and Local Pinning in a Chemical Reaction-Diffusion System," *Phys. Rev. Lett.*, vol. 109,

no. 9, p. 098301, 2012.

[138] C. Gu, *Chimera States in Nonlocally Coupled Oscillatory and Complex Oscillatory Systems*. Thesis, University of Calgary, 2013.

[139] C. Gu, G. St-Yves, and J. Davidsen, "Spiral Wave Chimeras in Complex Oscillatory and Chaotic Systems," *Phys. Rev. Lett.*, vol. 111, no. 13, p. 134101, 2013.

[140] J. Davidsen, R. Erichsen, R. Kapral, and H. Chaté, "From Ballistic to Brownian Vortex Motion in Complex Oscillatory Media," *Phys. Rev. Lett.*, vol. 93, no. 1, p. 018305, 2004.

[141] A. Goryachev, R. Kapral, and H. Chaté, "Synchronization defect lines," *Int. J. Bifurcation Chaos*, vol. 10, no. 07, pp. 1537–1564, 2000.

[142] C. R. Laing, "The dynamics of chimera states in heterogeneous Kuramoto networks," *Physica D: Nonlinear Phenomena*, vol. 238, no. 16, pp. 1569–1588, 2009.

[143] D. Kupitz and M. J. Hauser, "Interaction of a pair of parallel scroll waves," *The Journal of Physical Chemistry A*, vol. 117, no. 48, pp. 12711–12718, 2013.

[144] C. Monroe, D. M. Meekhof, B. E. King, and D. J. Wineland, "A "Schrödinger Cat" Superposition State of an Atom," *Science*, vol. 272, no. 5265, pp. 1131–1136, 1996.

[145] M. Brune, E. Hagley, J. Dreyer, X. Maître, A. Maali, C. Wunderlich, J. M. Raimond, and S. Haroche, "Observing the Progressive Decoherence of the "Meter" in a Quantum Measurement," *Phys. Rev. Lett.*, vol. 77, no. 24, pp. 4887–4890, 1996.

[146] D. Leibfried, E. Knill, S. Seidelin, J. Britton, R. B. Blakestad, J. Chiaverini, D. B. Hume, W. M. Itano, J. D. Jost, C. Langer, R. Ozeri, R. Reichle, and D. J. Wineland, "Creation of a six-atom Schrödinger cat' state," *Nature*, vol. 438, no. 7068, pp. 639–642, 2005.

[147] B. Lücke, M. Scherer, J. Kruse, L. Pezzé, F. Deuretzbacher, P. Hyllus, O. Topic, J. Peise, W. Ertmer, J. Arlt, L. Santos, A. Smerzi, and C. Klempt, "Twin Matter Waves for Interferometry Beyond the Classical Limit," *Science*, vol. 334, no. 6057, pp. 773–776, 2011.

[148] M. Arndt, O. Nairz, J. Vos-Andreae, C. Keller, G. van der Zouw, and A. Zeilinger, "Wave-particle duality of C60 molecules," *Nature*, vol. 401, no. 6754, pp. 680–682, 1999.

[149] M. Arndt and K. Hornberger, "Testing the limits of quantum mechanical superpositions," *Nature Physics*, vol. 10, no. 4, pp. 271–277, 2014.

[150] J. R. Friedman, V. Patel, W. Chen, S. K. Tolpygo, and J. E. Lukens, "Quantum superposition of distinct macroscopic states," *Nature*, vol. 406, no. 6791, pp. 43–46, 2000.

[151] B. Julsgaard, A. Kozhekin, and E. S. Polzik, "Experimental long-lived entanglement of two macroscopic objects," *Nature*, vol. 413, no. 6854, pp. 400–403, 2001.

[152] C. Gross, T. Zibold, E. Nicklas, J. Estève, and M. K. Oberthaler, "Nonlinear atom interferometer surpasses classical precision limit," *Nature*, vol. 464, no. 7292, pp. 1165–1169, 2010.

[153] M. F. Riedel, P. Böhi, Y. Li, T. W. Hänsch, A. Sinatra, and P. Treutlein, "Atom-chip-based generation of entanglement for quantum metrology," *Nature*, vol. 464, no. 7292, pp. 1170–1173, 2010.

[154] A. D. O'Connell, M. Hofheinz, M. Ansmann, R. C. Bialczak, M. Lenander, E. Lucero, M. Neeley, D. Sank, H. Wang, M. Weides, J. Wenner, J. M. Martinis, and A. N. Cleland, "Quantum ground state and single-phonon control of a mechanical resonator," *Nature*, vol. 464, no. 7289, pp. 697–703, 2010.

[155] A. I. Lvovsky, R. Ghobadi, A. Chandra, A. S. Prasad, and C. Simon, "Observation of micro-macro entanglement of light," *Nat Phys*, vol. 9, no. 9, pp. 541–544, 2013.

[156] N. Bruno, A. Martin, P. Sekatski, N. Sangouard, R. T. Thew, and N. Gisin, "Displacement of entanglement back and forth between the micro and macro domains," *Nat Phys*, vol. 9, no. 9, pp. 545–548, 2013.

[157] T. A. Palomaki, J. D. Teufel, R. W. Simmonds, and K. W. Lehnert, "Entangling Mechanical Motion with Microwave Fields," *Science*, vol. 342, no. 6159, pp. 710–713, 2013.

[158] D. Gordon and C. M. Savage, "Creating macroscopic quantum superpositions with Bose-Einstein condensates," *Phys. Rev. A*, vol. 59, no. 6, pp. 4623–4629, 1999.

[159] R. Zhang, S. R. Garner, and L. V. Hau, "Creation of Long-Term Coherent Optical Memory via Controlled Nonlinear Interactions in Bose-Einstein Condensates," *Phys. Rev. Lett.*, vol. 103, no. 23, p. 233602, 2009.

[160] A. Rispe, B. He, and C. Simon, "Photon-Photon Gates in Bose-Einstein Condensates," *Phys. Rev. Lett.*, vol. 107, no. 4, p. 043601, 2011.

[161] C. Vo, S. Riedl, S. Baur, G. Rempe, and S. Dürr, "Coherent Logic Gate for Light Pulses Based on Storage in a Bose-Einstein Condensate," *Phys. Rev. Lett.*, vol. 109, no. 26, p. 263602, 2012.

[162] A. I. Lvovsky, "Continuous-variable optical quantum-state tomography," *Reviews of Modern Physics*, vol. 81, no. 1, pp. 299–332, 2009.

[163] D. A. R. Dalvit, J. Dziarmaga, and W. H. Zurek, "Decoherence in Bose-Einstein condensates: Towards bigger and better Schrödinger cats," *Phys. Rev. A*, vol. 62, no. 1, p. 013607, 2000.

[164] M. Lettner, M. Mücke, S. Riedl, C. Vo, C. Hahn, S. Baur, J. Bochmann, S. Ritter, S. Dürr, and G. Rempe, "Remote Entanglement between a Single Atom and a Bose-Einstein Condensate," *Phys. Rev. Lett.*, vol. 106, no. 21, p. 210503, 2011.

[165] Z. Dutton and L. V. Hau, "Storing and processing optical information with ultraslow light in Bose-Einstein condensates," *Phys. Rev. A*, vol. 70, no. 5, p. 053831, 2004.

[166] C. Liu, Z. Dutton, C. H. Behroozi, and L. V. Hau, "Observation of coherent optical information storage in an atomic medium using halted light pulses," *Nature*, vol. 409, no. 6819, pp. 490–493, 2001.

[167] L. V. Hau, S. E. Harris, Z. Dutton, and C. H. Behroozi, "Light speed reduction to 17 metres per second in an ultracold atomic gas," *Nature*, vol. 397, no. 6720, pp. 594–598, 1999.

[168] N. S. Ginsberg, S. R. Garner, and L. V. Hau, "Coherent control of optical information with matter wave dynamics," *Nature*, vol. 445, no. 7128, pp. 623–626, 2007.

[169] M. Fleischhauer and M. D. Lukin, "Dark-state polaritons in electromagnetically induced transparency," *Physical Review Letters*, vol. 84, no. 22, p. 5094, 2000.

[170] D. F. Phillips, A. Fleischhauer, A. Mair, R. L. Walsworth, and M. D. Lukin, "Storage of light in atomic vapor," *Physical Review Letters*, vol. 86, no. 5, p. 783, 2001.

[171] J. M. Radcliffe, "Some properties of coherent spin states," *J. Phys. A: Gen. Phys.*, vol. 4, no. 3, p. 313, 1971.

[172] B. D. Esry, C. H. Greene, J. Burke, and J. L. Bohn, "Hartree-Fock Theory for Double Condensates," *Phys. Rev. Lett.*, vol. 78, no. 19, pp. 3594–3597, 1997.

[173] L. Pitaevskii and S. Stringari, *Bose-Einstein Condensation*. Oxford University Press, USA, 2003.

[174] M. L. Chiofalo, S. Succi, and M. P. Tosi, "Ground state of trapped interacting Bose-Einstein condensates by an explicit imaginary-time algorithm," *Phys. Rev. E*, vol. 62, no. 5, pp. 7438–7444, 2000.

[175] H. Pu and N. P. Bigelow, "Properties of Two-Species Bose Condensates," *Phys. Rev. Lett.*, vol. 80, no. 6, pp. 1130–1133, 1998.

[176] C. M. Trail, K. Almutairi, D. L. Feder, and B. C. Sanders, "Nonlinear phase shifts of light trapped in a two-component Bose-Einstein condensate," *Phys. Rev. A*, vol. 89, no. 6, p. 063823, 2014.

[177] D. M. Stamper-Kurn, M. R. Andrews, A. P. Chikkatur, S. Inouye, H.-J. Miesner, J. Stenger, and W. Ketterle, "Optical Confinement of a Bose-Einstein Condensate," *Phys. Rev. Lett.*, vol. 80, no. 10, pp. 2027–2030, 1998.

[178] Y. Li, Y. Castin, and A. Sinatra, "Optimum Spin Squeezing in Bose-Einstein Condensates with Particle Losses," *Phys. Rev. Lett.*, vol. 100, no. 21, p. 210401, 2008.

[179] Y. Li, P. Treutlein, J. Reichel, and A. Sinatra, "Spin squeezing in a bimodal condensate: spatial dynamics and particle losses," *Eur. Phys. J. B*, vol. 68, no. 3, pp. 365–381, 2009.

[180] M. Greiner, O. Mandel, T. W. Hänsch, and I. Bloch, "Collapse and revival of the matter wave field of a Bose-Einstein condensate," *Nature*, vol. 419, no. 6902, pp. 51–54, 2002.

[181] A. V. Gorshkov, A. André, M. D. Lukin, and A. S. Sørensen, "Photon storage in -type optically dense atomic media. II. Free-space model," *Physical Review A*, vol. 76, no. 3, p. 033805, 2007.

[182] G. Björk and P. G. L. Mana, "A size criterion for macroscopic superposition states," *Journal of Optics B: Quantum and Semiclassical Optics*, vol. 6, no. 11, p. 429, 2004.

[183] T.-L. Ho and V. B. Shenoy, "Binary Mixtures of Bose Condensates of Alkali Atoms," *Phys. Rev. Lett.*, vol. 77, no. 16, pp. 3276–3279, 1996.

[184] D. B. Hume, I. Stroescu, M. Joos, W. Muessel, H. Strobel, and M. K. Oberthaler, "Accurate Atom Counting in Mesoscopic Ensembles," *Phys. Rev. Lett.*, vol. 111, no. 25, p. 253001, 2013.

[185] B. M. Garraway and P. L. Knight, "Comparison of quantum-state diffusion and quantum-jump simulations of two-photon processes in a dissipative environment," *Phys. Rev. A*, vol. 49, no. 2, pp. 1266–1274, 1994.

[186] M. B. Plenio and P. L. Knight, "The quantum-jump approach to dissipative dynamics in quantum optics," *Rev. Mod. Phys.*, vol. 70, no. 1, pp. 101–144, 1998.

[187] J. Stuhler, A. Griesmaier, T. Koch, M. Fattori, T. Pfau, S. Giovanazzi, P. Pedri, and L. Santos, "Observation of Dipole-Dipole Interaction in a Degenerate Quantum Gas," *Phys. Rev. Lett.*, vol. 95, no. 15, p. 150406, 2005.

[188] M. Saffman, T. G. Walker, and K. Mølmer, "Quantum information with Rydberg atoms," *Rev. Mod. Phys.*, vol. 82, no. 3, pp. 2313–2363, 2010.

[189] J. S. Douglas, H. Habibian, C.-L. Hung, A. V. Gorshkov, H. J. Kimble, and D. E. Chang, "Quantum many-body models with cold atoms coupled to photonic crystals," *Nat Photon*, vol. 9, no. 5, pp. 326–331, 2015.

[190] A. González-Tudela, C.-L. Hung, D. E. Chang, J. I. Cirac, and H. J. Kimble, "Subwavelength vacuum lattices and atom-atom interactions in two-dimensional photonic crystals," *Nat Photon*, vol. 9, no. 5, pp. 320–325, 2015.

[191] O. Dutta, M. Gajda, P. Hauke, M. Lewenstein, D.-S. Lühmann, B. A. Malomed, T. Sowiński, and J. Zakrzewski, "Non-standard Hubbard models in optical lattices: a review," *Rep. Prog. Phys.*, vol. 78, no. 6, p. 066001, 2015.

[192] D. Witthaut and M. Timme, "Kuramoto dynamics in Hamiltonian systems," *Phys. Rev. E*, vol. 90, no. 3, p. 032917, 2014.

[193] D. C. McKay, C. Meldgin, D. Chen, and B. DeMarco, "Slow Thermalization between a Lattice and Free Bose Gas," *Phys. Rev. Lett.*, vol. 111, no. 6, p. 063002, 2013.

[194] A. Trombettoni and A. Smerzi, "Discrete Solitons and Breathers with Dilute Bose-Einstein Condensates," *Phys. Rev. Lett.*, vol. 86, no. 11, pp. 2353–2356, 2001.

[195] J. C. Eilbeck, P. S. Lomdahl, and A. C. Scott, "The discrete self-trapping equation," *Physica D: Nonlinear Phenomena*, vol. 16, no. 3, pp. 318–338, 1985.

[196] E. Brion, L. H. Pedersen, and K. Mølmer, "Adiabatic elimination in a lambda system," *J. Phys. A: Math. Theor.*, vol. 40, no. 5, p. 1033, 2007.

[197] I. Bloch, "Ultracold quantum gases in optical lattices," *Nat Phys*, vol. 1, no. 1, pp. 23–30, 2005.

[198] B. Gadway, D. Pertot, J. Reeves, and D. Schneble, "Probing an ultracold-atom crystal with matter waves," *Nat Phys*, vol. 8, no. 7, pp. 544–549, 2012.

[199] V. M. Bastidas, I. Omelchenko, A. Zakharova, E. Schöll, and T. Brandes, "Quantum signatures of chimera states," *Phys. Rev. E*, vol. 92, no. 6, p. 062924, 2015.

[200] T. E. Lee and H. R. Sadeghpour, "Quantum Synchronization of Quantum van der Pol Oscillators with Trapped Ions," *Phys. Rev. Lett.*, vol. 111, no. 23, p. 234101, 2013.

[201] R. Landig, L. Hruby, N. Dogra, M. Landini, R. Mottl, T. Donner, and T. Esslinger, "Quantum phases from competing short- and long-range interactions in an optical lattice," *Nature*, vol. 532, no. 7600, pp. 476–479, 2016.

[202] Q. Thommen, J. C. Garreau, and V. Zehnlé, "Classical Chaos with Bose-Einstein Condensates in Tilted Optical Lattices," *Phys. Rev. Lett.*, vol. 91, no. 21, p. 210405, 2003.

[203] X. Antoine, W. Bao, and C. Besse, "Computational methods for the dynamics of the nonlinear Schrödinger/Gross-Pitaevskii equations," *Computer Physics Communications*, vol. 184, no. 12, pp. 2621–2633, 2013.

[204] Winfried Auzinger and Othmar Koch, "Coefficients of various splitting methods (http://www.asc.tuwien.ac.at/˜winfried/splitting/)."

[205] G. M. Zaslavsky, *Hamiltonian chaos and fractional dynamics*. Oxford University Press on Demand, 2005.

[206] K. Zhang, "Hamiltonian chaos in a coupled BEC-optomechanical-cavity system," *Phys. Rev. A*, vol. 81, no. 1, 2010.

[207] A. J. Leggett, "Can a Solid Be "Superfluid"?," *Phys. Rev. Lett.*, vol. 25, no. 22, pp. 1543–1546, 1970.

[208] G. V. Chester, "Speculations on Bose-Einstein Condensation and Quantum Crystals," *Phys. Rev. A*, vol. 2, no. 1, pp. 256–258, 1970.